Influence of air-water interface condition on rotating flow stability : experimental and numerical exploration

Antoine Faugaret

THÈSE DE DOCTORAT
DE SORBONNE UNIVERSITÉ

Spécialité : Mécanique des Fluides

École doctorale nº391: Sciences Mécaniques, Acoustique, Electronique et Robotique de Paris

réalisée

au Laboratoire d'Informatique pour la Mécanique et les Sciences de l'Ingénieur

sous la direction de Laurent MARTIN WITKOWSKI

présentée par

Antoine FAUGARET

pour obtenir le grade de :

DOCTEUR DE SORBONNE UNIVERSITÉ

Sujet de la thèse :

Influence of air-water interface condition on rotating flow stability : experimental and numerical exploration.

soutenue le 25 septembre 2020

devant le jury composé de :

M.	Valéry BOTTON	Rapporteur
M.	David FABRE	Rapporteur
M.	Arnaud ANTKOWIAK	Président
Mme	Laurette TUCKERMAN	Examinatrice
Mme	Emmanuelle RIO	Examinatrice
M.	Yohann DUGUET	Co-encadrant
M.	Laurent MARTIN WITKOWSKI	Directeur de thèse

Remerciements

Si le choix a été fait de rédiger cette thèse en anglais, par soucis de continuité avec l'article qu'elle incorpore, et pour en faciliter l'accès aux éventuels doctorants (ou chercheurs) étrangers qui pourraient être amenés à étudier des sujets connexes, l'ensemble des personnes qui ont rendu ce travail de thèse possible sont francophones ou, tout du moins, parlent couramment français. Aussi, avant de rentrer dans le vif du sujet, voici quelques mots dans la langue de Molière afin de les remercier.

Je souhaite en premier lieu exprimer tout ma gratitude à Laurent Martin-Witkowski, qui m'a proposé cette thèse. Je le remercie pour l'initiation de la recherche sous sa direction, ainsi que pour m'avoir renouvelé sa confiance après deux stages de master. Je le remercie également pour les échanges riches d'enseignements au cours de ces années de thèse et pour l'autonomie qu'il m'a laissé au cours de son déroulement.

Cette thèse, ainsi que l'article, ne seraient pas ce qu'ils sont sans l'implication de Yohan Duguet que je remercie pour son intérêt et sa contribution au sujet. Je le remercie également pour les discussions enrichissantes et sources de nombreuses hypothèses qui ont permis l'avancement de la thèse.

Je remercie Yann Fraigneau, pour sa collaboration à l'article, ainsi que son support dans le développement et l'exploitation du code de calcul Sunfluidh.

Cette thèse a également connu des contributeurs au delà des murs du LIMSI. Ainsi, les mesures de déplacement des disques n'auraient pas été permises sans les apports de Yves Bernard et de Laurent Daniel du GeePS.

Je pense ici également aux membres du Jury : Mesdames Laurette Tuckerman et Emmanuelle Rio, Messieurs Arnaud Antkowiak, Valéry Botton et David Fabre. Ma reconnaissance envers ce jury est d'autant plus grande qu'ils ont dû subir le report de la soutenance pour cause de COVID. Je tiens donc à les remercier tous pour leur patience, mais aussi pour le temps consacré à lire, et peut être relire, ce manuscrit. Je souhaite remercier tout particulièrement Valéry Botton et David Fabre, pour avoir accepté la tâche de rapporteur, et pour tout l'intérêt et la conviction qu'ils y ont porté.

Je tiens à remercier François Lusseyran pour le partage de la LDV, les nombreux échanges qui s'en sont suivis, et son support avec Dantec. Par ailleurs, cette partie expérimentale n'aurait pas été permise sans le prêt ou la cannibalisation des matériels de

Smaïn Kouidri, Marie-Christine Duluc et de Diana Baltean, mais aussi de précédentes expériences du FAST. Mes remerciements à eux pour leur apport à ces travaux.

De façon plus globale, je remercie l'ensemble du département mécanique du LIMSI, pour l'ambiance et le cadre dont j'ai pu bénéficier au cours de ces années de thèse. Une pensée plus spécifique pour Ivan Delbende, qui a permis de faire démarrer cette thèse. Et comme le LIMSI ne se limite pas à ses chercheurs, j'ai également une pensée pour les équipes techniques, l'équipe CTEMO en particulier, qui a pris une part active dans la fabrication des bancs expérimentaux. Je remercie aussi la direction du LIMSI qui a permis mon accueil dans le laboratoire, et l'équipe administrative pour leurs réponses et leur patiente face aux diverses démarches.

Et parce que LIMSI ne serait pas au complet sans ses doctorants, je les remercie de m'avoir supporté durant ces longs mois, et pour les soirées crêpes, jeux de société, ou autres bons moments qui sont venus égayer la vie du bureau. Un merci particulier à Wen Yang pour nos échanges de codes, de retours d'expériences, ou de techniques expérimentales.

Enfin, ma prose est bien incapable de retranscrire le soutien indéfectible de mes parents au cours de toutes ces années d'études, et je n'ai donc à leur offrir que la simplicité et la sincérité d'un seul mot : Merci.

Contents

Nomenclature

α	dimensioned parameter used in model for K1 vitamin
β	dimensionless parameter used in pollutant model
ΔR	absolute uncertainty on the cavity radius
ΔH	absolute uncertainty on the fluid height
Δh	surface deflection
ϵ	convergence criterion
ϵ_R	gap between the disc and the cavity wall
Γ	angular momentum
κ	dimensionless parameter used in Robin condition model
κ^s	surface dilatational viscosity
λ	eigenvalue
$\boldsymbol{\tau}$	tangential vector
μ	dynamic viscosity
μ^s	surface shear viscosity
ν	kinematic viscosity
Ω	angular frequency of the disc
ω	vorticity
ω_θ	azimuthal vorticity
ω_z	axial vorticity
ψ	stream function
ρ	density
σ_0	reference surface tension

σ surface tension

θ angle or phase

c dimensionless pollutant concentration

C_0 reference pollutant concentration

c_d dimensioned pollutant concentration

Ca capillary number

D diffusion coefficient

f frequency

Fr Froude number

G aspect ratio

H height of fluid

i imaginary unit

m azimuthal wave number

Ma Marangoni number

$\mathbf{n}$ normal vector

p pressure

Pe Péclet number

R radius of the cavity

R_d radius of the disc

Re Reynolds number

Re_c critical Reynolds number

$\bar{\bar{S}}$ constraints tensor, or Cauchy stress tensor

$\bar{\bar{T}}$ viscous constraints tensor

t time

$\mathbf{u}$ velocity vector

U_r, U_θ, U_z base flow velocity components in radial, azimuthal, and axial directions, respectively

u_r, u_θ, u_z velocity components in radial, azimuthal, and axial directions, respectively

u_r^*, u_θ^*, u_z^* velocity components of perturbations in radial, azimuthal, and axial directions, respectively

Introduction

Fluids, rotation and instability : a never ending story

From space to laboratory

Earth. There are probably as many definitions of this little planet we live on as the numbers of souls on its surface. But imagine seeing this beauty from space, for the first time, like a space traveller only equipped with his ignorance. What would you see, how could you describe it ? A sphere that rotates quietly around its axis, mostly composed of water, and surrounded by a thin layer of gas. And there we are. The simplest vision of our world already enters the heart of the matter : the combination of rotation and fluids.

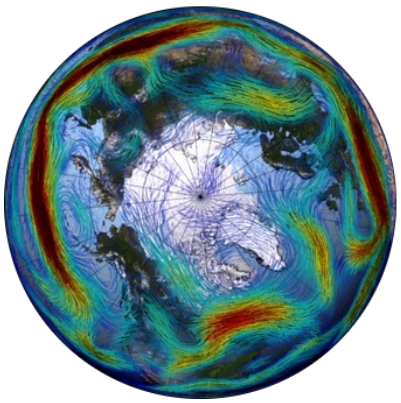

Figure .1 – Rossby wave around the North pole (animation from NASA's Goddard Space Flight Center).

The combination of these two elements gives rise to large scale phenomena, in oceans and in the atmosphere, such as Rossby waves illustrated in figure .1. At much smaller scale, interactions between rotation and fluids are still present. Turbomachines are abundant in the industry, where, no matter what the configuration (sphere(s), disc(s), blades,...) and the phase (gas, liquid), the flow drives or is driven by a rotating element.

This omnipresence of rotating fluids in nature and in human technical challenges justifies their importance in research. But whereas rotation and fluids are easily observable everywhere around us, one ingredient is still missing in our triptych : instabilities.

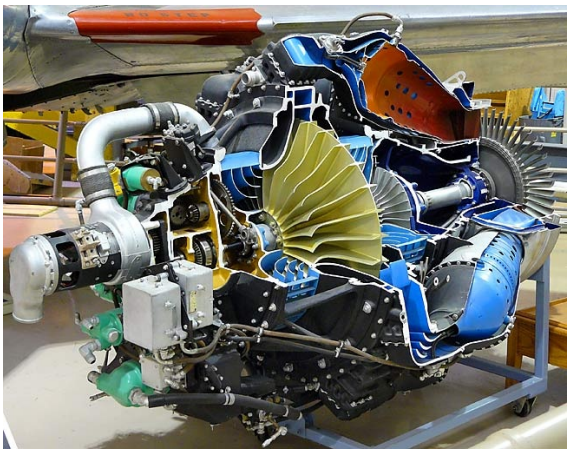

Figure .2 – Turbojets are a good example of turbomachines in which the flow is firstly driven by the rotor of the compressor, and then drives the turbine that rotates the compressor. Here, on this Rolls Royce Nene engine, the centrifugal compressor is at the intake (in pale green), while the turbine is at the end of the shaft, at the outlet of combustion chambers.

Instability : an essential quest

A system in an equilibrium state is called stable if a perturbation does not cause it to evolve towards another state. By extension, the system is said unstable if a small perturbation produces a deviation from the equilibrium state to another state. One common example is the pendulum with a rigid rod in a gravity field.

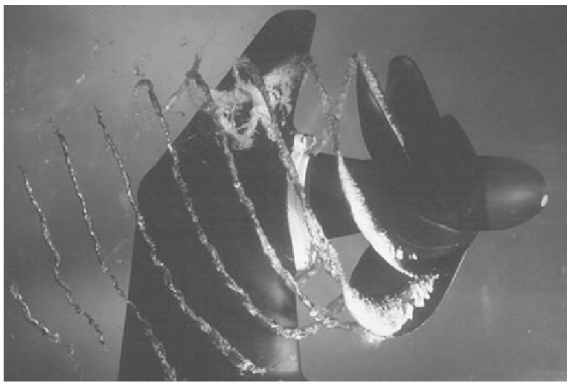

Figure .3 – Cavitation surge instability on a naval propeller. This instability is characterized by a periodic fluctuation in the cavitation extent, generating dramatic pressure fluctuations on the propeller. This can force vibrations of the shaft, and damage it. Cavitation can also destroy propeller blades and therefore many studies are devoted to its understanding, in order to avoid it.

Past this naive vision of instabilities are hidden complex phenomena with multiple faces. Their impact can be as negligible, positive, such as increasing mixing in chemical reactors, or detrimental : increasing the drag, vibrations, and even destroying the machine (figure .3).

Indeed, instabilities are not limited to man made mechanisms, but can also be seen in natural events : an example of a spectacular and harmless natural instability is given in figure .4.

Figure .4 – The famous Kelvin-Helmholtz shear instability can sometimes be seen in natural conditions, and not only in monitored laboratory environment. This picture was taken on January 26, 2019 by Hannah Martin, above the Mount Helena, Montana. The Kelvin-Helmholtz instability manifests itself when two layers of fluids with viscosities of the same order of magnitude, are moving at different velocities.

Beside the beauty of such phenomena, a better understanding of instabilities has practical interest. The first step is to be able to predict their occurrence. Then, regarding the goal, one may wish to avoid it, or, on the contrary, to force their growth. The ability to drive instabilities gave rise over the last decade to a growing interest of the instability community for control (see fig. .5).

Electroactive actuators ?

A possible solution for controlling fluid flows are electroactive actuators such as piezoelectric actuators, shape memory alloys, or electroactive polymers. Electroactive actuators are devices that generate a controlled movement as an electric tension is applied to them. On electroactive polymers, an electric stimulation is also used to modulate the shape of the material (see figure .6).

The main subject of this thesis is that of a rotating disk driving a fluid into motion. It is well known that any rotating system can generate vibrations and a perfectly axisymmetric system is difficult to achieve. A standard solution consists in adding calibrated masses to correct unbalanced rotation. This solution is efficient at high rotation speeds, on car wheels for example, but can not help in the case of small rotation speed. In the case of a fluid driven by a rotating disc, one needs to insure the most ideal flatness of the disc's surface especially as instabilities are involved. Therefore, once vibrations of the

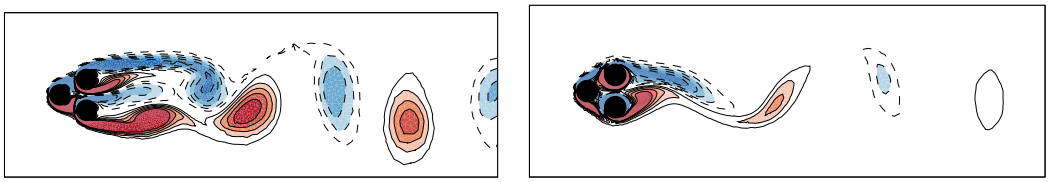

(a) Natural Flow. (b) Controlled flow.

Figure .5 – An exemple of instability control on the von Karman street under development at LIMSI. The goal is to reduce the drag behind three cylinders with a rotation of the two rear cylinders at a minimal cost : the energy spent to spin cylinders must not exceed the energy gain of the drag reduction (private communication with the author of the figures, G. Y. Cornejo Maceda). In figure .5a, cylinders are fixed, while in figure .5b, the top rear cylinder rotates clockwise and the bottom rear cylinder rotates counter clockwise, while the front cylinder does not rotate. This "boat tailing" configuration reduces the vortices in the wake, and therefore reduces the drag compared to the single cylinder configuration.

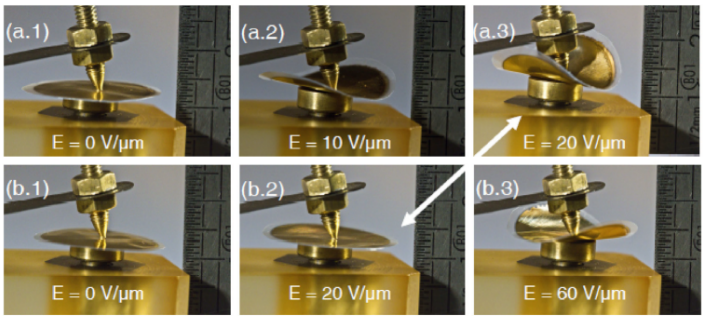

Figure .6 – Electroactive polymer under several tension. This polymer is composed of two layers of conductor material, separated by an insulating material. The potential difference between the two conductor layers forces the bending of the polymer.

disc are fully quantified, the adaptation of electroactive actuators should compensate the imperfections of the disc. If the imperfections are small, the use of piezo electric devices can be sufficient. If large deformations are targeted then electroactive polymers or shape memory alloys should be used. This can also lead to a second application which consists of shaping the disc surface to a desired pattern, in order to control instability.

Examples of applications of both solutions can be found in aeronautics, in order to control the flow around a wing (fig. .7). Piezoelectric actuators generate a traveling wave of the trailing edge, and allows to split large vortices structures into smaller ones. This ripple, inspired from birds' plumage movement, reduces the drag of the wing. Other projects use piezoceramic composite actuator to vary the camber of the wing, in order to adapt it regarding the flight envelope.

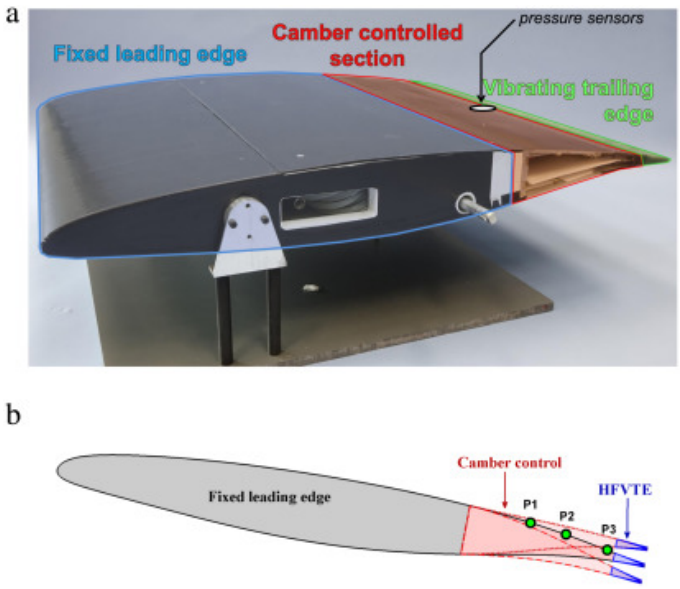

Figure .7 – Morphing wing prototype from the Institut de Mécanique des Fluides de Toulouse (IMFT), using piezoelectric actuators for the oscillating trailing edge, and an electroactive polymer for the camber variation.

A quick glance at the studied case

The configuration considered in this thesis is one of the simplest rotating flow experiments : a flat disc rotating at the bottom of a fixed cylindrical cavity. A liquid partially fills the cavity above the disc, and the upper interface of this liquid is only in contact with ambient air, without further constraint. Despite this simplicity, two different instabilities take place in such a configuration : at high rotation rates, deformations of the surface can draw polygons. But even without reaching such regimes, a first instability occurs while the surface is still flat. Only visible when a marker is added to the flow, this quiet instability appeared more complex than expected (fig. .8).

The observed instabilities raise three fundamental questions :

- Is this instability reproducible ?
- How sensitive are instabilities to mechanical vibrations ?
- Can instabilities be controlled with a dynamic shaping of the disc surface ?

Science is made of bounces

To answer these questions, an ANR project has been set up around the collaboration between the Laboratoire d'Informatique pour la Mécanique et les Sciences de l'Ingénieur (LIMSI) and the Génie électrique et électronique de Paris (GeePs) laboratory, using their

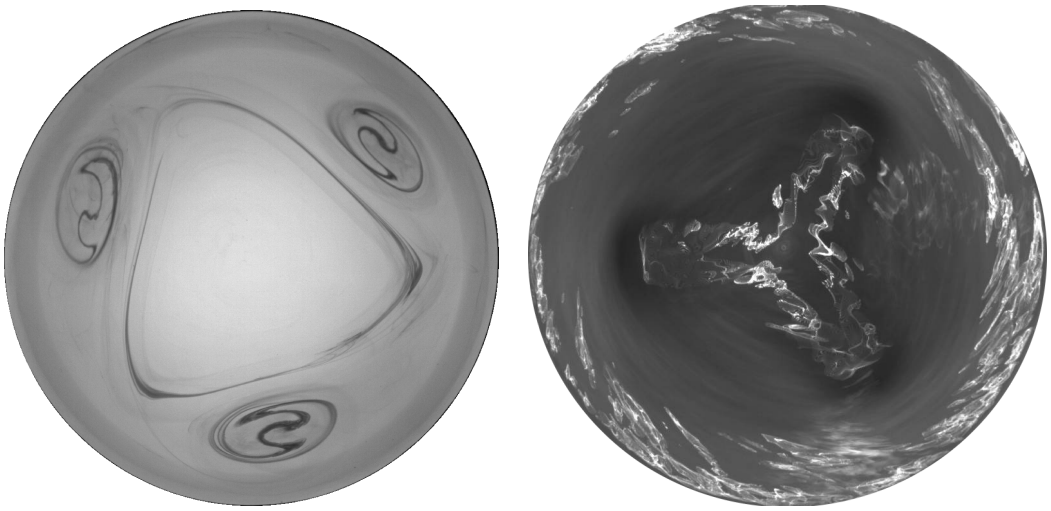

(a) Low rotation speed, flat surface (b) High rotation speed, shaped interface

Figure .8 – Two different instabilities generated by a rotating disc in a fixed cylindrical cavity (observed from above the disk in the present work setup). On the left, the surface is flat, and the pattern is only visible when marker is introduced (ink). On the right, the air water interface is heavily deformed, such as the disc is dewetted at its center, and along each arm of the pattern.

complementary skills. Indeed, this thesis was initially entitled "Rotating flow and electroactive actuator", with the same title as the ANR project that funded this work. However, the first measurements of vibrations of the experimental bench quickly invalidate the hypothesis of a premature growing of instabilities due to a mechanical noise forcing. Therefore, before expecting to control instabilities, we had to redirect our research in order to better understand the instability.

The use of very accurate velocity measurement devices such as Laser Doppler Velocimetry (LDV) and comparison with numerical simulations quickly convinced us that the ait water interface condition plays a major role on the instability at low rotation speed. For this reason, the major part of this thesis does not actually deal with actuators, but investigates and models the role played by the interface on the instability.

Organisation

The first chapter is dedicated to a survey of articles that are linked to the subject of this thesis, and a brief history of this configuration in LIMSI is also presented. The second chapter enters more directly into the subject. It is a stand-alone paper, submitted to Journal of Fluid Mechanics (JFM), that gathers almost all the results of the main studied case for a given fluid filling in the cavity.

The rest of this thesis extends the findings of the second chapter, but applied to different fluid filling heights. The pertinent key results of the article are summarized in

each chapter's introduction in order to make the reading easier. Repetitions were avoided as much as possible. However some points, such as experimental set-ups, and numerical codes details, are necessary both in the paper, and in the thesis. More details are given in the thesis chapters, especially on equations used in codes. Chapters III to V are respectively dedicated to experimental tools, equations and numerical methods. Chapter VIth focuses on matches and mismatches between experimental results and simulations performed with a traditional free slip condition at the surface. Chapter VII deviates from fluid mechanics, and concentrates on the study of the vibrating disc surface. After this solid mechanics interlude, the next chapter gathers first and second attempt to modify the condition at the surface : both are linked to a sudden change of the radial velocity at the flow surface. The last chapter before the conclusion of this thesis is a bit more sizable. It is dedicated to the building of a more complex model, taking into account the quantity of undetermined pollutants at the interface. These pollutants, acting like surfactants, modify the surface tension of the fluid : regarding the concentration of pollutants, the surface is more or less "stiffen". In order to clarify this model, the first part of the chapter is devoted to a small bibliography, listing articles that helped us in the construction of the model. Equations used are also detailed in this part. The second part of the chapter groups results of this model obtained on the same cases as in previous chapters. Finally, a third part revisits former simulations that were deemed of minor interest before the pollutant based model shed new light on them.

Chapter I

Problem description

Description of the configuration

The flow considered in this study is generated by a spinning disk located at the bottom of a fixed cylindrical cavity. This cavity is filled with a liquid. The top surface of the fluid remains free (only in contact with ambient air). For more convenience in the upcoming chapter, the aspect ratio G and the Reynolds number are introduced. The first one is defined as the ratio between the radius of the cavity R and the height H of fluid above the disk : $G = H/R$, while the second compares inertia forces to diffusive forces : $Re = R^2\Omega/\nu$. Here, Ω denotes the disc rotation rate, while ν is the kinematic viscosity.

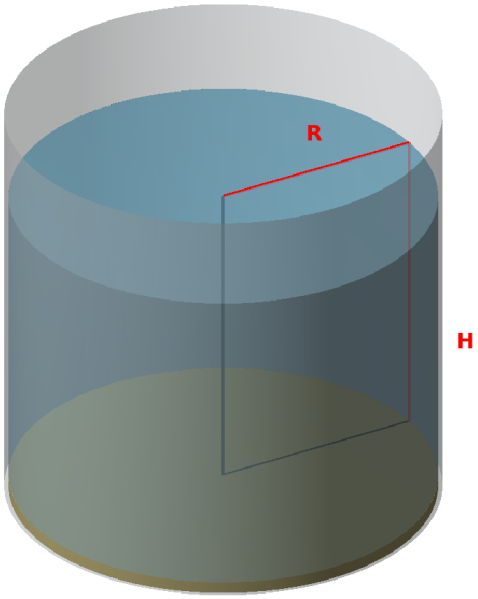

Figure I.1 – Sketch of the cavity. R is the radius of the cavity, H is the height of the fluid at rest (in blue) above the rotating disc (in yellow). A more detailed description of the set-up is given in Chapter III : Experimental tools.

Bibliography

This chapter is dedicated to an exploration of the bibliography that is linked, in one way or another, to instabilities in a rotating flow with a free surface. Since only few articles effectively deal with this precise topic, many of the papers quoted below introduce more global concerns on rotating flows, or on some specific phenomenons observed in such configuration.

Therefore, this bibliography starts with global thoughts about the flow described above or between infinite discs. Then bounding the domain in the radial direction, we get closer to our configuration and introduce the first concern of science in bounded rotating flows, with or without a free surface. After a parenthesis on experimental set-ups used to reproduce geostrophic flows, a fourth part focuses on the instability that occurs when high

rotation rates are reached with a large deformation of the free surface. The final part of this bibliography focuses on flat free surface rotating flows.

A last section returns to what has already been developed in the laboratory on rotating flows and sets the logical and chronological framework within which this thesis falls.

Early works

Semi infinite domain

In the beginning of the 20^{th} century, Ekman published in [1] the solution for a rotating disc in a steady flow. His result, known as Ekman transport, brings a new light on geophysical flows, as it explains the deviation of the flow near the ground, under combined effects of wind and the Coriolis force. A bit later, in 1921, von Kármán solved the problem of a flow initially at rest above an infinite rotating disc ([2]). Bödewadt then brought the solution to the "opposite" problem of a fluid in solid body rotation flow above an infinite plane. These three flows were gathered under the name of "BEK Flows" (Bödewadt, Ekman, and von Karman) by Lingwood [3]. In this configuration, the domain extends to infinity in both axial and radial directions.

Flows between two discs of infinite radius

Six years after the end of the second world war, Batchelor published results for the two boundary layers that develop between two co-rotating discs ([4]). Stewartson also used the two disc configuration, but while one is rotating, the second remains fixed. In this rotor-stator configuration, and despite what Batchelor predicted two years earlier, Stewartson demonstrated the existence of a single boundary layer on the rotor, while the tangential velocity of the flow remains zero everywhere else ([5]). This led to a controversy that lasted thirty years, only settled in 1983, when Kreiss and Parter [6] demonstrated the co-existence of the two solutions...

All these works can be considered to be cornerstones to studies of flow above and between rotating discs. It also illustrates the depth of rotating flow studies, highlighting how what could be considered as minor change in the configuration can have a major impact on the solution of the problem.

Confined rotating flows

In many practical applications, the flow is not only bounded in the axial direction, but also in the radial direction. Indeed, rotating fluids in confined geometry have been widely used through the ages. An example can be found as early as in the $\mathrm{IV}^{\mathrm{th}}$ century B.C. In the Hanging Gardens of Babylon, a device for pumping water was used to obtain lush vegetation. This device was later known as "Archimedes' screw". Enclosed rotating flows are not just ghosts of a fallen civilization's technology, but are also present in most modern turbines used in aircraft or naval propulsion, or for electricity production.

In scientific research, configurations studied rely on simpler geometries, composed of a fixed cylinder with a rotating disc. Two variants are mainly used. In the first one, a lid, attached to the fixed cylindrical wall, is placed in direct contact with water. In the second one, the surface remains in contact with ambient air, as illustrated in figure I.1.

In both cases, when the disc is spinning, fluid is set into rotation in its vicinity. Provided that the upper layers of fluid rotate slower than the disc, the fluid is also flushed toward the periphery. Since the radial extent of the cavity is finite, the fluid is forced to change direction and to flow vertically along the cylinder wall. By continuity, the fluid flows along the upper bound of the fluid, and returns toward the rotating disc along the axis. This creates a large recirculation in the meridional plane.

Vortex Breakdown

For a certain range of parameters (G and Re), the fluid may flow in opposite direction to this main meridional circulation in a limited region along the axis. This creates a small recirculation bubble called vortex breakdown.

Surprisingly, this phenomenon was firstly observed in a completely different configuration : in 1957 by Peckham and Atkinson, described in [7] the sudden change in the physiognomy of a columnar vortex at the tip of a delta wing, and gave it the name of vortex breakdown. By extension, this name was later used in a closed cylindrical cavity, as described above.

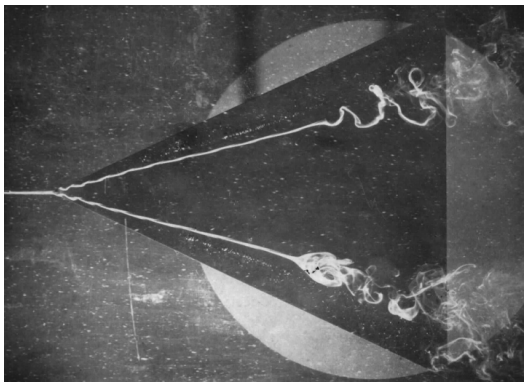

Figure I.2 – Vortex Breakdown on a delta wing. (Lambourne & Bryer, 1962, [8])

Returning to the cylindrical closed configuration (with a lid), H.U. Vogel experimentally determined in 1968 pairs of parameters (G,Re) for which vortex breakdown occurs [9].

H.L. Lugt then conducted in 1982 the first simulation of vortex breakdown in a closed cylindrical cavity of aspect ratio 1.58 [10], and found good agreement with Vogel's predictions.

Two years later, M.P. Escudier published an article entitled "Observation of the flow produced in a closed cylindrical container by a rotating end wall" [11], where he experimentally highlights the formation of recirculation bubbles along the rotation axis of a vertical cylinder, identified as the vortex breakdown (figure I.3).

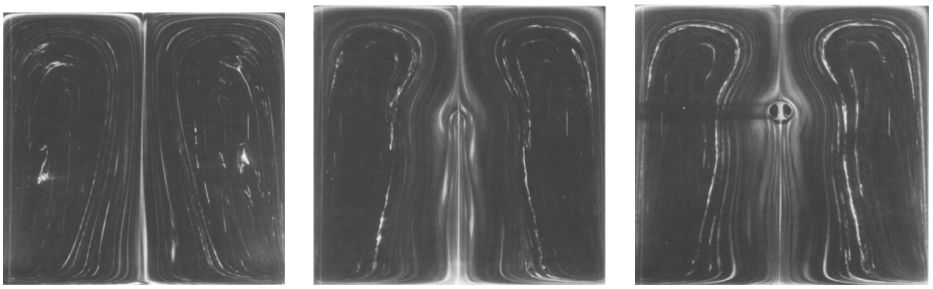

(a) Re=1002 (b) Re=1449 (c) Re=1492

Figure I.3 – Evolution of the columnar vortex (the white vertical line at the axis of rotation in figure I.3a) in a meridional plane, in function of Re, for G=2. The bubble is clearly visible on the axis of ration in figure I.3c. Pictures extracted from [11].

It has been thought that the recirculation bubble is necessarily located on the rotation axis. However, when the upper lid is removed, the recirculation bubble may then be detached from the axis.

This was highlighted in 1993, when A. Spohn *et al.* repeated the experiment of Escudier, but this time without the lid [12]. Spohn studied many aspect ratios, from G=0.5 to G=4, with a step of 0.25. Unlike the previous set-up that used a lid, Spohn described the existence of vortex breakdown for its lowest aspect ratio. But the measurement of the Reynolds number for which bubbles appear was only carried out for aspect ratios higher than G=1. One of the other differences he showed was the location of the bubble : in the absence of a lid, bubbles are attached to the free surface and not to the axis of rotation (figure I.4).

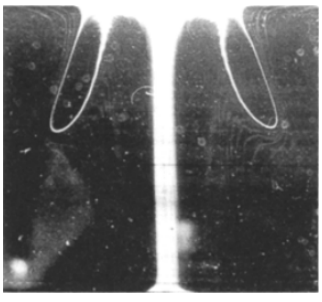

Figure I.4 – Recirculation bubbles for Re=2075 and G=2. Although G is the same as in figure I.3, the experiment introduced here had no lid at the top, on the contrary to [11]. Picture extracted from [12].

Much more recently, E. Serre has numerically investigated vortex breakdown in a cylinder of aspect ratio G=4, with a free surface ([13] and [14]). And in 2005, M. Piva introduced a new parameter into the experiment, with the variation of the rotating disc diameter [15].

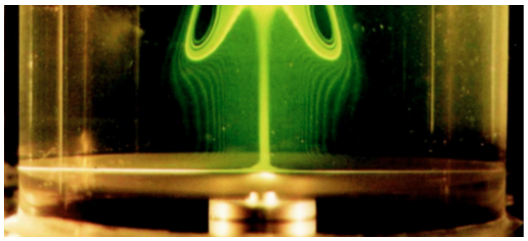

Figure I.5 – Vortex Breakdown in a cylinder of aspect ratio G=1, with a free surface. Figure extracted from [15].

In the same year, R. Iwatsu [16] published a very complete numerical study for aspect ratios from G=0.25 to G=4, including discussions of previous publications.

The occurrence of Vortex breakdown and its origin has been the subject of debate. It has been sometimes believed that the vortex breakdown is triggered by an instability. Actually, this is not the case, but in confined rotating flows, instabilities are responsible for other captivating phenomena that we are now presenting.

Unstable flows between two discs

Configurations used to study instabilities in confined flows put into motion by a rotating disc are numerous. Therefore, we do not claim here to conduct an exhaustive inventory of publications dealing with the subject, but simply to reference a sample of articles that show an instability pattern close to the flat free surface case detailed in a further section.

In 1984, H. Niino and N. Misawa used an experimental apparatus to reproduce the barotropic instability that occurs in oceans and atmosphere [17]. Their set-up is quite complex, composed of a cylindrical cavity that rotates with the lid in one direction while the disc placed at the bottom spins in exact counter rotation, plus another smaller disc that can rotate independently. The whole set up is placed on a rotating table (see fig. I.6). Despite this complexity, they were able to find a good agreement between the linear stability analysis and their experimental determination of the critical Reynolds number. Although they used a lid, their configuration gave rise to vortices that look similar to those observed in our flat free surface configuration.

Still with the aim of reproducing an atmospheric phenomenon in the laboratory, A.C. Barbosa Aguiar *et al.* published an article about a model of Saturn's North pole hexagon [18]. To do so, they built a set up with a rotating cavity that was used in two configurations. The first one is a closed rotating cavity with only an annulus at the top that

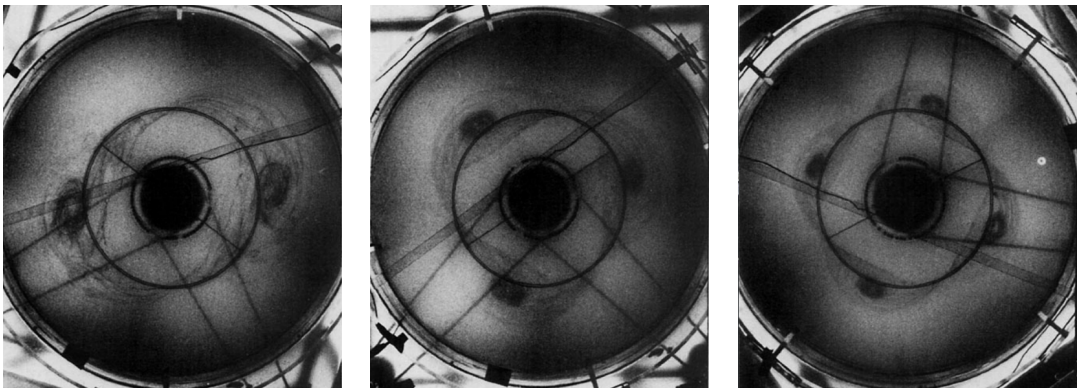

(a) m=2 (b) m=3 (c) m=4

Figure I.6 – Vortices observed in [17]. Black lines are distribution belts.

spin in counter rotation. In the second one, the external part of the cavity (lid, wall and bottom) spins in one direction while the central part (one disc at the top and one at the bottom around the axis) spins in the other direction. Note that the bottom is not flat : it displays a slope of 5°, with its highest point at the axis.

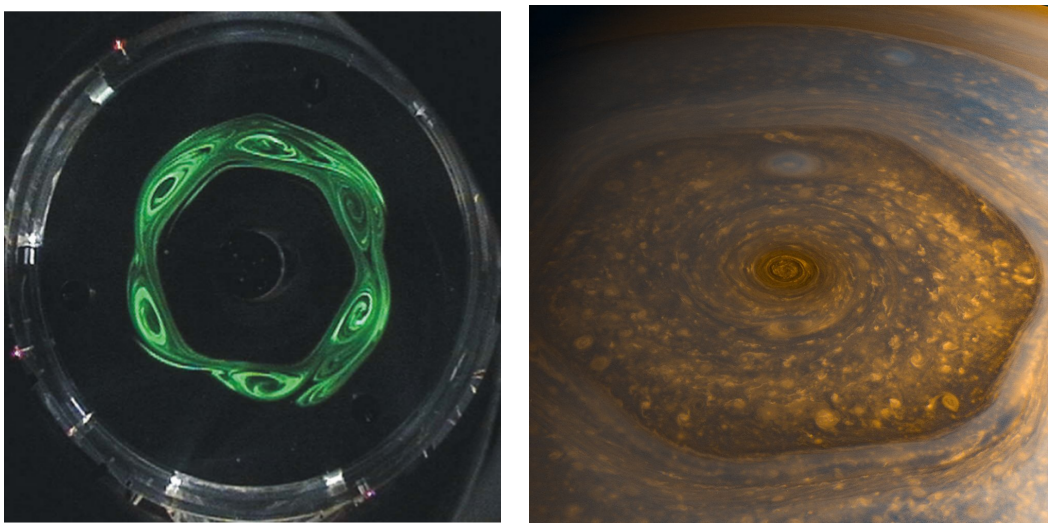

(a) experimental model of Saturn hexagon, from [18].

(b) Saturn North pole hexagon (picture took by the Cassini orbiter, november 2012).

Figure I.7 – Experimental attempt to reproduce the Saturn North pole Hexagon in a laboratory.

A more common configuration is a fixed cylindrical cavity where the flow is driven by a rotating lid, as the one used by M.P. Escudier in 1984. Many articles based on such configurations deals with instability patterns that occur in small aspect ratio. Here we can quote, among many others, the article published by A.Y. Gelfgat in 2015 [19]. This paper includes a wide bibliography and many aspect ratios from 0.1 to 1.0. Another interesting

publication is the numerical study by O. Daube and P. Le Quéré, on the first bifurcation for an aspect ratio of 0.1 [20]. The authors showed the highly subcritical behaviour of the bifurcation, and observed a huge gap between their numerical prediction of the first instability compared to the results obtained by G. Gauthier in his thesis, in 1998 [21]. Indeed the critical Reynolds numbers differ by a factor of 10 between direct simulations and experimental results.

Free surface with deformation

One of the first experiments of a free surface deformation in a rotating flow is probably Newton's bucket. However, the initial goal of this experiment did not concern fluid mechanics : it was an illustration of a philosophical question on rotation and its associated relative frame of reference. Still, in this experience, the rotation moulds the fluid whose surface takes the shape of a parabola. This case configuration is a bit different from previously considered cavities, since the wall rotates with the bottom. Therefore, one may ask whether the result is the same when the vertical wall is stationary ?

H. Goller started to answer this question in his article in 1968 about measurements of the shape of the free surface in a fixed cylinder, with a flow driven by a bottom rotating plate [22].

A. Siginer computed in 1993 the shape of the surface for several aspect ratios from 1/4 to 4 ([23]), while the more classical case of Newton's bucket has been re-visited in 2015 by J. Mougel *et al.* [24].

A new breath in free surface rotating fluid was given in 1990 [25], when G.H. Vatistas published an article about the discovery of a polygonal shaped interface for sufficiently large values of the Froude and Reynolds number. This article was followed by many others in the three last decades, such as [26] from which are extracted the pictures of figure I.8.

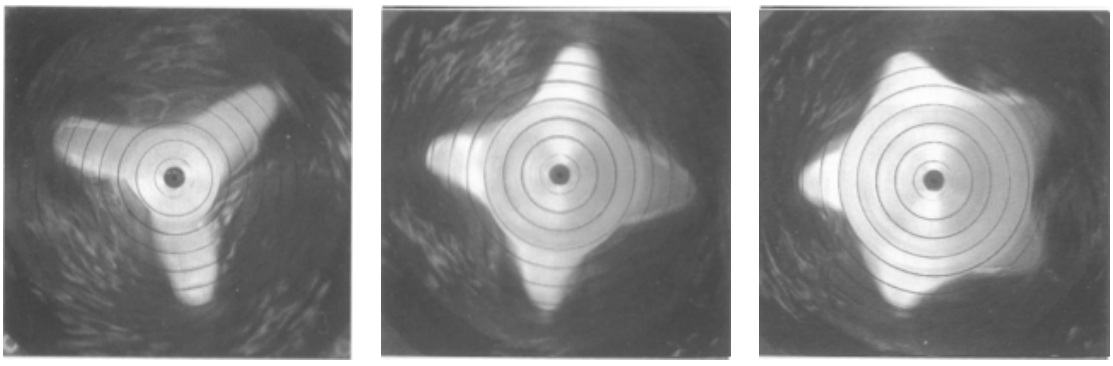

Figure I.8 – Rotating polygons described in [26].

This polygonal shaping of the interface was "rediscovered" more recently in 2006, by T.R.N Jansson [27] and was followed by several other papers : [28], [29], [30], [31], highlighting the attractiveness of the instability with surface deformation.

Even for much smaller rotation rates, and while the interface remains flat, another instability occurs. This instability, harder to visualize, is the main content of this thesis.

Flat free surface

According to our research, the first publication on rotating flow in a vertical cylindrical cavity, with a flat free surface is a numerical study released in 1985, by Jae Min Hyun [32]. In this article, the author describes the base flow in the exact same configuration as ours, for aspect ratios from 0.1 to 1. It gives an interesting framework for numerical approaches, with the dimensionless Navier Stokes equations in the (ω, ψ, Γ) formulation (vorticity, stream function and angular velocity, respectively - see section V.1.2) and the boundary conditions associated with, including the justification of the hypothesis of the flat free surface. Computation were carried out with a finite difference method, mostly with a 41×41 grid. Results include plots of stream function and azimuthal velocity contours in a meridional plane, revealing a recirculation along the outer border.

In 2004, Iwatsu realized an analysis of steady flows [33] and according to the aspect ratio, distinguished the cases $G \ll 1$ and $G \gg 1$. Thanks to progress, both in hardware and in computer science, this paper brings more details on the flow topology than the previous analysis by Hyun.

The two previous papers only deal with steady flows. The first article that evoked the existence of an instability in a fixed cylindrical cavity, with a free surface, dates back, to our knowledge, to 1993 [12]. Actually this article was already referenced in section Vortex Breakdown, since it was the main interest of this paper. However, among their experimental observations, Spohn *et al.* noticed radial oscillations of bubbles in a meridional plane. For aspect ratios from G=0.5 to G=2.75, they reported a transition from steady to unsteady flow for a Reynolds number around 2150. For G=3.0 to 4.0, this Reynolds number increases up to 2920. Asides from the oscillations of bubbles, no visualization was made of an instability pattern.

Two years later, D.L. Young *et al.* [34] noticed the appearance of an oscillation in their LDV measurements of the azimuthal velocity, for a Reynolds number around 1900. Their experience was built around a cylindrical cavity of $184mm$ of internal diameter. The fluid is put into motion by the $182mm$ disk placed at the bottom of the cavity. The aspect ratio used in their experiences is G=2. The main topic of this article is the illustration of period doubling of the oscillations for a Reynolds number around 2200 and the transition to chaos for higher Reynolds numbers.

It was only in 2002 that a new article [35] dealing with our exact configuration is published. It is the work of A.H. Hirsa, J.M. Lopez and R. Miraghaie. This is the first article out of three published on the subject : this one and the second [36] are fairly short, and most of their results are gathered in the third, published in 2004 [37]. In all these publications, two aspect ratios are investigated : G=2 and G=0.25. Their experimental set-up is small since the glass cylinder that composes the cavity is only $5cm$ diameter

wide. Here, the disc is not inside the cavity, but the cavity is held fixed above a rotating disk made of glass. The disk is driven by a stepper motor. In their numerical simulations, the authors used an "extended system" of twice the height of the considered aspect ratio, with two co-rotating disks : one at each end of the cylinder. The baseflow is correctly reproduced by such an "extended system" as the symmetry mimics the free slip boundary condition at the free surface. But the authors enable an odd or even parity with respect to the mid height, leading to the growth of different instability modes, which do not exist in the experiment : the "extended system" deeply modifies the instability modes, both their pattern and theirs critical Reynolds numbers for which they growth.

M.J. Vogel *et al.*, used the same experimental apparatus in 2004 [38], but with a small difference : they added insoluble surfactant at the surface that forms a Langmuir monolayer (an insoluble layer of one-molecule thickness), and reported the patterning of the initially uniformly distributed monolayer to a mode 3 for a Reynolds number of 2000 (the aspect ratio used is 0.25). This short paper merges two previous studies from J.M. Lopez *et al.*. The first one has been described above, and the second one deals with the influence of a monolayer on the base flow in an annular channel. This article ([39]) is not described here, but will be developed in the second bibliography, in chapter IX.

As for the first article introduced in this section, publications from Serre *et al.* ([13] and [14]) previously quoted in section Vortex Breakdown deserve a second quotation here. Indeed, its authors ran simulations above the critical Reynolds number, showing azimuthal pattern with two or three vortices, and describing the instability as a Neimark–Sacker bifurcation.

In 2007, a group from IRPHE performed an exhaustive study of the symmetry breaking. In their article S. Poncet and M.P. Chauve [40] used a rheoscopic marker, Kalliroscope, to experimentally visualize the pattern, and to determine the critical Reynolds numbers of the instability threshold and the Reynolds number of the secondary bifurcations. They explored numerous aspect ratios, from 0.0179 to 0.107, highlighting the existence of a hysteresis cycle and arguing in favour of a subcritical bifurcation. Their experiment eventually included a "hub", *i.e.* an inner cylinder rotating withe the disc. The authors reported that below a certain radius (that depends on the aspect ratio), the presence of the hub has no influence on the instabilities (neither on the threshold, nor on the mode).

Using papers from Vogel *et al.* [38] and Hirsa *et al.* [39] as a framework for their paper [41], YY. Kwan *et al.* proposed, in 2010, an intensive mathematical proof to build a model for incompressible flow with a surfactant monolayer. Then, they briefly compared their model to the previous experiment of J.M. Vogel *et al.*, with a fast-spectral method simulation that shows the surfactant clearing in the vicinity of the external wall, and a good agreement with experiments.

More recently, in his thesis at LIMSI [42], L. Kahouadji returned to the results of Poncet *et al.* [40]. He performed the linear stability analysis of the same aspect ratios as in these experiments. Agreements are very good, both on the mode and the critical

Reynolds number for aspect ratio higher than 0.0714, but deteriorate quickly when the aspect ratio drops below this value. Some of these results were published in [43].

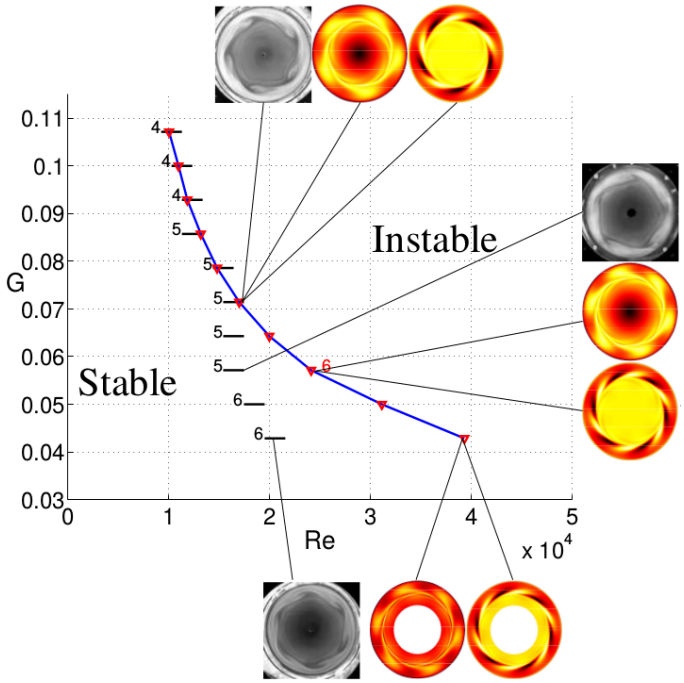

Figure I.9 – Comparison of numerical results of [42] (blue line with red triangles) and experimental results of [40] (black segments) for several values of G. The case G=1/14 (≈0.714) is the limit of the interval of agreement between experiments and numerics. Figure extracted from [42].

In the same period, Cogan *et al.* performed a complete numerical study for G=1.5 ([44]). The authors started with a linear stability analysis for the four first modes, and then conducted several direct numerical simulations (DNS) approaches to show the non linear dynamics of the flow and the pattern of the instability. The agreement between DNS and linear stability analysis appeared to be excellent.

History of rotating flows at LIMSI

LIMSI has several years of expertise in rotating flows, with many publications on rotor-stator or rotor-rotor configurations such as [20], [45], [46] and [47]. The open cavity subject is more recent. It started in 2008 with the thesis of L. Kahouadji [42], and the publication of the article [43]. Numerical simulation of the free surface shape published in this thesis were used in 2012 as the basis for a Master internship [48]. A first demonstrator was build in order to experimentally quantify the deformation of the free surface. But this experiment had many flaws : large vibrations, non rectified plexiglas cylinder,

irregular rotation...

In 2013 a much more ambitious project was achieved with a second Master internship [49] : a larger experiment was built, with a perfectly controlled rotation speed. The first runs tried to reproduce the 2007 experiment from the IRPHE [40]. Despite the same experimental protocol, noticeable discrepancies were observed on the critical Reynolds number. Experiments were reproducible, but it was already noted that Kalliroscope, a fluid with particles used as marker to reveal vortices under a certain light, may modify the flow and thus, instability thresholds.

These results were extended in 2014, with another Master internship [50], investigating many hypotheses for the causes of discrepancies. This included geometrical issues of the cavity, viscosity check, new aspect ratios, rotation regularity check, new marker (ink), new fluid (water glycerol mixture), validation with in a rotor-stator configuration, addition of surfactants... But none of the prospected paths bring a clue about discrepancies. The report ended with the possible stimulation of an instability by the mechanical vibrations of the rotation.

In parallel to this present work, W. Yang led a study on rotating polygons using the same experimental set up [51].

Chapter II

Article published in *Journal of Fluid Mechanics*

J. Fluid Mech. (2020), *vol*. 900, A42. © The Author(s), 2020.
Published by Cambridge University Press
doi:10.1017/jfm.2020.473

Influence of interface pollution on the linear stability of a rotating flow

Antoine Faugaret[1,2], **Yohann Duguet**[2], **Yann Fraigneau**[2] and **Laurent Martin Witkowski**[2,3,†]

[1]Collège Doctoral, Sorbonne Université, F-75005 Paris, France

[2]Université Paris-Saclay, CNRS, LIMSI, 91400 Orsay, France

[3]Faculté des Sciences et Ingénierie, UFR d'Ingénierie, Sorbonne Université, F-75005 Paris, France

(Received 6 January 2020; revised 19 April 2020; accepted 5 June 2020)

The boundary conditions at a liquid–gas interface can be modified by the presence of pollutants. This can in turn affect the stability of the associated flow. We consider this issue in the case of a simple open cylindrical cavity flow where a liquid is set in motion by the rotation of the bottom. The problem is addressed using an experimental set-up, a linear stability code and direct numerical simulation. A robust mismatch between numerical and experimental predictions of the onset of instability is found. We model the possible effect of unidentified pollutants at the interface using an advection–diffusion equation and a closure equation linking the surface tension to the superficial pollutant concentration. The chosen closure is inspired by studies of free-surface flows with surfactants. Numerical stability analysis reveals that the base flow and its linear stability threshold are strongly affected by the addition of pollutants. Pollutants tend to decrease the critical Reynolds number; however, the nonlinear dynamics is less rich than without pollutants. For sufficiently high pollution levels, the most unstable mode belongs to a different family, in agreement with experimental findings.

Key words: rotating flows

1. Introduction

Fluid flow simulations rely on a mathematical formulation associating given governing equations with specific boundary conditions. The choice for the boundary conditions is sometimes not trivial, in particular in the presence of a liquid–gas interface. Beyond the difficulties stemming from a deformable interface, it appears that, in practice, the correct boundary conditions are not well known even for a perfectly flat interface. The classical boundary condition considered in textbooks is commonly deduced from the balance of tangential stresses at the interface. For a gas–liquid interface, where the dynamic viscosity of the gas is negligible with respect to that of the liquid, this leads to a 'free slip' condition, which is simple to implement in simulation codes. Unfortunately this ideal boundary condition is not necessarily representative of realistic experiments, even for liquids as common as plain water. Contamination by pollutants present in the ambient air

† Email address for correspondence: laurent.martin_witkowski@sorbonne-universite.fr

can influence the rheology of the interface and drastically impact the effective boundary conditions (Lopez & Hirsa 2000; Martín & Vega 2006). Such modifications can deeply alter the flow and, as a consequence, the numerical predictions with a free-surface condition are no longer representative of the true physical flow. Considering how difficult it is to experimentally ensure that a gas–liquid interface is free from any chemical pollution, it is crucial to know how to model the interface, without necessarily knowing all the physical properties in detail. Such issues arise for instance in flow where Marangoni effects (modifications of the surface tension due to, for example, temperature effects) may interfere with and impact the flow dynamics. The simplified phenomenology of surface pollutants assumes that, although the precise chemical composition of the pollutants is in essence unknown, their qualitative effect is to reduce the effective surface tension (Ponce-Torres & Vega 2016). This suggests an effect akin to that of insoluble surfactants added on the free surface. In several studies of free-surface flow with controlled amounts of surfactants (Lopez & Hirsa 2000; Hirsa, Lopez & Miraghaie 2001), the amount of pollutants is supposed so small that they are confined to a Langmuir monolayer located at the interface. We assume therefore for simplicity that pollutants do not penetrate the bulk of the flow. Advected by the local velocity field tangent to the interface, the pollutants cluster at some given locations, their accumulation being only resisted by weak diffusion. The resulting inhomogeneity of the concentration field at the interface induces a local change in the surface tension. The gradients of effective surface tension lead to additional stresses that modify the global stress balance.

In this investigation we choose a flow case feasible in the laboratory as well as in numerical simulations, where such ideas can be tested. In particular, we focus on a simple flow likely to develop instability modes via a classical Hopf bifurcation scenario. The selected most unstable mode, its growth rate and the associated onset Reynolds number serve as quantitative indicators of how reliable a given set of boundary conditions are. The flow consists of a cylindrical cavity partially filled with liquid, in most cases water. The top of the cavity is open while its bottom rotates at constant angular velocity. The sidewalls do not rotate and are fixed in the laboratory frame. For simplicity, we restrict ourselves to the parameter regime where the fluid interface remains approximately flat even as the instability develops and saturates. A sketch of the experimental set-up can be found in figure 1. The two main parameters for this flow are the geometric aspect ratio $G = H/R$, where H is the undisturbed liquid height and the inner cylinder radius R, and the Reynolds number $Re = \Omega R^2/\nu$ where Ω is the rotation rate and ν is the kinematic viscosity. This flow has been previously studied both numerically and experimentally. The earliest publication we found about this configuration is a numerical investigation of the base flow for an aspect ratio G between 0.1 and 1 (Hyun 1985). Under the assumption that the flow remains axisymmetric, the transition to unsteadiness has been studied numerically for $G = 2$ by Daube (1991) and the transition point was found near $Re = 2975$. Evidence for an instability breaking the axisymmetry of the base flow was given only later. In Young, Sheen & Hwu (1995), no visualisation of the pattern was shown; however, laser Doppler velocity measurements revealed the growth of an instability near $Re = 2000$ for a $G = 2$ geometry. This is consistent with $Re = 1910$, the value found in a numerical simulation by Lopez *et al.* (2004). The first experimental visualisations of non-axisymmetry were performed by Hirsa, Lopez & Miraghaie (2002*b*) and Lopez *et al.* (2004) in the same geometry, and compared with numerical results for $G = 2$ and $G = 1/4$ in Lopez *et al.* (2004). For the larger aspect ratio ($G = 2$), numerical predictions and experimental results tend to agree, yet for the shallower configuration, mismatches in critical Reynolds number and azimuthal wavenumber m were reported. In particular, the wavenumber selection was described in these works as sensitive to the presence of surface contaminants.

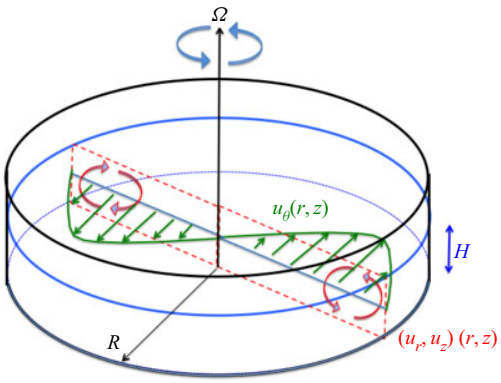

FIGURE 1. Sketch of the axisymmetric base flow for small aspect ratio $G = H/R$.

Among recent publications, the experimental work by Poncet & Chauve (2007) surveys many aspect ratios ranging from $G = 0.0179$ to 0.107. Larger aspect ratios G from 0.3 to 4 have been studied numerically as well (Iwatsu 2004; Serre, Tuliszka-Sznitko & Bontoux 2004; Cogan, Ryan & Sheard 2011). For higher rotation rates, a different regime takes over, with strong deformations of the interface and sometimes mode switching (Suzuki, Iima & Hayase 2006; Tasaka & Iima 2009). Polygonal patterns at the deformed interface have been reported by Vatistas, Wang & Lin (1992), Jansson *et al.* (2006), Iga *et al.* (2014) and modelled by Tophøj *et al.* (2013).

In the present investigation, we revisit the primary instability mechanism using a joint experimental and numerical approach. We focus on the primary instability in the case of an approximately flat interface. For small enough angular velocities the centrifugal acceleration remains much smaller than gravity and the curvature of the fluid interface can be indeed neglected in the small Froude number hypothesis. The main aspect ratio under scrutiny corresponds to $G = 1/14$. As shown in table 1, the experimentally determined thresholds are lower by least 75 % than those of Poncet & Chauve (2007). The various possible reasons for this discrepancy have been reviewed in our experimental set-up with great care, among them residual vibrations, lack of axisymmetry of the cavity, finite curvature of the free surface, presence of a meniscus, ionisation of the water. In all cases these hypotheses were ruled out as quantitatively insignificant. Note that quantitative discrepancies with experimental measurements have been also already reported earlier for this flow for low G. In Kahouadji, Martin Witkowski & Le Quéré (2010), the stability thresholds in Re determined by linear-stability analysis (LSA) were compared with Poncet and Chauve's experimental estimates for varying values of G. In both studies the threshold value Re_c increases with decreasing G. The agreement between numerics and experiments is very satisfying; however, it deteriorates for $G \leq 0.07$–0.08 (see figure 3*a* in Kahouadji *et al.* 2010), with a mismatch on Re_c of 100 % for $G \approx 0.04$. Following Lopez and co-authors, we assign such a mismatch between experiments and linear stability analysis to the unavoidable presence of pollutants at the interface, and hence to the simplistic free-slip model for the boundary conditions at the liquid interface. The present investigation is devoted to a quantitative analysis of the influence of these pollutants, via a simple phenomenological model, on the linear stability threshold of this flow.

The outline of the paper is as follows. In § 2, we give a brief description of the flow and its primary instability. We detail the experimental methods as well as the numerical methods for the linear and nonlinear stability. Section 3 is devoted to a critical comparison

	Experiment (LDV)	Poncet	ROSE	Sunfluidh
Re_c	[3160–4230]	[14 367–16 420]	17 006	[17 000–17 100]
$f_{m=5}$	[Noise–0.764]	—	0.709	[0.707–0.699]

TABLE 1. Critical Reynolds number and angular frequency of the pattern for the $m = 5$ instability for $G = 1/14$. For Sunfluidh, linear interpolation leads to $Re_c = 17\,010$. When relevant, a lower and an upper bound are given for Re_c, with the corresponding values for the frequency. Experimental results by Poncet & Chauve (2007) are included for comparison.

between experimental and numerical results. In § 4, we introduce a new model for the free surface where surface pollution is taken into account. Section 5 discusses the possible simplification of the model in the limit of high surface pollution. The final § 6 contains a summary of the present investigation together with open questions and perspectives for future work.

2. Flow set-up and related investigation techniques

2.1. *Base flow description*

We briefly recall the main features of the base flow as described by Iwatsu (2004) and Yang *et al.* (2019). It is axisymmetric with three non-zero velocity components. Its structure for small aspect ratio G is sketched in figure 1. We use a classical direct cylindrical coordinate system (r, θ, z), where r is the radial distance, θ the azimuthal angle and z the distance from the rotating bottom. In the vicinity of the instability threshold, the azimuthal velocity profile possesses a simple radial structure almost independent of z except in the boundary layers. In the regimes we focus on, the azimuthal velocity increases with the radial distance from $r = 0$ to $r \approx 0.67 - 0.68R$, where R is the radius of the set-up, and decreases to zero as the wall is approached. The latter zone is labelled 'outer region'. This azimuthal velocity is driven by the steady rotation of the disc at angular velocity Ω at the bottom of the cavity. Just above this rotating disc, the fluid is pushed radially outwards towards the fixed cylindrical end wall in a boundary layer similar to a von Kármán boundary layer. This generates a recirculation in the meridional plane, confined approximately to the outer region. For $r \leq 0.5R$ the flow is in perfect solid body rotation.

Above a given rotation rate, this base flow is known to support an instability breaking its axisymmetry. Ignoring in a first stage the geometrical and rheological parameters, a simplistic explanation for this symmetry breaking is as follows: a shear instability, akin to a Kelvin–Helmholtz instability along a curved streamline, develops where the azimuthal velocity profile displays the strongest curvature. Given the cylindrical geometry, a direct analogy with the instability of Stewartson layers in the split disc configuration (Stewartson 1957) has been suggested in order to justify the relative size of the instability region (Poncet & Chauve 2007). Beyond this simple picture, the bifurcation scenarios leading to the presence of different non-axisymmetric patterns with a dominating wavenumber $m \neq 0$ as in figure 2, are not entirely clear from the literature. Lopez *et al.* (2004) describe the bifurcation as a standard Hopf bifurcation. Experiments in Poncet & Chauve (2007) reveal the existence of hysteresis, suggesting a possibility for subcritical bifurcation. In the present work, we focus on the emergence of a $m = 5$ mode, the most unstable one predicted by linear instability theory for the aspect ratio G considered. A competing

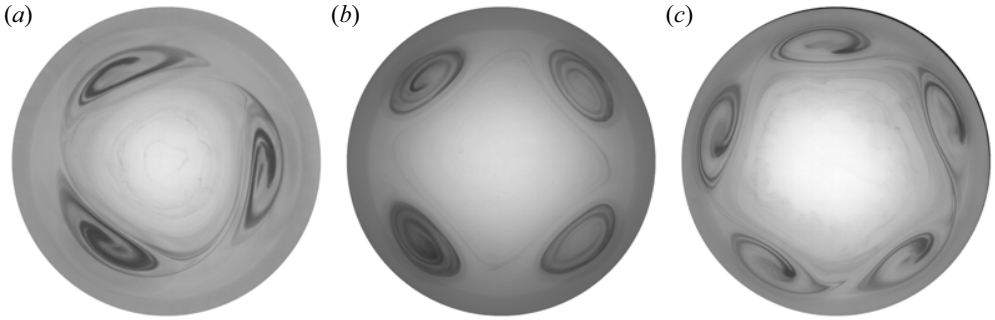

FIGURE 2. Instability patterns breaking the axisymmetry of the flow. Photograph taken from above (ink visualisation) in our experimental set-up. Modes $m = 3$, 4 and 5 obtained for different aspect ratios and different values of Re above the effective Re_c; (*a*) $m = 3$, $G = 3.5/14$, $Re = 2160$, (*b*) $m = 4$, $G = 1.5/14$, $Re = 5623$, (*c*) $m = 5$, $G = 1/14$, $Re = 4714$.

unstable mode with $m = 4$, though theoretically expected to appear for parameters where the mode $m = 5$ is already unstable, has also been investigated.

2.2. *Experimental technique*

The main element of the experimental set-up is a cylindrical shaped Plexiglas cavity. Its internal radius is $R = 140.3 \pm 0.05$ mm, and the thickness of the Plexiglas is 6.8 mm. The value of R is used to define the Reynolds number $Re = \Omega R^2/\nu$. The cavity was engineered from a single block, so that the cylinder and the bottom are monolithic, preventing any risk of leak. Its bottom is drilled along its axis in order to mount a brass foot that hosts the shaft of the rotating disc, itself also made of brass. The radius of the disc is $R_d = 139.6$ mm, its thickness 8.5 mm and its mass 5 kg. The shaft is held in place with two ball bearings, and the sealing is insured by a spring-loaded double-lip seal. An aluminium rigid sleeve coupling, relying on a thrust ball bearing, is used to connect the disc shaft and the motor reducer unit. The motor used is a direct current motor (Parvex RX320E-R1100) with a 1 : 12 reducer. The rotation speed is controlled using a closed-loop tachometer. Special attention was paid to minimising the gap between the disc edge and the vertical wall of the cavity. The liquids used in this experimental investigation are tap water, de-ionised water and a water–glycerol mixture. As the cavity is not thermo-regulated, the fluid temperature is monitored continuously, with a digital thermometer that allows it to be known with an accuracy of 0.1 K. The corresponding kinematic viscosity is then evaluated using an empirical formula (Cheng 2008). The experimental Reynolds number, based on the angular velocity Ω, the radius and the kinematic viscosity are hence known within a given accuracy of the order of a per cent for the range of parameters investigated. The relative error is expected to increase as the rotation rate decreases.

Flow measurements are made using a laser Doppler velocimetry (LDV) device, composed of a Dantec Laser linked to a BSAFlow processor. The liquid is seeded with Dantec 10 micrometre diameter silver coated hollow glass spheres (S-HGS-10). These are not provided as suspension and thus prevent the introduction of additional surfactant. We also avoided to premix the particles without any additional solutant. Because of the cylindrical geometry, as the laser beams are placed for the acquisition of u_θ they undergo a deviation that both shifts the location of the focus and impacts the quantitative measurements. This is fixed at the post-processing stage using the technical corrections

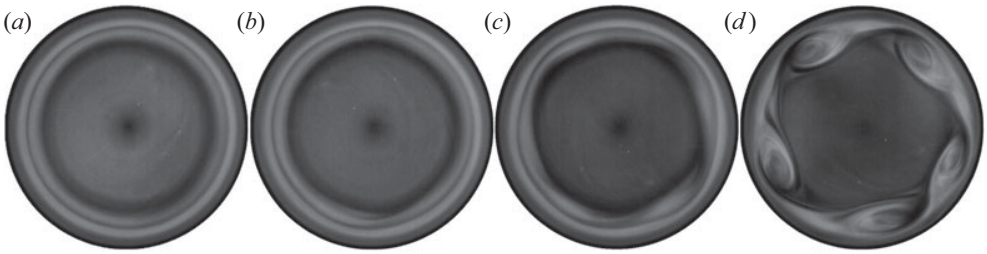

FIGURE 3. Instability growth for a $m = 5$ mode for a water + Kalliroscope mixture initially at rest: $G = 1/14$, Reynolds number $Re = 16\,550$; (*a*) $t = 52$ s, (*b*) $t = 60$ s, (*c*) $t = 71$ s, (*d*) $t = 99$ s.

suggested in Huisman, van Gils & Sun (2012). For visualisations such as in figure 2, the flow patterns were highlighted by injecting either Kalliroscope or ink into the fluid. The protocol to find experimentally the critical Reynolds number is to progressively increase the azimuthal velocity with steps of 0.5 r.p.m. for the water and for the 20 % water–glycerol mixture, and steps of 1 r.p.m. for the 55 % water–glycerol mixture. After each increase of the rotation speed, a waiting time of 5–10 min is followed by LDV acquisition performed over another five minutes duration. This procedure allows the base flow to be almost established before the instability grows.

2.3. *Experimental evidence for $m = 5$ instability*

We describe the experimental instability leading to a steadily rotating $m = 5$ mode, using Kalliroscope visualisations or pointwise LDV measurements. The flow is initially at rest. The angular velocity is directly set to a finite value defining the target Reynolds number Re, the value used in figure 3 being $Re = 16\,650$. For low enough Reynolds numbers, the flow remains axisymmetric as in figure 3(*a*). Above threshold, an annulus characterised by stronger shear appears around $r = 0.7R$ (figure 3*b*). An $m = 5$ mode emerges (figure 3*c*) and evolves towards a steadily rotating configuration with 5 co-rotating vortices (figure 3*d*). In the time sequence presented, the Reynolds number is well above the threshold as will be seen later. In such a case, the emergence of the instability is almost concomitant with that of the base flow, which is here approximately 80 s. A similar scenario occurs for other values of m, in particular for $m = 4$ which has been observed for other nearby values of Re. The vortex pattern rotates with a constant angular velocity smaller than Ω. The angular frequency f of the pattern can be deduced using $f = 2\pi f_d/(m\Omega)$, where f_d is the dimensional frequency obtained experimentally using pointwise LDV measurements at a location fixed in the laboratory frame. The main frequency f varies moderately over the range $Re = [4230, 16\,300]$. A Fourier transform of the time series is shown in figure 4 in the case $m = 5$ for $Re = 4230$ and $Re = 16\,300$. The main frequency and the related harmonics dominate the spectrum.

2.4. *Numerical methodology for free-slip interfaces*

As a complementary part of this investigation, we have used numerical tools based on the incompressible Navier–Stokes equations in order to investigate both the linear and nonlinear aspects of the symmetry-breaking instability. The present section first introduces the numerical methods used. It also features a comparison with the experimental results of § 2.3.

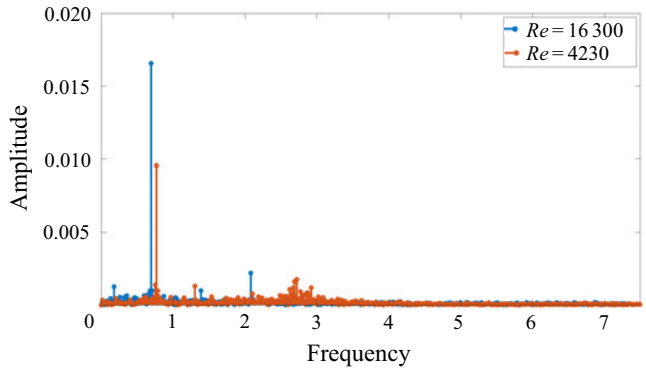

FIGURE 4. Experimental frequency amplitude spectrum of azimuthal velocity component measured at radius $0.76R$ and height $0.9H$ for the saturated $m = 5$ regime at $Re = 4230$ and $Re = 16\,300$. The maximum amplitudes correspond to the non-dimensional frequencies $f = 0.76$ and $f = 0.73$, respectively.

2.4.1. *Mathematical model*

We adopt the point of view of a single-phase flow. The velocity field $\boldsymbol{u}(r, \theta, z, t)$ inside the liquid is governed by the incompressible Navier–Stokes equations in the (non-rotating) laboratory frame

$$\boldsymbol{\nabla} \cdot \boldsymbol{u} = 0, \tag{2.1}$$

$$\frac{\partial \boldsymbol{u}}{\partial t} + (\boldsymbol{u} \cdot \boldsymbol{\nabla})\boldsymbol{u} = -\boldsymbol{\nabla} p + \frac{1}{Re}\boldsymbol{\nabla}^2 \boldsymbol{u}. \tag{2.2}$$

Equations (2.1)–(2.2) have been non-dimensionalised using the length scale R and the time scale Ω^{-1}, and the dimensionless fluid density is taken as unity. From here on all the variables are non-dimensional except when explicitly noted.

The flow obeys no slip at all solid boundaries. This implies

$$u_r = u_\theta = u_z = 0 \tag{2.3}$$

at the fixed vertical boundary at $r = 1$, whereas

$$u_r = u_z = 0, \quad u_\theta = r \tag{2.4a,b}$$

on the rotating disc at $z = 0$.

The boundary condition at the liquid–gas interface at $z = G$ is classically derived from the stress balance at the interface. As the viscosity of the air is much smaller than the water one, we can neglect the gas phase altogether. We first consider the generic free-slip boundary conditions

$$\frac{\partial u_r}{\partial z} = 0, \quad \frac{\partial u_\theta}{\partial z} = 0, \quad u_z = 0 \quad \text{at } z = G. \tag{2.5a–c}$$

A few precautions are necessary to justify the plane interface hypothesis. A numerical estimation of the height $h(r)$ as a function of the rotation speed is possible for the steady base flow. This is achieved using the variation of the numerical code ROSE with coordinate transformations used in Yang *et al.* (2020). Two sets of parameters typical of the present

range of interest have been considered. The first set is a least favourable parameter case ($G = 1/14$, $\Omega = 0.95\,\text{rad s}^{-1}$), i.e. $Re = 18\,620$ and $Fr = (\Omega^2 R)/g = 0.013$ where g is the gravity. In this case, the total height variation from the centre to the periphery is $\Delta h = h(r = 1) - h(r = 0) = 6.8\,\%$ of the undisturbed fluid height. The second set is for the rotation rate at which the instability is first detected ($Re \sim 3000$), $\Omega = 0.15$ rad s^{-1} and $Fr = 3.34 \times 10^{-4}$, Δh is less than $0.2\,\%$. Such small values, respectively 0.68 and 0.017 mm (too small to be measured experimentally for the latter), justify the flat interface hypothesis considered in the numerical part.

As in all mesh-based numerical methods, the singularities of the velocity field occurring at both corners $(r = 1, z = 0)$ and $(r = 1, z = G)$ are smoothed out in practice by the finite mesh without the need, as for spectral methods, for regularising functions (Serre & Bontoux 2007) or singular splitting (Duguet, Scott & Le Penven 2005). This is consistent with the 'natural' regularisation occurring in the experiment in the presence of a very thin gap.

2.4.2. *Linear stability analysis*

In order to determine the critical Reynolds number Re_c for the onset of instability, we use an in-house linear stability solver named ROSE, based on a finite difference method in r and z. The technique as well as the equations written in cylindrical coordinates are found in Kahouadji, Houchens & Martin Witkowski (2011). The steady axisymmetric base flow is first determined by solving (2.1) and (2.2) together with the associated boundary conditions using a Newton–Raphson solver. The steady solution is solved for in an $(\omega, \psi, u_\theta, c)$ formulation, where

$$\omega = \frac{\partial u_r}{\partial z} - \frac{\partial u_z}{\partial r}, \quad u_r = \frac{1}{r}\frac{\partial \psi}{\partial z}, \quad u_z = -\frac{1}{r}\frac{\partial \psi}{\partial r}. \tag{2.6a–c}$$

The Newton–Raphson solver allows for additional scalar fields $c(r, z)$ such as temperature or concentration, as further discussed in § 4.

Let $(\boldsymbol{U}, P)$ represent the velocity-pressure field for such a steady axisymmetric solution of (2.2), and let $(\boldsymbol{u}^*, p^*)$ be a small-amplitude perturbation to $(\boldsymbol{U}, P)$. The dynamics of the perturbation is governed by the linearised stability equations

$$\boldsymbol{\nabla} \cdot \boldsymbol{u}^* = 0, \tag{2.7}$$

$$\frac{\partial \boldsymbol{u}^*}{\partial t} + (\boldsymbol{U} \cdot \boldsymbol{\nabla})\boldsymbol{u}^* + (\boldsymbol{u}^* \cdot \boldsymbol{\nabla})\boldsymbol{U} = -\boldsymbol{\nabla} p^* + \frac{1}{Re}\boldsymbol{\nabla}^2 \boldsymbol{u}^*. \tag{2.8}$$

It is associated with Dirichlet boundary conditions $\boldsymbol{u}^* = 0$ on all solid boundaries together with a boundary condition on $\boldsymbol{u}^*$ at the interface similar to that for $\boldsymbol{u}$ in (2.5). The velocity field and the pressure field are decomposed using a complex ansatz of the form $\mathrm{e}^{\lambda t + \mathrm{i} m\theta}$, as will be detailed in § 4.2. The neutral curve corresponds to parameter values where the real part $\mathrm{Re}(\lambda) = 0$, and it is identified in practice using a one-dimensional secant method. All meshes used are Cartesian in the meridional plane $(O, \boldsymbol{r}, \boldsymbol{z})$. For $G = 1/14$ the mesh consists of 701×101 grid points.

2.4.3. *Direct numerical simulation*

For the nonlinear validation of the stability thresholds we have used the direct numerical simulation (DNS) code Sunfluidh developed at LIMSI for incompressible flows. It is based on a projection method to ensure a divergence-free velocity field. The equations are

discretised on a staggered structured non-uniform grid using a finite volume approach with a second-order centred scheme in space. A second-order backward Euler differentiation is used for time discretisation. Details can be found in Yang *et al.* (2020). The interface condition is as in (2.3) and (2.4). The code offers the possibility to enforce a given rotational symmetry $\mathcal{R}_m$ characterised by a fundamental azimuthal wavenumber $m \geq 0$, such that every velocity field verifies

$$(\mathcal{R}_m \boldsymbol{u})(r, \theta, z) = \boldsymbol{u}\left(r, \theta + \frac{2\pi}{m}, z\right) = \boldsymbol{u}(r, \theta, z) \quad (m \neq 0), \tag{2.9}$$

or axisymmetry for $m = 0$. If $m \neq 0$ the simulation only needs to be carried out over an angular sector $0 \leq \theta \leq 2\pi/m$ with azimuthal periodicity. For the simulations without symmetry imposed, we have used a mesh consisting of $180 \times 180 \times 64$ cells in r, θ and z, respectively.

3. Critical comparison of the different approaches

3.1. *Comparison between the numerical methods*

For identical parameters, we report excellent agreement between the base flows computed by the two methods for all Re. Whereas the base flow can be converged for all Re using the Newton method, it is only accessible for $Re < Re_c$ using time stepping. However, since the base flow is apparently the only axisymmetric solution of the system, it is also found using DNS for all Re by simply imposing $m = 0$ (two-dimensional axisymmetric case) and stepping forward in time. The value of Re_c for $m = 5$ is first identified by LSA using a secant method. In the DNS code, the procedure used to identify Re_c is different; above and below Re_c, an arbitrary perturbation of finite but small amplitude is applied to the system after an initial transient, with the $\mathcal{R}_5$ symmetry imposed or not. This impulse response leads to either exponential decay towards the base flow, or exponential growth towards a nonlinear regime at large times. A linear interpolation of these rates leads to an evaluation of the critical threshold Re_c. Both approaches agree quantitatively very well regarding the prediction of Re_c for $m = 5$ since the relative error is close to 0.3 % (see table 1). Interestingly, this comparison, as well as the lack of unstable impulse response for $Re < Re_c$ (even for larger-amplitude impulses), both suggest that the instability is supercritical and not subcritical, at least for a clean interface obeying the boundary condition (2.5). Note that the ROSE computation in table 1 was performed using a 701×101 grid. Numerical comparison with Kahouadji *et al.* (2010) confirms that this resolution is sufficient for an estimation of Re_c with an accuracy of less than one per cent. Two additional computations were performed using different meshes. The Re_c was estimated to 17 032 with a 351×51 grid, and to 16 992 with a 1401×201 grid. The maximum variation of Re_c is less than 0.16 % compared to the value in table 1.

3.2. *Mean flow structure*

Since both numerical approaches yield a truly similar base flow solution, a comparison with the experimental base flow measured using LDV would be relevant at this point. As we shall see, measurements below Re_c turn out to be experimentally difficult. Another comparison, which is easier to perform, concerns the mean velocity profiles obtained for $Re > Re_c$ by either temporal or spatial average. Such a comparison is displayed in figure 5. For the eigenmodes computed using ROSE, their average is by construction zero. Hence, only the base flow obtained by LSA is included in figure 5, whereas the spatial average is

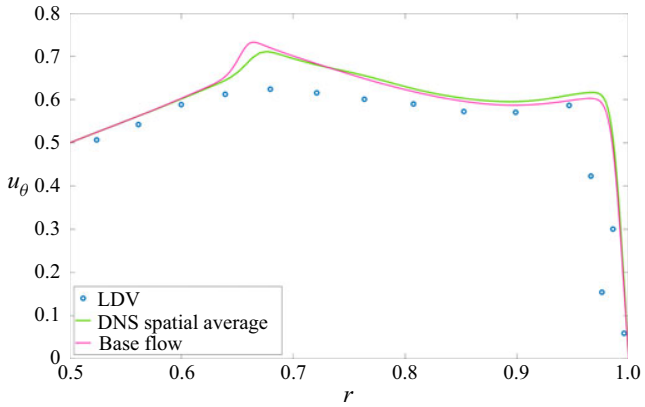

FIGURE 5. Velocity profiles of $u_\theta(r)$ below the free surface ($z = 0.8G$) for $G = 1/14$ and $Re = 18\,620$. Comparison between the base flow, spatially averaged DNS and the temporal average for LDV (experiment). LDV acquisition timespan is much larger than the instability period.

taken for the DNS data and the time average for experimental LDV data. A common value of $Re = 18\,620$ is chosen for the comparison. Although the agreement is satisfactory, a noticeable overshoot appears around $r \approx 0.67$ in all numerical azimuthal velocity profiles, with no equivalent in LDV measurements despite sufficient measurement accuracy. The same mismatch, presence of the overshoot area in numerics, but not in experiments, was also reported for comparable parameters in Yang *et al.* (2019). The computations performed on different meshes all display this overshoot, which rules out a numerical artefact.

3.3. *Threshold detection*

The most dramatic mismatch between numerics and experiments concerns the critical Reynolds number. While both numerical simulations agree on a critical Reynolds number of approximately 17 000 (see table 1), LDV measurements display persistent oscillations in the azimuthal velocity field for Re as low as 4200, with a normalised frequency $f_5 = 0.76$, indicative of the presence of the $m = 5$ mode. This upper bound on the value of Re_c is smaller by a factor of 4 than the previous experimental estimates by Poncet & Chauve (2007). These values can be found in table 1. The discrepancies are robust; although the exact same spin-up protocol as Poncet & Chauve (2007) was observed, the respective ranges of Re_c differ. We note that the threshold detection by Poncet & Chauve (2007) is based on Kalliroscope visualisations. Kalliroscope appears in our set-up as a poor diagnostic for Re_c for this flow case; the threshold detection is erratic and protocol dependent. Indeed the estimation of Re_c fluctuates between 6200 to 9300. At times, Kalliroscope is even unable to detect the instability, even well above the value of Re_c predicted numerically. The use of ink for visualisation, and LDV for quantitative measurements, both confirm that the thresholds detected with Kalliroscope are over-evaluated. The saturated mode is displayed in figure 2 at a value of Re approximately 4 times lower than the theoretical threshold $Re_c^{(LSA)}$. Its spatial structure is directly comparable to that of the saturated flow above $Re_c^{(LSA)}$ displayed in figure 3(*d*).

On the one hand, there is perfect numerical agreement between LSA and DNS about the estimation of Re_c, on the other hand, there is a troubling match with

	Lopez *et al.* Water	Experiment 55 % glycerol	Experiment 20 % glycerol	ROSE	ROSE
m	3	3	3	3	2
Re_c	2000	[1850–2160]	[1875–2520]	4690	3480

TABLE 2. Critical Reynolds number for $G = 1/4$. Comparison between experiments by Lopez *et al.* (2004), present experiments and LSA. The percentage of glycerol indicated is a weight percentage.

Poncet & Chauve (2007) at odds with the experimental/numerical discrepancy we report. We have hence carried out an exhaustive investigation of the possible reasons for such a discrepancy by focusing on experimental imperfections. A classical reason for discrepancies in rotating machines is the presence of mechanical noise that could force an instability by direct or parametric resonance. The experimental displacement of the disc surface was measured using a pair of LK-G10 sensors, and their associated LK-GD500 controller. Displacements were evaluated to approximately 10^{-4} m, with a mean frequency corresponding to the disc rotation, yet no link with the pattern frequency was found. This does not suggest any obvious experimental flaw in our experimental methodology.

Eventually, in order to confirm our experimental approach, we switch temporarily to a different geometry with $G = 1/4$ where a direct and favourable comparison with the experimental results of Lopez *et al.* (2004) can be made. For these parameters there is also a robust mismatch between experiments and numerics; LSA predicts the most unstable mode $m = 2$ with $Re_c = 3500$, whereas Lopez's experiments at $Re = 2000$ show a mode $m = 3$, predicted using LSA to be unstable only for $Re \geq 4600$. We have then conducted our own experiments with two different mixtures of water with 20 % and 55 % glycerol. The motivation for these two different mixtures is to allow for a wider span of rotation speeds; using water the instability would have occurred for rotation speed below 1 r.p.m. where the signal-to-noise ratio in the LDV degrades. In both cases the mode $m = 3$ is detected, either using ink or LDV, for $Re = 2160$ in the 55 % glycerol fluid (see figure 2*a*) and $Re = 2520$ in the 20 % glycerol fluid. All the results are gathered in table 2. This side study confirms, in good agreement with Lopez *et al.* (2004) that numerics overestimate the experimental thresholds in Re. The discrepancy reported here for $G = 1/14$ has hence a robust physical origin, which the rest of this paper is devoted to.

3.4. *Nonlinear dynamics*

The mismatch between numerics and experiments for $G = 1/14$ is even more dramatic further above Re_c. Although DNS initially displays an azimuthal wavenumber $m = 5$ close to Re_c (see figure 6*a* at $Re = 17\,100$), the instability pattern evolves towards $m = 7$ as Re is pushed to 18 620, less than 9 % above Re_c. Poncet & Chauve (2007) have also reported an evolution of the modal content of the flow with Re, yet with m decreasing as Re is increased. A similar decrease of m with Re was also observed qualitatively in our experiment for Re sufficiently higher than Re_c. However, the wavenumber $m = 5$ remains experimentally stable from $Re = 4200$ to at least $Re = 18\,620$. The frequency spectrum is shown in figure 7(*a*) for $Re = 18\,620$. Given such a mismatch, larger values of Re were not investigated, neither experimentally nor numerically. Differences in the nonlinear dynamics for $Re = 18\,620$ also emerge in velocity measurements; while experimental time series display a single frequency, the signals from DNS display a broader spectrum

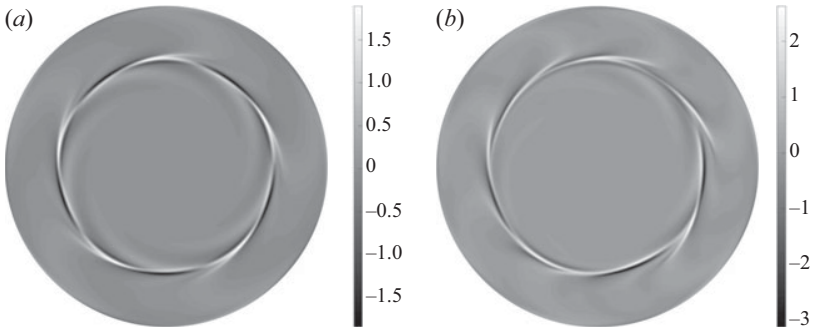

FIGURE 6. DNS axial vorticity fluctuation for the free-surface condition, $Re = 17\,100$ slightly above Re_c (*a*), and $Re = 18\,620$ (*b*). With the increase of Re, the mode $m = 5$ selected at Re_c evolves into a modulated $m = 7$ pattern.

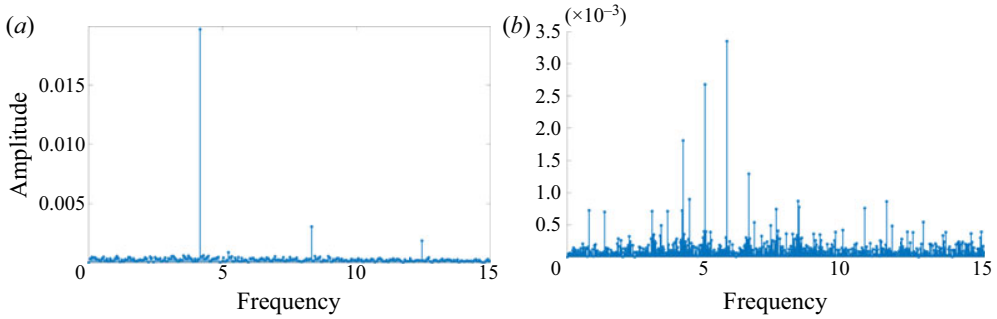

FIGURE 7. Comparison of frequency amplitude spectra for $u_\theta(t)$ measured at $r = 0.76$, $z = 0.8G$, for the saturated $m = 5$ regime at $Re = 18\,620$. (*a*) Experimental data, maximum peak at $f = 4.15$. (*b*) DNS with free-surface condition, same parameters. The frequencies are not normalised by the azimuthal wavenumber.

and richer dynamics, see figure 7. In addition to the mismatch in the modal behaviour between experiments and DNS, the vorticity patterns (figures 6*a* and 6*b*) do not match the experimental (figures 2 and 3*d*) very convincingly. This raises doubts about whether the mode predicted in the numerics does indeed correspond to the structure observed experimentally.

3.5. *Limitations of the clean interface hypothesis*

Lopez *et al.* (2004) have suggested that mismatches in critical Reynolds numbers between theoretical and experimental predictions arise due to the presence of pollutants at the interface. The main idea is that the pollutants change the boundary condition at the interface. One can draw a parallel with the evolution from free slip to no slip examined by Peaudecerf *et al.* (2017) in a channel flow with superhydrophobic surfaces, in presence of carefully added surfactants. As it is nearly impossible, in standard laboratory conditions, to achieve an experiment with a perfectly clean interface at all times, it is necessary to take additional effects into account in order to properly model the behaviour of the fluid at a realistic liquid–gas interface. Previous publications with a similar experimental set-up, in which the adsorption of pollutants at the interface was carefully controlled, already

demonstrated the crucial influence of pollution of the base flow (Hirsa *et al.* 2001; Hirsa, Lopez & Miraghaie 2002*a*). There, pollutants were assimilated to a monolayer of vitamin *K*1, considered as a surfactant, yet any insoluble (or weakly soluble) surfactant would have a similar effect.

In the next section, we model explicitly the presence of pollutants at the interface in the Navier–Stokes equations and investigate its qualitative as well as quantitative influence on the linear stability of the flow.

4. Modelling of interface pollution

4.1. *Modification of the effective surface tension*

The present modelling of the pollution at the interface is directly inspired by the modelling in Hirsa *et al.* (2001) and Kwan, Park & Shen (2010). Let $c_d(r, \theta, t)$ be the dimensional instantaneous concentration of the pollutants at the interface, the closure equation between the surface tension σ and c_d reads

$$\sigma = \sigma_0 \left(1 - \frac{\alpha}{2\sigma_0} c_d^2\right), \tag{4.1}$$

where σ_0 is the reference surface tension of the solvent (for water, $\sigma_0 = 72.8$ mN m^{-1}); α is a dimensional constant coming from the Taylor expansion around $c_d = 0$ of the model in Kwan *et al.* (2010), and depends from the chemical species of the pollutant. Equation (4.1) is non-dimensionalised as

$$\bar{\sigma} = 1 - \frac{\alpha C_0^2}{2\sigma_0} c^2, \tag{4.2}$$

where $\bar{\sigma} = \sigma/\sigma_0$ and $c = c_d/C_0$. Here, C_0 represents the average mass concentration of pollutant at the interface, such as

$$C_0 = \frac{1}{\pi R^2} \int_0^{2\pi} \int_0^R c_d(r, \theta, t) r \, \mathrm{d}r \, \mathrm{d}\theta. \tag{4.3}$$

Since the ambient pollution is undetermined, the value of the α coefficient is unknown. Thus (4.2) is modified as follows

$$\bar{\sigma} = 1 - \frac{\beta Ca}{2} c^2, \tag{4.4}$$

where $Ca = \mu \Omega R/\sigma_0$ is a capillary number, μ is the dynamic viscosity and β is a new non-dimensional control parameter defined by

$$\beta = \frac{\alpha C_0^2}{\mu \Omega R}. \tag{4.5}$$

Note that β can be linked to a Marangoni number, based on C_0 and the diffusion D^s such that $Ma = (\alpha C_0^2 R)/(D^s \mu)$, and to the Péclet number $Pe^s = \Omega R^2/D^s$ so that $\beta = Ma/Pe^s$.

We assume that pollutants are advected by the velocity field of the fluid while diffusing with a simple non-dimensional diffusion coefficient D^s. Moreover, we assume that no transport occurs from the surface to the bulk of the flow, so that the bulk concentration can be neglected (Bandi *et al.* 2017). In practice, β is limited by chemistry considerations;

high values of β correspond to a highly polluted surface. Under these conditions, diffusion into the bulk becomes possible. Starting from the Boussinesq–Scriven surface fluid model for a Newtonian fluid–gas interface (Scriven 1960), and under the hypothesis of negligible surface dilatational viscosity and surface shear viscosity (Hirsa *et al.* 2001), the boundary conditions can be written as

$$\frac{\partial u_r}{\partial z} = \frac{1}{Ca}\frac{\partial \bar{\sigma}}{\partial r}, \quad \frac{\partial u_\theta}{\partial z} = \frac{1}{Ca}\frac{1}{r}\frac{\partial \bar{\sigma}}{\partial \theta}, \quad u_z = 0. \tag{4.6a–c}$$

Using (4.4) and the expression of β, (4.6) can hence be rewritten

$$\frac{\partial u_r}{\partial z} = -\beta c\frac{\partial c}{\partial r}, \quad \frac{\partial u_\theta}{\partial z} = -\beta c\frac{1}{r}\frac{\partial c}{\partial \theta}, \quad u_z = 0. \tag{4.7a–c}$$

The introduction of β allows for a simpler study since it is the only input parameter for the LSA.

4.2. *Modelling of pollutant concentration*

When all pollutants stay at the interface $z = G$, their concentration $c(r, \theta, t)$ obeys a superficial advection–diffusion equation of the form

$$\frac{\partial c}{\partial t} + \boldsymbol{\nabla}^s \cdot (c\boldsymbol{u}^s) + c(\boldsymbol{\nabla}^s \cdot \boldsymbol{n})(\boldsymbol{u} \cdot \boldsymbol{n}) = \frac{1}{Pe^s}\Delta^s c, \tag{4.8}$$

where $\boldsymbol{\nabla}^s$ represents the gradient operator in the directions tangent to the interface, $\boldsymbol{\nabla}^s$ represents the gradient operator in the directions tangent to the interface and Δ^s is the associated Laplacian (Stone 1990). In (4.8), the original velocity field $\boldsymbol{u}$ is split into a normal component $(\boldsymbol{u} \cdot \boldsymbol{n})\boldsymbol{n}$ and the resulting tangential component $\boldsymbol{u}^s = \boldsymbol{u} - (\boldsymbol{u} \cdot \boldsymbol{n})\boldsymbol{n}$. In the simple case where $\boldsymbol{n} = \boldsymbol{e}_z$, (4.8) reduces to

$$\frac{\partial c}{\partial t} + \boldsymbol{\nabla}^s \cdot (c\boldsymbol{u}^s) = \frac{1}{Pe^s}\Delta^s c. \tag{4.9}$$

We consider a decomposition into base flow and perturbation, where the perturbation is written using a complex ansatz of the form $\mathrm{e}^{\lambda t + \mathrm{i}m\theta}$, such that $u_r = U_r + u_r^* \mathrm{e}^{\lambda t + \mathrm{i}m\theta}$, $u_\theta = U_\theta + \mathrm{i}\, u_\theta^* \mathrm{e}^{\lambda t + \mathrm{i}m\theta}$ and $c = C + c^* \mathrm{e}^{\lambda t + \mathrm{i}m\theta}$. For the steady axisymmetric base flow characterised by the velocity field $\boldsymbol{U}$ and the concentration field C, (4.9) becomes

$$\frac{1}{r}\frac{\partial rCU_r^s}{\partial r} - \frac{1}{Pe^s}\left(\frac{\partial^2 C}{\partial r^2} + \frac{1}{r}\frac{\partial C}{\partial r}\right) = 0. \tag{4.10}$$

By subtracting (4.10) from (4.9), the equation for the disturbance concentration $(\boldsymbol{u}, c)$ reads

$$-\lambda c^* = \frac{1}{r}\left(\frac{\partial rCu_r^*}{\partial r} + \frac{\partial rU_r c^*}{\partial r}\right) + \frac{\mathrm{i}\, mU_\theta c^*}{r} - \frac{mCu_\theta^*}{r} - \frac{1}{Pe^s}\left(\frac{\partial^2 c^*}{\partial r^2} + \frac{1}{r}\frac{\partial c^*}{\partial r} - \frac{m^2 c^*}{r^2}\right). \tag{4.11}$$

The diffusion coefficient D^s for the pollutants is usually one or two orders of magnitude smaller than the kinematic viscosity and thus, in the present case, superficial diffusion effects remain small with respect to advection effects.

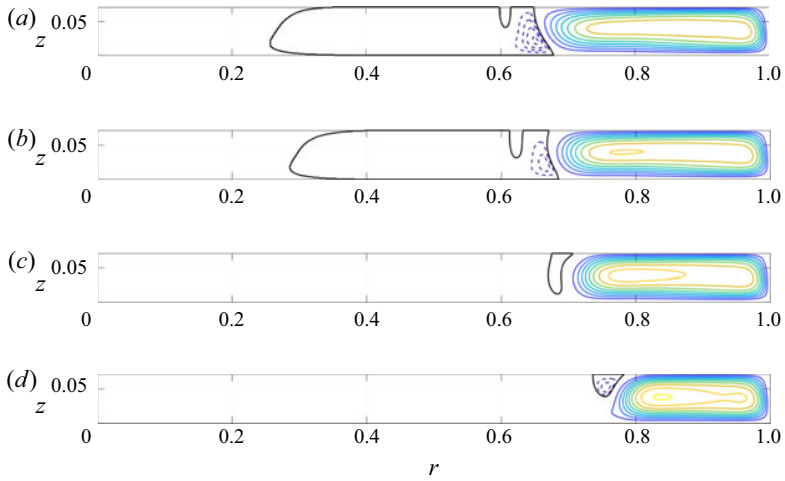

FIGURE 8. Evolution of the streamfunction ψ for the base flow with increasing concentration β, $Re = 18\,620$ and $G = 1/14$. The same contour values are chosen for all cases. Negatives and positives contours use different scales to highlight the weak recirculation bubble. Negatives contour values (dashed): four equispaced levels in $[\psi_{min} - \psi_{min}/5]$. Positives contour values: (solid lines): nine values equispaced levels in $[\psi_{max}/10 - \psi_{max}]$. Zero contour level (solid black lines). $\psi_{min} = -8.1 \times 10^{-5}$ and $\psi_{max} = 2.3 \times 10^{-3}$; (*a*) $\beta = 0$, (*b*) $\beta = 0.1$, (*c*) $\beta = 0.2$, (*d*) $\beta = 0.5$.

The constraint (4.3) reads in non-dimensional form

$$\frac{1}{\pi}\int_0^{2\pi}\int_0^1 c(r,\theta,t)r\,\mathrm{d}r\,\mathrm{d}\theta = 1, \tag{4.12}$$

and reduces for the steady axisymmetric base flow to

$$2\int_0^1 C(r)r\,\mathrm{d}r = 1. \tag{4.13}$$

For the base flow, axisymmetry implies $\partial C/\partial r = 0$ at the axis. The constraint (4.13) also imposes a zero mass flux at $r = 1$. For the perturbation field c^*, the boundary conditions depend on the value of the azimuthal wavenumber m (Kahouadji *et al.* 2011). For $m \geq 1$ (the case of interest), $c^* = 0$ is imposed at the axis and $\partial c^*/\partial r = 0$ at the outer wall. All superscripts * are from here on dropped for simplicity.

4.3. *Structure of the modified base flow*

As demonstrated in Lopez & Chen (1998), the presence of a surfactant layer at the interface modifies the structure of the base flow. However, the potential influence on its linear stability has not been investigated yet. In this subsection, we study the influence of the pollution concentration β, modelled using the surfactant law (4.1), on the base flow for $G = 1/14$ and $Re = 18\,620$. Increasing β causes a small but monotonic decrease of the length of the meridional recirculation, see figure 8. This is accompanied by the progressive disappearance of the overshoot in U_θ, evident in figure 9. This observation is directly consistent with the experimental measurements, in which no overshoot has been found for $z = 0.8G$.

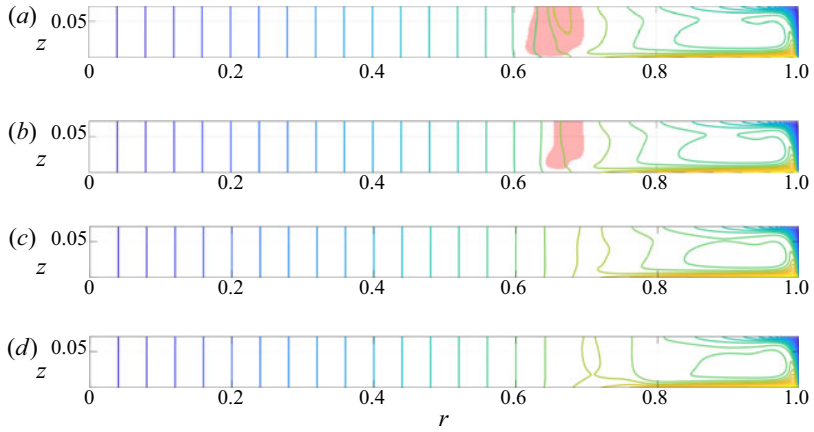

FIGURE 9. Evolution of the azimuthal velocity U_θ for the base flow for increasing β, $Re = 18\,620$ and $G = 1/14$. 21 equispaced levels in [0–1]. Translucent red patches represent overshoot areas, i.e. locations where $U_\theta \geq 1.01\,r$; (*a*) $\beta = 0$, (*b*) $\beta = 0.1$, (*c*) $\beta = 0.2$, (*d*) $\beta = 0.5$.

4.4. *Linear instability thresholds for* $G = 1/14$

The present model is based on four independent non-dimensional parameters G, Re, Pe^s and β. We have investigated quantitatively the influence of β on the instability thresholds Re_c for $m = 4$ and 5, with G fixed to 1/14 except when noted. The numerical resolution is unchanged compared to the pollution-free case. The Péclet number, although in principle larger, is hence limited to $Pe = 10^3$ in order to prevent steeper gradients and numerical issues. The focus on $m = 4$ and 5 mirrors the modal selection predicted for the reference case $\beta = 0$, and is also consistent with experimental findings at onset.

The neutral curves $Re_c(\beta)$ obtained as β is varied are shown in figure 10, where neutral modes $m = 4$ and 5 appear as squares and five-pointed stars, respectively. The neutral curves have been determined by identifying the parameters where $\mathrm{Re}(\lambda) = 0$ using a secant method. In some intervals of β the curve $Re_c(\beta)$ happens to be multi-valued, see e.g. $\beta = 0.3$ for $m = 4$; several thresholds can be found for this value of β, although no trivial physical interpretation has been found. In such cases, the code was modified to determine the critical value of β for a given value of Re. Note that the influence of the numerical resolution on Re_c for $\beta = 5$ has been verified using the same numerical grids as for $\beta = 0$ (351×51 and 1401×201), with variations below 0.58 %.

The most striking result in figure 10 is the dramatic drop in Re_c occurring at $\beta \approx 0.48$ for $m = 4$ and $\beta \approx 0.14$ for $m = 5$. The asymptotic value of Re_c predicted for large β and approached for β as small as 0.2, is also below 3000 in much closer agreement with experimental estimations (shown as the blue stripe in figure 10) than the numerical prediction with $\beta = 0$. These results suggest that a minute amount of surfactants can dramatically impact the flow stability, while additional pollution does not worsen the phenomenon further. In other words the effect of pollution is almost binary; either the interface is perfectly clean and the stability of the flow obeys the classical prediction from § 3, or it is not and the stability characteristics of the flow are of a fully different kind. This scenario is consistent with the experimental reproducibility of Re_c.

For the mode $m = 5$, a sharp change of slope is evident for $Re_c = 17\,259$, $\beta = 0.14$. This marks the presence of a codimension-two point, where two different marginal curves

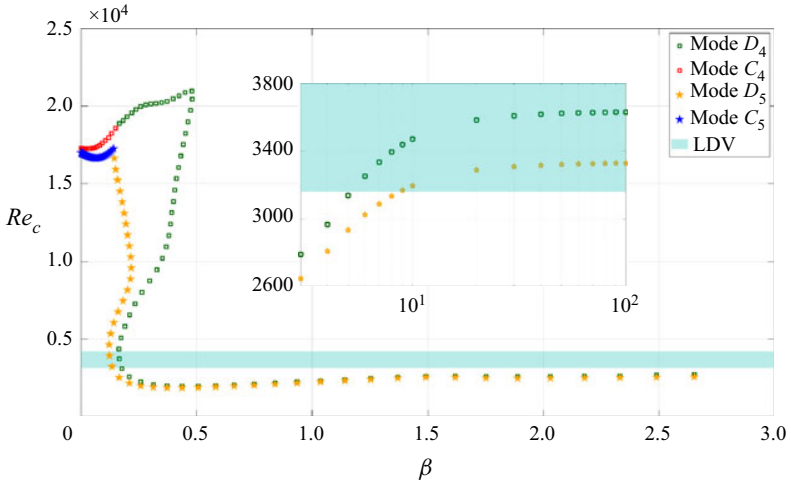

FIGURE 10. Neutral curve $Re_c(\beta)$ estimated from LSA for $G = 1/14$ and for the modes $m = 4$ (squares) and $m = 5$ (stars). The blue stripe corresponds to the experimental value of Re_c, independent of the model based on β. The thickness of the stripe is based on lower and upper bounds for Re_c from table 1. The inset figure represents in semi-log coordinates the continuation of the curves for $\beta \in [3{:}100]$.

for two different modes $m = 5$ intersect in a double Hopf bifurcation; on each side of the corresponding value of β, these are not the same family of eigenmodes that go unstable first, despite a common azimuthal wavenumber m. The crossing of eigenvalues is confirmed in figure 11 where the pair of eigenvalues is displayed on each side of the crossing. In each case, the branch taking over for larger β does apparently not extend down to $\beta = 0$; it corresponds to a new instability not found in the clean interface case. The computation of the branches beyond the codimension-two point was performed by a restriction of the number of eigenvalues computed around a shift. This shift was set equal to the angular frequency of the most unstable eigenvalue for the previous couple of parameters (Re_c, β). The evolution of the two leading eigenvalues as functions of both β and Re is detailed in figure 12(*a*). The least stable eigenvalue for the 'clean' case $\beta = 0$ is labelled 'C_m', where $m = 5$, whereas the least stable eigenvalue for the 'dirty' case $\beta \gg 1$ is simply labelled 'D_m'. From figure 12(*a*) it appears that the trajectories of the eigenvalues C_5 and D_5 in the complex plane, for variations of Re and β, follow different routes; C_5 becomes destabilised by increasing Re but stabilised by increasing β, whereas D_5 is destabilised by both increasing β and increasing Re.

In the case $m = 4$, an equivalent codimension-two point can be identified in figures 10 and 11, at $Re_c = 18\,869$, $\beta = 0.17$. For this mode, the drop in Re_c is more dramatic than for $m = 5$, and does not occur immediately after the codimension-two point. Instead, the new branch (in green in figure 10) continues to increase until at $Re_c = 20\,951$, $\beta = 0.48$ where it turns back. Again the trajectory of the corresponding eigenvalues C_4 and D_4 is documented in figure 12(*b*). The trajectories of C_4 in the complex plane are similar to those of C_5. However, the scenario for D_4 differs from that for D_5; an increase in Re stabilises the corresponding eigenmode whereas an increase in β destabilises it.

Interestingly, the asymptotic value of Re_c for $m = 4$ as well as the corresponding value of β at which the lowest values of $Re_c(\beta)$ are reached, seem to match that for $m = 5$. This suggests that the value of Re_c does not, for large β, depend on the value of m, at

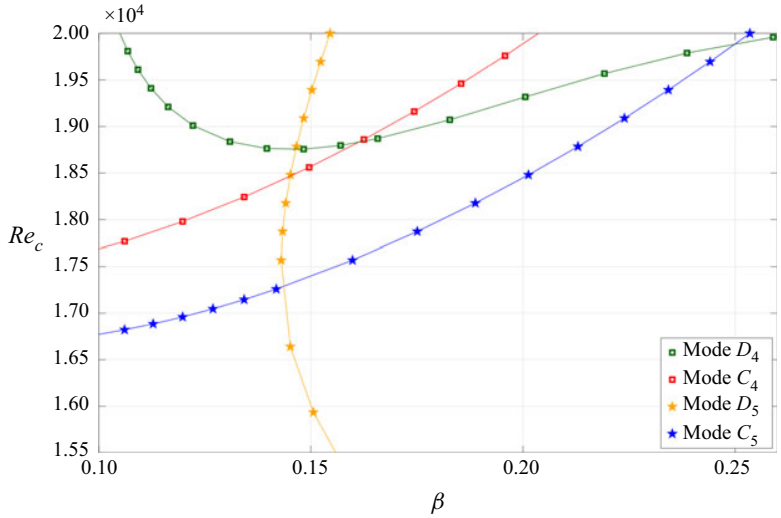

FIGURE 11. Zoom on codimension-two points of figure 10 in the (β, Re_c) plane, for $G = 1/14$, $m = 4$ and $m = 5$.

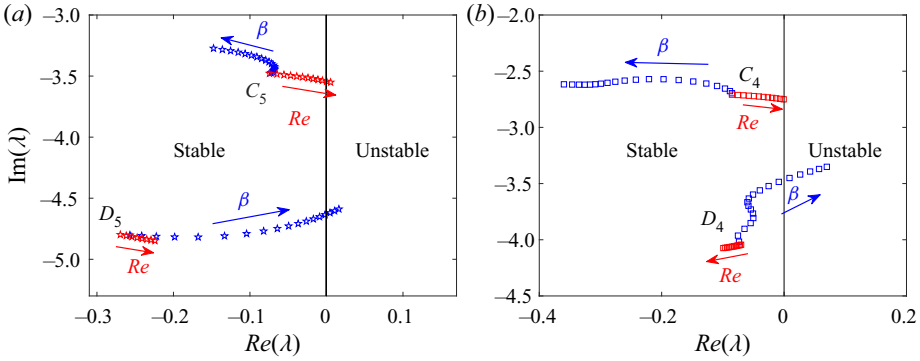

FIGURE 12. Evolution of the eigenvalues associated with the most dangerous modes ('clean' mode C and 'dirty' mode D) as a function of Re and β for $G = 1/14$; (*a*) $m = 5$ and (*b*) $m = 4$. The two evolutions start at $Re = 15\,000$ and $\beta = 0$. The C and D eigenvalues follow the lines indicated by the red arrows as Re is increased from 15 000 to 17 200 while $\beta = 0$. The eigenvalues evolve with varying β (at constant $Re = 15\,000$, blue arrows) with equally spaced steps from 0 to 0.18 for $m = 5$, and from 0 to 0.5 for $m = 4$.

least for this value of G. Preliminary computations for $G = 1/4$ have not confirmed this observation. A parametric study of Re_c as a function of both G and m would shed light on this question, but this lies outside the present scope.

The evolution of the angular frequency of the pattern at $Re = Re_c$ is displayed in figure 13 for both $m = 4$ and 5 as β is varied. Direct comparison of this figure with figure 10 shows that each jump to a new branch corresponds to a discontinuity in angular frequency. Again, the quantitative match with the experimental angular frequency is much more satisfying at finite β than around $\beta = 0$. For large β, the data approach the blue stripe in figure 13 within 1 % or less.

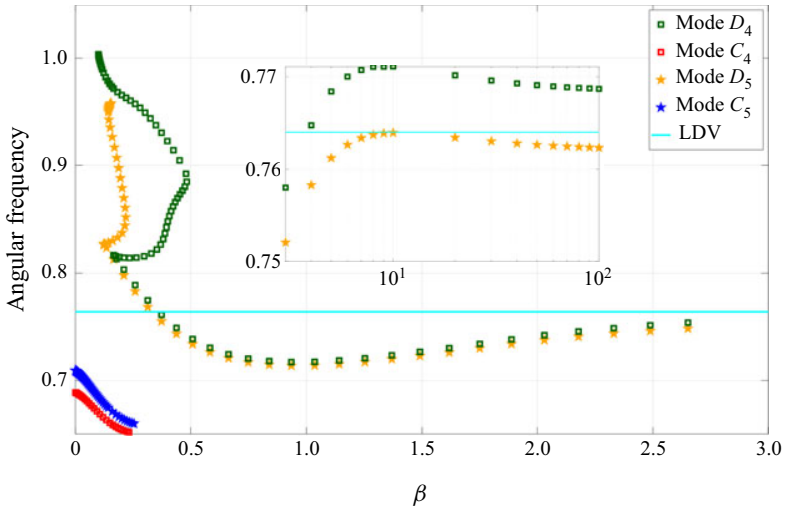

FIGURE 13. Angular frequency of the pattern $-\mathrm{Im}(\lambda)/m$ at $Re = Re_c(\beta)$ for $G = 1/14$, obtained using LSA for the modes $m = 4$ (squares) and $m = 5$ (stars). The blue line corresponds to the experimental value obtained using LDV (cf. table 1). The inset figure represents in semi-log coordinates the continuation of the curves for $\beta \in [3 : 100]$.

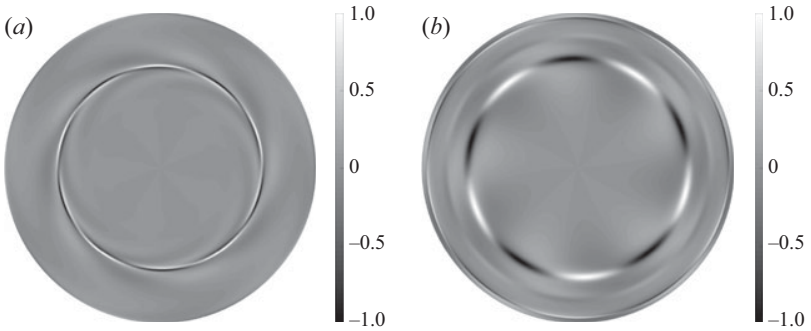

FIGURE 14. Vorticity $\omega_z(r, \theta)$ at the fluid interface (normalised by its maximum) for the least stable eigenmode $m = 5$ at $Re = 18\,620$; (*a*) $\beta = 0$, (*b*) $\beta = 5$.

Visualisations in physical space of the different modal families for a common wavenumber m are displayed in figure 14. From figures 10 and 13 it is now clear that these two eigenmodes correspond to two different modal families. For the $\beta = 0$ case the marginal eigenmode corresponds to the one found in Kahouadji *et al.* (2011).

Closer to the codimension-two point, the representation of ω_z as in figure 14 does not highlight the discrepancies between the two modes. However, the differences between them stand out again when representing the perturbation kinetic energy in a meridional plane (cf. figure 15); for the dirty mode the kinetic energy is much more localised close to $r \approx 0.7$ than for the clean mode. As for the eigenfrequencies, the variations in angular frequency are less dramatic than those in Re_c, nevertheless angular frequencies predicted for large β are in much better agreement with experimental values than the ones predicted for $\beta = 0$.

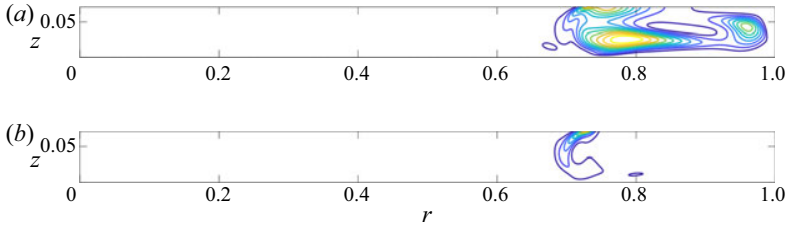

FIGURE 15. Meridional sections of local kinetic energy of the eigenmodes (normalised by its maximum) for the clean branch (a) and the dirty branch (b) at the codimension-two point ($Re = 17\,259$, $\beta = 0.14$). The ten isolines are equispaced between 0 (dark blue) and 1 (bright yellow).

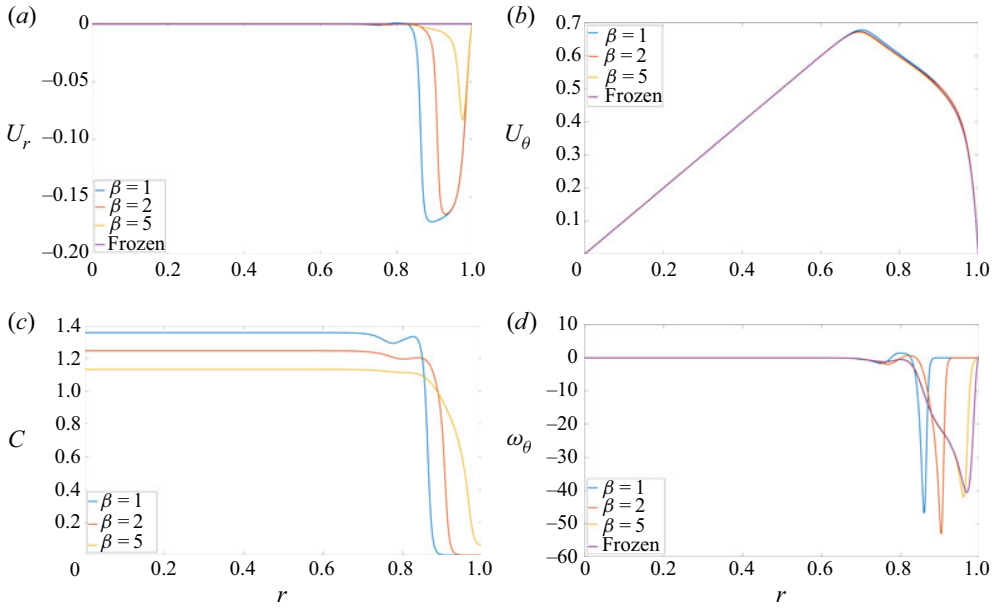

FIGURE 16. Comparison of several fields of the base flow at the interface, for a few values of β, at $Re = 18\,620$. (a) Radial velocity U_r, (b) azimuthal velocity U_θ, (c) pollutant concentration C, (d) azimuthal vorticity ω_θ. The results for the frozen surface condition are also included.

In order to evaluate the amount of pollution needed to switch from one family of branches to another, owing to (4.4), it is possible to estimate the variation of the surface tension at some point on the neutral curve. For instance, at onset $\beta = 1$, $Re_c = 2241$ (see figure 10), the non-dimensional concentration variation for C is $O(1)$, consistently with the finding in figure 16(c) (even if the value of Re is smaller, the concentration jump is the same. The main effect of decreasing Re is to soften the slope). Equation (4.4) reduces to $\tilde{\sigma} = 1 - Ca$ so that the capillary number is now a direct measure of the variation of surface tension. For the regime of interest with water, $Ca = 10^{-3}$, so that the surface tension varies by less than 1 %, which is indeed small and nevertheless leads to a large change in Re_c.

All the results above support the numerical prediction for finite β (non-clean interface) being consistent, both regarding the base flow and its marginally unstable eigenmodes,

with the experimental findings, whereas the clean interface ($\beta = 0$) hypothesis is not.

5. Frozen interface condition

5.1. *Search for a simpler parameter-free interface condition*

The results from the previous section have shown that a simple surface pollution model can capture qualitatively and quantitatively well the main features of the instability under investigation without any description of the physical processes related to the surface contamination. While it is possible to make the model quantitatively closer to the real case by adding more parameters, we search in this section for an even simpler model for the interfacial conditions. In particular, we would ideally like to have an analytically simple boundary condition for the velocity at the liquid–gas interface that is parameter free and does not request simulating additional concentration fields. This would make the implementation of such a model easy to achieve in practice in existing numerical codes, without depending on the precise (and usually unknown) details on the adsorption at the interface. The results of § 4 suggest the presence of a well-established asymptotic regime for large β, and the synthetic interfacial condition sought for is requested to match the large β limit. Several authors have already reported that the presence of pollutants is not compatible with the traditional hypothesis of free slip at the interface (Magnaudet & Eames 2000; Hirsa *et al.* 2002*b*; Martín & Vega 2006; Peaudecerf *et al.* 2017; Rastello, Marié & Lance 2017). In particular, whereas in our flow case the larger azimuthal velocity remains weakly affected by pollutants, the radial component of the velocity is severely diminished, making the hypothesis of vanishing u_r at the interface plausible (Spohn & Daube 1991; Lopez & Hirsa 2000). This is achieved in the numerical codes by changing the free-slip boundary conditions at the interface from (2.5) into

$$u_r = 0, \quad \frac{\partial u_\theta}{\partial z} = 0, \quad u_z = 0 \quad \text{at } z = G. \tag{5.1a–c}$$

The prime advantage of such an interfacial condition is its simplicity; as requested it is parameter free, chemistry free, it does not request coupling with an equation for the concentration and it does not rely on any closure for the effective surface tension. In the following, we assess numerically whether imposing this interfacial condition $U_r = 0$ for the base flow is a satisfying hypothesis.

5.2. *Base flow*

We estimate first how much the 'frozen' condition (5.1) is consistent with large values of β by assessing the spatial structure of the base flow. Note that 'frozen' refers here to the no-slip condition at the interface in contrast to free slip, and not to the fact that the interface is not allowed to deform. Figure 16 shows various radial profiles at the interface for the base flow, as β is increased beyond the values shown previously. Values of β up to 10^2 or 10^4 have been considered in order to monitor the dependence of the base flow on β. Figure 16(*a*,*b*) displays the radial and the azimuthal velocity components, respectively $U_r(r)$ and $U_\theta(r)$ evaluated at $z = G$. The length of the radial interval where the radial velocity U_r is non-zero decreases with increasing β, and the minimum value of U_r also approaches zero, suggesting absolute convergence to a homogeneous $U_r = 0$ profile. This justifies, for β large enough, $U_r = 0$ as an interfacial boundary condition, in agreement with previous experimental observations.

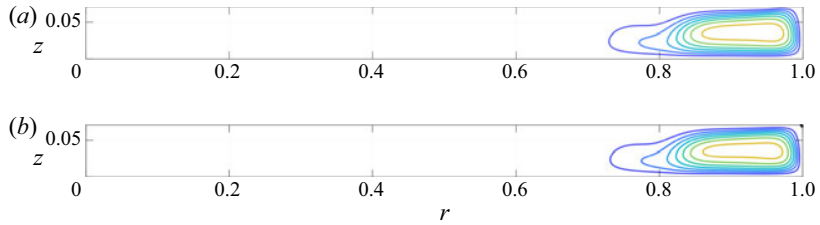

FIGURE 17. Comparison of ψ between $\beta = 5$ and the frozen surface condition at $Re = 18\,620$ (computed with ROSE). Iso-contour levels as in figure 8; (*a*) $\beta = 5$, (*b*) frozen surface.

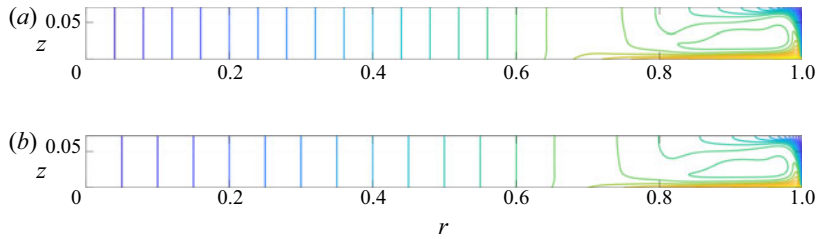

FIGURE 18. Meridional (r, z) cut for $\beta = 5$ and the frozen surface condition for $Re = 18\,620$ (computed with ROSE). Iso-contour levels as in figure 9; (*a*) $\beta = 5$, (*b*) frozen surface.

The major difference in the concentration curves (16*c*) is the non-zero concentration of pollutants, observed for every radial position when $\beta \gtrsim 5$. For smaller values of β, the concentration is advected towards the axis by the meridional recirculation, allowing for a small clean area to remain close to the outer wall. This leads to completely different vorticity profiles at the interface; for smaller values of β the vorticity is gathered around the radial position where the drop of concentration occurs. However, for $\beta \approx 5$ and above, the vorticity is stretched over a larger radial range, and converges to the frozen interface case. Interestingly, despite the fact that U_r is not exactly zero at the interface, all base flow profiles between $\beta = 5$ and the frozen surface condition appear identical, as is visually clear from figures 17 and 18.

5.3. *Nonlinear dynamics*

The condition (5.1) is here explicitly imposed in the nonlinear DNS calculations too. The simulation has been conducted with the same spatial resolution as in § 2. The newly computed instability pattern is shown in figure 19 past the initial transient. Without imposing any rotational symmetry, we see that, above Re_c, the most unstable mode emerges with an azimuthal wavenumber $m = 5$. Compared with simulations based on free slip (see figure 7*b*), the present nonlinear regime is much more predictable; this $m = 5$ mode persists for the whole observation time of up to $t = 1400$ time units) and the frequency spectrum remains limited to multiples of the fundamental frequency. The comparison between the numerical and experimental pointwise spectra is displayed in figure 20 for the same value of Re, and deserves to be compared with figure 7. From such a cross-comparison, it is a non-ambiguous fact that the frozen condition leads to a much better spectral reproduction of the experimental flow. In addition, although such comments are subjective, we report that the aspect of the pattern in figure 19 is visually

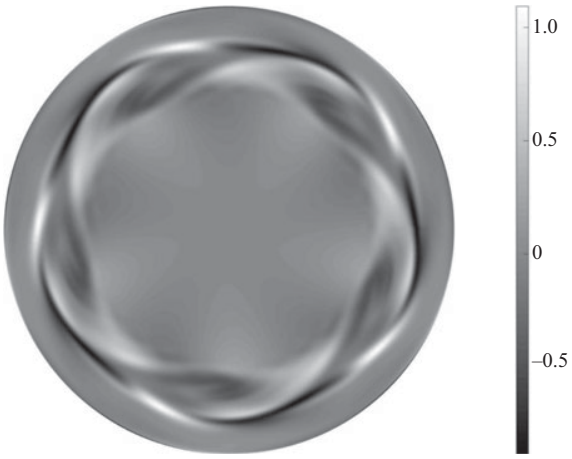

FIGURE 19. Axial vorticity of the fluctuations at the interface, DNS with frozen condition $u_r = 0$ at the interface for $Re = 18\,620$.

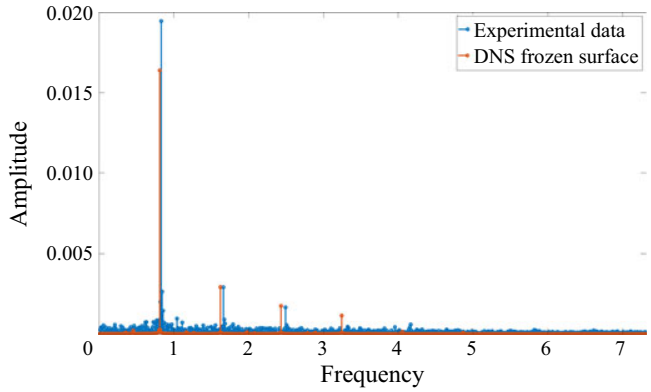

FIGURE 20. Comparison of amplitude spectra of u_θ measured at ($r = 0.76$, $z = 0.8G$): experimental data (blue) versus DNS for the frozen surface condition (orange), $Re = 18\,620$.

closer to the experimental one than those of figure 6(*b*) for the free-surface condition. More quantitatively, the approximate radius range where the axial vorticity fluctuations are concentrated in figure 19 is [0.59–0.91], while in figure 6(*a*) they are limited to [0.64–0.72]. From figure 3(*d*) we can estimate the width of this annular stripe in the experiment as [0.62–0.92]. Interestingly, the spatial structure of the linear eigenmodes (see e.g. figure 14) differs strongly from the structure of the nonlinearly saturated flow, which indicates that the role of the nonlinear terms goes beyond the sole saturation effects. This subsection confirms that the instability pattern with a frozen surface is much closer to the experimental pattern than the pattern from the free-surface simulation.

5.4. *Critical Reynolds number and least stable mode*

We observe in figure 10 that $Re_c(\beta)$ hardly evolves once β is large enough (larger than e.g. 5). This behaviour is confirmed for larger β, where the increase in Re_c remains limited.

β	$m = 4$	$m = 5$
5	3139	2934
100	3632	3330

TABLE 3. Critical Reynolds number estimated by LSA for $G = 1/14$.

	$\boldsymbol{u}^*$ free	$\boldsymbol{u}^*$ frozen
$\boldsymbol{U}$ free	17 006	18 959
$\boldsymbol{U}$ frozen	2776	10 555

TABLE 4. Value of Re_c for $m = 5$ and four sets of boundary conditions for the couple $(\boldsymbol{U}, \boldsymbol{u}^*)$.

The instability pattern appears similar to those shown in figure 14, which suggests that the most unstable mode of the frozen condition again belongs to an unstable branch different from the 'clean' unstable mode identified with the free-slip condition. Since the base flows for either large β or for the frozen interface condition have a very similar structure, we expect, for the frozen surface condition, a critical Reynolds number quantitatively comparable to those reported in table 3. However, it appears that for this new condition, LSA predicts $Re_c = Re_{c5} = 10\,555$ for $m = 5$, confirming DNS ($Re_c = 10\,584$). While this represents a drop of 39 % compared to the original critical Reynolds number for the free-surface condition ($Re_c = 17\,006$), it is still well above the experimental value by a factor of approximately 3. Similarly, using the same frozen condition, the threshold for the mode $m = 4$ at $Re_{c4} = 11\,152$ and remains very close to Re_{c5}.

5.5. *Conclusions on the frozen surface condition*

The nonlinear dynamics captured in DNS using the frozen surface condition is in excellent qualitative match with experimental measurements both from the point of view of the dynamics and the modal content of the saturated flow. This is again confirmed by the good agreement between the amplitude spectra shown in figure 20. The base flow with the frozen surface condition is hardly distinguishable from the base flow obtained using the pollutant model for $\beta \geq 5$. Nevertheless, once again, the comparison of the values of Re_c is not favourable, as for the frozen surface Re_c is 260 % (10 555 vs 2934) higher than for $\beta = 5$, which discredits the frozen condition as a direct substitute to the free-slip condition. This negative conclusion is further confirmed for $G = 1/4$ (the value considered by Lopez *et al.* 2004), where the most unstable mode remains poorly representative of experimental visualisations and Re_c is pushed even further up. These quick tests reveal how sensitive the instability threshold is to the choice of boundary conditions.

The quantitative discrepancy in Re_c can eventually be resolved by introducing a new boundary condition of a mixed type. Whereas the hypothesis of vanishing U_r is satisfying for the steady base flow and large enough values of β (see § 5.2), it is not justified for time-dependent perturbations. We suggest separating the velocity field $\boldsymbol{u}$ into its base flow component $\boldsymbol{U}$ and its perturbations $\boldsymbol{u}^*$ and applying a different set of boundary conditions to $\boldsymbol{U}$ and $\boldsymbol{u}^*$. The situation is summed up in table 4, where the four possible combinations of boundary conditions are considered and Re_c has been re-computed using ROSE for each case. Consistently with the previous arguments, we focus on the mixed-type boundary

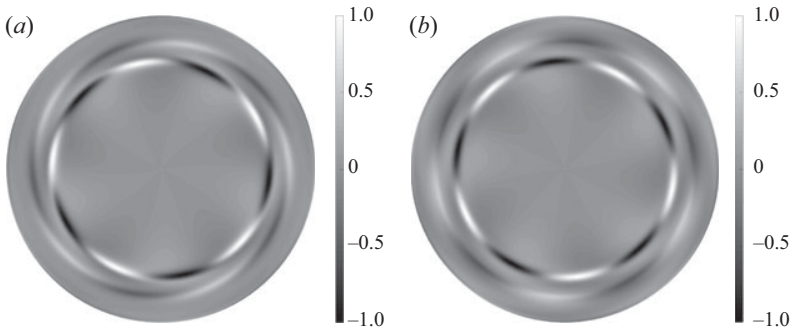

FIGURE 21. Vorticity $\omega_z(r, \theta)$ at the fluid interface (normalised by its maximum) for the least stable eigenmode $m = 5$ at $Re = 18\,620$. (*a*) Frozen surface, (*b*) mixed condition. The mixed condition corresponds to a frozen surface condition for the base flow, and free-surface condition for the perturbation field.

condition where the base flow obeys a frozen condition whereas the perturbation obeys the free-slip condition. The value of Re_c is now 2776, much lower than the fully frozen threshold value of 10 555. The quantitative mismatch is now reduced down to 6 % (2779 vs 2934) and 31 % (2779 vs 4230) compared to $\beta = 5$ and experimental Re_c, respectively, while the spatial structure (see figures 14 and 21 for the eigenmodes) is compatible with the frozen case.

6. Discussions and perspectives

The hydrodynamic instability occurring inside a fixed, cylindrical cavity with a rotating bottom has been investigated for a small form factor depth/radius $G = 1/14$. The selection of a least stable mode with azimuthal wavenumber $m = 5$, predicted by linear instability analysis, is verified experimentally, as well as numerically using DNS assuming no stress at the liquid interface. Using water – the most widespread liquid – as the experimental fluid, a robust quantitative and qualitative mismatch is evidenced between our experiments and our numerics. The mismatch concerns the presence of an overshoot in the azimuthal velocity profile and, crucially, the value of Re_c for the development of the instability is overestimated in the numerics by a factor of more than 4. Regarding the mismatch between our experimental estimation of Re_c and the literature, the use of Kalliroscope as a marker (used precisely for the identification of instability thresholds) is our best suspect to explain the discrepancy. The results obtained here using LDV, quantitatively safer, demonstrate that thresholds formerly deduced from visualisation using markers, are over-evaluated. The linear and nonlinear numerical approaches, however, report a robust threshold Re_c, that still differs strongly from the experimental one. After a cautious search for possible experimental flaws, the standard free-slip interface condition ($\sigma = \text{cst}$, $h = \text{cst}$, free-slip interface) used in the simulations emerged as the most credible source of mismatch, in line with former investigations by Spohn & Daube (1991) and Hirsa *et al.* (2002*a*); in experiments, such an ideal interfacial condition cannot be matched due to residual ambient air pollution. The inevitable presence of pollutants at the interface modifies the surface tension of the flow and, as a consequence, impacts the velocity field of the base flow and shifts the instability threshold. A pollution model has been implemented into the linear stability solver, based on a modification of the effective surface tension by the presence of a superficial concentration of unknown pollutants. Using a quadratic closure between the

tension surface and the superficial pollutant concentration inspired by surfactant studies yields results quantitatively consistent with experiments; for sufficiently large value of β (the parameter that pilots the surface contamination), Re_c drops by more than 80 % and the mismatch on Re_c goes down approximately from 400 % to 30 %.

Interestingly, the instability mode selected for finite pollutant concentrations does not belong to the same modal families as predicted by linear stability theory in the clean interface case; new branches of 'dirty' modes destabilise for small yet finite concentration levels and take over as least stable modes. The corresponding eigenmodes are very stable for clean interface conditions and have not been identified before. In terms of bifurcations, the robust mismatch in Re_c, angular frequency and flow structure between numerics and experiments can hence be explained, at least for the case of the modes $m = 4$ and 5 investigated here, as a jump from one modal family to another one as the contamination of the surface increases. The spatial structure of the base flow is also more consistent with LDV measurements; the meridional recirculation length is reduced and the overshoot in azimuthal velocity vanishes. For $\beta \gtrsim 5$, the flow at the interface verifies an approximate no-slip condition for the radial velocity component. As a consequence, in an effort to deliver a simpler parameter-free model boundary condition for unclean liquid/gas interfaces, the 'frozen condition' $u_r = 0$ was also simulated. Whereas it displays better qualitative agreement as well as simpler nonlinear dynamics consistent now with experiments, at least for low G, the threshold value Re_c remains too high compared to experiments. This new quantitative mismatch is eventually resolved once and for all by considering an interfacial boundary condition of a mixed type; frozen for the steady base flow and free slip for the unsteady perturbations.

Interfacial experiments involving water have long had the reputation of being 'difficult' in the sense that Marangoni effects linked with variations of the surface tension are hard to tame. The present hypothesis of a modification of the surface tension by pollution effects is one such illustration. The surprising effect of this pollution is, despite relatively small modifications of the structure of the base flow, an important quantitative impact on the stability thresholds. Besides, not only does the instability mode change its growth rate, it also belongs to another family of destabilised modes compared to the clean interface case. From such a simple conclusion it is tempting to critically revisit the discrepancies between experimental studies and to deduce that higher values of Re_c (as reported in Poncet & Chauve 2007) are linked to a cleaner interface due to different experimental conditions. While this is *a priori* possible (and very difficult to assess rigorously), it does not remove the caveat that Kalliroscope visualisations are not reliable in terms of measurements. Besides an interaction of the marker itself with the solvent cannot be excluded for high Kalliroscope concentrations. We are hence not in a position to conclude about the values reported by various teams using Kalliroscope or other markers, and encourage instead the use of non-intrusive techniques such as LDV for more reliable estimations. Other experimental improvements could here be useful, such as measuring simultaneously several velocity components, including smaller components such as the axial one and the radial component near the interface. This could allow for a critical evaluation of the model interfacial condition suggested in § 5.

While the present study is essentially a proof of concept that the stability characteristics of a given flow case depend heavily on the surface pollution, the simplicity of the analytical model in § 4 must be kept in mind. The advantage of such a simple model is a straightforward identification of the mechanisms altering the spatial structure of the base flow. The main difficulty lies in the mathematical parametrisation of a chemically complex phenomenon. Adsorption of pollutants by the interface is an unsteady process that depends on the precise chemical composition of the ambient particles in the air and

of the exact properties of the liquid. None of these hypotheses have been included in the present model, resulting in a simple law parametrised by one unique real parameter β and unable to cope with different chemical compositions and solubility effects. Further chemical complications can occur for increased concentration levels, notably bulk diffusion (necessitating a volumetric model rather than a superficial one) and later the formation of micelles inside the bulk of the fluid. Ideally, the modelling of pollution effects should be compared with an experimental set-up where the superficial concentration of each pollutant can be quantitatively controlled and properly modelled. It is not excluded that each different pollutant contributes differently to the final surface tension rather than all obeying the quadratic law of equation (4.1).

Finally, the present set-up is still academically simple in the sense that no deformation of the interface needs to be considered at such low rotation rates. A first way to incorporate more realistic effects is to consider the possibility for small deformations of the interface coupled with oscillations within the fluid. This situation might lead to the existence of additional families of eigenmodes and even richer dynamics. While this is technically much more involved, especially on the numerical side (see e.g. Yang *et al.* 2020), one can wonder whether pollution effects can also affect the thresholds in the large deformation regime investigated by many others (Vatistas, Abderrahmane & Siddiqui 2008; Tophøj *et al.* 2013) also in the presence of additional surfactants (Jansson *et al.* 2006). These regimes involve not only finite deformations of the fluid interface but also partial dewetting, which makes the dynamics of the concentration field more complex by involving moving triple contact lines. Eventually, it will be interesting to see how the trend evidenced in the present study (the decrease of Re_c by ambient pollution despite a calmer nonlinear regime) can be extended to other unstable flow configurations.

Acknowledgements

This work was supported by the French Agence Nationale de la Recherche under the ANR ETAE Project no. ANR-16-CE08-0011. HPC resources from GENCI-IDRIS (grant no. 2017-2a10308) are also acknowledged. The authors thank I. Delbende, F. Gallaire, W. Herreman, F. Lusseyran, W. Yang for fruitful discussions, the technical team CTEMO at LIMSI, as well as F. Moisy and M. Rabaud for their help on the experimental facility.

Declaration of interests

The authors report no conflict of interest.

REFERENCES

BANDI, M. M., AKELLA, V. S., SINGH, D. K., SINGH, R. S. & MANDRE, S. 2017 Hydrodynamic signatures of stationary Marangoni-driven surfactant transport. *Phys. Rev. Lett.* **119** (26), 264501.

CHENG, N. S. 2008 Formula for the viscosity of a glycerol-water mixture. *Ind. Engng Chem. Res.* **47** (9), 3285–3288.

COGAN, S. J., RYAN, K. & SHEARD, G. J. 2011 Symmetry breaking and instability mechanisms in medium depth torsionally open cylinder flows. *J. Fluid Mech.* **672**, 521–544.

DAUBE, O. 1991 Numerical simulation of axisymmetric vortex breakdown in a closed cylinder. In *Vortex Dynamics and Vortex Methods* (ed. C. R. Anderson & C. Greengard), Lectures in Applied Mathematics, vol. 28, pp. 131–152. American Mathematical Society.

DUGUET, Y., SCOTT, J. F. & LE PENVEN, L. 2005 Instability inside a rotating gas cylinder subject to axial periodic strain. *Phys. Fluids* **17** (11), 114103.

HIRSA, A. H., LOPEZ, J. M. & MIRAGHAIE, R. 2001 Measurement and computation of hydrodynamic coupling at an air/water interface with an insoluble monolayer. *J. Fluid Mech.* **443**, 271–292.

HIRSA, A. H., LOPEZ, J. M. & MIRAGHAIE, R. 2002*a* Determination of surface shear viscosity via deep-channel flow with inertia. *J. Fluid Mech.* **470**, 135–149.

HIRSA, A. H., LOPEZ, J. M. & MIRAGHAIE, R. 2002*b* Symmetry breaking to a rotating wave in a lid-driven cylinder with a free surface: experimental observation. *Phys. Fluids* **14** (6), 29–32.

HUISMAN, S. G., VAN GILS, D. P. M. & SUN, C. 2012 Applying laser Doppler anemometry inside a Taylor–Couette geometry using a ray-tracer to correct for curvature effects. *Eur. J. Mech.* B/*Fluids* **36**, 115–119.

HYUN, J. M. 1985 Flow in an open tank with a free surface driven by the spinning bottom. *J. Fluids Engng* **107** (4), 495–499.

IGA, K., YOKOTA, S., WATANABE, S., IKEDA, T., NIINO, H. & MISAWA, N. 2014 Various phenomena on a water vortex in a cylindrical tank over a rotating bottom. *Fluid Dyn. Res.* **46** (3), 031409.

IWATSU, R. 2004 Analysis of flows in a cylindrical container with rotating bottom and top underformable free surface. *JSME Intl J.* **47** (3), 549–556.

JANSSON, T. R. N., HASPANG, M. P., JENSEN, K. H., HERSEN, P. & BOHR, T. 2006 Polygons on a rotating fluid surface. *Phys. Rev. Lett.* **96** (17), 174502.

KAHOUADJI, L., HOUCHENS, B. C. & MARTIN WITKOWSKI, L. 2011 Thermocapillary instabilities in a laterally heated liquid bridge with end wall rotation. *Phys. Fluids* **23** (10), 104104.

KAHOUADJI, L., MARTIN WITKOWSKI, L. & LE QUÉRÉ, P. 2010 Seuils de stabilité pour un écoulement à surface libre engendré dans une cavité cylindrique tournante à petit rapport de forme. *Mécanique et Industries* **11** (5), 339–344.

KWAN, Y. Y., PARK, J. & SHEN, J. 2010 A mathematical and numerical study of incompressible flows with a surfactant monolayer. *Discrete Continuous Dyn. Syst.* **28** (1), 181–197.

LOPEZ, J. M. & CHEN, J. 1998 Coupling between a viscoelastic gas/liquid interface and swirling vortex flow. *J. Fluids Engng* **120** (4), 655–661.

LOPEZ, J. M. & HIRSA, A. 2000 Surfactant-influenced gas-liquid interfaces: nonlinear equation of state and finite surface viscosities. *J. Colloid Interface Sci.* **229** (2), 575–583.

LOPEZ, J. M., MARQUES, F., HIRSA, A. H. & MIRAGHAIE, R. 2004 Symmetry breaking in free-surface cylinder flows. *J. Fluid Mech.* **502**, 99–126.

MAGNAUDET, J. & EAMES, I. 2000 The motion of high-Reynolds-number bubbles in inhomogeneous flows. *Annu. Rev. Fluid Mech.* **32** (1), 659–708.

MARTÍN, E. & VEGA, J. M. 2006 The effect of surface contamination on the drift instability of standing Faraday waves. *J. Fluid Mech.* **546**, 203–225.

PEAUDECERF, F. J., LANDEL, J. R., GOLDSTEIN, R. E. & LUZZATTO-FEGIZ, P. 2017 Traces of surfactants can severely limit the drag reduction of superhydrophobic surfaces. *Proc. Natl Acad. Sci.* **114** (28), 7254–7259.

PONCE-TORRES, A. & VEGA, E. J. 2016 The effects of ambient impurities on the surface tension. *EPJ Web Conf.* **114**, 02098.

PONCET, S. & CHAUVE, M. P. 2007 Shear-layer instability in a rotating system. *J. Flow Visual. Image Process.* **14** (1), 85–105.

RASTELLO, M., MARIÉ, J. L. & LANCE, M. 2017 Clean versus contaminated bubbles in a solid-body rotating flow. *J. Fluid Mech.* **831**, 592–617.

SCRIVEN, L. E. 1960 Dynamics of a fluid interface: equation of motion for Newtonian surface fluids. *Chem. Engng Sci.* **12** (2), 98–108.

SERRE, E. & BONTOUX, P. 2007 Vortex breakdown in a cylinder with a rotating bottom and a flat stress-free surface. *Intl J. Heat Fluid Flow* **28** (2), 229–248.

SERRE, E., TULISZKA-SZNITKO, E. & BONTOUX, P. 2004 Coupled numerical and theoretical study of the flow transition between a rotating and a stationary disk. *Phys. Fluids* **16** (3), 688–706.

SPOHN, A. & DAUBE, O. 1991 Recirculating flows in a cylindrical tank. In *Proceedings of the 5th International Conference on Computational Methods and Experimental Measurement* (ed. A. Sousa, C. A. Brebbia & G. M. Carlomagno), pp. 155–166. Elsevier.

STEWARTSON, K. 1957 On almost rigid rotations. *J. Fluid Mech.* **3**, 17–26.

STONE, H. 1990 A simple derivation of the time-dependent convective-diffusion equation for surfactant transport along a deforming surface. *Phys. Fluids* **2** (1), 111–112.

SUZUKI, T., IIMA, M. & HAYASE, Y. 2006 Surface switching of rotating fluid in a cylinder. *Phys. Fluids* **18** (10), 101701.

TASAKA, Y. & IIMA, M. 2009 Flow transitions in the surface switching of rotating fluid. *J. Fluid Mech.* **636**, 475–484.

TOPHØJ, L., MOUGEL, J., BOHR, T. & FABRE, D. 2013 Rotating polygon instability of a swirling free surface flow. *Phys. Rev. Lett.* **110** (19), 194502.

VATISTAS, G. H., ABDERRAHMANE, H. A. & SIDDIQUI, M. H. K. 2008 Experimental confirmation of Kelvin's equilibria. *Phys. Rev. Lett.* **100** (17), 174503.

VATISTAS, G. H., WANG, J. & LIN, S. 1992 Experiments on waves induced in the hollow core of vortices. *Exp. Fluids* **13** (6), 377–385.

YANG, W., DELBENDE, I., FRAIGNEAU, Y. & MARTIN WITKOWSKI, L. 2019 Axisymmetric rotating flow with free surface in a cylindrical tank. *J. Fluid Mech.* **861**, 796–814.

YANG, W., DELBENDE, I., FRAIGNEAU, Y. & MARTIN WITKOWSKI, L. 2020 Large axisymmetric surface deformation and dewetting in the flow above a rotating disk in a cylindrical tank: spin-up and permanent regimes. *Phys. Rev. Fluids* **5** (4), 044801.

YOUNG, D. L., SHEEN, H. J. & HWU, T. Y. 1995 Period-doubling route to chaos for a swirling flow in an open cylindrical container with a rotating disk. *Exp. Fluids* **18** (5), 389–396.

Chapter III

Experimental tools

The configuration of the cavity, which appears to be basic, still hides many difficulties in its realization. Many rotating flow experiments use a lid, as this configuration is actually easier to build : the "lid" is at the bottom, while the spinning disc is at the top, avoiding sealing issue around the shaft, and allowing for an easier cleaning. In our configuration, with a free surface, we can't use such artifice. Our disc is located at the bottom of the cylindrical cavity (see fig. III.1). Hence, the shaft crosses the cavity, and we have to insure a perfect sealing around it. The second issue is the quality of the rotation, both in term of regularity of the rotation speed, and to prevent unbalanced rotation. If this last requirement is not met, it may add a translation to the fluid movement, and give birth to a sloshing phenomenon. Since the gap between the cavity vertical wall and the disc is small, any translation or precession movement could make the disc scrap the cavity.

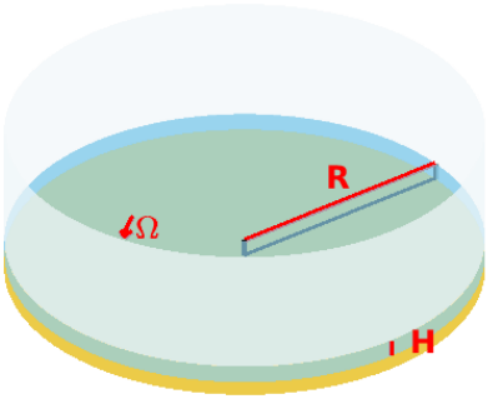

Figure III.1 – Simplified view of the largest cavity, with correct proportions. R is the radius of the cavity, H is the height of the undisturbed fluid (in blue) above the disc (in yellow), and Ω is the disc rotation rate.

Most of the technical elements of the main cavity are given in chapter II. Here we come back on these technical data, and add details that were not provided earlier, including a second experimental bench. We also give further information on the acquisition chain, measurement tools, markers, and fluids used in our experiments.

First cavity

At the beginning of the project, a first apparatus was built with the same geometrical characteristics as the one used at IRPHE by Poncet and Chauve ([40]). The cylindrical cavity, made of plexiglas, was borrowed from a former set-up (FAST [52]). Motor reducer unit, control card and power supply were also recycled from this former experiment. However, the disc was initially belt-driven. This system was changed to a simpler direct coupling and therefore, a new frame and a new aluminium foot were machined to carry the cavity. The motor reducer unit is screwed into this foot, and suspended below the table, in the same alignment as the rotation axis of the disc. The coupling between the reducer shaft and the disc is done with an aluminium sleeve. We recall that the

internal radius of this cavity is $R = 140.3\ mm$. The thickness of the wall is e=6.8 mm, and the maximal height above the surface of the disc is $H \approx 71.5\ mm$. The rotating disc is placed at the bottom of the cavity. Two different discs can be used. The one that was mainly used is made of brass. Its radius is $R - \epsilon_R$=139.6 mm, where ϵ_R represent the gap between the edge of the disc and the vertical wall. In the rest of this thesis, we will use R for both cavity and disc radius. The thickness of this disc is 8.5 mm and its mass is close to 5 kg. The maximum displacement of its surface while put into rotation is estimated to 0.3 mm. This measurement was made using both a mechanical comparator and a Keyence LK-G10 laser sensor. More details on surface displacements are given in chapter VII. The second disc is made of aluminium and was only used in preliminary tests about the influence of the flatness of the disc, since its surface was not accurately machined. Shafts are cohesive with their respective discs : they are screwed into it, and crosses the bottom of the cavity.

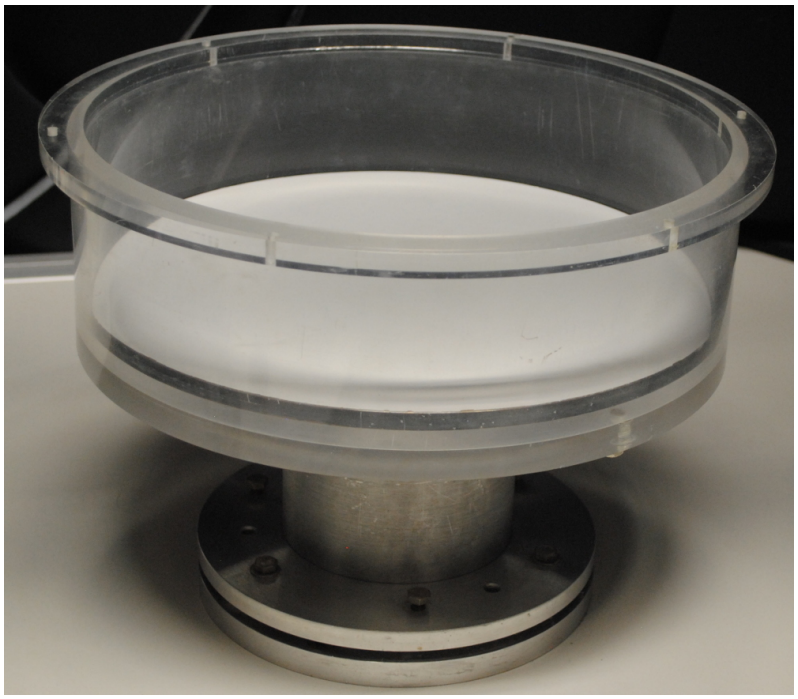

Figure III.2 – Photography of the large cavity, made of plexiglas. The brass disc is coated with a thin white plastic film, to enhance contrast with ink. The foot is made of aluminium.

The main advantage of this cavity is its size : as the radius is large, it is easier to control the height of the fluid H for small aspect ratios. But its main drawback is that this set-up is limited to aspect ratios below $G \sim$0.5.

Second cavity

The need for a higher cavity in the study of rotating polygons ([51]), and the will to explore higher aspect ratio leads us to design a second experiment. As we were confident in the motor and its servo solution (see below), we choose to keep this base, and to build a new structure to host the cavity.

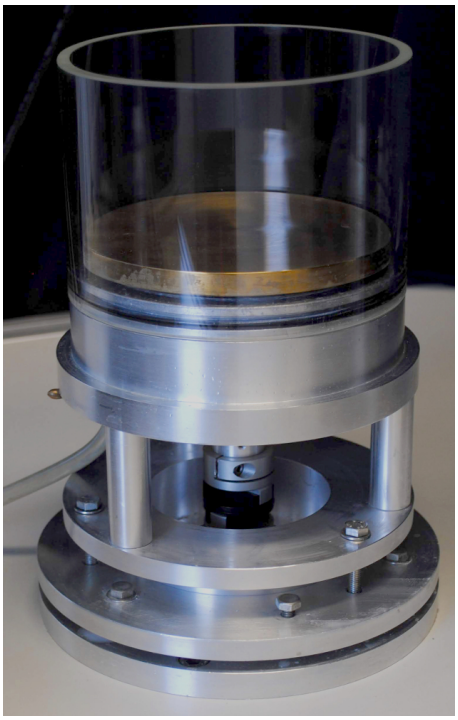

Figure III.3 – Photography of the small cavity, made of aluminium, brass (disc) and glass (cylindrical wall). One can see at the bottom the Oldham coupling for rotation irregularities absorption.

The previous rigid sleeve coupling is now replaced by an Oldham coupling, in order to prevent any misalignment of the disc shaft and the motor shaft. To manage enough space to place this coupling, the base of the cavity is raised by three braces. This base is machined in aluminium, and includes two conical bearings in a back-to-back arrangement to steer the rotation of the shaft. The disc material is brass, and its dimensions are $R - \epsilon_R$=68 mm for the radius and 10.1 mm for the thickness. The sealing is done below the disc, and no more on the shaft, but still with a single lip spring loaded seal. The vertical wall of the cavity is a glass cylinder, which inner radius is R=70 mm and thickness is 5.2 mm. This cylinder is fitted on the base, and an O-ring ensures the sealing between those two elements. The height H=114 mm of the cavity allows one to reach aspect ratios up to G=1.5.

Driving and monitoring the rotation

Both experimental set-ups use the same direct current motor (Parvex RX320E-R1100), coupled with a 1:12 reductor. A tachymeter deliver a tension of 6 mV per round of the motor, or 72 mV per round of the disc. This difference is due to the presence of the reducer. A voltmeter Agilent 34401A is used to monitor the rotation of the disc. The rotation speed is controlled with a servo loop, done by a Parvex card. This card has an ± 10 V input to control the motor speed. We coupled this input to an Mbed micro-controller. If required, this allows us to perfectly control spin up and spin down phases.

Data Acquisition

There are two kinds of data we can acquire from our experiment. The first one are images, or movies, captured by an IDS camera (UI-3370CP), mounted at the vertical of the cavity. This camera uses a 11.264×11.264 mm^2 sensor of 4.19 Mpx, coupled with a 35 mm F1.4 Fujinon lense (CF35HA-1). The camera is linked to a computer by USB3, and allows to record movies at 80 frames per seconds with a 2048×2048 resolution, up to 12 bits grey scale. In practice, an 8 bits greyscale was used.

For more quantitative measurements of the velocity, we used a Dantec laser doppler velocimetry device (LDV). It is composed of a laser head Flow Explorer, coupled to a BSAFlow processor. It allows the acquisition of the local velocity of only one component. To do so, the fluid has to be seeded with particles that will be detected by the laser. The particles we employed are also provided by Dantec, and are silver coated hollow glass, with a size of 10 μm.

Laser Doppler Velocimetry

The principle of LDV relies on detection of particles across fringe pattern, such as obtained with a Michelson interferometer in the fringes of equal thickness configuration : two coherent laser beams cross and create a pattern of alternatives bright and dark stripes (see fig. III.4). The frequency f_r of reflected beams on coated particles crossing the brightening fringes are detected by a sensor. We suppose here that particles are small and with a comparable density than that of the fluid to be carried at the same speed than the flow, without influencing it. If we denote by d_i the inter-fringe gap, *i.e.* the width of brightening fringe, the velocity of the particle u_p is given by the relation $u_p = f_r d_i$. d_i depends on the wave length λ of the laser and of the angle θ_L of beams through the relation $d_i = \lambda/(2\sin(\theta_L/2))$. One can pair both previous relations through the equation :

$$u_p = f_r \frac{\lambda}{2\sin(\theta_L/2)}. \tag{III.1}$$

However, equation (III.1) does not give any information about the direction of the flow : the measured frequency would be the same for both flows of same velocity, but opposed direction. Therefore, a Bragg cell generate a scrolling of the fringes. Knowing

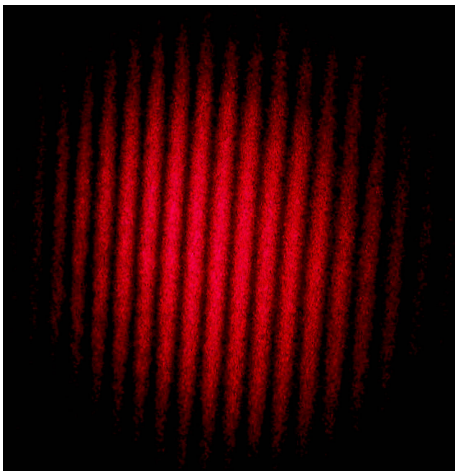

Figure III.4 – Fringes of equal thickness obtained with a Michelson interferometer. For the LDV device we used, in the air, inter-fringe gap is $\approx 6\ \mu m$.

this scrolling speed (and thus its direction), one can access to the direction of the flow.

Optical corrections

Due to the triple medium crossed by the laser (which implies three different optical indices), we had to apply a geometrical correction to the position of convergence of the two laser beams. Indeed, as d_i is paired with θ_L, a variation of the angles of beams implies an erroneous evaluation of the fringes width, and thus of the velocity. Using Snell-Descartes laws, and intersection coordinates between a line and a circle, one can easily calculate the position of the effective point of measurement. These corrections were published in [53]. Details are given in appendix C

Zeroing lasers intersection

Corrections described above require lasers intersection to match the axis of rotation. Laser can easily be translated along the X and Z axis, relatively to the laboratory frame, thanks to a motorised horizontal stage and a manually operated vertical displacement (see fig. III.5). Stages are mounted on an aluminium plate relying on three micrometer screws, in order to adjust horizontality.

Nevertheless, no device allows for an easy rotation of the global laser group around its z axis, and it has to be placed manually on the table to try to cross the optical axis of the laser and the rotation axis of the disc. This leads to inaccuracies in positioning that may explain later the mismatch between experimental and numerical velocity profiles. Even if the laser optical axis is perfectly merged with the radius of the disc, the operator still have to adjust the position of the beam at the vertical of the center of the disc. This point location is also prone to inaccuracy. Two solutions were use to locate it. The first

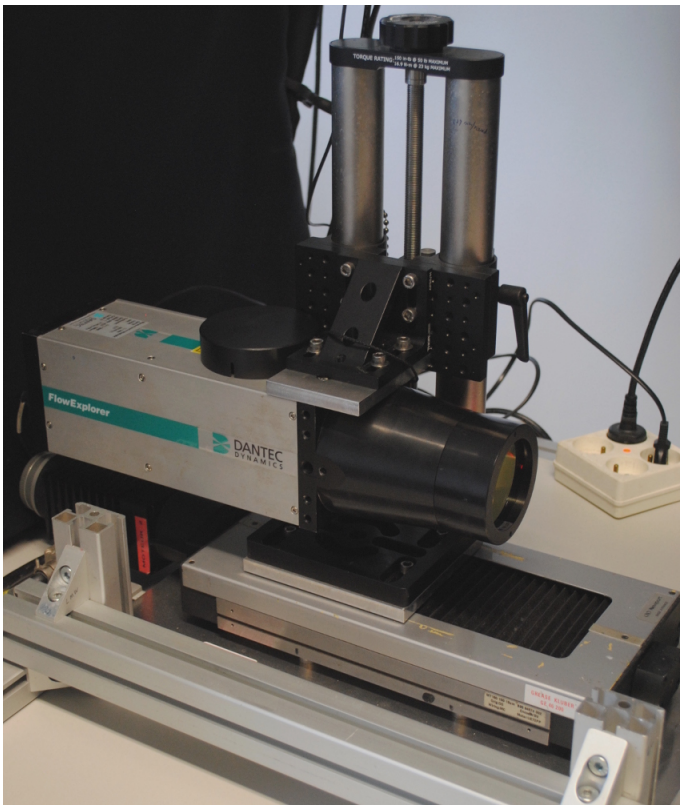

Figure III.5 – Dantec LDV head, gathering laser and photosensitive cell. The head is mounted on a manual screw driven vertical stage. The assembly is fixed on a motorized horizontal stage.

one relied on perpendicular bisectors of a triangle inscribed on the disc to place its center. Then, a solid shape was placed on the disc, with one of its edge orthogonal to the disc's surface, at the vertical of the center. The convergence of the beam was then adjusted on this edge. The second solution to find the center uses the camera above the disc. The dimensions of the disc on its image taken by the camera allows for finding the coordinates of the pixel corresponding to the disc's center. Then, using the live capture of the camera, the intersection of the beam was adjusted to match these coordinates. Note that this last solution is only suitable for azimuthal measurements.

Experimental protocol

The increase of Re is obtained by an increase of the disc rotation rate Ω. As long as an instability is not triggered and no hysteresis is present, the protocol to increase Ω does not matter. On the opposite, as soon as an instability may occur, the threshold detection may be protocol dependent. Velocity was increased by steps, and held constant on a plateau between two steps. The requested time to accelerate the disc from one plateau to

another is very short compared to the timespan of the plateau itself. Even if the disc is quite heavy, and thus has an important inertia, the motor has enough torque for the acceleration of the disc to be almost instantaneous. The spin-up time for the fluid is always much larger than the time required for the disc to accelerate. If the flow is dominated by viscous effects then the transition time would scale as R^2/ν, H^2/ν, or RH/ν. In our case, the regime is always dominated by convective effects with boundary layers and thus the time evolution of the system is given by the Ekman time $t_{Ek} = \frac{R}{\sqrt{\nu\Omega}}$.

Initially, following the protocol used by Poncet and Chauve in [40], we used the Ekman time as reference for each plateau with a given Ω. As t_{Ek} decreases with the increase of Ω, plateau are increasingly shorter. For exemple, for Ω=1 rpm, $t_{Ek} \approx 433s$, while for Ω=8 rpm, $t_{Ek} \approx 153s$. However, there is no reason to link the base flow spin-up time to the growth rate of the instability. Therefore we switched to a constant timespan for each plateau. We chose an arbitrary timespan between 10 min to 15 min; followed by 5 min of acquisition when LDV was used. This crude and empirical protocol does not guarantee either that at a given Re, the growth rate of the instability is large enough to observe the instability. However, our hope is that during the plateau, the noise level is large enough to feed the instability so that it can be observed.

The accuracy on Re_c determination is also limited by the step of 1 rpm between each plateau. At times, this step was reduced to 1/2 rpm or 1/3 rpm. An alternate option to increase the accuracy of the bounding of the instability threshold is to use a more viscous fluid. Doing so allows one to reach higher rotation rates for a given Re, and also to reduce the issue of particles sedimentation (see below section Markers). However, increasing the rotation rate also increases the surface deformation, and an increased caution must be observed during experiment to stay in admissible Ω values to keep valid the flat surface hypothesis.

Fluids & Markers

Fluids

Although we mostly used water as experimental fluid (tap, de-ionized or distilled water), we also used water glycerol mixtures. The reason for the choice of glycerol is that it is non toxic and fully soluble in water. It thus allows an easy adjustment of the viscosity, and can easily be cleaned, in contrast to silicon oils.

Solutions of water diluted glycerol have been widely studied, so that the properties of such mixtures are well tabulated in many articles such as [54] or handbooks of physics and chemistry. Especially, one can easily access to the optical indices of such mixtures ([55]), and to their viscosity, regarding the mass percentage of glycerol and temperature. Indeed, with the use of glycerol, temperature becomes a major focus : compared to water, water-glycerol solutions have an increased dependency of their viscosity to temperature, especially for high percentage of glycerol. As none of our cavity are thermo-regulated, temperature has to be monitored continuously. Viscosity was then estimated according to an experimentally fitted analytical expression given in [56]. This expression was already

checked with rheology measurements during the very first experiments, back in 2013, and estimated adequate compared to the inaccuracies of low viscosity measurements.

Ethanol was also marginally experimented, but experimental restrictions (alcohol-plexiglas reaction, vapours) limited these experiments.

Markers

To obtain visualisation of the pattern, markers are needed. The first one we used was Kalliroscope. This rheoscopic fluid was created in 1960 by the artist Paul Matisse. It is composed of small particles of crystalline guanine that are supposed to orient themselves according to vorticity of the flow. Crystalline guanine particles average dimensions are $6 \times 30 \times 0.07 \mu m^3$ with a density of 1.62 $g.cm^{-3}$, according to [57]. Depending on their orientation, and thanks to their high index of refraction (1.85), the reflection of light on these flakes produces a greyscale visualization. This marker was widely used, including, among others, Taylor-Couette (fig. III.6), or Rayleigh-Bénard experiments. This was also the visualisation tool used in [40]. Note that due to the drop of Crystalline guanine production, Kalliroscope is no longer sold since 2014.

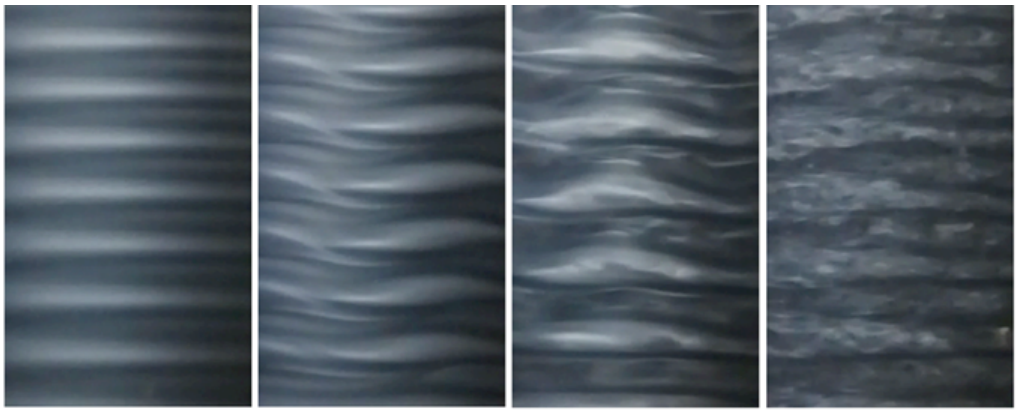

Figure III.6 – Taylor-Couette instabilities revealed thanks to Kalliroscope.

Some issues with the reproducibility of our results forced us to re-consider the neutrality of Kalliroscope, and thus, the use of this marker. We kept it only for visualisation purpose, without any quantitative aspect. For a better detection of thresholds we switched to ink diluted into water. This marker is less intrusive, and fully soluble into water. The ink was injected at the surface at a single random location, for one disc rotation, using a syringe. This advantage is also its main flaw : in highly mixing flow, the ink is adsorbed too quickly to allow for any visualisation. Even in slowly rotating flows, the fluid has to be seeded with ink repeatedly. However it gives great results on higher density fluids, such as water glycerol mixture.

The influence of Kalliroscope flakes on rotating flows was reported as early as 1985 ([58]) : in vertically oriented Couette-Taylor experiment, Kalliroscope flakes influenced

the size of Taylor vortices. It was observed that particles were clustering in the core of vortices, resulting in a coupling with the gravitational field. Although Matisse and Gorman claimed the neutrality of Kalliroscope ([59]), the results from Dominguez *et al.* ([58]) are consistent with our observations about sedimentation and clustering of Kalliroscope particles.

Chapter IV

Governing equations

Basic equations

Since we remain in the approximation of a continuous medium, and since we restrain the study to Newtonian fluids, we can describe the motion of the flow with Navier-Stokes equations :

- **Mass conservation equation :**

$$\frac{\partial \rho}{\partial t} + \nabla \cdot (\rho \mathbf{u}) = 0$$

where ρ is the volumetric mass density of the fluid, and $\mathbf{u}$ is the velocity field.

- **Momentum conservation equation :**

$$\frac{\partial \rho \mathbf{u}}{\partial t} + \nabla \cdot (\rho \mathbf{u} \otimes \mathbf{u}) = \rho \mathbf{F} - \nabla p + \nabla \cdot (\mu \nabla \mathbf{u})$$

where μ is the dynamic viscosity of the fluid.

For the rest of this thesis, we will make the assumption that the flow is incompressible ($\nabla \cdot \mathbf{u}$=0) and we will neglect volume forces, except gravity ($\mathbf{F} = \mathbf{g}$). For the pressure, we will use the reduced pressure $p = P_0 + \rho g z$. We can now simplify the previous equations :

$$\begin{cases} \nabla \cdot (\mathbf{u}) = 0 \\ \dfrac{\partial \mathbf{u}}{\partial t} + (\mathbf{u} \cdot \nabla)\mathbf{u} = -\dfrac{1}{\rho}\nabla p + \nu \Delta \mathbf{u} \end{cases}$$

where $\nu = \frac{\mu}{\rho}$ is the kinematic viscosity of the fluid, and $\Delta = \nabla^2$. μ is assumed to be constant.

Regarding to the geometry, it is convenient to use cylindrical coordinates. The components of the velocity field $\mathbf{u}$ are now defined as $\mathbf{u} = (u_r \mathbf{e_r} + u_\theta \mathbf{e}_\theta + u_z \mathbf{e_z})$. Navier-Stokes equations become :

$$\begin{cases} \dfrac{1}{r}\dfrac{\partial (r u_r)}{\partial r} + \dfrac{1}{r}\dfrac{\partial u_\theta}{\partial \theta} + \dfrac{\partial u_z}{\partial z} = 0 \\ \dfrac{\partial u_r}{\partial t} + u_r \dfrac{\partial u_r}{\partial r} + \dfrac{u_\theta}{r}\dfrac{\partial u_r}{\partial \theta} + u_z \dfrac{\partial u_r}{\partial z} - \dfrac{u_\theta^2}{r} = -\dfrac{1}{\rho}\dfrac{\partial p}{\partial r} + \nu \left[\Delta u_r - \dfrac{u_r}{r^2} - \dfrac{2}{r^2}\dfrac{\partial u_\theta}{\partial \theta} \right] \\ \dfrac{\partial u_\theta}{\partial t} + u_r \dfrac{\partial u_\theta}{\partial r} + \dfrac{u_\theta}{r}\dfrac{\partial u_\theta}{\partial \theta} + u_z \dfrac{\partial u_\theta}{\partial z} + \dfrac{u_r u_\theta}{r} = -\dfrac{1}{\rho r}\dfrac{\partial p}{\partial \theta} + \nu \left[\Delta u_\theta - \dfrac{u_\theta}{r^2} + \dfrac{2}{r^2}\dfrac{\partial u_r}{\partial \theta} \right] \\ \dfrac{\partial u_z}{\partial t} + u_r \dfrac{\partial u_z}{\partial r} + \dfrac{u_\theta}{r}\dfrac{\partial u_z}{\partial \theta} + u_z \dfrac{\partial u_z}{\partial z} = -\dfrac{1}{\rho}\dfrac{\partial p}{\partial z} + \nu \Delta u_z \end{cases}$$

where $\Delta\xi = \frac{1}{r}\frac{\partial}{\partial r}(r\frac{\partial \xi}{\partial r}) + \frac{1}{r^2}\frac{\partial^2 \xi}{\partial \theta^2} + \frac{\partial^2 \xi}{\partial z^2}$ is the Laplacian operator in cylindrical coordinates, and ξ any component of the velocity field.

Dimensionless form

In order to obtain the dimensionless form of previous Navier-Stokes equations, we used the radius of the cavity R and the angular frequency Ω of the disc to build the characteristic scales :

$$\begin{cases} \mathbf{u} = R\Omega\bar{\mathbf{u}} \\ t \to \dfrac{\bar{t}}{\Omega} \\ p \to \rho(R\Omega)^2\bar{p} \\ r \to R\bar{r} \end{cases}$$

Applying these changes to Navier-Stokes equations leads to :

$$\begin{cases} \dfrac{\partial \bar{u}_r}{\partial \bar{r}} + \dfrac{\bar{u}_r}{\bar{r}} + \dfrac{1}{\bar{r}}\dfrac{\partial \bar{u}_\theta}{\partial \theta} + \dfrac{\partial \bar{u}_z}{\partial \bar{z}} = 0 \\ \dfrac{\partial \bar{u}_r}{\partial \bar{t}} + \bar{u}_r\dfrac{\partial \bar{u}_r}{\partial \bar{r}} + \dfrac{\bar{u}_\theta}{\bar{r}}\dfrac{\partial \bar{u}_r}{\partial \theta} + \bar{u}_z\dfrac{\partial \bar{u}_r}{\partial \bar{z}} - \dfrac{\bar{u}_\theta^2}{\bar{r}} \\ \qquad = -\dfrac{\partial \bar{p}}{\partial \bar{r}} + \dfrac{1}{Re}\left[\Delta(\bar{u}_r) - \dfrac{\bar{u}_r}{\bar{r}^2} - \dfrac{2}{\bar{r}^2}\dfrac{\partial \bar{u}_\theta}{\partial \theta}\right] \\ \dfrac{\partial \bar{u}_\theta}{\partial \bar{t}} + \bar{u}_r\dfrac{\partial \bar{u}_\theta}{\partial \bar{r}} + \dfrac{\bar{u}_\theta}{\bar{r}}\dfrac{\partial \bar{u}_\theta}{\partial \theta} + \bar{u}_z\dfrac{\partial \bar{u}_\theta}{\partial \bar{z}} + \dfrac{\bar{u}_r\bar{u}_\theta}{\bar{r}} \\ \qquad = -\dfrac{1}{\bar{r}}\dfrac{\partial \bar{p}}{\partial \theta} + \dfrac{1}{Re}\left[\Delta(\bar{u}_\theta) - \dfrac{\bar{u}_\theta}{\bar{r}^2} + \dfrac{2}{\bar{r}^2}\dfrac{\partial \bar{u}_r}{\partial \theta}\right] \\ \dfrac{\partial \bar{u}_z}{\partial \bar{t}} + \bar{u}_r\dfrac{\partial \bar{u}_z}{\partial \bar{r}} + \dfrac{\bar{u}_\theta}{\bar{r}}\dfrac{\partial \bar{u}_z}{\partial \theta} + \bar{u}_z\dfrac{\partial \bar{u}_z}{\partial \bar{z}} \\ \qquad = -\dfrac{\partial \bar{p}}{\partial \bar{z}} + \dfrac{1}{Re}\Delta(\bar{u}_z) \end{cases} \tag{IV.4}$$

where Re is the Reynolds number, defined as $Re = \frac{R^2\Omega}{\nu}$.

Boundary conditions

Cavity side wall

On the vertical wall of the cavity, boundary conditions are assumed to be impermeability and non slip. As the wall is immobile, this can be translated this to velocity components :

$$u_r = u_\theta = u_z = 0 \tag{IV.5}$$

Disc

As for the wall, we suppose non slip condition and impermeability of the disc. But this "wall" is not immobile in the laboratory frame. Indeed, it rotates at an angular speed of Ω, hence the velocity components become :

$$\begin{cases} u_r = u_z = 0 \\ u_\theta = r\Omega \end{cases}$$

which can be written in a dimensionless form :

$$\bar{u_r} = \bar{u_z} = 0,\ \bar{u_\theta} = \bar{r}$$

Liquid-Gas Interface

A few words on the flat surface hypothesis

In real flows, the centrifugal force increases with rotation speed, and pushes the fluid outward, digging the surface in the centre of the disc. The most well-known example is Newton's bucket parabolic surface, that leads nowadays to liquid mirror telescope technology (fig. IV.1).

Approaches with surface deformation were realized in [42], [51] and [15]. Without entering too deeply in surface deformation analysis, such as in the two first references, one can consider the leading order of the free surface deflection, Δh. According to [15], starting from the normal stress balance, and considering that the pressure in the flow writes $p_l = p - \frac{\Delta h}{Fr}$, we obtain :

$$\frac{\Delta h}{Fr} - p + \frac{2}{Re}\frac{\partial u_z}{\partial z} = 0$$

Here, a new dimensionless number is introduced : the Froude number Fr, defined as $Fr = \frac{\Omega^2 R}{g}$, and that compares centrifugal forces to gravity. Previous equation can easily be rewritten as :

$$\Delta h = Fr\left(p - \frac{2}{Re}\frac{\partial u_z}{\partial z}\right)$$

This equation gives an excellent first approximation of the shape of the free surface, even for heavily deformed interface ([60]), and although the pressure and the velocity are computed with a flat free surface.

For the hypothesis of flat surface remains valid, we need to check that $\Delta h \to 0$, and thus, that $Fr \to 0$. This can only be achieved if the disc rotation rate Ω is small enough. Practically, rotation rates in experiments never goes up to $20rpm$, and were even mostly

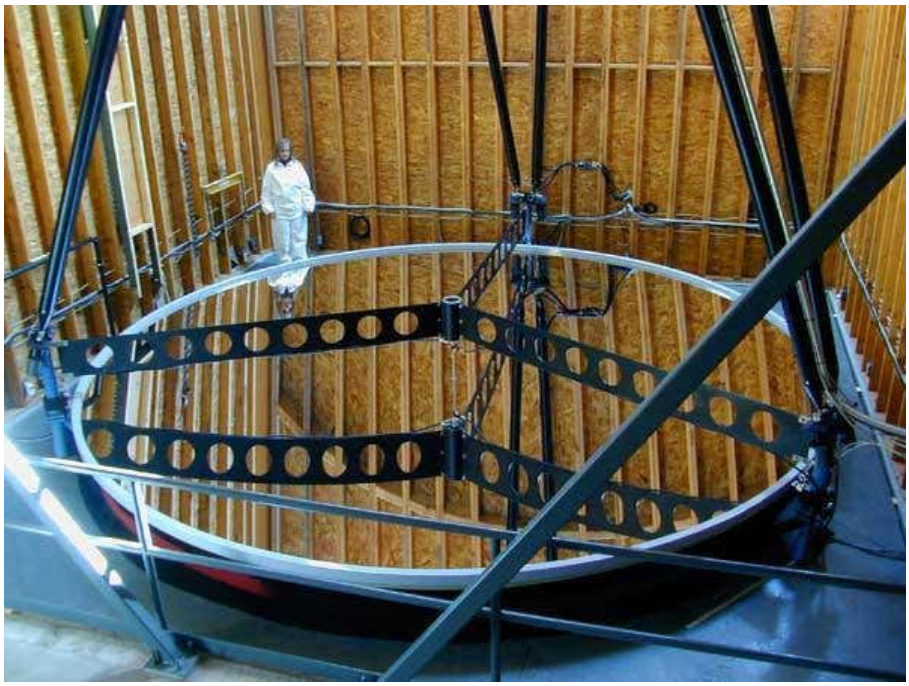

Figure IV.1 – The almost paraboloid surface of Large Zenith Telescope, the largest Liquid Mirror Telescope. The shape of the surface is due to the rotation of the container in which a reflective liquid (mercury) is held.

below $8rpm$. In the largest cavity, that indeed generates the largest Fr, a rotation at $20rpm$ gives Fr=0.06. For such value of the Froude number, computation using the code developped in [42] shows a maximum deflection of 20% at r=0 and for G=1/14, which is the aspect ratio that is mainly studied in this thesis. However, as it will be seen, the region where the instability takes place is around r=0.7. There, the interface is barely deformed. Thus, and since $Fr \ll 1$ over the whole rotation speed span, the flat surface hypothesis is a quite good approximation. This scenario will be retained in the rest of this thesis, and will deeply simplify the numerical simulations. Experimentally we will be mindful not to take a too viscous fluid to avoid the need of a higher rotation speed to destabilize the flow. The influence of moderate deformations of the interface was numerically checked in [42]. The author demonstrated that it has minor to no impact on the instability threshold, at least for small G.

Now that this assumption is made, one can detail the boundary condition at the surface within this context.

Kinematic boundary conditions

The kinematic boundary conditions came from the non miscibility condition between the two phases :

$$\mathbf{u_l} = \mathbf{u_g}$$

This impermeability condition does not imply any constraint on u_r and u_θ components, but leads to a condition on u_z :

$$u_z = 0 \tag{IV.7}$$

Dynamic boundary conditions

As long as the motion is not driven by the gas, a liquid-gas interface is often considered as a stress-free boundary. This is the assumption adopted in the first part of this thesis. Other approaches are detailed in chapters VIII and IX.

To determine the dynamic boundary conditions at the interface, a no-shear condition ($\mu_l \gg \mu_g$) is assumed in the two tangential directions to the surface :

$$\boldsymbol{\tau}.\overline{\overline{S}}.\mathbf{n} = 0,$$

Since the surface is assumed to remain flat, $\boldsymbol{\tau}$ can either be $\mathbf{e}_\theta$ or $\mathbf{e_r}$ and $\mathbf{n}$= $\mathbf{e_z}$. $\overline{\overline{S}} = -p\mathbb{1} + \overline{\overline{T}}$ is the Cauchy stress tensor. The surface tension is here assumed to be constant, and thus, does not play any role. The fluid is supposed to be Newtonian, hence $\overline{\overline{T}} = 2\mu\overline{\overline{D}} + \lambda_L tr(\overline{\overline{D}})$, where λ_L is the first Lamé parameter, and $\overline{\overline{D}}$ is the symmetrical part of the velocity gradient, such as $\overline{\overline{D}} = \frac{1}{2}\left(\overline{\overline{\nabla}}\mathbf{u} + {}^T\overline{\overline{\nabla}}\mathbf{u}\right)$. We made the hypothesis that the flow is incompressible, thus $\lambda_L tr(\overline{\overline{D}}) = \nabla \cdot \mathbf{u} = 0$, and the system finally reduces to :

$$\frac{\partial u_r}{\partial z} = 0, \qquad \frac{\partial u_\theta}{\partial z} = 0 \tag{IV.8}$$

The jump condition on the normal constraint reads :

$$\mathbf{n}_l.\overline{\overline{S_l}}.\mathbf{n}_l - \mathbf{n}_g.\overline{\overline{S_g}}.\mathbf{n}_g = 0 \tag{IV.9}$$

where $\mathbf{n}_g = -\mathbf{e}_z$ and $\mathbf{n}_l = \mathbf{e}_z$.

Since the interface is flat, there is no pressure jump due to surface tension : $p_l = p_g$, where indices l and g respectively refer to liquid and gas medium. Thus, equation (IV.9) can be shortened to $\mathbf{n}_l.\overline{\overline{S_l}}.\mathbf{n}_l = 0$. Using the same tensor as detailed above, this jump condition simply leads to :

$$\frac{\partial u_z}{\partial z} = 0 \tag{IV.10}$$

Chapter V

Numerical methods

One of the strengths of this thesis is to cross experimental and numerical approaches. After the introduction of experimental tools in the chapter III : Experimental tools, focus is now on numerical codes that were used.

Numerical simulation is closely interrelated to modern fluid mechanics. The power of numerical simulation is to provide a large quantity of data that is inaccessible - or hardly accessible - in experiments. This allows for an in-depth immersion into the flow, and for an accurate knowledge of it. Although some could think simulations make experiments obsolete, this work actually blurs boundaries between experimental and numerical approaches : even in the simple configuration considered, only their complementarity allowed for a deeper understanding.

Our numerical simulations rely on two in-house codes. The first one, called ROSE, is a linear stability analysis code, while the second, Sunfluidh, is a direct numerical simulation (DNS) of Navier Stokes equations. Both of them are introduced in details in this chapter, and validated by comparison to literature.

Linear stability analysis : computing with ROSE

About ROSE

ROSE stands for ROtating Surface Evolution. This code was previously developed by L. Kahouadji and L. Martin Witkowski [42] and more recently upgraded by W. Yang [51] to track surface deformation, where it earns its current name. The code gets some inspiration on the method published by Ryskin and Leal [61],[62],[63] for solving fluid mechanics problems with or without boundary deformation. ROSE allows for fast simulation of steady flows in cylindrical geometry, and a search of the critical Reynolds number for which the flow becomes unstable, for a prescribed azimuthal wave number m.

Its limits are the intrinsic ones of linear stability analysis (LSA) : it is only valid close to the critical Reynolds number, and under the hypothesis of zero nonlinear effects. Transient growth ([64]) is another issue that is not addressed by ROSE.

Equations

For more convenience, and since only dimensionless velocities will be used, the notation $\bar{.}$ for dimensionless quantities is dropped from here.

Linear stability analysis relies on a splitting of the solution into two parts : the base flow on the one hand, and the perturbations on the other hand. Both are treated independently due to the linearization. The perturbations are cast around the base flow solution, with an ansatz of the form $\xi(r,z)e^{\lambda t+im\theta}$, where $m \geq 0$ is the azimuthal wave number and $\xi(r,z)$ is any component of the velocity or pressure field.

For each field, the ansatz take the form :

$$\begin{cases} u_r = U_r + \epsilon \Re(u_r^* e^{\lambda t + im\theta}) \\ u_\theta = U_\theta + \epsilon \Re(i u_\theta^* e^{\lambda t + im\theta}) \\ p = P + \epsilon \Re(p^* e^{\lambda t + im\theta}) \end{cases}$$

These equations are injected into equations (IV.4) that are then linearized to the first order, and split in two systems thanks to linearity. The first one will be the system of equations for the base flow, and the second will be the system of equations for the perturbations.

Base flow

Considering only the base flow related elements, which is assumed steady and axisymmetric, Navier-Stokes equations can be rewritten withouh any time and θ derivatives, and thus come down to :

$$\begin{cases} \dfrac{\partial U_r}{\partial r} + \dfrac{U_r}{r} + \dfrac{\partial U_z}{\partial z} = 0 \\ U_r \dfrac{\partial U_r}{\partial r} + U_z \dfrac{\partial U_r}{\partial z} - \dfrac{U_\theta^2}{r} = -\dfrac{\partial P}{\partial r} + \dfrac{1}{Re}\left(\Delta U_r - \dfrac{U_r}{r^2}\right) \\ U_r \dfrac{\partial U_\theta}{\partial r} + U_z \dfrac{\partial U_\theta}{\partial z} + \dfrac{U_r U_\theta}{r} = \dfrac{1}{Re}\left(\Delta U_\theta - \dfrac{U_\theta}{r^2}\right) \\ U_r \dfrac{\partial U_z}{\partial r} + U_z \dfrac{\partial U_z}{\partial z} = -\dfrac{\partial P}{\partial z} + \dfrac{1}{Re}\Delta U_z \end{cases} \tag{V.2}$$

Since the base flow is axisymmetric, it is computed in $2D$ in a plane $(O,\mathbf{e_r},\mathbf{e_z})$, on a Cartesian grid. It is convenient to introduce a $\omega - \psi - \Gamma$ formulation, where ω is the azimuthal vorticity, ψ is the stream function, and Γ is the angular momentum. The relations between those new variables, and the primitive variables U_r,U_θ,U_z are :

$$U_r = \frac{1}{r}\frac{\partial \psi}{\partial z},\ U_z = -\frac{1}{r}\frac{\partial \psi}{\partial r},\ \omega = \frac{\partial U_r}{\partial z} - \frac{\partial U_z}{\partial r},\ \Gamma = rU_\theta$$

Using these new variables, and after few operations on (V.2), the system can be rewritten as :

$$\begin{cases} 0 = r\omega - \left(\dfrac{\partial^2 \psi}{\partial r^2} - \dfrac{1}{r}\dfrac{\partial \psi}{\partial r} + \dfrac{\partial^2 \psi}{\partial z^2}\right) & \text{(V.3a)} \\ 0 = \dfrac{\partial}{\partial r}\left(\dfrac{1}{r}\dfrac{\partial \psi}{\partial z}\omega\right) - \dfrac{\partial}{\partial z}\left(\dfrac{1}{r}\dfrac{\partial \psi}{\partial r}\omega\right) - \dfrac{\partial}{\partial z}\left(\dfrac{\Gamma^2}{r^3}\right) \\ \quad - \dfrac{1}{Re}\left(\dfrac{\partial^2 \omega}{\partial r^2} + \dfrac{1}{r}\dfrac{\partial \omega}{\partial r} - \dfrac{\omega}{r^2} + \dfrac{\partial^2 \omega}{\partial z^2}\right) & \text{(V.3b)} \\ 0 = \dfrac{\partial}{\partial r}\left(\dfrac{\partial \psi}{\partial z}\Gamma\right) - \dfrac{\partial}{\partial z}\left(\dfrac{\partial \psi}{\partial r}\Gamma\right) - \dfrac{r}{Re}\left(\dfrac{\partial^2 \Gamma}{\partial r^2} - \dfrac{1}{r}\dfrac{\partial \Gamma}{\partial r} + \dfrac{\partial^2 \Gamma}{\partial z^2}\right). & \text{(V.3c)} \end{cases}$$

The stream function-vorticity (V.3a) equation is easily derived from the definition of the azimuthal vorticity. The angular momentum transport equation (V.3c) came from the equation on U_θ, multiplied by r^2. The last equation for the vorticity transport (V.3b) is the result of the subtraction of the cross derivatives of the equations on U_r and U_z.

Once discretized on the Cartesian grid with the standard finite differences, the non-linear system for the unknown on grid points (V.3) is solved iteratively with a Newton-Raphson method : it consists in approximating the function as its first order Taylor expansion in order to find a root. $\phi(x) = 0$, where ϕ are the discretized Navier-Stokes equations and x are the unknown on each grid point, is approximated by $0 = \phi(x_n) - \phi'(x_n)(x_n - x_{n+1})$, where $\phi'(x_n)$ is actually a Jacobian of the system. Thus, $\phi^{prime}(x_n)(x_{n+1} - x_n) = -\phi(x_n)$ is solved iteratively until $x_{n+1} - x_n \leq \epsilon$ where ϵ is the selected convergence criterion. At each Newton iteration, Pardiso solver is used to solve the large sparse nonsymmetric linear system.

u=0 is an appropriate initial guess for the Newton method to reach convergence for moderate Re values. For larger Reynolds numbers, it is usually necessary to start from a previously converged solution for a lower Re. This is the basic continuation method.

Perturbations

The equations for the perturbations do not use the same $\omega - \psi - \Gamma$ formulation as the base flow, but keep primitive variables u_r, u_θ, u_z,p. Here, we only consider first order terms related to perturbations in the linearized Navier-Stokes equations :

$$
\begin{cases}
0 = \frac{1}{r}\frac{\partial r u_r^*}{\partial r} - \frac{m u_\theta^*}{r} + \frac{\partial u_z^*}{\partial z} \\
-\lambda v_r^* = \frac{2}{r}\frac{\partial}{\partial r}\left(r u_r^* U_r\right) - \frac{1}{r}\left(m u_\theta^* U_r - i m u_r^* U_\theta + 2 i u_\theta^* U_\theta\right) \\
\qquad + \frac{\partial}{\partial z}\left(u_r^* U_z + u_z^* U_r\right) + \frac{\partial p}{\partial r} \\
\qquad - \frac{1}{Re}\left[\frac{\partial^2 u_r^*}{\partial r^2} + \frac{1}{r}\frac{\partial u_r^*}{\partial r} - \frac{1}{r^2}\left((1+m^2)u_r^* + 2 m u_\theta^*\right) + \frac{\partial^2 u_r^*}{\partial z^2}\right] \\
-\lambda v_\theta^* = \frac{1}{r}\frac{\partial}{\partial r}\left(r u_\theta^* U_r\right) + \frac{1}{r}\left(u_\theta^* U_r + 2 i m u_\theta^* U_\theta - i u_r^* U_\theta - i\frac{\partial}{\partial r}(r u_r^* U_\theta)\right) \\
\qquad - \frac{\partial}{\partial z}\left(i u_z^* U_\theta - u_\theta^* U_z\right) + \frac{m p}{r} \\
\qquad - \frac{1}{Re}\left[\frac{\partial^2 u_\theta^*}{\partial r^2} + \frac{1}{r}\frac{\partial u_\theta^*}{\partial r} - \frac{1}{r^2}\left((1+m^2)u_\theta^* - 2 m u_r^*\right) + \frac{\partial^2 u_\theta^*}{\partial z^2}\right] \\
-\lambda v_z^* = \frac{1}{r}\frac{\partial}{\partial r}\left(r u_r^* U_z + r U_r u_z^*\right) + \frac{1}{r}\left(i m u_z^* U_\theta - m u_\theta^* U_z\right) + \frac{\partial}{\partial z}\left(2 u_z^* U_z + p\right) \\
\qquad - \frac{1}{Re}\left[\frac{\partial^2 u_z^*}{\partial r^2} + \frac{1}{r}\frac{\partial u_z^*}{\partial r} - \frac{m^2 u_z^*}{r^2} + \frac{\partial^2 u_z^*}{\partial z^2}\right]
\end{cases}
$$

ROSE solves this generalized eigenvalue problem using the ARPACK library with shift invert strategy. It provides a selected number of eigenvalues around a given shift, and for a prescribed azimuthal mode. The flow is said to be unstable when at least one eigenvalue has a real part greater than zero, meaning that the growth rate of the instability is positive. ROSE uses a secant method to converge to Re_c.

Boundary conditions

The boundary conditions come directly from equations (IV.5), (IV.6), (IV.8), (IV.10) and (IV.7). Along the vertical wall and on the disc, we impose a no slip condition, while the free surface is treated like a symmetry plane. Note that the axis is not formally a physical boundary condition. Still, the choice of the cylindrical coordinates imposes a special treatment at r=0.

Base flow

The boundary conditions have to be recast into the $\omega - \psi - \Gamma$ formulation.

- **Axis** (r=0) **:**

$$\omega = \psi = \Gamma = 0.$$

- **Wall** (r=1) **:**

$$\omega = \frac{1}{r}\frac{\partial^2 \psi}{\partial r^2},\ \psi = \Gamma = 0.$$

- **Disc** (z=0) **:**

$$\omega = \psi = 0,\ \Gamma = r^2.$$

- **Gas-liquid interface** (z=G) **:**

$$\omega = \psi = 0,\ \frac{\partial \Gamma}{\partial z} = 0. \tag{V.5}$$

Perturbations

- **Axis :**

$$\begin{cases} m = 0 : u_r^* = u_\theta^* = \dfrac{\partial u_z^*}{\partial r} = 0 \\ m = 1 : \dfrac{\partial u_r^*}{\partial r} = \dfrac{\partial u_\theta^*}{\partial r} = u_z^* = 0 \\ m \geq 2 : u_r^* = u_\theta^* = u_z^* = 0 \end{cases}$$

- **Wall :**

$$u_r^* = u_\theta^* = u_z^* = 0$$

- **Disc :**

$$u_r^* = u_\theta^* = u_z^* = 0$$

- **Gas-liquid interface :**

$$\frac{\partial u_r^*}{\partial z} = \frac{\partial u_\theta^*}{\partial z} = u_z^* = 0$$

Validation & Mesh

To validate the LSA code, we set the aspect ratio to G=1.5 : this aspect ratio was numerically investigated in a former article, in light of both linear stability analysis and DNS, with a spectral-element solver, in [44]. The results of the comparison between ROSE and this publication are gathered in table V.1.

	m=1	m=3
Cogan *et al.* (LSA)	2152	2525
ROSE (301×201)	2146	2515

Table V.1 – Validation of Re_c determined with ROSE on the case G=1.5. Reference used for comparison is [44].

Although the compared codes use different numerical methods, excellent agreement was found between ROSE results and previously published works : only 0.3% and 0.7% relative error are observed on Re_c of modes 1 and 3, respectively.

The classical mesh used for G=1/14 was 701 × 101 in r and z, respectively. For G=0.25, the grid used 401 × 101 nodes. Comparisons of Re_c values with a grid refined twice in each direction are given in the next chapter.

DNS code : Sunfluidh

Motivations

In addition to linear stability analysis, we performed direct numerical simulations (DNS) of the flow using Sunfluidh. The DNS approach directly solves the Navier-Stokes equations (V.2) without additional modelling of the nonlinear terms. This provides computational results that are as close as possible to real physics of the flow. The simulation takes into account non linear effectsand thus allows for a study of complex time dynamic. However, computations come at an heavier time and hardware cost compared to the linear stability analysis. Using two codes (LSA and DNS) with completely different methods to solve the Navier-Stokes equations also gives the opportunity to perform a cross validation directly in our configuration.

The DNS code outputs include instantaneous fields of velocity and pressure, time averaged velocity fields, and velocity time series on specified probes. We recall here that averaged velocity fields are not necessarily equivalent to the base flow, unless it remains steady. However, averaged fields are easily comparable to mean velocity measured by LDV : DNS is the ideal bridge between LSA and experiments.

Introduction to Sunfluidh

Sunfluidh is a finite volume code based on a staggered grid to discretize velocities (in the middle of edges), and pressure (in the center of cells). It was initially developed for simulations of both 2D and 3D unsteady incompressible flows, or flows in the low Mach number hypothesis. The code is maintained by Y. Fraigneau.

The equations solved are the Navier-Stokes equations :

$$\rho\left(\frac{\partial \boldsymbol{u}}{\partial t} + (\boldsymbol{u}\cdot\nabla)\boldsymbol{u}\right) = -\nabla p + \nabla\cdot\bar{\bar{S}},$$

where p is the pressure, and

$$S_{ij} = \mu\left(\frac{\partial u_i}{\partial x_j} + \frac{\partial u_j}{\partial x_i}\right)$$

is the stress tensor. As the flow is incompressible, the continuity equation is reduced to

$$\nabla\cdot\boldsymbol{u} = 0$$

Spatial discretization uses a second order centered conservative scheme, while the temporal discretization is done with a second order backward differentiation formulation (BDF2). Here, the method is semi implicit : only the viscous terms of the Navier-Stokes equations are evaluated at t^{n+1}, while convective terms are explicitly evaluated from

known fields at t^n and t^{n-1}. The stability of the numerical scheme is therefore improved, and timesteps can be larger. The stability mostly relies on the Courant–Friedrichs–Lewy (CFL) condition. Typical values are chosen in the interval [0.3-0.4]. We remind that in three dimensions, the CFL is given by :

$$CFL = \Delta t \left(\sum_{i=1}^{3} \frac{|u_{x_i}|}{\Delta x_i} \right).$$

The equations V.2.2 are solved by a projection method, that required two steps. Firstly, during the prediction stage, the velocity is estimated at a time t^{n+1}. Secondly, in the correction stage, the pressure field at t^{n+1} is computed, and the velocity determined previously is corrected with the verification of the divergence-free of the momentum equations V.2.2. Incompressibility is imposed at this stage with a Poisson equation on pressure. More detailed explanations are given in the appendix of [65].

Depending on if the domain is reduced or not in the azimuthal direction (see below, Domain limitation in θ), this equation is solved in two different ways. If the domain is complete ($0 \leq \theta \leq 2\pi$), partial diagonalization of the Laplacian operator is preferred. This direct method is efficient, is not currently implemented for domains limited to a certain angle in θ. Therefore, for the few times we were faced with this case, we used a successive over relaxed (SOR) method coupled to a multigrid cycle.

Boundary conditions

Unlike in the LSA, there is only one set of boundary conditions for the whole flow. On the outer vertical wall, the standard no-slip condition is applied, plus the impermeability of the wall :

$$u_r = u_\theta = u_z = 0.$$

The disc is treated as an impermeable no-slip wall, with an azimuthal velocity r :

$$u_r = u_z = 0, \; u_\theta = r$$

At the axis, there is no special constraint on the axial velocity and u_r is the only component required to compute the discrete fluxes. Therefore the discussion is limited to a plane orthogonal to the axis $\mathbf{e}_z$. Considering $u_x\mathbf{e}_x + u_y\mathbf{e}_y$, the velocity into this plane, where $\mathbf{e}_x$ and $\mathbf{e}_y$ are the unit vectors in Cartesian coordinates, the azimuthal velocity component can be expressed as $u_\theta = -u_x \sin(\theta) + u_y \cos(\theta)$. Taking the limit as $r \to 0$ gives :

$$\lim_{r \to 0} u_\theta = -u_x^0 \sin(\theta) + u_y^0 \cos(\theta) \tag{V.7}$$

where $u_x^0\mathbf{e}_x + u_y^0\mathbf{e}_y$ is the velocity at the axis. In order to obtain u_x^0 and u_y^0, we multiply the equation(V.7) by $\sin(\theta)$ and $\cos(\theta)$, respectively. Then the integration over a circle around the axis gives :

$$\begin{cases} u_x^0 = \lim\limits_{r\to 0}\left(-\dfrac{1}{\pi}\displaystyle\int_0^{2\pi} u_\theta(r,\theta')\sin(\theta')d\theta'\right) \\ u_y^0 = \lim\limits_{r\to 0}\left(\dfrac{1}{\pi}\displaystyle\int_0^{2\pi} u_\theta(r,\theta')\cos(\theta')d\theta'\right) \end{cases}$$

In practice, the integration is performed over a radius whose size is half the radial length of the first cell, and over the finite number of cells in the azimuthal direction. The projection on u_r finally gives :

$$\lim_{r\to 0} u_r = u_x^0\cos(\theta) + u_y^0\sin(\theta)$$

The interface is also impermeable and remains flat, thus the boundary conditions imposed at the surface are equivalent to a free-slip :

$$\frac{\partial u_r}{\partial z} = \frac{\partial u_\theta}{\partial z} = 0,\ u_z = 0$$

The computational domain is like a parallelepiped that is bent on itself in the azimuthal direction, to form a torus with a zero inner radius. Therefore, we have to insure the continuity of the flow across the two walls that face each other : periodicity conditions are imposed on these walls.

Mesh & Performance

DNS was mostly used in the G=1/14 case. The mesh used for this aspect ratio contains 2073600 nodes, distributed on a refined grid with 180 cells in r, 180 cells in θ, and 64 in z. This grid appears to be sufficiently refined with a decent physical time of computation : the performance time index is around $10^{-6}s/cell/timestep$.

Sunfluidh allows for both sequential and parallelised procedures. Most runs were done uning OpenMP parallelization, on six threads of an Intel Xeon E5-2643 v3 processor of the local LIMSI cluster. This choice was made after scalability tests, as shown in table V.2

Thread count	physical time elapsed (s)	CPU time (s)
1	80.32	80.32
2	48.08	95.14
4	32.52	117.10
6	22.86	122.54
8	19.45	136.13
12	16.51	172.46

Table V.2 – Sunfluidh scalability test on 50 iterations, with OpenMP parallelization.

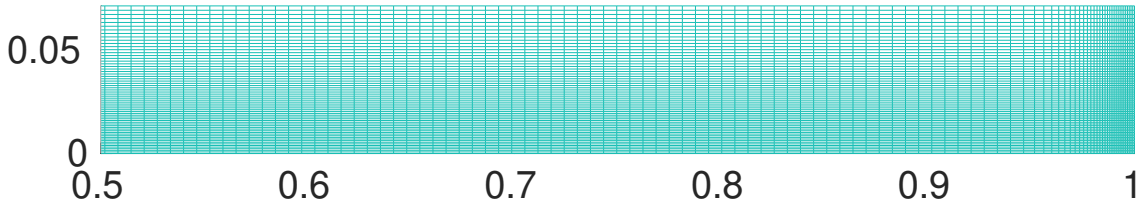

(a) Meridional plane

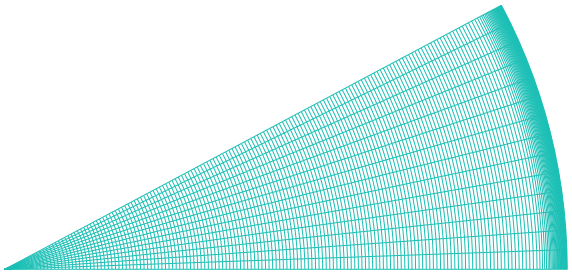

(b) Azimuthal plane

Figure V.1 – Representation of the mesh used for G=1/14, in planes (r,z) (V.1a), and (r,θ) (V.1b). θ is restricted to $\pi/6$ in the illustration, as the mesh is regular in θ.

A few runs were also done using the MPI parallelization on the Ada cluster from IDRIS, using 64 threads.

Critical Reynolds determination using DNS

Although DNS is not the best tool to find the critical Reynolds number, it is still possible to estimate it. It requires at least two simulations at different values of Re, and to have a clue of the range where Re_c might be. In our case, we can easily determine Re_c with LSA, and we can check if the DNS agrees with this value.

To do so, once knowing the neighbourhood of Re_c, we run two simulations below this value. Once the steady state is reached, we introduce an impulse of small amplitude in one of the velocity components (1% on u_θ), everywhere in the flow. In this way, all modes are excited. As $Re < Re_c$, none of these modes are unstable, therefore after a short time, their amplitude will decay. The most stable will quickly vanish, while the least stable will still be visible in velocity time series long after the impulse. The closer to Re_c the simulation is run, the longer this most unstable mode will survive. The idea is to estimate the decay rate, *i.e.* the slope of the sinusoidal envelope, in a semi-log graph. The decay rate is evaluated at one point in the flow. This value is then ploted in a graph, with Re on the x-axis, and the value of the slope on the y-axis. The linear interpolation from these two points crosses the x-axis in Re_c : the Re value for which the most unstable mode has a 0 growth rate. Note that if the simulations are done for $Re > Re_c$ the steady state may not be visible. However if Re is sufficiently close to Re_c, the growth rate may be so small that the introduction of a pulse is still possible. In this case, the slope will be positive (growth rate instead of decay rate), and the final state of the simulation will be a fully developed instability. Note that to monitor the instability, the choice was made to use a velocity probe, solution that appears successful. Another possibility would have been to

monitor a global quantity such as the kinetic energy.

Numerical values of Re_c are given in the next chapter.

Domain limitation in θ

In LSA, the user can select the azimuthal mode m to be studied. At first sight, this does not seem possible in DNS. However, with a limitation of the domain to $2\pi/m$ in θ direction, one can force the azimuthal wavenumber by filtering modes that are not m or its harmonics. Such a procedure is used later in this thesis in order to avoid complex nonlinear behaviour interfering with the mode of interest.

Validation

In order to check the ability of Sunfluidh to perform accurate simulations of the case considered, we used the results of [15], for G=1, and Re=1120. Since Re is below Re_c, only steady flows will be compared. Indeed, LSA predicts the most unstable mode to be m=1 at Re_c=2007. Other computations at Re=6000 are also given in [66]. However at such a Reynolds number the flow is turbulent and therefore comparison appears risky. The only other publication that may have served as reference for a comparison of the computed azimuthal mode is [37], yet in this paper, simulations were performed with a double geometry which is not representative of our cavity. Thus, validation is limited here to the axisymmetric flow. The determination of the most unstable mode and its Re_c will be cross validated with ROSE in the next chapter, and somehow validate the 3D simulation..

The computed base flows, both with Sunfluidh and ROSE, show a good agreement between each other (see figure V.2). But the comparison with M. Piva and E. Meiburg ([15]) is more difficult as isocontours are unfortunately not indicated in this publication. The width of the recirculation bubble at the free surface can still be compared : the isocontour ψ=0 that delimits the recirculation bubble hits the surface in r=0.25 for the three codes. There is small discrepency on the location where this isocontour intersects the z axis. But this is a straight criterion.

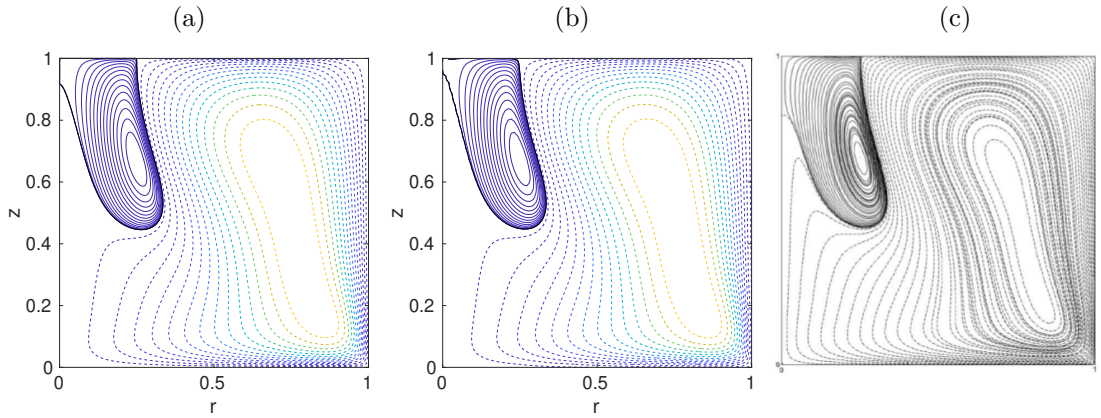

Figure V.2 – Meridian streamlines comparison between ROSE (left), Sunfluidh (center), and [15] (right), for Re=1120 and G=1. 15 isocontours are quadratically spaced between $\psi_{min} = -2.31 \times 10^{-4}$ and 0 (solid lines) and 15 more are quadratically spaced between 0 and $\psi_{max} = 9.52 \times 10^{-3}$ (dotted lines). The isocontour ψ=0 is plotted as a solid black curve. The grid used with ROSE is 301×301, while the used with Sunfluidh is 100×300×100 in (r,θ,z) respectively. Both are cartesian and regular.

Chapter VI

Free surface flow

In this chapter are compared experimental results and numerical simulations using a free surface condition : as a first approach, the surface of the flow is considered perfectly stress-free. The corresponding boundary conditions are those previously given in equations IV.8, IV.10 and IV.7 and developed for both codes in chapter V.

First we will return to experiments carried out for G=1/14. As we saw in the chapter I, [40] and [42] shared, for this aspect ratio, good agreement both on the azimuthal wave number of the most unstable mode, and on its critical Reynolds number. However, our own experiments reveal discrepancies with numerics. Details about experiments and numerics are introduced, as well as some hypotheses that were investigated to understand these discrepancies.

Secondly, we will study aspect ratios G=0.25, 1, 1.5 and 2. Still in order to identify the causes for discrepancies, these specific values of G were chosen since they were already partially explored in former publications. For G=2, we were limited by the size of our glass cylinder that did not allow us to reach such an aspect ratio. Therefore, all experimental results are extracted from [35].

G=1/14 : Numerical approach

The first aspect ratio we focus on is 1/14. This ratio was previously studied experimentally in [40], where the first unstable mode is reported to have an azimuthal wave number m=5, and to start growing at Re_c=16420. It was numerically investigated in [43], where it was revealed to be close to the limit of agreement between experiments and numerics (see figure I.9). For smaller G, the uncertainty on the height of the fluid ΔH is less and less negligible compared to the height of the fluid H itself, and so is the vertical displacement of the surface of the disc. In addition, in [40], detection of the mode only relies on visualizations, that can be very tricky for low values of G. All these reasons may have explain the causes of discrepancies for such G. But as exposed in chapter II, discrepancies were actually already existent for G=1/14, that neither ΔH nor the disc surface defects could explain.

Numerical critical Reynolds number

After ROSE was validated in section Validation & Mesh, influence of the mesh on Re_c is now evaluated. The results are exposed in table VI.1.

$n_{R_{cells}} \times n_{Z_{cells}}$	701×51 ([43])	351×51	701×101	1401×201
Re_c	16972	17032	17006	16992

Table VI.1 – Comparisons of ROSE Re_c computations on several grids, for G=0.0714 and m=5. First column correspond to the grid used in [43].

One can see that Re_c does not evolve much (0.35% of the maximum Re_c) and stays around 17000 although the mesh size is multiplied by 4 between columns 2 & 3, and 3 & 4.

We specify here that ROSE shares the same core as the code used in [43]. Therefore it is no surprise that the match on Re_c is excellent and it also explains why [43] was not used as a reference for the validation. It is interesting to observe that Re_c apparently does not display the same sensitivity to refinement in each direction : an increase of the radial cells number lowers Re_c (columns 2 & 1), while an increase of the axial cell number increases Re_c (columns 1 & 3). When both are increased with the same ratio, *i.e.* the aspect ratio of cells remains constant, the lowering effect of the axial cells number seems to be predominant (columns 2, 3 & 4). According to these results, the choice was made to keep the 701×101 grid as the standard grid for G=1/14. Indeed, this grid shows an error of less than 0.1% compared to the 1401×201 grid, for a less expensive (yet unevaluated quantitavely) time cost.

Following the method given in section V.2.4 : Critical Reynolds determination using DNS , we cross validated this value Re_c value with DNS computations. With a grid resolution of $(180 \times 180 \times 64)$ in (r,θ,z), respectively, we evaluate the slope a at Re=16900 and 17000, for a time span between $t_{impulse}$+1400 and $t_{impulse}$+2000. For Re=16900, $t_{impulse}$=200, while for Re=17000, $t_{impulse}$=300.

Re	16900	17000
a	-0.0028993	-0.0002765

Table VI.2 – Decay rate of the most unstable mode between t=$t_{impulse}$+1400 and $t_{impulse}$+2000, for Re=16900 and 17000.

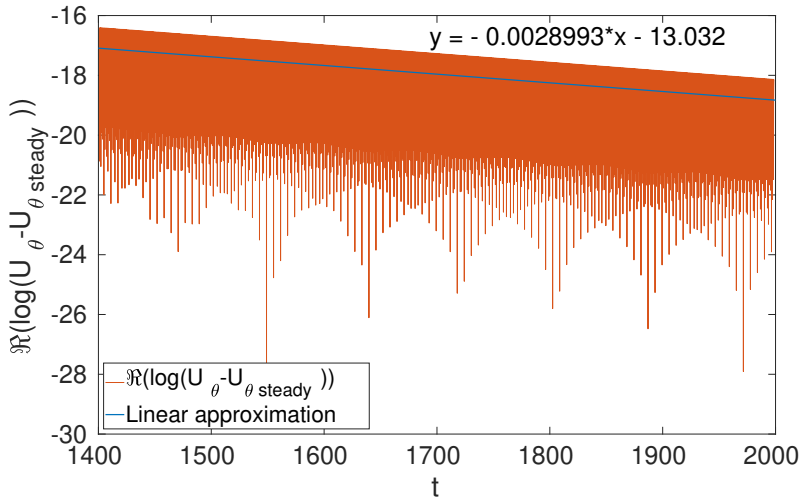

Figure VI.1 – Estimation of the decay rate at Re=16900 for G=1/14.

According to the slopes given in VI.2, one can estimate $Re_c \approx$17010. Taking ROSE's prediction for three different grids (351×51, 701×101 and 401×201), and performing a Richardsons extrapolation allows for an evaluation of Re_c=16976. Thus, the difference between the predictions of ROSE and Sunfluidh is only of 0.2%. Some explanation on

the Richardson extrapolation can be found in the appendixes of [42]. To be perfectly rigourous, extrapolations should also have been performed with Sunfluidh, both on refined timesteps and refined grids. However, this come to a cost of a longer computation time. Since the agreement already revealed to be excellent, such computations were not performed.

Instability pattern at Re_c

The agreement on the Re_c value between the two codes is excellent, but the unstable mode that grows in the DNS is unknown : a mismatch is still possible on the wavenumber. To clarify this, we can check visually the azimuthal wavenumber in a (O,r,θ) plane in DNS. To do so, it was chosen to represent the axial vorticity ω_z :

$$\omega_z = \frac{1}{r}\left(\frac{\partial(ru_\theta)}{\partial r} - \frac{\partial u_r}{\partial \theta}\right)$$

In order to identify the perturbations, one can subtract the mean flow from the complete velocity fields. This mean flow can be a temporal mean through a selected time span (we used $10\times 2\pi$ period, or 10 disc rotations) or spatial, on (θ). These two ways to calculate the mean flow appeared almost equivalent, once the flow is fully established. Therefore, we preferentially used the spatial average, that naturally satisfies the periodicity. Alternatively, the base flow can also be computed in 2D, with imposed axisymmetry. The comparison of LSA and DNS perturbations is displayed in figure VI.2.

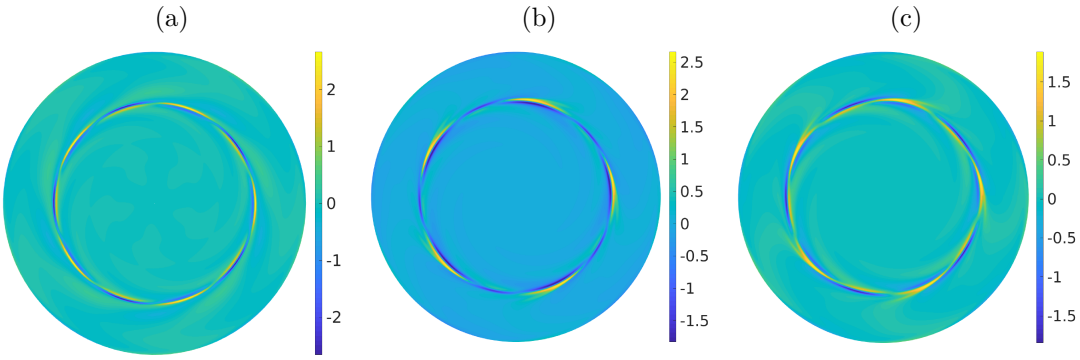

Figure VI.2 – ω_z perturbations in the (O,r,θ) plane, for G=1/14, z=G, Re=17100. VI.2a are perturbations from LSA, normalized with respect to the DNS value of $max(\omega_z)$. VI.2b are fluctuations from DNS, at t=4200, computed by subtracting of the 2D axisymmetric base flow, while VI.2c are fluctuations from DNS at the same time, but computed from the subtraction of the spatially averaged mean flow. The wave number m=5 is easily visible in the vorticity stripes, around r=0.67 : a pattern of alternatively positive and negative values of ω_z is repeated 5 times over the 2π radian angle. The mesh used is given in figure V.1, page 70.

Thanks to the figure VI.2 we can conclude that the two codes agreed both on Re_c and on the wave number m=5 of the most unstable mode, for G=1/14.

Frequency of the most unstable mode at $\mathbf{Re_c}$

The frequency of the mode is defined as the inverse of the time required for one vortex to travel 2π radians. This frequency is normalized regarding the frequency of the disc. If we denote f_m and f_d the frequencies of the mode and of the disc, respectively, we can obtain their dimensionless form with respect to f^* :

$$\frac{f_m}{f_d} = \frac{\bar{f_m} f^*}{\bar{f_d} f^*}$$

Now, considering that $f^* = \frac{1}{t^*}$, and that t was non-dimensionalized as $t = \bar{t}t^* = \frac{\bar{t}}{\Omega_d}$, we obtain :

$$f = \frac{f_m}{f_d} = \frac{\Omega_m}{\Omega_d} = \frac{\bar{f}_m}{\bar{f}_d},$$

where Ω_m and Ω_d are respectively the angular velocities of the mode and of the disc. In conclusion, this ratio is the same, whether we deal with frequency or angular velocity. Thus, we will keep calling "frequency" both the normalised frequency and the angular frequency (noted f). In the case of ROSE, this value is easily accessible, as it is the imaginary part of the most unstable eigenvalue, divided by the wave number m.

$n_{R_{cells}} \times n_{Z_{cells}}$	701×51	351×51	701×101	1401×201
f	0.711	0.711	0.709	0.709

Table VI.3 – Comparisons of the normalized frequency of the m=5 mode computed with ROSE on different grid size, for G=0.071. Respective Re_c values are given in table VI.1.

We did not observe the same influence of the mesh size on the frequency as on Re_c. The perturbations are reduced to 0.28% of the maximum f value. Therefore, the rest of ROSE simulations on the case G=1/14 were realized with the 701×101 mesh, as it seems to be a good balance between accuracy and computation time.

With DNS, the frequency is not given so directly, and it has to be evaluated with a Fourier transform applied to velocity temporal series. This was done essentially on the u_θ component(VI.3a).

From figure VI.3b, one can extract the frequency value of the main peak : f=0.699. Other peaks are only harmonics of the main frequency. One can note that the Reynolds number used in this simulation is 0.53% above the previously determined Re_c. This value was chosen in order to stay in the neighbourhood of Re_c, but with a growth rate that allows for moderate simulation time. This can be compared to the ROSE prediction for Re=17100: f=0.710. The difference on frequency between DNS and LSA for Re=17100 is less than 1.55%. Note that for Re=17000 (just below Re_c), the frequency of the decaying m=5 mode is 0.707, even closer to ROSE prediction at Re_c. The increase of 0.59% of Re in DNS implies a frequency drop by 1.13%. With ROSE, the variation of +0.55% of the Reynolds number only produces a decrease of 0.14% on f.

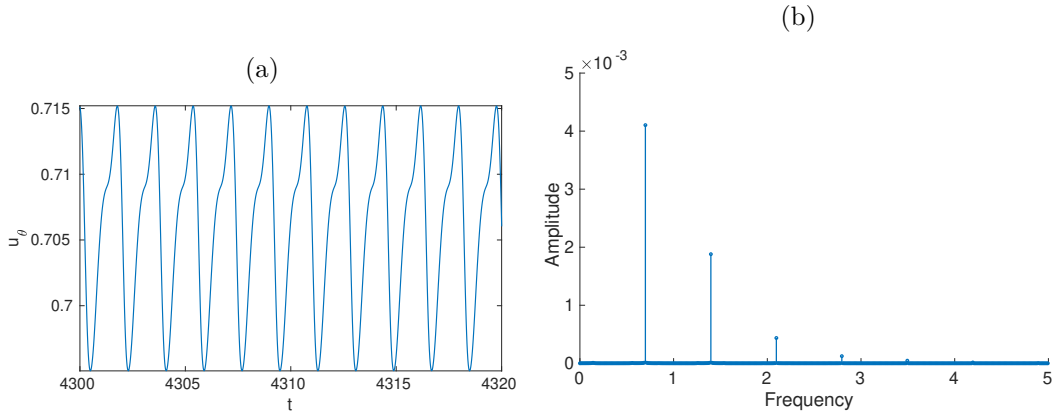

Figure VI.3 – u_θ signal (VI.3a) for G=1/14, Re=17100, and the corresponding Fourier transform (VI.3b). The probe is located at (0.68,0.0,0.9G).

Mode transition for $\mathbf{Re > Re_c}$ and long time simulation dynamics

In chapter II, we briefly mentioned that for Re=18620 the mode m=5 quickly transits to a m=7. Such an evolution of the azimuthal wavenumber is the opposite of what is reported in [40], where for a given G, the wave number decreases with increasing Re. This decay of the azimuthal wave number was also observed in our experiments.

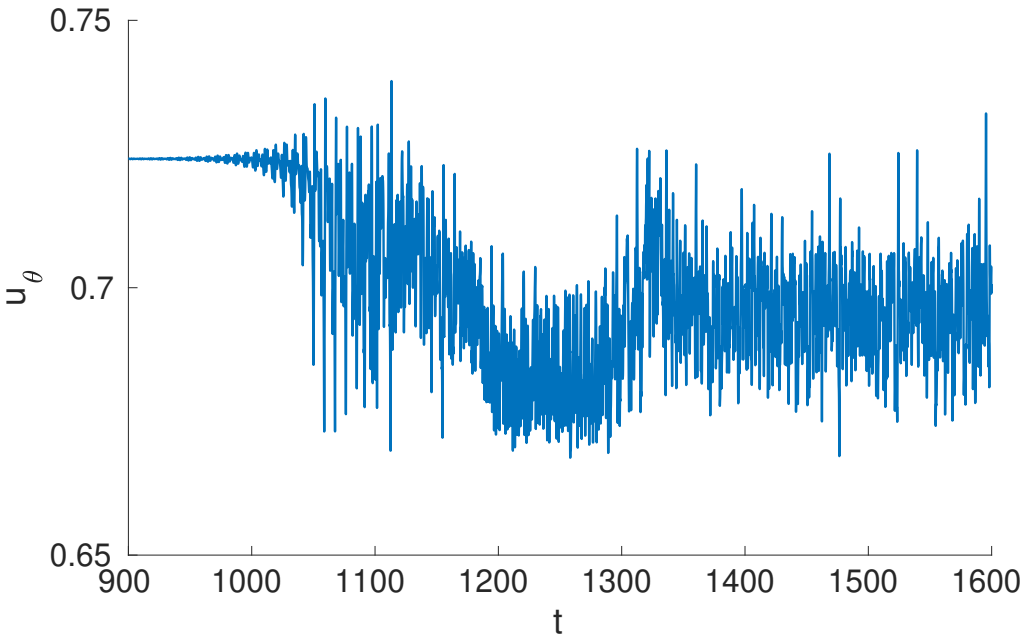

Figure VI.4 – Azimuthal velocity captured in DNS by a probe located at (0.68,0.0,0.9G), for G=1/14 and Re=18620.

The time series extracted from a DNS computation and plotted in figrure VI.4 shows a complex evolution as soon as the instability grows, around t=900. This evolution is

better seen on the tracking of the kinetic energy of each unstable mode, represented in figure VI.5. From t=900 to $\approx$ 1020, the modes m=4 and m=5 grow slowly with a slight prevalance of m=5 between t=1000 to t=1075. Nenertheless, the vorticity pattern rather shows m=4 (figure VI.6a) at t=1020, while it only prevails between t=1075 to t=1115. Then, it transits to a temporary m=6 mode (fully established around t=1130, figure VI.6b), before a m=7 azimuthal wave number dominates after t=1295, and becomes well visible for $t > 1330$ (figure VI.6c). However, this m=7 does not completely prevail, and a competition with mode m=6 still occurs between t=1430 and 1600. The simulation was not carried further. In addition to the competition between two modes, one can notice an asymmetric damping of the intensity of the axial vorticity that may be due to a low frequency mode. A similar damping is barely visible in the figure VI.6a, where vorticity at the bottom of the figure is not as strong as on top.

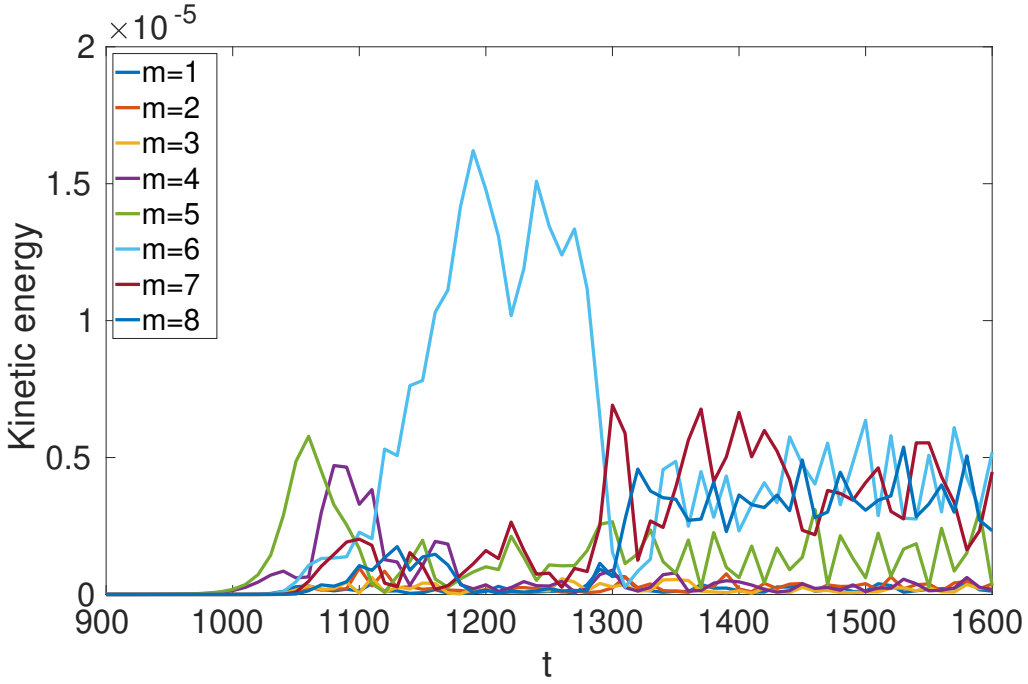

Figure VI.5 – Evolution of the Kinetic energy of the modes 3 to 8, between t=900 and t=1600, for G=1/14 and Re=18620.

The growth rate of each mode at Re=18620 was evaluated with ROSE. Results are displayed in table VI.4. According to this table, mode m=4 is the less unstable, while m=7 is clearly predominant. This is a completly different story from what the non linear dynamics highlighted in figure VI.5. Of course, this is not surprising, since Re=18620 is already 9.5% above Re_c : the transition from m=5 to m=4 is already a secondary bifurcation and thus, the axisymmetric base flow computed with ROSE is no longuer effective to determine thresholds and growth rates. Fixing this would require to consider the mode m=5 as the new base flow, and then to compute the perturbations around this new state. This would imply an in-depth rewriting of ROSE, and thus, this was not performed here.

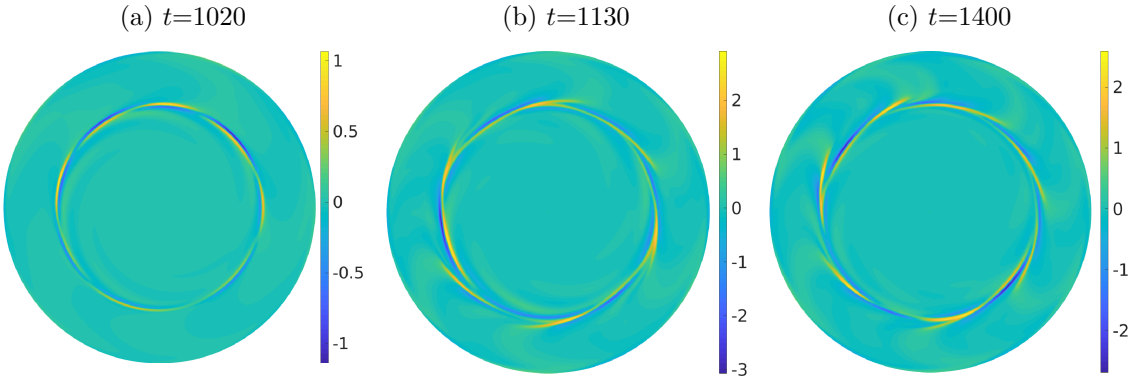

Figure VI.6 – Axial vorticity ω_z of fluctuations, based on spatially averaged mean flow, for three different times, at z=G Re=18620. Successive wavelengths are visible although a low frequency mode damped the amplitude of ω_z in VI.6a.

m	4	5	6	7
$\Re(\lambda)$	0.07266	0.1104	0.1038	0.5563

Table VI.4 – Comparison of the growth rate of modes 4 to 7, for G=1/14, and Re=18620.

Actually, the mode transition is not due to the increase of Re. Indeed, this was also observed at Re=17100 : although the velocity profile shows that a permanent regime seems to be reached between t=4000 to 4400 (figure VI.3), small oscillations appear for t >4400 that quickly escalates to a chaotic dynamics, observed between t=4500 to 6600 (see fig. VI.7). The azimuthal wave number m=5 is predominant up to t ≈5960, where some modifications of the pattern appear, that look like fringes (see fig. VI.8). It marks the beginning of competition with the mode m=6 that is visible at t ≈6260, and is finally dominant up to t=6500. Between this time and t=6600 a new modulation is visible in the pattern, that tends to damp the intensity of the vorticity without any symmetry, exactly as previously described for Re=18620. At Re=17100, only m=5 is unstable, according to LSA. m=6 is unstable only above Re=17358, which confirms that this mode transition is actually a secondary bifurcation.

Spin-down in DNS : hysteresis in numerics ?

Experiments from Poncet and Chauve ([40]) has brought to light the existence of hysteresis. To clarify whether hysteresis can be present in DNS computation or not, we performed a series of ten simulations. The common starting point of these simulations is the unstable state at Re=18620. As we study only the hysteresis of the mode 5, simulations were done in a partial domain, restricted to an angle of $2\pi/5$ in (θ). With this filtering, the chaotic dynamic exposed in figure VI.4 is not present. Each simulation reaches a final state at Re between 18424 to 16660, with an interval of 196 between each

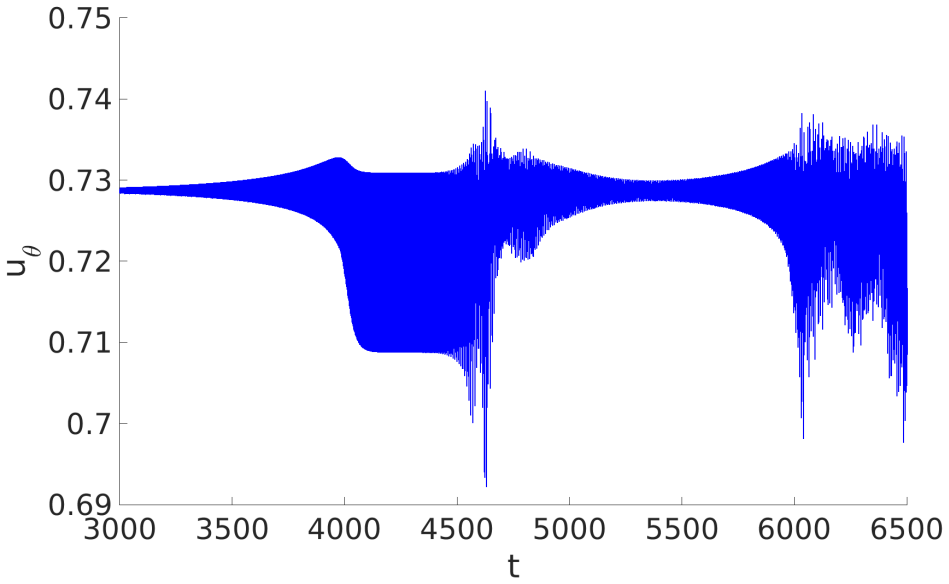

Figure VI.7 – Evolution of azimuthal velocity in DNS for G=1/14, Re=17100. The probe is located at (0.68,0.0,0.9G).

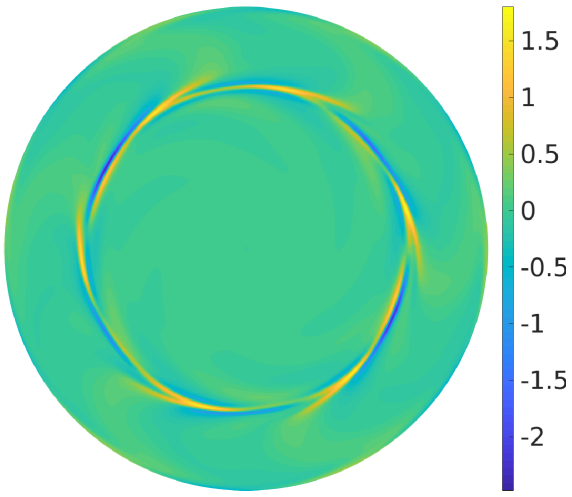

Figure VI.8 – Azimuthal wavenumber m=6 visible in the axial vorticity of perturbations, at t=6500, for G=1/14 and Re=17100.

of them.

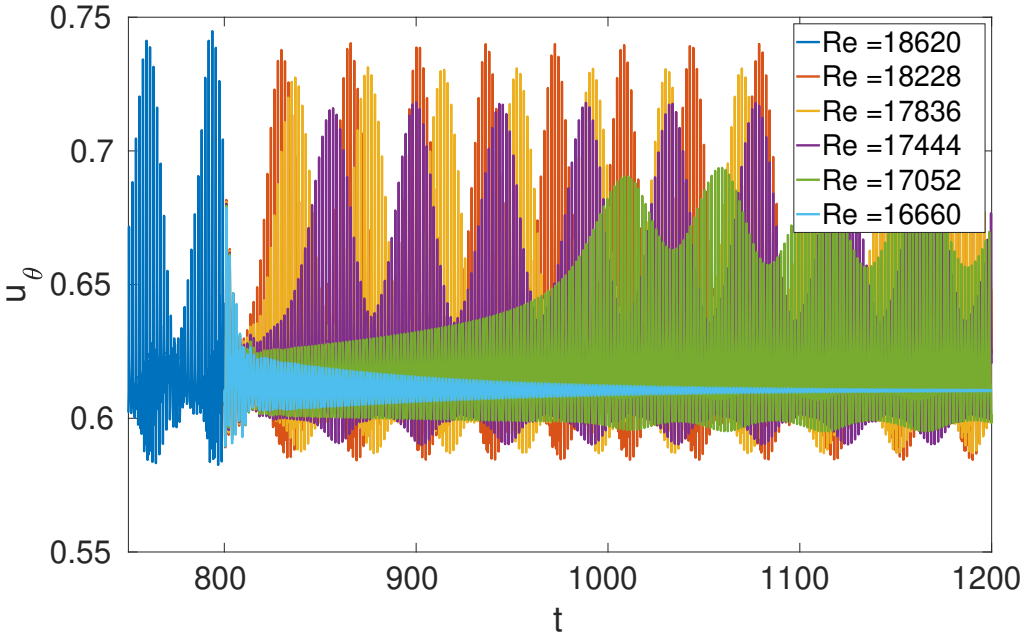

Figure VI.9 – Azimuthal velocity u_θ as a function of time, computed with Sunfluidh around the stability threshold. Starting from Re=18620 at t=800, ten simulations between Re=18424 and Re=16600 have been performed. However, for a better visibility, only five simulations are represented, with a step in Reynolds number of 392 between each of them. The probe is located at (0.82,0.63,0.5G).

For all simulations with final Re between 18424 and 17052, the decrease of Re only affects the amplitude of the oscillations. As soon as Re gets closer to Re_c it seems harder for the instability to survive, and for Re=17052, it takes around 200 time units for the pattern to develop while it was much faster for higher Reynolds numbers (≈75% faster for Re=17444). As soon as $Re < Re_c$ oscillation are damped and instability vanishes. Thus, there is no numerical evidence in favour of the existence of hysteresis.

G=1/14 : Experimental results

Following the procedure described in the section III.5 (page 51), we searched for the experimental critical Reynolds number for G=1/14. It quickly appears that the instability was not difficult to trigger, and the first observed unstable mode has an azimuthal wavenumber m=5, which matches with the numerical prediction for this value of G. But the instability started to be visible for Reynolds numbers far below the numerically determined critical Reynolds number. Mismatches with numerics reveal to be not limited to Re_c : the base flow and the azimuthal pattern also show heavy differences. Details were already reported in chapter II : experimental Re_c below 4200 (more than 75% smaller than the numerical prediction), absence of overshoot in experimental u_θ profile, absence of

similarity in the pattern... Note that from time to time it happens that the first detected unstable mode had a wave number m=4. These minor cases were not judged relevant : it is reported in [42] that the critical Reynolds numbers for m=4 and m=5 are close, and according to [37] and [40], the mode selection is sensitive to variations in the experimental protocol. Since the adoption of the protocol based on extended constant-duration plateaus, only the mode m=5 was observed.

Threshold detection : markers and fluids

Kalliroscope

The choice to use Kalliroscope as a marker appears to be natural considering that many publications on rotating flows used such marker, especially in Taylor-Couette flow ([67] and [68] are examples among many others). Moreover, Kalliroscope was used in [40] to visualize transition from steady to unsteady flow, and azimuthal patterns. However, we had never been able to match the reported Re_c by Poncet and Chauve. Globally, our experiments appear to be reproducible, and Re_c was first estimated around 9800. But, in some cases, we were not able to detect any azimuthal wavelength, even well above the numerical Re_c. There, only a chaotic flow was revealed by the marker. We noticed that this behaviour was more probable when the flow was heavily seeded, but we failed at establishing an obvious quantitative connection between Kalliroscope concentration and threshold detection.

Another issue encountered is the sedimentation rate. According to [59], Kalliroscope in water have a sedimentation velocity around 0.1 cm/h, which means it should require 10 hours for flakes in calm water to drop from the interface to the disc. However we observed that sedimentation can occur over a much lower time interval, that was incompatible with the time required in experiments. Indeed, experiments with Kalliroscope were mostly based on the Ekman time, according to the protocol used in [40]. There it takes at least 16 min to reach 3 rpm. Added to the time of observation, this was sometimes sufficient for most of the particles to fall to the bottom of the cavity. Despite the later increase of the rotation speed, the layer of particles remains stuck to the disc, and no visualisation was possible. In later experiments with LDV, we used plateaus of 10 to 15 min plus at least 5 min of acquisition. These long plateaus make it difficult to use Kalliroscope for critical Reynolds number detection as the observed sedimentation time is close to the plateau duration.

Ink

The flaws of Kalliroscope forced us to repeat our experiments with the same initial protocol, but with the injection of diluted blue ink at the end of each plateau. Introduced with a syringe and a thin needle, the total volume of ink added to the cavity was less than 1 mL, so that the total volume inside the cavity can be considered as constant. In threshold detection experiments, the amount of ink that is introduce into the cavity is small enough that the fluid does not turn completly blue. Indeed, if the threshold Reynolds number is so high that it requires too many repeated injections, the fluid becomes blue.

Then, contrast is no longer sufficient to allow visualisations. Therefore, highlighting hysteresis with this marker is hardly possible.

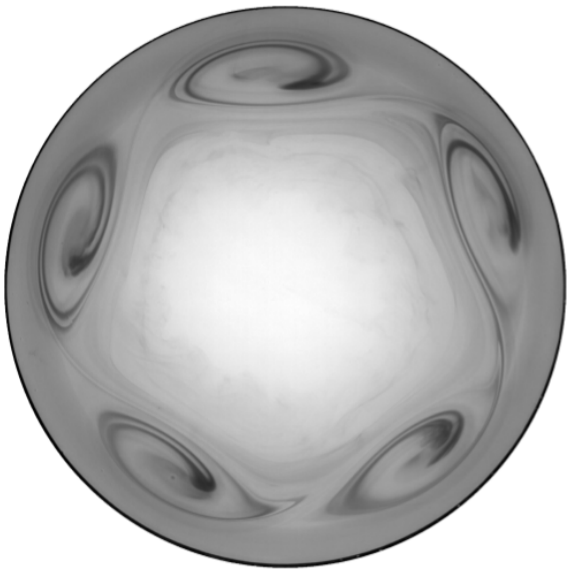

Figure VI.10 – Instability pattern visualized with ink in a 40% mass glycerol mixture, for $G = 1/14$, and $Re \approx 4700$.

With this marker, the critical Reynolds number was evaluated between 3300 and 6200. If we consider the highest boundary of the previous estimation of Re_c with Kalliroscope, this Re_c was over evaluated by 55%. New experiments were done with smaller amounts of Kalliroscope : both modes 4 and 5 were observed for Re_c=6476 and Re_c=6507, respectively. No evident conclusion can be made on the behaviour of Kalliroscope, but it is clear that its use has to be considered with the highest precaution, especially for quantitative results. It also confirms that instabilities are present far below the Re_c predicted numerically.

LDV

Experiments done with LDV locate the critical Reynolds number between 3160 and 4230 with water. Compared to previous experiments with ink and Kalliroscope (and based on the Ekman time), the upper bound is here 30% lower. This gap corresponds to only 1 *rpm*. This very small difference reinforces the hypothesis that the Ekman time is not suitable for the instability detection protocol. The LDV measurement were repeated with a 20% glycerol mixture, and confirmed that Re_c is between 2520 and 3780.

Besides Re_c determination, LDV brings a quantitative aspect with measurements of frequencies and velocities. However, in the absence of qualitative visualization, it is hazardous to conclude on the wavenumber only with LDV acquisitions. A cautious look at the surface can sometimes reveal the mode by direct visualization : the particle concentration

is higher in the vortices, which makes the identification of the main mode straightforward. A misinterpretation of the mode would lead to an error on the corresponding frequency.

Viscosity

In addition to the sensitivity of the instability to each marker, we performed a verification of the influence of viscosity on Re_c. These results are shown in table VI.5. As explained in chapter III, increasing the viscosity should lead to better accuracy in the threshold detection, as well as a reduction of transient times.

Glycerol %	0	20	20	25	40
ν ($\times 10^{-6}$)	0.971	1.63	1.53	1.78	3.35
T ($°C$)	21.5	20.6	23.0	22.9	19.9
Detection method	LDV	LDV	ink	ink	ink
Re_c [stable-unstable]	[3160-4230]	[3181-3780]	[2690-4030]	[2300-3450]	[3070-3680]

Table VI.5 – Experimental critical Reynolds number Re_c of the first unstable mode m=5, for G=1/14, with various viscosities. All these experiments were done in the large cavity. The steps were 0.5 *rpm*, and 1 *rpm*, for LDV and Ink experiments, respectively.

Glycerol addition does not seem to have any obvious influence on Re_c. For the range of concentration considered - 0 to 40% in mass - Re_c stays between 2700 and 4200, approximately.

Mismatches beyond $\mathbf{Re_c}$

Until now, only Re_c values obtained with both numerics and experiments have been compared. Since no match was observed, we formulated the hypothesis that an experimental flaw may be responsible for an early triggering of the instability. The possibilities to explore the flow with LDV brought new elements that cannot be justified by the vibrations of the bench.

Indeed, the LDV hardware allows for analysis of the flow beyond the sole critical Reynolds number detection. Acquiring velocities at several points along a radius makes it possible to draw a velocity profile that can be compared to the base flow from ROSE, and to mean flow from DNS. These comparisons reveal a clear mismatch between numerics and experiments. Note that LDV hardware was installed after the quantification of the disc vibrations (chap. VII).

In figure VI.11, we compare four different velocity profiles. The two DNS profiles confirm the equivalence of mean velocities, whether they are calculated using a spatial or a temporal average. The comparison of ROSE base flow, and DNS mean flow highlights that, although the flow is fully unstable (Re=18620> Re_c), mean flow and base flow are very close. The only noticeable deviations are located just before the boundary layer, at

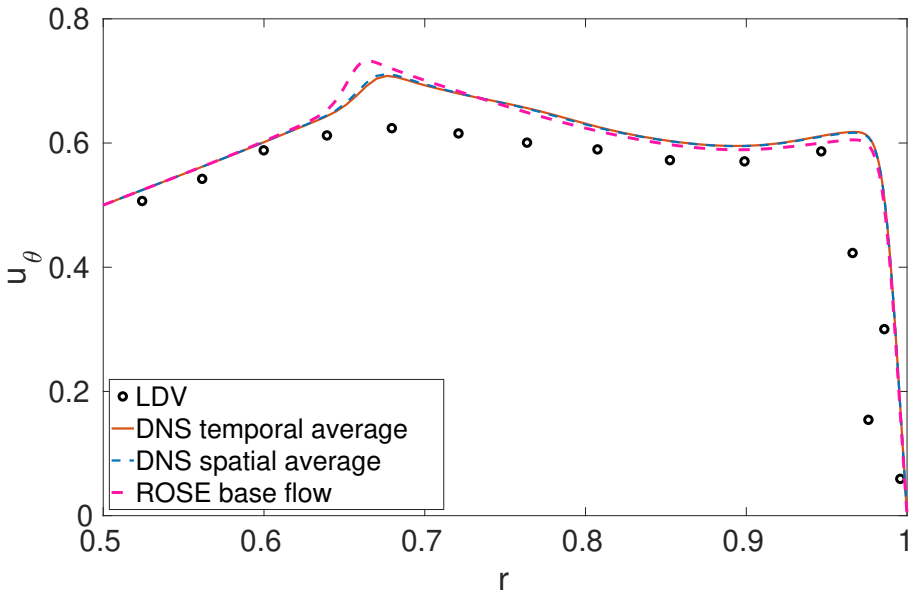

Figure VI.11 – Comparison of u_θ velocity profile, in z=0.8G , at Re=18620, for G=1/14.

r=0.97, and in the "bump" at r=0.67. This last point is especially important. In numerics, the bump corresponds to an overshoot of the velocity, *i.e.* $u_\theta|_{z=G} > u_\theta|_{z=0}$. This overshoot is not seen in experimental points, and the associated velocity profile is actually much smoother than numerical ones. One can see that despite the optical correction on LDV measurements, a gap still exists between experimental and numerical velocities in the solid body rotation area (r <0.6). Solid body rotation and overshoot are illustrated in the meridional plane, in figure VI.12.

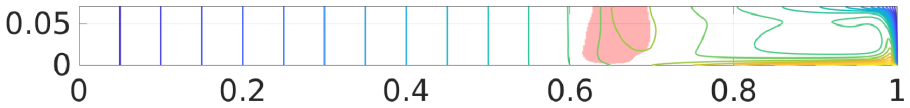

Figure VI.12 – u_θ base flow iso values computed with ROSE, at Re=18620, for G=1/14. Red patch correspond to $u_\theta > 1.01r$. 21 iso values are equally spaced between 0 and 1.

The mismatch in the mean flow is even more apparent for the u_z component. Note that measurements were made at z=0.5G to allow for a wider range accessible with LDV, avoiding any problem of reflection of the beams on the surface, or collision with the edge of the disc. Figure VI.13 shows larger differences between mean flow and base flow. However, the radius for the minimum value of u_z is still located around r=0.7. Despite an insufficient discretization in experiments between r=0.8 and r=0.9, the radius where u_z is minimal can still be evaluated around r=0.86. This means that the length of the recirculation in the meridional plan is over-evaluated by ∼20% in numerics. If the recirculation is expected to be present only for r >0.86, u_z should be almost zero for r <0.86. The negative values in experimental data may be due to an imperfect horizontality of the laser,

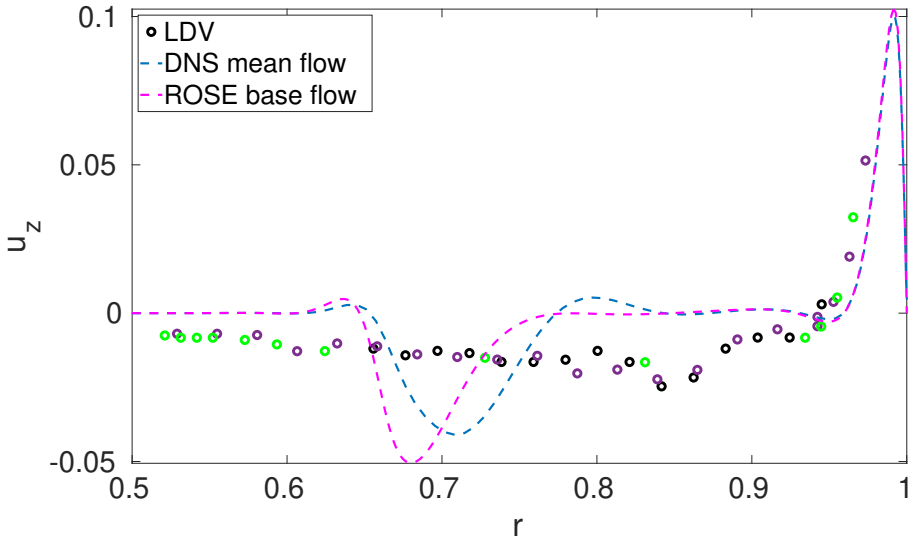

Figure VI.13 – Comparison of u_z velocity profiles, at z=0.5G , for Re=18620, and G=1/14. The three colors for the dot symbols correspond to three repeated experiments.

leading to the acquisition of the projection of u_θ. Indeed u_θ is quite large compared to u_z. Recirculation in numerics can easily be seen with the stream function ψ, as represented in figure VI.14.

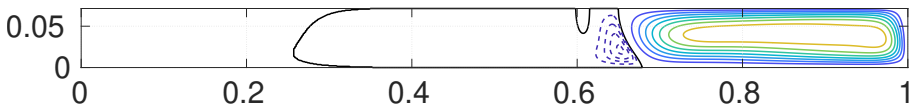

Figure VI.14 – Streamfunction ψ of the base flow computed with ROSE, at Re=18620, for G=1/14. The values of ψ are given in chapter II : Article published in *Journal of Fluid Mechanics*.

Ideally, the comparison of base flows should have been done for $Re < Re_c$. However, in experiments, Re_c corresponds to a very low rotation speed around $2rpm$, leading to the acquisition of a small magnitude velocity signal, with a lot of noise. Therefore, to have something fully comparable, we chose a Reynolds number sufficiently high for the instability to be developed both in numerics and in experiments. The value of Re was chosen far enough from Re_c in order to allow for a fast natural growth of the instability in DNS, and thus, to reduce the computation time.

Mode transition as Re increases

It was reported in [40] that the increase of the rotation rate, and therefore, of the Reynolds number, was followed by a second transition, when Re=36945. There, the azimuthal wave number evolves from m=5 to m=4 (fig. VI.16). We looked for this mode switching, firstly with Kalliroscope, which is more adapted than ink for such an

experiment, since it allows for a continuous visualization of the flow without additional seeding. With Kalliroscope, the transition was observed for Re between 25750 and 27910. The experiment was repeated twice using LDV device. As displayed in figure VI.15, the transition Re was then evaluated around 30000. Note that in figure VI.15, in order to illustrate the transition between m=5 and m=4, the frequencies are not divided by m, but only normalized with the disc frequency. It also confirms the good reproducibility of mean velocity measurements, although a deviation corresponding to 1 rpm is observed between the transition Reynolds numbers of the two runs.

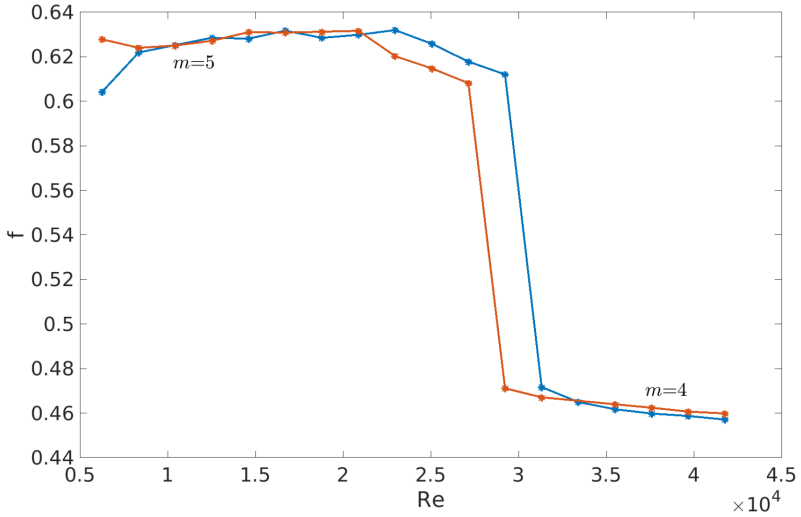

Figure VI.15 – Evolution of the frequency f as a function of Re. Colours represent two different acquisitions series for G=1/14.

It is interesting to note that the Reynolds numbers for which the secondary bifurcation occurs are under-evaluated by ≈7% in experiments using Kalliroscope, and compared to LDV measurements. This is unexpected, since the first threshold was more easily over-evaluated when using Kalliroscope. Here, agreement is fairly good, and we can suppose that Kalliroscope is more "effective" in high mixing flows than in quiet flows.

Actually, the experiment with Kalliroscope was an attempt to highlight hysteresis (see fig. VI.17). Although its existence has been called into question by numerical simulation, hysteresis was easily observed during this experiment. However the Re values for which is observed the mode transition do not match with the results of Poncet and Chauve. Note that this experiment was performed before the instability threshold was found to be as low as $Re_c \leq$4200. Since this experiment was not repeated with LDV, we cannot conclude if the hysteresis is effectively present in this flow, or if it is a perverse effect of a shift of the thresholds during the spin-up phase, and attributable to Kalliroscope. Indeed, the last transition from m=5 to m=0 during the spin-down phase matches the first threshold of our spin-up phase, while the last transition of our spin-down phase occurs for Re ≈4300, which matches the Re_c determined using the LDV.

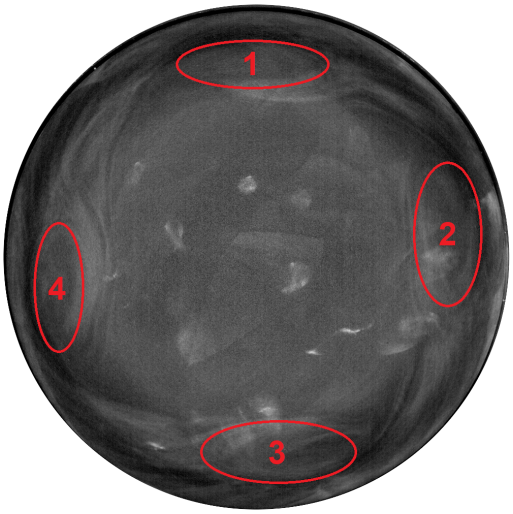

Figure VI.16 – Despite the low contrast between particles of Kalliroscope in suspension, and particles lying on the disc, the azimuthal wave number m=4 is still visible for G=1/14 and Re=26500.

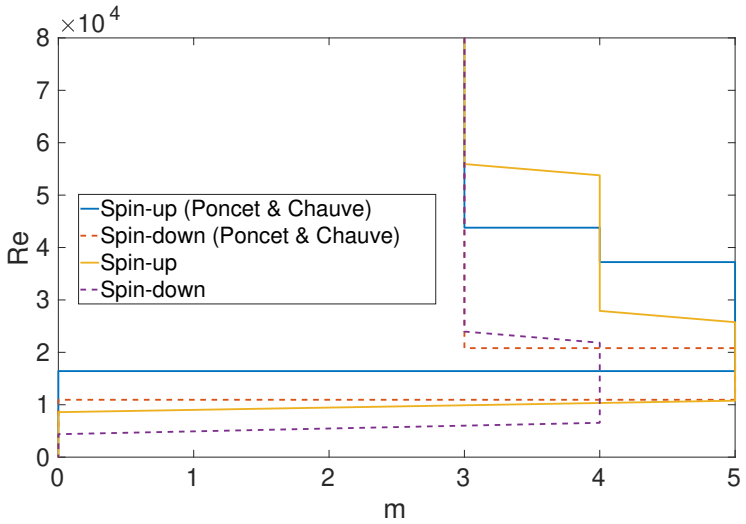

Figure VI.17 – Comparison of spin-up and spin-down phases between our experiment and the experiment of Poncet and Chauve ([40]). Spin-up phases are the solid lines, and spin-down phases are the dotted lines. Note that the "horizontal lines" are a guide for the eye but have no physicall relevance, as m can only be an integer.

For all experiments, the plateaus were based on the Ekman time. They were conducted in the beginning of this thesis. An in depth definition of the protocol should be conducted, but this is beyond the scope of this thesis, and should be considered as a perspective.

G=1/14 : Conclusion

What was believed at the beginning of the investigation to be a simple validation case revealed unexpected difficulties. No match with previous publications was found, except for the most unstable mode m=5. Experiments with different viscosities did not solve the issue, and the use of new markers actually increased the mismatch. The in-depth analyses of the experimental flow, thanks to LDV, has shown unsuspected yet robust differences with the computed mean flow. Although a flaw in our experimental bench does not seems to be able to explain these mismatches, we are still looking for a reliable validation of experimental results in order to be more confident in our set-up and its associated measurements.

These experimentations also bring lights on possible evolutions of the bench : placing the cavity inside a wider fluid tank would allow for a reduction of the uncertainty on the optical measurements. In addition, this solution would also reduce the oscillation of temperature inside the cavity. The sensitivity of the LDV device also highlights issues with the mechanical noise, evaluated later in this thesis (see VII). This noise perturbates the clean detection of the instability, and the evolution of its growth rate (in order to compare it with LSA values). This point echoes the project at the genesis of the ANR that founded this thesis : the eventuality to put a retroaction loop inside the disc, in order to control its vibrations. Finally, the acquisition of u_r is currently not possible. If it is not impossible to plan it, solution to do so are difficut to deploy. The use of a PIV device would give acces to more information than it currently possible with the LDV.

G=0.25

In order to be fully confident in our experimental set-up and protocol, we need an experimental validation. Therefore, the cavity was filled with more liquid, in order to reach G=0.25, and to confront our data for this new aspect ratio to results reported in [37]. According to this article, the most unstable mode for this aspect ratio is m=3, at Re ≈2000. However authors noted that “if lower quality water was used, then an m=2 rotating wave was observed”. It is interesting to note that the authors were not able to numerically reproduce this instability, unless they forced an odd parity in the axial direction. This lead to the right mode, with a critical Reynolds number of 1450. But this solution is not physical, as it allows for perturbations of the flow to cross the surface.

This aspect ratio was the only other one for which experimental results have been published and that was reproducible in our first cavity. Moreover, the results in [37] are not affected by any supposed negative effect of Kalliroscope, since detection of the instability was done with DPIV (Digital Particle Image Velocimetry).

Experimental results

The first tests were done in the largest cavity. Since the critical Reynolds number is expected to be low, we used a 55% in weight water glycerol mixture, in order to have a wider span of rotating speed : the experimental threshold determined in [37] (Re=2000), is reached for a rotation speed below $1rpm$ if the fluid is pure water. Initial experiments used Kalliroscope, and the protocol was the same as detailed in III.5. The flow started to show an ellipse for R ≈3540, followed by a less symmetric pattern, kind of a intermediate between m=2 and 3, was observed for Re ≈5950. This pattern is visible in figure VI.18b. Finally a clear m=2 pattern was visible for Re ≈6340.

(a) Re=3540 (b) Re=5950 (c) Re=6340

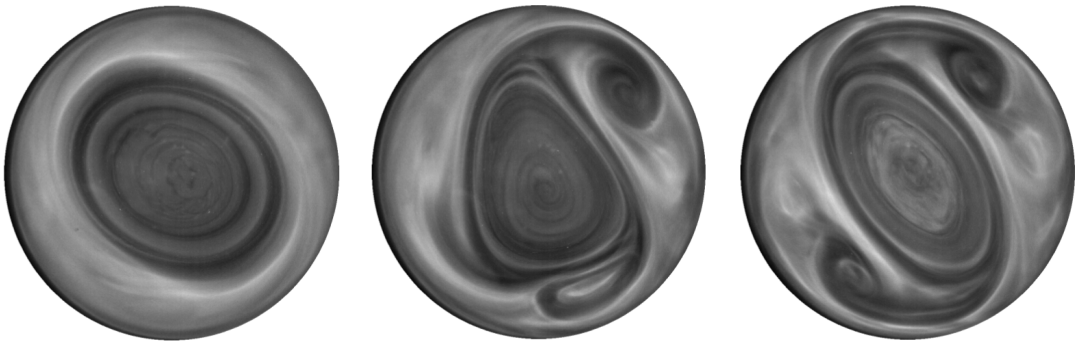

Figure VI.18 – Sequence of instability growing in a 55% glycerol mixture seeded with Kalliroscope, for G=0.25.

Switching the marker to ink initially brings similar results, but with different Reynolds numbers. The symmetry is lost at Re ≈5030, where the flow displayed an ellipse around its core region. The transition pattern, although not as clearly seen as with Kallirsocope, is supposed to be present for Re ≈5350, before the mode m=2 became well determined, at Re ≈5940. The whole sequence is shown in figure VI.19.

(a) Re=4760 (b) Re=5030 (c) Re=5350 (d) Re=5940

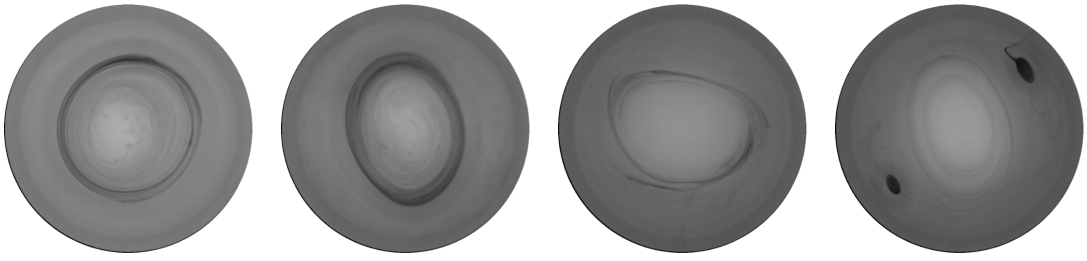

Figure VI.19 – Sequence of instability growing in a "dirty" 55% glycerol mixture, for G=0.25.

Based on these experiments, the critical Reynolds number is hard to evaluate. If the loss of symmetry is considered as the threshold, Re_c is at least 151% higher than in the

experimental results of Lopez *et al.*, in the most favourable case with ink. However it is interesting to note that the experiment with ink was performed in a fluid that rested for two to three days in the cavity. If we consider that, despite the lid which we covered the setup when it was not used, the fluid has become dirty, an interesting parallel can be made with "low quality water" effects described by Lopez *et al.* Using such fluid, the first mode they observed was m=2. Unfortunately, no associated value of Re_c is given in this case.

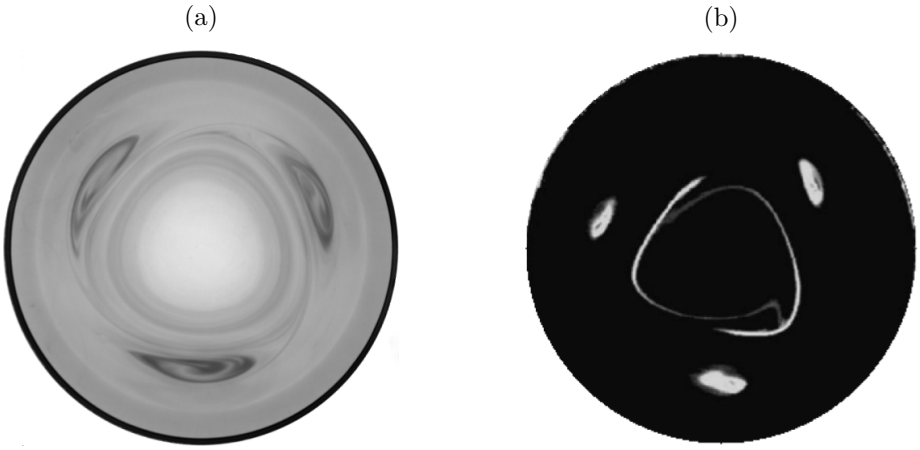

Figure VI.20 – Azimuthal wave number m=3 observed with ink in a 55% weight water glycerol mixture, at Re=2160, and for G=0.25 (left). On the right is displayed an experimental visualization from Miraghaie *et al.* ([36]).

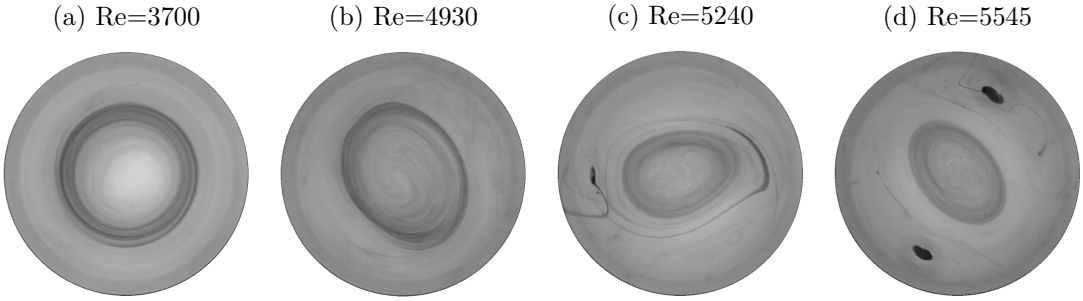

Figure VI.21 – Sequence of instability growing in a clean 55% glycerol mixture, for G=0.25.

The experiment was repeated with a clean water glycerol mixture. Using ink, the first mode observed has an azimuthal wave number m=3, and grew for $Re_c \approx$2150, as shown in figure VI.20a. This time, the difference with the results of Lopez *et al.* and Miraghaie *et al.* is only 7.5%. Increasing Re interestingly gives almost the same sequence as shown in figure VI.19 with dirty water glycerol mixture : after the flow has lost its symmetry at Re_c=2150, a circle is observable again at $Re \approx$3700. The ellipse is clearly visible at $Re \approx$4930, and is followed by the undefined pattern, at $Re \approx$5240 (see fig VI.21). The m=2 pattern then grows for $Re \approx$5545. The reproducibility of this sequence suggests

that pollution may not be the only cause of the lack of detection of the mode m=3 in previous experiments. Indeed we previously reported that Kalliroscope seemed to fail to reveal the low Reynolds threshold, for G=1/14. The experimental protocol may also be an issue, with inadequate times for the plateaus for the lowest Reynolds numbers values.

In order to confirm the excellent agreement on experimental Re_c, the threshold detection was also realized with LDV. Results are summed up in table VI.6.

	Lopez *et al.*	20% glycerol	55% glycerol
Re_c	≈2000	[1900-2520]	[1790-2150]

Table VI.6 – Experimental critical Reynolds number of the wave number $m = 3$, for $G = 1/4$. The experiment with the 20% glycerol mixture used LDV to detect the threshold, while the other experiment, with 55% glycerol, was based on ink visualization.

From this table, one can see that our experimental critical Reynolds numbers have the same order of magnitude, very close to the result published in [37]. Experiment vs. experiment confrontation does not show the same difference as observed previously for G=1/14. Yet, our experimental apparatus dimensions are not comparable at all with [37], while they were identical with [40]. Both our results displayed in table VI.6 were obtained with the largest cavity. The frequency corresponding to the LDV measurement (second column of the table) is f=0.597. An experiment with water in the smaller experimental set-up exhibited instability at Re_c as low as 1615. The associated frequency is f=0.618.

Numerical results

On the numerical side, we used ROSE with a 401×101 cell mesh to obtain the critical Reynolds number. In [37], authors used a doubled geometry to simulate the free surface : their geometry is twice as high as the real one, and the top is a spinning disc in exact co-rotation with the bottom disc. Actually, this configuration is not similar to the free surface configuration. Although the base flows are the same, the double geometry allows unstable modes to cross the median plane ($u_z \neq 0$ on this plane for the perturbations), while, for the free surface case, u_z=0 both for the base flow and the perturbations.. It appears that the most unstable mode in the double geometry is actually a mode that crosses the median plan (in z=$h/2$), as shown in figure VI.22.

For this configuration, the critical Reynolds number of the mode m=3 obtained with ROSE is Re_c=1456. This value is very close to the critical Reynolds number reported in [37], which is 1450. But the real geometry has very different results (see table VI.7). The authors themselves recognized that their model is not acceptable although their numerical results get closer to experiments than the stress free surface model. They explained mismatches by imperfections of the surface : surfactant contamination and a surface which is not perfectly flat. But this last point does not seem to hold, since, according to [42], the effect of deformation on Re_c appears to be irrelevant to justify the observed mismatch : for G=1/14; variation of Re_c with and without surface deformation is smaller than 4%.

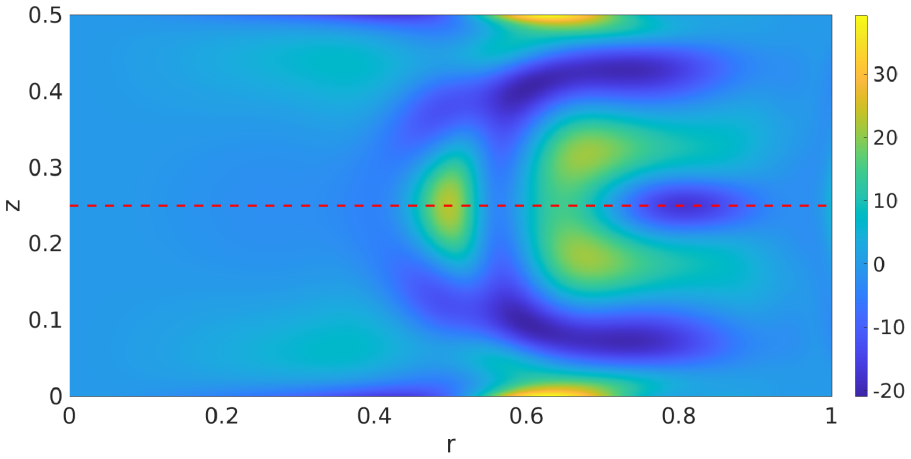

Figure VI.22 – Azimuthal vorticity ω_θ of the fluctuations of the mode m=3 in a meridional plane, in the case of the double geometry for G=0.25, at Re_c=1456. The median plane is represented by the red dotted line at z=0.25. This should correspond to the free surface, yet, $\omega_\theta \neq 0$ and therefore, the free surface condition ($\omega_\theta = 0$) is not respected by this unstable mode.

	Lopez *et al.* (doubled)	ROSE (doubled)	ROSE	
	m=3	m=3	m=2	m=3
Re_c	1450	1456	3481	4691

Table VI.7 – Numerical critical Reynolds number of the most unstable modes for G=0.25. The mention "doubled" refers to a doubled height geometry, with two rotors in exact co-rotation, one at the bottom and the second at the top.

With the flat free surface condition, the most unstable mode has an azimuthal wave number of 2, and starts growing at Re_c=3481. The mode m=3 is unstable only after Re_c=4691. The frequencies of modes 2 and 3 are respectively $f_{m=2}$=0.553 and $f_{m=3}$=0.576, which is in very good agreement with experiments. Indeed, the relative errors with experimental frequencies (≈0.6) are only 8% and 4%, respectively.

The comparison of the mean flow for Re=1895 corroborates previous observations for G=1/14 : computed velocity profiles show an overshoot of u_θ at r ≈0.5 for the case G=0.25 (see figure VI.23a), that is not observed in LDV measurements. The axial velocity profile shows an over evaluation of the length of recirculation in a meridional plane, as it was reported for G=1/14. This is exhibited in the figure VI.23b, where the minimum of u_z in the simulation is located at a radius below 0.6, while in the experiment, this minimum is rather around r=0.7. Note that the Reynolds number considered here was supposed below Re_c. Therefore, since base flow and mean flow are equivalent for $Re < Re_c$, the comparison of ROSE base flow with LDV azimuthal velocities is fully legitimate. Yet,

later experiments reveal that Re_c was overevaluated, and that for Re=1895, the flow can already be unstable.

(a) u_θ in z=0.8G

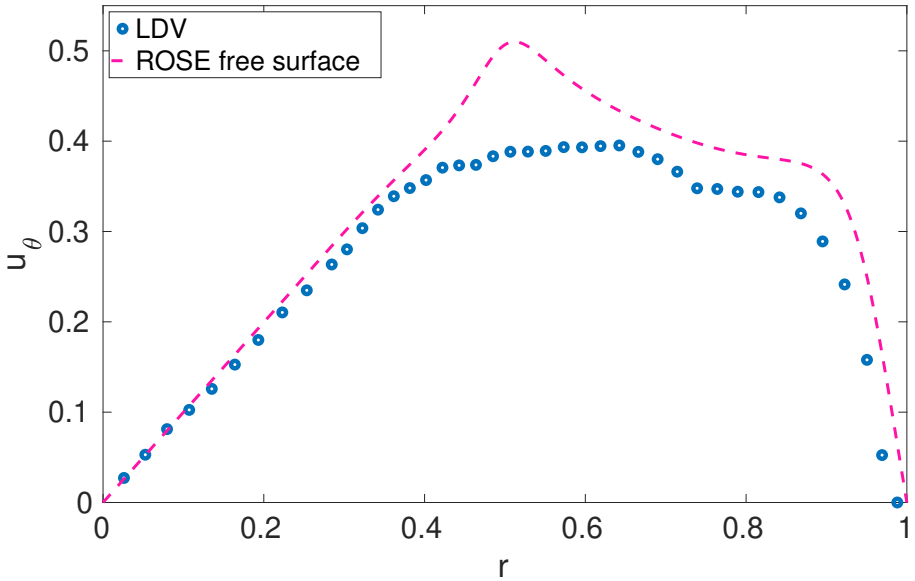

(b) u_z in z=0.5G

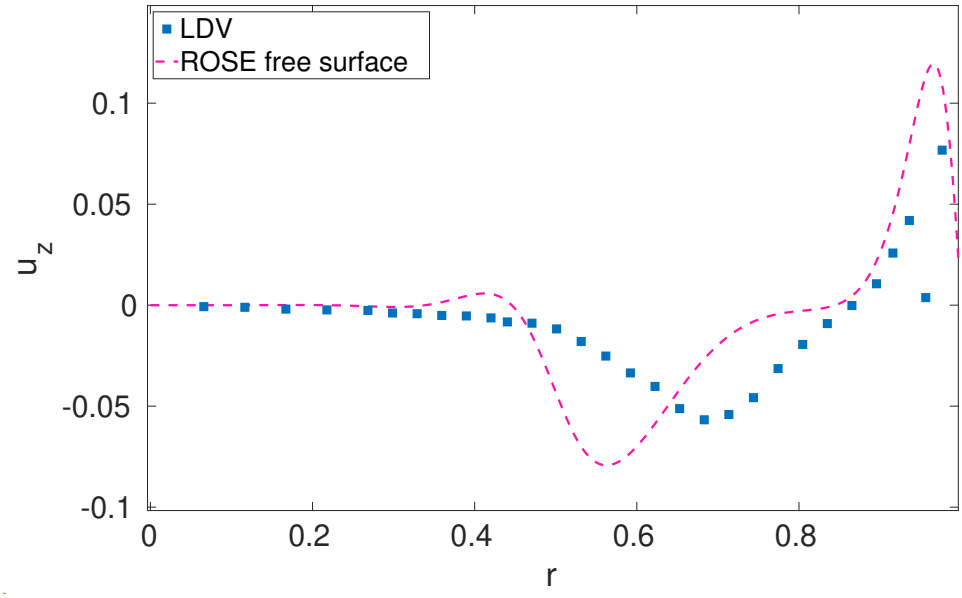

Figure VI.23 – Comparison of velocity profiles : ROSE base flow and LDV measurements, for G=0.25 and Re=1895.

Since G=1/14 shows a chaotic behaviour over long timescales and for $Re \approx 1.1 Re_c$, a simulation was done at Re=3829, corresponding to a Reynolds number 10% above the Re_c value reported in table VI.7 (this gap was 9.5% in the case of G=1/14).

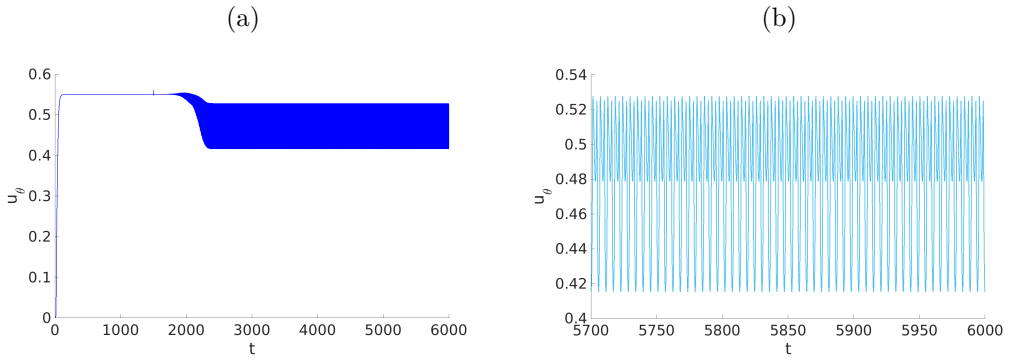

Figure VI.24 – u_θ signal for G=0.25 and Re=3829. The small peak at t=1500 corresponds to the introduction of a pulse, to stimulate the growth of the instability. The probe is located at (0.5,0,0.8G).

Figure VI.24 illustrates that no evolution is visible in the azimuthal velocity profile, once the instability is fully developed. Indeed, the pattern of velocity oscillations stays unchanged over 3600 time units, which represents almost 573 rotations of the disc. It is interesting to note that the vorticity pattern at this Re matches well with experimental observations at Re=5545.

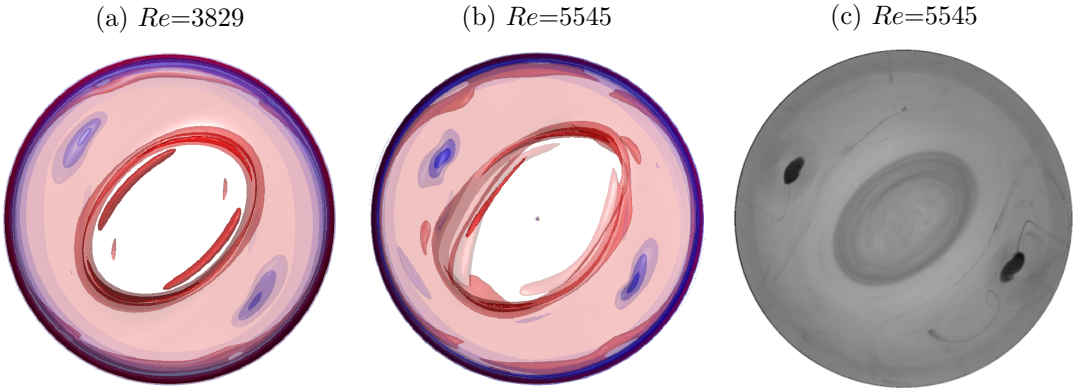

Figure VI.25 – Numerical axial vorticity patterns at t=5900 for Re=3829 (left) and Re=5545 (center), compared to experimental visualization at Re=5545 (right), for G=0.25.

As in the case G=1/14, the simulation for G=0.25 at Re=5545 shows a modulation in its velocity timeseries. The simulation was extended, and confirmed the existence of this modulation on more than 2000 time units (318 disc revolutions). Another run, for Re=6000 was done, in order to look for a possible chaotic behaviour, like for G=1/14. But once again, the width modulation remains constant, this time over 2400 time units,

or 382 disc revolutions (see fig. VI.26a). This modulation can be seen in the loss of the central symmetry of the mode m=2 between Re=3829 and Re=5545, in figure VI.25b. Figure VI.26b suggests that this might correspond to the beginning of the asymmetric transition pattern described earlier in VI.3.1.

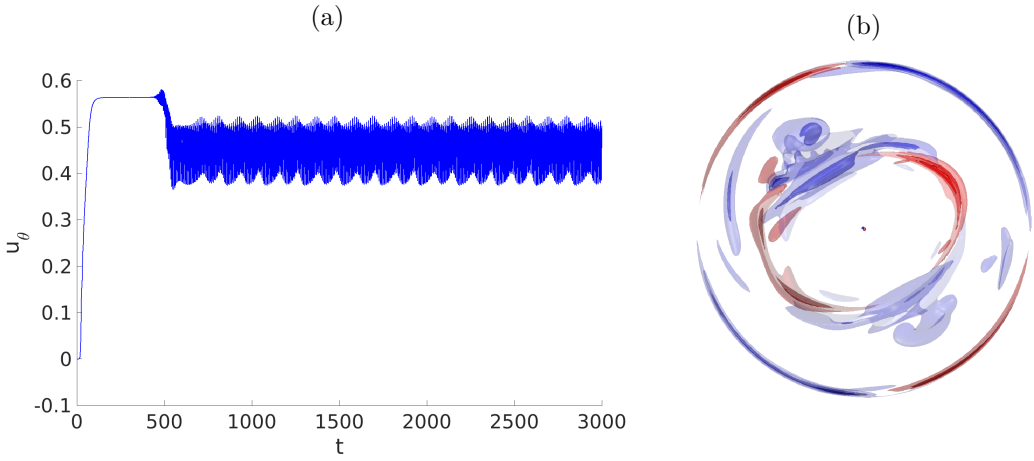

Figure VI.26 – u_θ time series for G=0.25 and Re=6000 (left), and the corresponding vorticity pattern for perturbations at t=2900. The probe is located at (0.5,0,0.8G). The five red isofurfaces are equally spaced in [0,4.93] in red, and the five blue isosurfaces are equally spaced in [-2.73,0].

Conclusion on G=0.25

For G=0.25, we have obtained very good agreement in both experiments vs. experiments and numerics vs. numerics, compared to [37]. However, we were confronted with the same trouble as these authors : comparison of experiments with simulation presents large disagreements, as for G=1/14. Indeed, simulations with a stress-free interface do not seem able to reproduce the experimental flow, since both m and Re_c values did not match between experiment and numerical prediction, and even base flows differ. However, increasing G apparently delays the emergence of the rich spectrum observed in long time simulations and for $Re \approx 1.1 Re_c$.

Exploration of higher aspect ratios

In addition to G=0.25, the authors of [37] also explored G=2, both numerically and experimentally. Their conclusions for this aspect ratio are completely different from those for G=0.25. Firstly, their experimentally determined Re_c is in good agreement with [34]. Secondly, their numerics also match experiments. Note that in their simulation, they still used the double geometry discussed above for G=0.25. But here simulations are valid, because the most unstable mode does not cross the median horizontal plan. This agreement suggests that for larger aspect ratios, instability is less sensitive to any experimental perturbation responsible for the premature triggering for smaller G. Unfortunately, none of our cavities allow us to study G=2 and thus our comparison will be based on data

given in previously quoted articles. However we can access G=1.5, the aspect ratio used to validate ROSE and extensively explored in [44]. We also compared LDV measurements to numerics for G=1 at Re=1120.

G=2

The experimental results are not much developed in [37], but their data can be found in the former publication [35]. Therefore, in the upcoming section, experiments refer to [35], while [37] is used for numerics. The first comparison we focused on was, one more time, the determination of Re_c, which was only done with ROSE. Table VI.8 gathers Re_c values of previously quoted articles, and prediction from ROSE. The grid used contained 201×401 cells.

	Hirsa *et al.* [35]	Lopez *et al.* [37]	Young [34]	ROSE
	m=4	m=4	-	m=4
Re_c	[1900-2000]	1910	[1850-1900]	1914
f at Re=2100	0.156	-	0.160	0.161

Table VI.8 – G=2, comparison of Re_c and f for Re=2100 ($Re > Re_c$). The frequency from Hirsa *et al.* was determined by a graph interpretation.

ROSE matches Re_c and m given in reference articles. In [34], the mode was not visualised in the azimuthal plane, but only LDV signals around Re_c were given. The frequency of the oscillations in the velocity signal at Re=2100 is f_{Ydim}=2.345Hz, which corresponds to a dimensionless frequency of $m \times f_Y$=0.639, according to experimental data given in the article. Interestingly, the fluid used in these experiments was composed at 85% glycerine by volume (≈87,7% in mass percentage). This frequency is not adjusted regarding the azimuthal wave number : if we suppose that m=4, then f_Y=0.16, which is consistent with values in [35] : for Re=2100, the dimensionless frequency is f_H ≈0.156, for m=4. For Re=2100, ROSE estimates f=0.161, which confirms the excellent agreement between numerics and experiments for this G. Note that for Re_c, ROSE predicts f=0.157.

No visualisation such as figure VI.20a is given for G=2, except some DPIV slices, where patterns are not as visible as in pictures with ink or Kalliroscope. Thus comparison of vorticity patterns is not as insightful as for lower G.

The simulation from which figure VI.27 is extracted, was extended up to t=12000, to check for the long time scale evolution. Although this extension from t=10000 to t=12000 corresponds to more than 318 disc rotations, no complex dynamics was observed, unlike what we reported for G=1/14. Only a purely sinusoidal oscillation is present in azimuthal velocity time series (fig. VI.28). The frequency of this oscillation is f=0.156, only 0.64% smaller than the frequency obtained with ROSE and reported above.

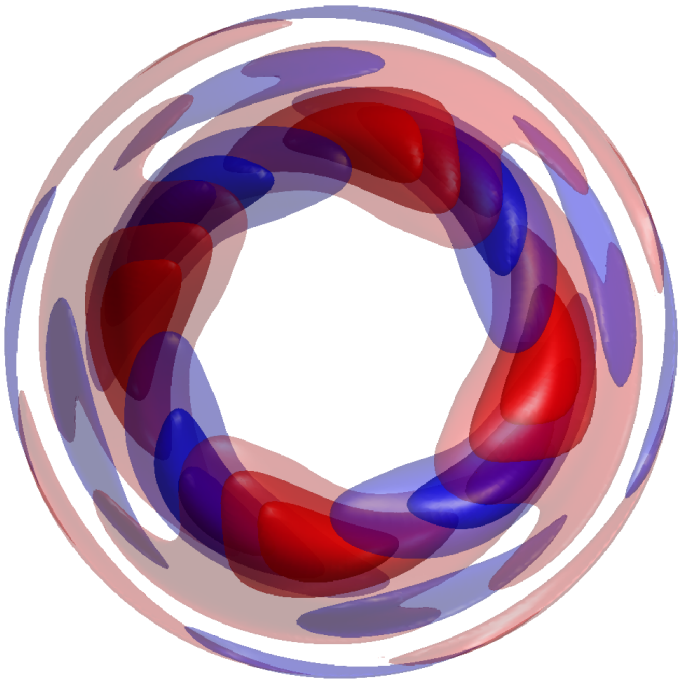

Figure VI.27 – Axial vorticity isosurfaces of fluctuations from DNS, for Re=1950, and for G=2. This snapshot was taken at t=10400, once the instability is fully established. Isosurfaces are divided in two subspaces : 5 red isofurfaces equally spaced in [0,0.11] in red, and 5 blue isosurfaces equally spaced in [-0.15,0]. Translucence indicates the vorticity intensity : translucence increases when ω_z tends to 0.

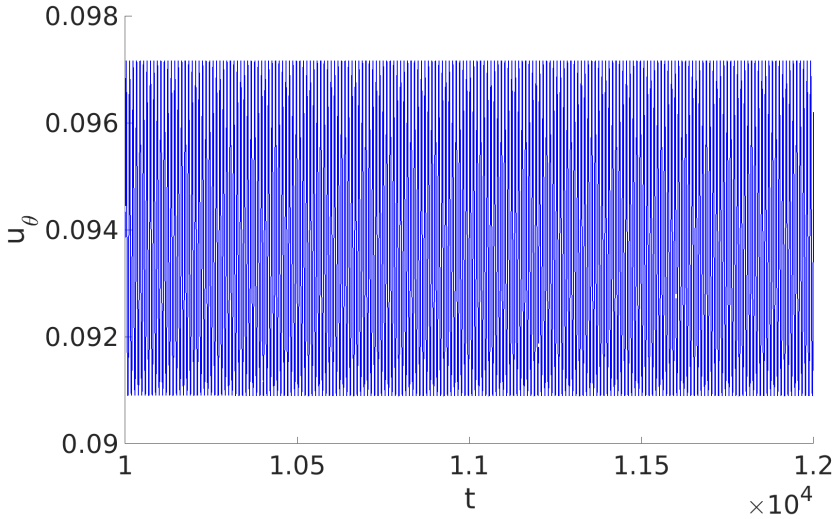

Figure VI.28 – Long time scale simulation for Re=1950, and G=2. The probe is located at (0.5,0,0.5G). The displayed time span is equivalent to a bit more than 318 rotation of the disc.

G=1.5

In section Validation & Mesh, we validated ROSE for the aspect ratio G=1.5. We found that the most unstable mode occurs at $Re_c \approx$2150, with a wave number m=1, which is in perfect agreement with [44]. The new feature of this mode is its frequency f=-0.0487, *i.e.* the rotating wave counter-rotates very slowly with respect to the disc, with a period around 20 times longer.

m	0	1	2	3	4
Re	2655	2150	2664	2520	2806
f	0.222	-0.00487	0.303	0.321	0.328

Table VI.9 – Re_c and f for m=0 to 4, and G=1.5, computed with ROSE.

Table VI.9 gathers Re_c and f for the five first modes. Corresponding simulations were performed on a 245×381 grid. With the exception of m=0 and m=1, all other modes share almost the same frequency. Experiments were done in the small cavity, as it is the only one with a sufficiently high cylinder. Three different fluids were used : water, 20% and 40% water-glycerol mixtures. The corresponding theoretical periods of the mode m=1 for these three fluids are given in table VI.10.

fluid	water	20% glycerol	40% glycerol
Ω_c (rpm)	3.67	5.93	11,57
$T_{m=1}$ (s)	336	208	106

Table VI.10 – Evaluation of the period T of the mode m=1 in the small cavity, for G=1.5, and Re=2150, with a fluid temperature of 26°C. These estimations are based on ROSE computations.

Experiments with this aspect ratio display a very long transient (see fig. VI.29a), that makes threshold detection tedious and risky. Indeed, the experiment from which is extracted figure VI.29a lasts four hours. Visualization with ink did not prove to be efficient either. At Re=2356, after a long transient, velocity time series acquired with LDV shows three states. The first one, for t between 2350 and 4160 has a main frequency of $m \times f$=0.401. This is followed by a short transition, between t=4160 and t=4490, then, a third state appears, and last up to t=6770. This state is marked by a very low frequency mode corresponding to the increase of the mean velocity. In addition to this mode, the main frequency is $m \times f$=0.538, followed by a second oscillation of close amplitude, with a frequency $m \times f$=0.838. We note that this second peak was also present in the first state, at $m \times f$=0.806. None of these frequencies are normalized regarding the azimuthal number, as we have no clue about it, and thus, they are reported as $m \times f$ instead of f. Despite a rich spectrum, no evidence of a mode m=1 with f=0.0487 was observed.

Other experiments were performed on this aspect ratio, including a spin-down phase

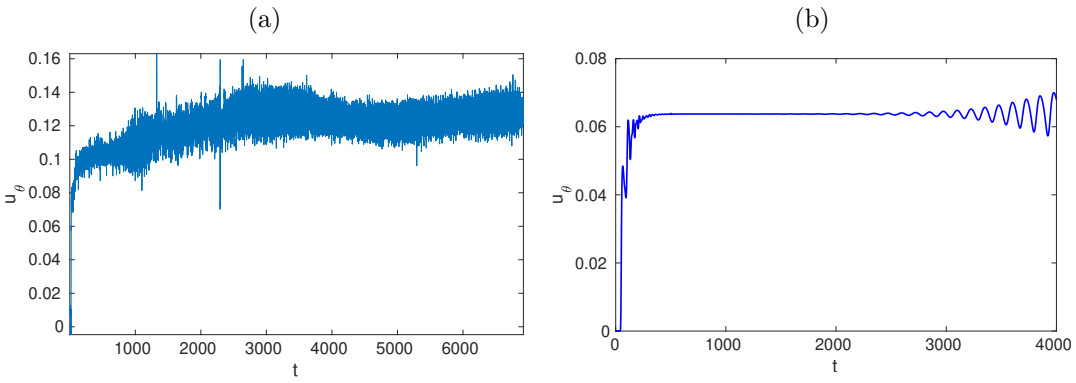

Figure VI.29 – Transients for G=1.5, experimental on the left, and numerical on the right. In the experiment, the flow (water) is initially at rest, and the disc is set in motion at Ω=4.59 *rpm*. The temperature evolves from 18.1°C to 20.3°C which translates into a Re value between 2232 and 2356. The measurement point is located at r=0.84, z=0.99G. Time and azimuthal velocity are dimensionless. In numerics, the probe is located at r=0.6, z=0.75G. A small impulse was introduced at t=500.

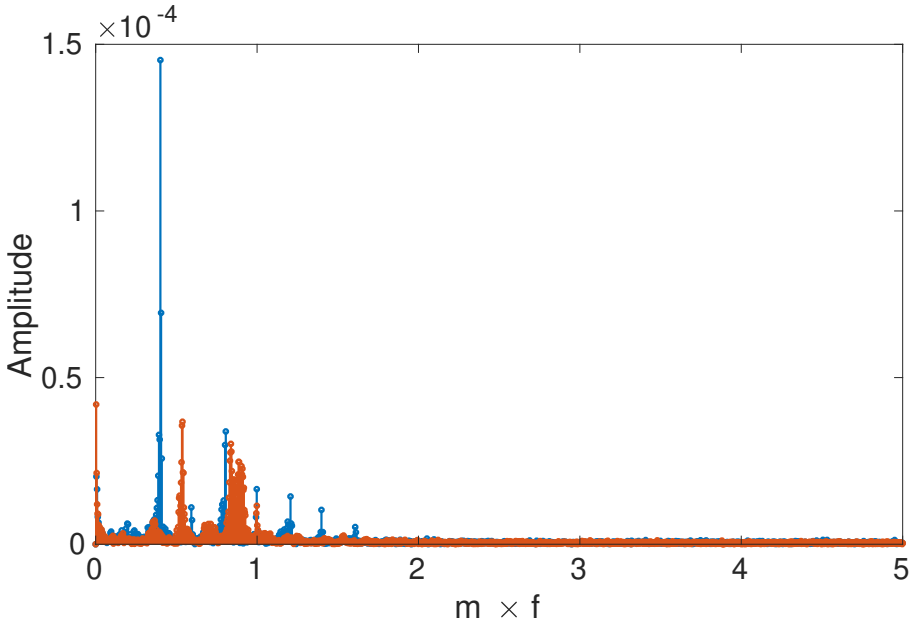

Figure VI.30 – Fourier transform of the LDV acquired azimuthal velocity time series at Re=2356 (figure VI.29a). Blue peaks correspond to the signal between t=2350 and t=4160, while orange peaks correspond to the signal between t=4490 and t=6770. Frequency is normalised according to the disc rotation rate.

from Re=3620 to 1820 in steps of 360. Except for Re=2540 and Re=2180, no other Reynolds number shows a clear dominance of a single frequency in Fourier spectrum. For these two Re values, main frequency is around $m \times f$=[0.48,0.49]. For Re=2900 to 3620, Fourier spectrum shows competition between two frequencies of comparable amplitude. Table VI.11 gives the value of theses frequencies, and shows that the second frequency at each Re corresponds to the main frequency of the lower Re step. This suggests that several modes have very close instability thresholds. For Re=1820, up to six frequencies are present. Note that this Re is below the numerical Re_c, that the two successive acquisitions at this Re do not show the same frequencies on their respective spectrum, and that the amplitude of the last acquisition seems to be decreasing. In addition to the long transient, we can suspect that Re=1820 is indeed below Re_c.

Re	3620	3260	2900
$m \times f$	0.9 | 1.0	1.0 | 0.54	0.56 | 0.47

Table VI.11 – Frequencies of oscillation of highest amplitude for Re between 2900 and 3620, and G=1.5. The main frequency is on the left, and the second on the right. Frequencies are not normalised regarding the mode, that is unknown. Therefore, they are given as $m \times f$.

Although probes are not located at the same position and, therefore, the direct comparison is not possible between figures VI.29a and VI.29b, one can see with this last figure that simulations performed at Re=2356 also display a long transient state, despite the introduction of a perturbation at t=500 to stimulate the growth of the instability. The simulation was extended to t=5600. There, the instability is not yet fully established. However simulation was not pursued further as its time cost appears prohibitive (more than 48 hours for 400 time units) and that our main concern remained G=1/14. However, the pseudo-frequency in the time span t=[5200,5600] is f=0.0479, which is only 1.6% smaller than ROSE prediction. The corresponding azimuthal wavenumber is indeed m=1, as shown in figure VI.31. Note that for t=4000 instability is not fully developed and thus vorticity magnitude are not representative of the final state flow. Obviously, since the simulation was not prolonged, we have no clue about the long timescale evolution of the flow, and we can only suggest that it should be similar to that for G=2.

G=1

We saw in section V.2.5 that we had a good agreement between our DNS results and [15] for G=1 and Re=1120, for the base flow. Using our smallest cavity, we choose to compare experimental and numerical base flows, since Re=1120 is well below Re_c. Indeed, ROSE predicts, for G=1, the growth of an azimuthal wave number m=1, only at Re=2007.

On figure VI.32, one can observe that the experimental profile is close to the numerical one : fitting is not perfect, but order of magnitude of extremal values and their location tend to match well. We recall that the axial velocity is one order of magnitude smaller

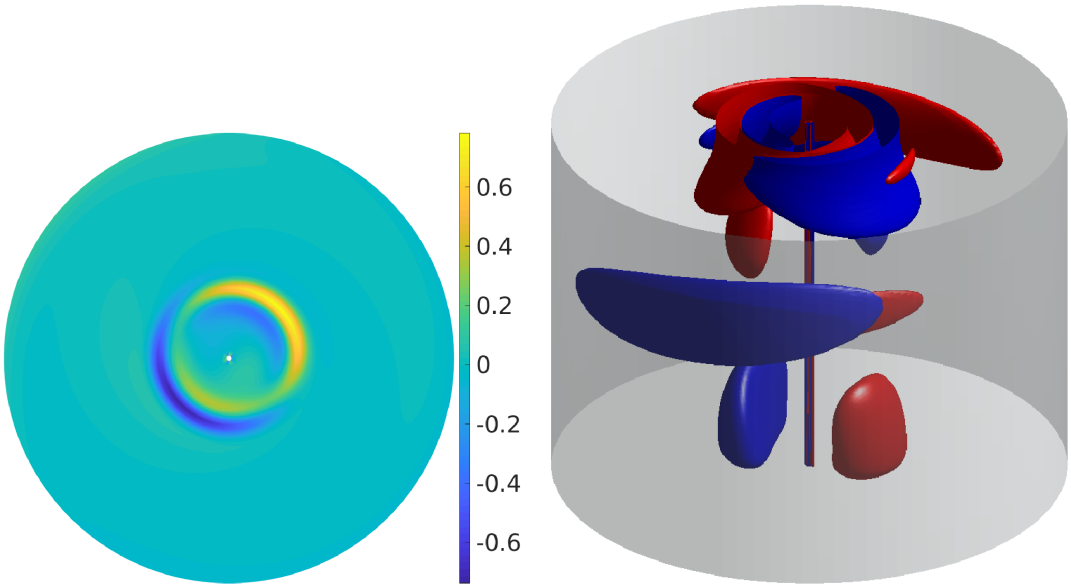

Figure VI.31 – Axial vorticity pattern of fluctuations for G=1.5, at Re=2356. Left : vorticity at z=G, corresponding to an instantaneous field at t=4000 in figure VI.29b. Right : isosurfaces of ω_z=±0.1.

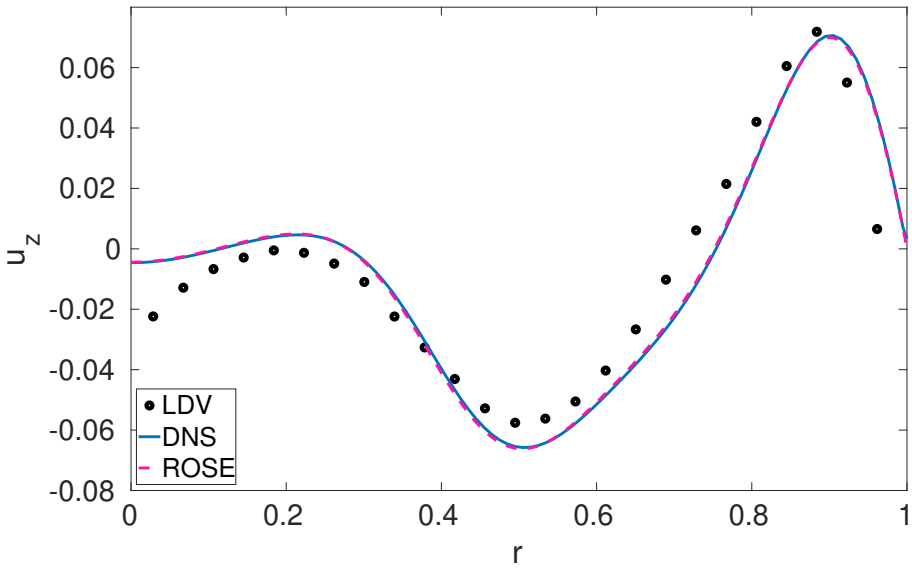

Figure VI.32 – Axial velocity profile $u_z(r)$, at z=0.5G for Re=1120, and G=1.

than the azimuthal velocity, and thus harder to measure experimentally.

Although no experiments were done for threshold detection, table VI.12 gives the most unstable modes predicted by ROSE. One can see that Re_c for m=2 is only 8.2% larger than Re_c for m=1. Once again, the frequency for m=1 is negative, and the mode counter-rotates with respect to the disc.

m	1	2	3
Re_c	2007	2172	2304
f	-0.148	0.380	0.392

Table VI.12 – ROSE prediction of Re_c and f of the three first unstable modes, for G=1.

As for larger G values introduced above, DNS required long time scales to observe the growth of instability. Indeed, the simulation at Re=2075 was run up to t=8400 (more than 1330 revolutions), and the saturation was not reached yet (fig. VI.33). As for G=1.5, the computation was not extended further.

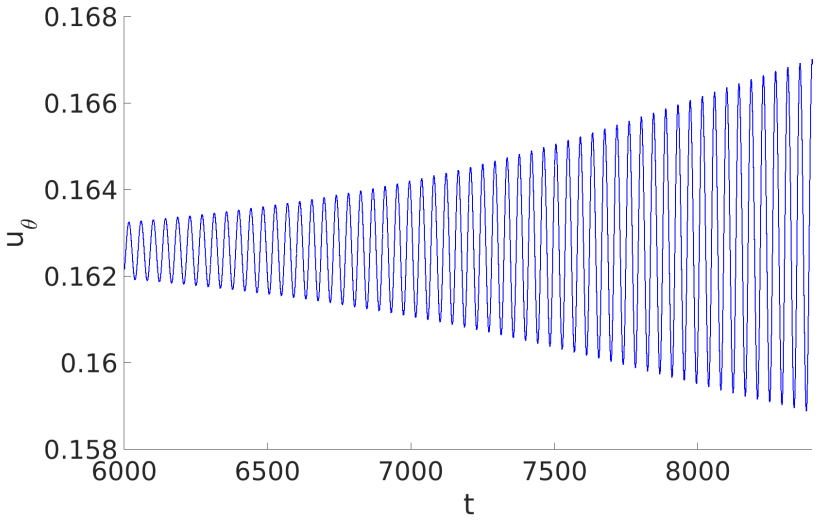

Figure VI.33 – DNS probe recording of u_θ at Re=2075, for G=1. The probe is located at (0.55,0,0.5G).

Although the growing mode shows an azimuthal wave number m=1 (fig. VI.34), the corresponding pseudo-frequency for t between 8100 and 8400 is f=0.0235, which is 84% smaller than the prediction using ROSE reported in table VI.12. This numerical mismatch was completely unexpected and it was the only time it was observed.

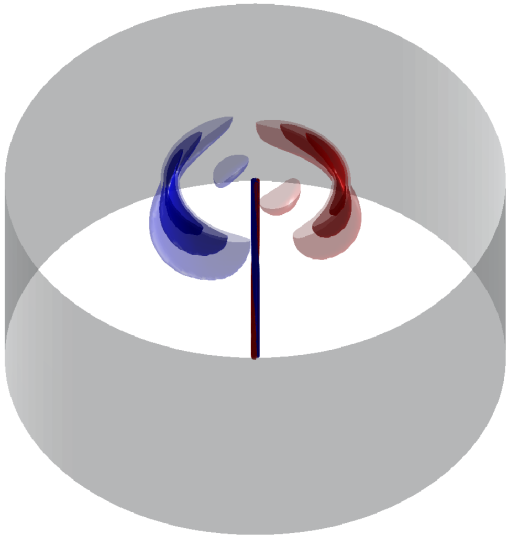

Figure VI.34 – ω_z isosurfaces of flutuations at t=8400, for Re=2075 and G=1. Red isosurfaces are equally spaced in ω_z=[0,0.35] while blue isosurfaces are equally spaced in ω_z=[0,-0.35]. As in figure VI.27, translucence indicates the vorticity intensity : translucence increases when ω_z tends to 0.

Conclusion

Every aspect ratio explored has brought evidence of disagreements, as well as agreements. Indeed, G=2 exhibits good agreement between experiments and numerics, while the results for lower aspect ratios are more inconsistent. Small aspect ratios (G=1/14 and G=0.25) are especially concerned by the mismatches, since respective Re_c are much lower than numerical prediction, and even their experimental base flow differs from numerical ones. For G=0.25, disagreement is obvious since the most unstable mode is not the same in experiences and in simulations. The mismatch for G=1/14 is much more tricky, and only a look at the instability pattern and to the long time evolution of the flow in DNS confirms the existence of differences.

It seems that reducing G in simulation promotes a fast transition to a chaotic behaviour. In contrast, increasing G leads to a better agreement on the base flow. Unfortunately, no validation of the most unstable mode was possible for G=1 and G=1.5. For this last value of G, one can only suppose the mismatch on m, since no evidence of the contra-rotative m=1 mode was observed in Fourier spectra.

The most troubling feature is the important mismatch in the comparison between experimental results for G=1/14. No evident cause for this mismatch was found, and we suggested that, in addition to a possible negative effect of Kalliroscope, a mechanical vibration from our experimental set-up could trigger instability by resonance. This interaction would be more dramatic on low G configuration, since small aspect ratios seem more sensitive to external perturbation.

Chapter VII

Evaluating the vertical displacement of the disc surface

The mismatches reported in previous chapters were quickly associated to an experimental flaw. Indeed, previous publications ([40] and [43]) displayed a strong agreement between experiments and numerics for $G \geq 1/14$. Several tests were realized before the beginning of this thesis, including viscosity monitoring, influence of the gap between the disc edge and the cavity wall, non neutrality of the marker, switching of the disc and even the switching of the direction of rotation. But none of them was concluding. Therefore, we suspected vibrations of the experimental set-up to force instabilities growth by resonance. We knew from comparator estimations that the displacement of the disc surface in the largest cavity was close to 0.3 mm. But we had no clue about the frequency of this phenomenon. To evaluate this frequency, we used two Keyence LK-G10 sensors, able to measure displacement of a surface in the $\pm$ 1.0 mm range with an accuracy around 10 μm. These sensors are connected to a Keyence LK-GD500 controller, which delivers a tension of $\pm$ 10 V, regarding a given measurement span. The smallest sensitivity is 1 $mm/10V$, but distance window can be reduced, for an accuracy gain. All the following measurements were made on or inside the largest cavity. Note that all the spectra included in this chapter have their amplitude multiplied by four, so that the amplitudes of the peaks match with the measurements of the vertical displacement.

Figure VII.1 – LK-GD500 controller (left), with Keyence LK-G10 sensor (right) .

Recording the signal of sensors through several revolutions gives a periodic signal from which can be estimated the frequencies with Fourier transform. It also gives the displacement amplitude of the disc surface. Nevertheless, this measurement is only local, and to obtain the global topology of the surface it would require synchronised measurements for many radii. Here, we only expect to find the frequencies of the main modes of vertical displacement.

In addition to the brass disc used in our experiments, a second disc made of aluminium was also tested. This disc is thinner and lighter than the brass disc. Its surface was not accurately machined and is thus prone to larger imperfections. This disc was also used in early tests, which demonstrated that the premature growth of the instabilities was

independent from the disc mounted in the experiment.

Oscilloscope as a bridge

Method

At the beginning of the measurement campaign, we only had access to one Keyence sensor. The bridge between this sensor and the computer was insure by a LeCroy WaveAce 202 numerical oscilloscope. The time of acquisition depended on the calibre, and so was the timestep : signals were discretised on 3000 dots in time, whatever was the signal length, and on 256 values (8 bits) for the tension measurement. Keyence sensor sensitivity was set between 20 $\mu m/10V$ and 250 $\mu m/10V$. To estimate the displacement of the disc surface we needed to know the vertical calibre V_c used on the oscilloscope and the sensitivity S_s of the sensor. Then, by counting the number n_v of vertical divisions, we have $A_d = n_v \times V_c \times S_s/256$, where A_d is the displacement amplitude of the surface. In the same way, we can evaluate the period T of the signal just by counting the number n_h of horizontal division and by knowing the horizontal calibre H_c : $T = n_h \times H_c/(3000 \times n_p)$, where n_p is the count of periods. Figure VII.2 shows the signal obtained on the oscilloscope.

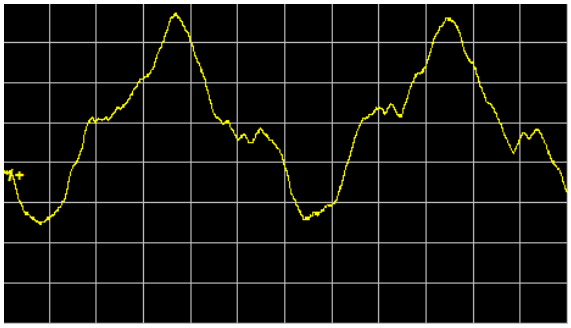

Figure VII.2 – Raw signal acquired from the oscilloscope, for the brass disc, at r=124mm. Oscilloscope calibres were 1 s/div and 2 V/div, while sensor sensitivity was set to 25$\mu m/V$.

Measurement and post processing

First attempt with the brass disc

Once data was transferred to the computer, post-processing was performed with MatLab. Using the measurement made on the brass disc surface, the displacement amplitude of the disc surface can be estimated thanks to the relations given above : in r=124 mm, displacement is evaluated to ∼205 μm. Then the frequencies of the main modes are obtained with a Fourier transform, after the mean value of the signal is subtracted (see fig. VII.2). The amplitude of each mode is normalized with respect to the radius where measurements were made, and frequencies with respect to the disc rotation rate. According

to this, the main peak occurs for f=1, which probably corresponds to an inclination of the disc surface. The second peak is at f=3, that can be understood with the signal profile in figure VII.2 : on each side of the positive peak, one can see two plateaus that may be small variations in the slope of the inclination.

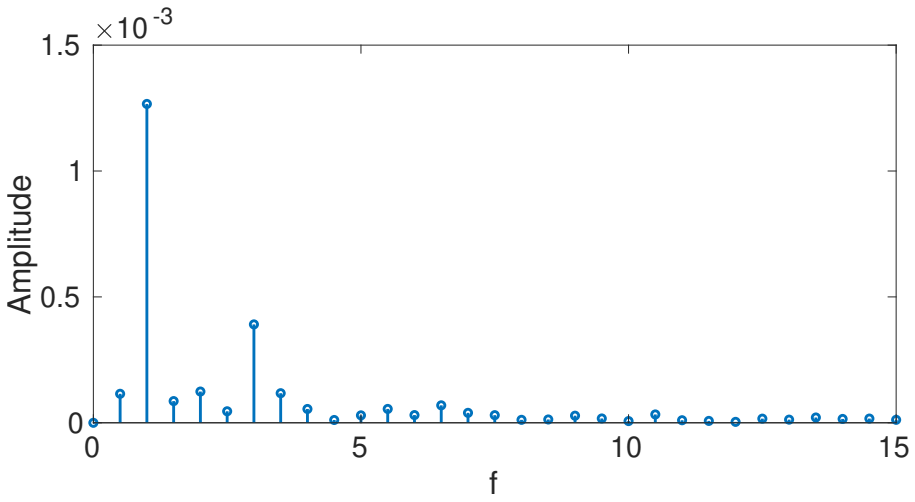

Figure VII.3 – Main frequencies of oscillation of the largest cavity with the brass disc, using same data as figure VII.2.

This first measurement did not show any obvious connection between the instability mode frequency and the oscillatory frequency of the disc surface. Yet the discretization on the frequencies scope is not dense enough to catch values with a step smaller than f=0.5.

Comparison of two discs

We repeated this measurement for both discs, but with a better sensitivity. We tried to focus the sensor on the same radius in both cases, however, a small difference remains : in the absence of a dedicated support, the sensor was found hard to Zero. Actually, the sensor has to be placed at a certain distance from the disc, corresponding to half the field of measurement of the sensor. But the higher is the accuracy, the harder it is to remain in this “zero zone“ : tightening a screw can drive the sensor out of position. The radii compared in figure VII.4 are r=115 mm for the aluminium disc, and r=118 mm for the brass disc. For acquisitions with the aluminium disc, sensor sensitivity was 37.5 $\mu m/V$, while for the brass disc, it was 15 $\mu m/V$. For both discs, oscilloscope calibres were 2 V/div (vertically) and 10 s/div (horizontally).

From figure VII.4b we observe once again predominant peaks for f=1 and f=3, for both discs. For these two wavenumbers, amplitudes of the aluminium disc are approximately twice times larger than those of the brass disc : as expected, the flatness of the aluminium disc is worse than the one of the brass disc. Note that for the aluminium disc, a strong peak is observed for f=2. Its absence in the brass disc signal confirms that it

(a) Signal

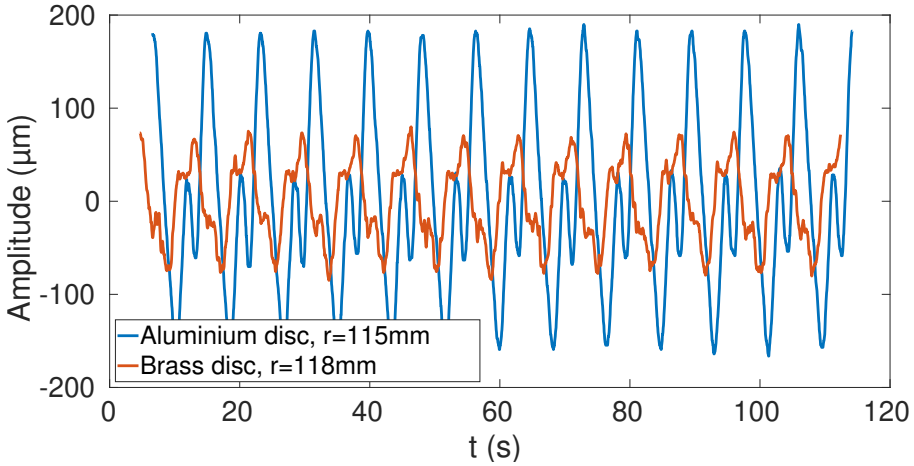

(b) Fourier transform

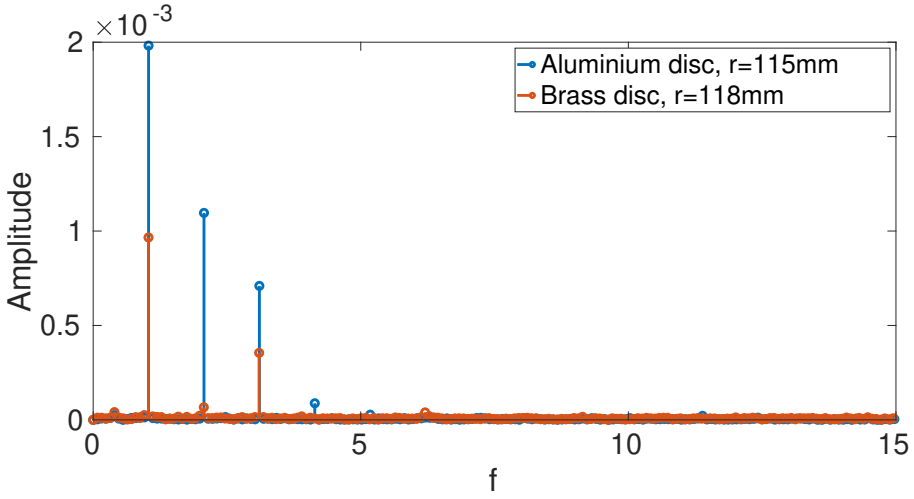

Figure VII.4 – Surface displacement for the aluminium (in blue) and the brass disc (in orange). VII.4b shows the associated Fourier transform. As observed in VII.4a, the amplitudes of the aluminium disc are twice as large as those of the brass disc. The aluminium disc also displays an additional mode of vibration m=2.

only involves a flaw of the aluminium disc surface, such as a fold along the diameter.

As for today, it is hard to tell if peaks for f=1 and f=3 are due to imperfections of the surface of discs only, or if a flaw in the rigid sleeve coupling or the thrust ball bearing can be responsible for a non-negligible part of the displacement.

Detection of a peak

During these previous acquisitions, we periodically saw a negative peak on the oscilloscope screen, without being able to record it. We get more lucky on later measurements, as shown in figure VII.5.

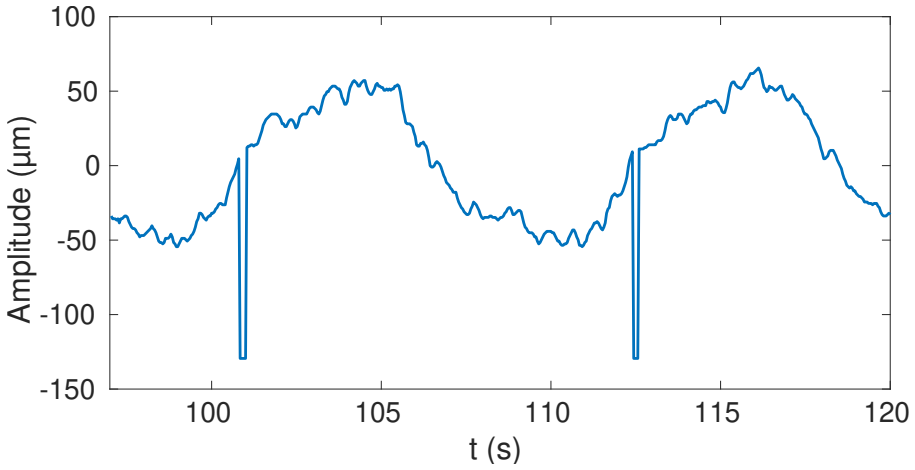

Figure VII.5 – Example of peak with a strong periodicity, on the brass disc, for r=79 mm.

We were very doubtful on the origin of this peak : it did not appear on each measurements, but when it did, it shown a periodicity that could imply a phenomenon on the disc surface, such as a brutal vertical motion, even from a small amplitude, that would result in a stall from the sensor. This "drop peak" was observed for several rotation speed and radius, and with both disc, and always resulted in a drop of the tension to the lower limit of the sensor. Once this peak was discovered, we had strong expectations it could partially explain mismatches reported in previous chapters. However, this peak can also be an artefact due to a defect from the sensor or from the acquisition chain.

Displacement of the cavity

Some other measurements were made with this first acquisition chain, directly on the edge of the cavity, and on the aluminium sleeve of the foot : if the shaft is bent, or if the misalignment between the shaft of the disc and the rigid sleeve is too pronounced, this leads to a forcing on the guiding ball bearings and the whole cavity would show a

precession movement (see figure VII.6).

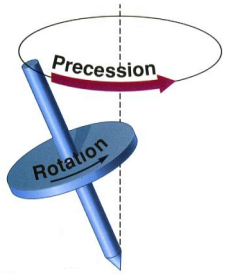

Figure VII.6 – Illustration on a spinner of the precession mouvement compared to rotation.

The evaluation of vertical and horizontal displacements of the plexiglas container can help to discriminate the origin of displacements : if the cavity displacement amplitude is comparable to the displacement of the disc surface, this would incriminate a major flaw in coaxiality. Results of axial and radial displacements of the cavity are summed up in table VII.1. Displacement of the cavity with the aluminium disc mounted is twice larger than with the brass disc. This factor 2 echoes a previous comparison between both discs. From figure VII.7d, below the domination of f=1, we can see the presence of small peaks for f=2 and f=3 for the aluminium disc, while for the brass disc (fig. VII.7b), there is no noticeable peak for f=3. Therefore, modes 2 and 3 observed previously for the aluminium disc can be partially caused by a flaw in the shaft, while the mode 3 reported for the brass disc seems to be mostly attributable to the disc surface deformation.

	brass disc	aluminium disc
vertical (μm)	13	27
horizontal (μm)	15	38

Table VII.1 – Amplitude of displacement taken on the upper edge of the cylindrical cavity.

We can conclude that there exists a small precession movement, but the displacement amplitude of the cavity is approximately one hundred time smaller than these of reported at the surface of both discs. The precession movement itself depends on the selected disc : with the aluminium one, displacements of the cavity are two times larger than with the brass one. At this point, we may suggest that the movement of each disc surface is essentially caused by small deformations of their respective surface, or to an orthogonality defect between the shaft and the disc.

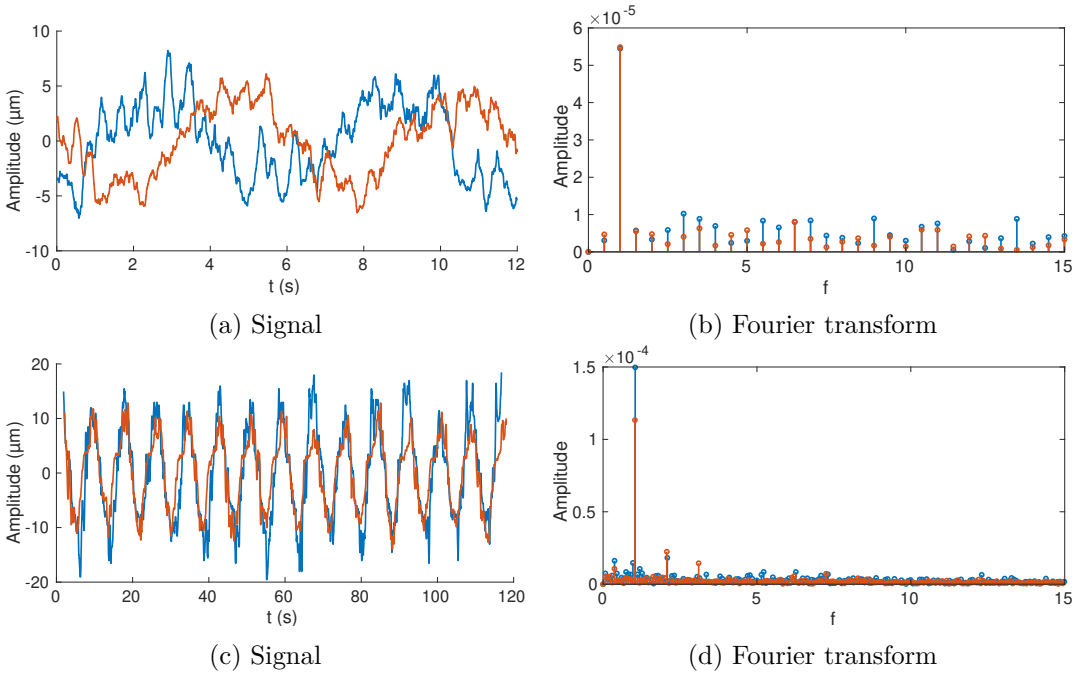

(a) Signal

(b) Fourier transform

(c) Signal

(d) Fourier transform

Figure VII.7 – Measurements on the cavity upper edge. Figures VII.7a and VII.7b correspond to measurements with the brass disc, while figures VII.7c and VII.7d were made with the aluminium disc. For both of them, orange plots are radial displacements, and blue plots are axial displacements.

New acquisition chain

In order to avoid the limits of the oscilloscope, we switched to a National Instrumental dAq, directly linked to MatLab. Data are now acquired through 600 s, with 1000 $samples.s^{-1}$. We also add a second sensor. Initially, we used a LK-G150, with a maximum displacement of ± 400 mm. A rigid frame with aluminium mounts simplified initial placement of sensors, and robustness of measurements (see figure VII.8). Nevertheless, after zeroing sensors, it remains a small drift leading to an incertitude of ~ 10 μm. We expected that the larger range of LK-G150 could catch without saturation the peak discussed earlier. But this sensor has been quickly changed for another LK-G10 sensor, more adapted to our discs displacements : their amplitudes are small enough for the LK-G150 to never get out of its "zero zone".

With this two sensors set-up, three kinds of measurements were performed :

- Two sensors placed in r=109 mm, but with a π phase shift.
- One sensor in r=109 mm, and the second in r=54 mm, with no phase shift.
- One sensor in r=109 mm, and the second in r=0 mm.

These configurations of sensors location should allow us to determine whether the surface displacement is due to a vertical jump of the whole disc, to local surface defects, or to some precession movement. Every acquisition was done with a 100 $\mu m/V$ sensitivity.

Figure VII.8 – Rigid frame with LK-G10 and LK-G150 sensors.

π phase shift

This new measurement campaign was started with the two sensors in phase opposition, in order to check whether the drop can be detected in the same time on both sensors, of with a phase shift of π. The first case would alleged in favour of vertical drop of the whole disc, while the second would imply a groove in the disc surface. Sensors are placed in r=109 mm, on each side of the disc center, on the same diameter. This radius was chosen because it is approximately the radius were vortices are visible with a fluid filling of h=10 mm.

Figure VII.9a gives many interesting insights :

- The drop occurs at the beginning of the descending phase, while we previously saw it during the ascending phase. This confirms that if it has a physical reality, it is not linked to the disc, but to the thrust ball bearing or the rigid sleeve coupling since only the variation of position of the shaft in the sleeve can explain this change in the location of the peak.
- Despite the much higher data rate, the drop is not present at each period. Its apparition remains slightly random although, when it was captured, it was always on the same position at each period.
- The second sensor never recorded the peak. One could suppose that sensors are not placed at the exact same radius and therefore, do not capture the exact same signal. However the peak was observed both for smaller and higher radius in previous measurements.

Sensors were then inverted, and so was their plug in the controller. Each time, the peak appeared in only one of the acquired series, always linked to the same sensor. It was

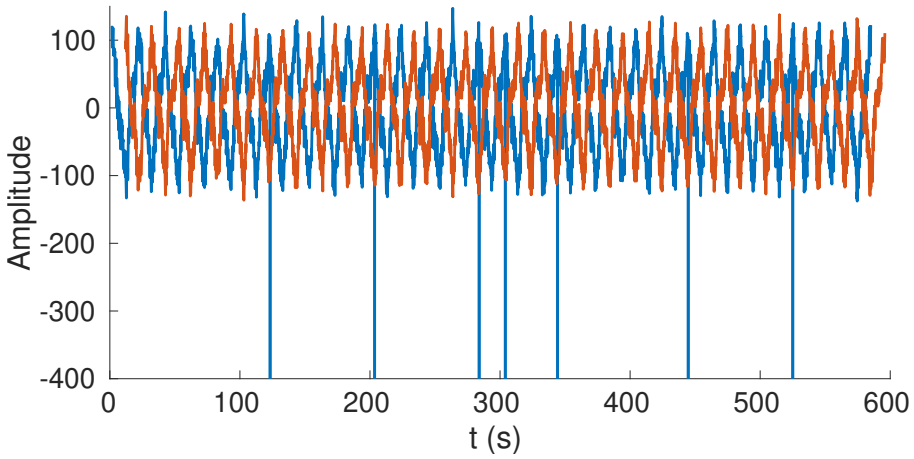

(a) Signal

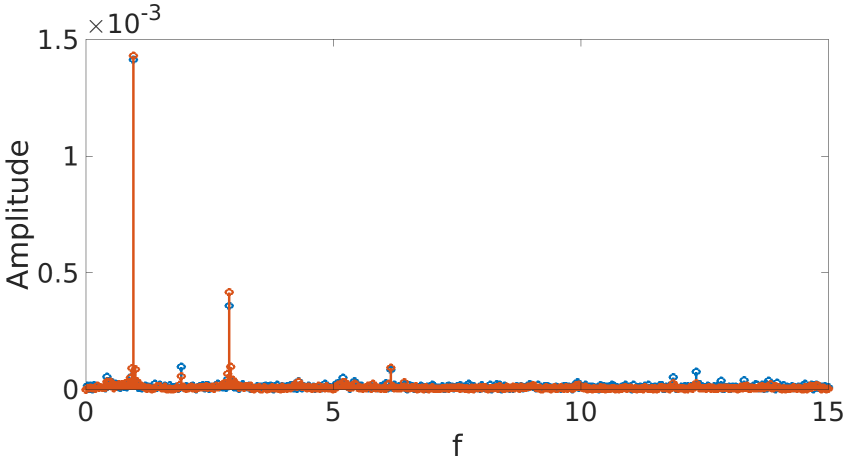

(b) Fourier transform

Figure VII.9 – Sensors in phase opposition, at r=109 mm. Maximum displacement amplitudes in figure VII.9a are 285 μm and 274 μm.

then obvious that this peak resulted from a faulty sensor.

The same measurements were repeated for the aluminium disc, with the exact same conclusions. With this disc, the two sensors gave the same maximum displacement amplitude of 487 μm.

Linearity of the slope

Since we can not scan the whole surface of the disc with our control set-up, we choose to simply evaluate the linearity of the slope with two points, and to check for any traces of residual vertical movement of the whole disc, with a sensor placed at the vertical of the rotation axis. Measurements for r=0 mm, r=54 mm and r=109 mm are reported in the table VII.2. Note that they were only realized on the brass disc.

r (mm)	0	54	109
displacement (μm)	34	91	189

Table VII.2 – Amplitude of displacement for three radius of the brass disc.

Two antagonist observations can be made from table VII.2 :

- The existence of a displacement in r=0 mm is synonym of a vertical translation of the whole disc, probably caused by irregularity in the thrust ball bearing.
- Amplitudes reported for r=109 mm is 2.08 times larger than for r=54 mm. This match very well with the 2.02 factor between radius, and therefore supports the hypothesis of a linear slope of the surface, with a zero vertical displacement of the rotation axis. A non perfect placement of the sensor in r=0 mm does not fully justify the non zero displacement : if the surface slope was perfectly linear, a 34 μm displacement would only be observed in r ≈20 mm, which is too far from the center.

The global movement of the surface can hardly be associated to a simple and unique cause but more probably to a combination of at least two flaws, making them harder to identify and correct. However, the amplitude displacement remains small, with less than 300 μm. For G=1/14, the smallest aspect ratio considered in this thesis, the height of the fluid above the disc is H=10 mm, and vertical displacements then represent 3% of H.

Comparison of figures VII.10a and VII.9a reveals that the amplitude for r=109 mm is smaller in later measurements. The replacement of the three ball bearings between these two measurement campaigns is probably responsible for the amelioration of the rotation quality. Indeed, we suspected ball bearings to be partially rusty and planned their replacement in order to reduce noise and small amplitude vibrations while operating the experiment.

Conclusion

An in-depth study of the vertical displacement of the largest cavity was conducted in order to try to identify causes of oscillations in the disc surface. The main frequencies of these oscillations were also estimated, in order to check for a relation with flow instability frequencies. It appeared difficult to isolate only one reason of the movement. Although the amplitudes of displacement are small compared to the height of the fluid, even for G=1/14. Yet, if our system was sensistive to an oscillary forcing, this amplitude would be large enough to promote the instability. Still no oscillatory mode of the disc shares a frequency with the instability that occurs in the flow for G=1/14. As a consequence, the hypothesis of forced instability by resonance with an oscillatory mode of the disc does not seem relevant any more for this flow. Nevertheless, the replacement of ball bearings brings a small improvement to the rotation quality.

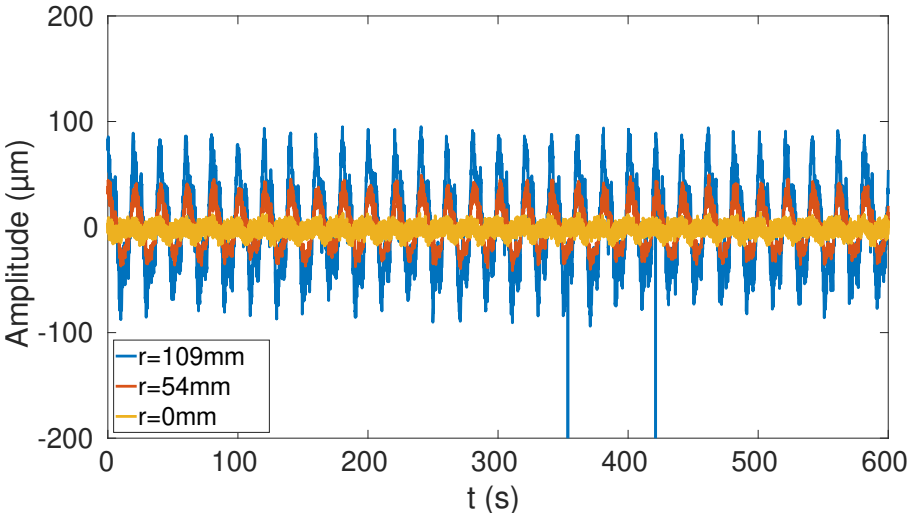

(a) Signal

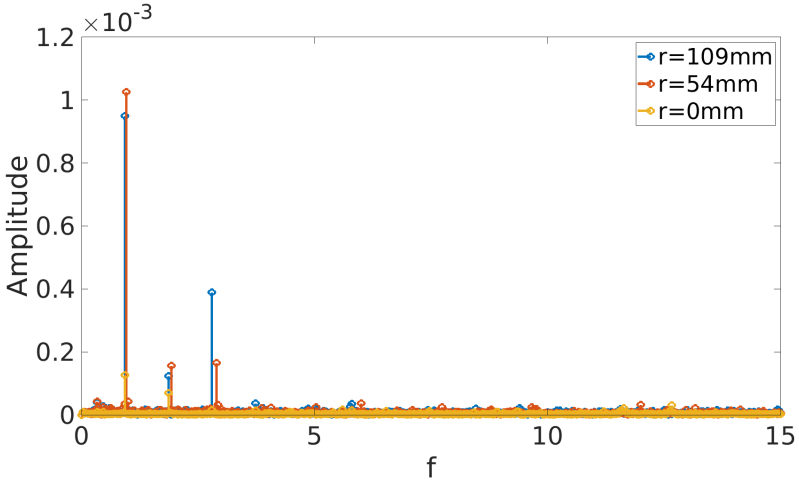

(b) Fourier transform

Figure VII.10 – Vertical displacements of the disc surface for three radius of the brass disc.

Chapter VIII

Numerical investigation of the effect of the boundary condition at the interface

The hypothesis of an instability triggered by a mechanical noise was heavily questioned during the quantification of disc displacements. Moreover, the absence of major flaw of the experimental set-up, added to the good agreement on experimental comparison for G=0.25 and G=1 discussed in VI.4, exculpate the experimental bench to be responsible for the early growth of instabilities. Even legitimated, experimental results still show important mismatches with numerics for small G, and every preliminary test had to be reassessed in order to find an other admissible hypothesis that could explain these disagreements.

The only promising clue was a single ROSE simulation done with an improvised boundary condition. Although the initial suggestion behind the new boundary condition applied in this computation relied on an observation made during one of our experimental campaign, its numerical counterpart can seem somewhat brutal. Actually, this approach of the air water interface founds its origin in [69]. There, the authors suggested that the radial velocity u_r tends to 0 when the surface is polluted. However, with this new surface condition, their code failed to match experimental velocity profiles for G=1.75 at Re=1850. Echoes of this idea can found in some others articles, such as [70]. There, authors noted that in presence of a sufficiently high concentration of surfactant at the surface, "the Marangoni stress acts like a no-slip surface". This behaviour was also described in [71]. In 2003, a new observation of the role of the surface cleanliness was introduced in [37] for G =0.25 : as discussed in chapter VI, Lopez *et al.* noticed that if the fluid had a higher amount of surface-contaminants, the most unstable mode switches from m=3 to m=2.

The role of the radial velocity at the surface was actually, after viscosity and irregularity of the rotation rate, one of the first investigated possibilities for mismatches : from experiments with Kalliroscope, we observed almost immobile particles at the surface, and quickly came to the same conjecture than in the articles quoted above. However the complete cancellation of the radial velocity seemed excessive, and ROSE prediction on Re_c remained far from experimental findings. Therefore, this investigation was not pursued further. The advent of LDV and, as a consequence, the ability to acquire velocity profiles, motivated us to reconsider this boundary condition : simulations with zero radial velocity at the interface revealed changes on the base flow compared to previous simulations with the standard free slip condition, and the comparison with experimental velocity profile concluded that the new condition was not as incoherent as we once thought.

Frozen surface

New condition at the interface

As explained above, the first alternative to the free slip condition at the flow surface consisted in considering the extreme case of a completely "frozen" radial velocity component. Right now, the boundary condition that was used at the interface corresponds to equations (IV.7), (IV.8) and (IV.10). Where $\frac{\partial u_r}{\partial z}$=0 was imposed, we now set u_r=0. This is translated on the base flow of ROSE by a simple modification of the equation (V.5) of the boundary conditions at the interface. These boundary conditions become :

$$\omega = \frac{1}{r}\frac{\partial^2 \psi}{\partial z^2},\ \psi = 0,\ \Gamma = r^2. \tag{VIII.1}$$

Of course, impermeability of the interface is kept, and so is the hypothesis of a flat surface, so that u_z remains zero at the interface. The condition on u_θ does not evolve either, and therefore, no modification of the code is required on Γ. This new modelling of the interface condition will be referred as "Frozen surface" for more convenience.

G=1/14

In chapter II, we discussed about similarities in base flows computed with a frozen surface conditions or with a pollutant-based model that will be introduced later in this thesis (see chap. IX). It was also reported that with the frozen surface, Re_c drops to 10555, which represents a reduction of 38% compared to result with the free slip surface (Re_c=17006), but is still 151% larger than the upper bound of the experimental estimation of Re_c (Re_c=[3160 - 4230]). Despite this mismatch, the vorticity pattern computed using DNS revealed closer to experimental visualisations. Although purely qualitative, this resemblance was particularly convincing. In this section, more direct comparisons with free surface simulations and experiments are added, in order to follow step by step the progression from the free surface simulations to the more complex models presented in chapter IX.

Influence on the base flow

Experiments performed by Hirsa *et al.* ([39]) had revealed that a minor change in the surface condition can drastically modify the base flow. As done in section Mismatches beyond $\mathbf{Re_c}$, the base flow computation at Re=18620 was renewed, but with the frozen boundary condition. The profiles of U_θ and U_z from these new simulations (see fig. VIII.1b) were added in the former figures VI.11 and VI.13, respectively.

The first heavy transformation of the flow is the vanishing of the overshoot in U_θ at r=0.67, displayed in figure VIII.1a. Although the fit is not perfect for $r \in [0.65; 0.8]$, this damping increases the agreement between experiments and simulations carried out with the frozen surface condition, especially for $r > 0.8$. Experimental inaccuracies, such as misplacing the zero, may be responsible for the remaining discrepancies.Another major effect of this modification of the surface boundary condition is visible in figure VIII.1b : the radial length of the recirculation is reduced by approximately 53% in comparison to the free surface simulation. The location of the minimum value of U_z evolves from ≈ 0.7 to ≈ 0.85 which lowers the gap with experimental measurements from 17.6% to 1.2%. DNS profile of the mean flow shows an even better agreement with experimental data on this area.

The direct comparison of base flows computed with either free and frozen surfaces confirms previous observations. Figures VIII.2a and VIII.2b perfectly highlight differences

(a) u_θ in z=0.8G

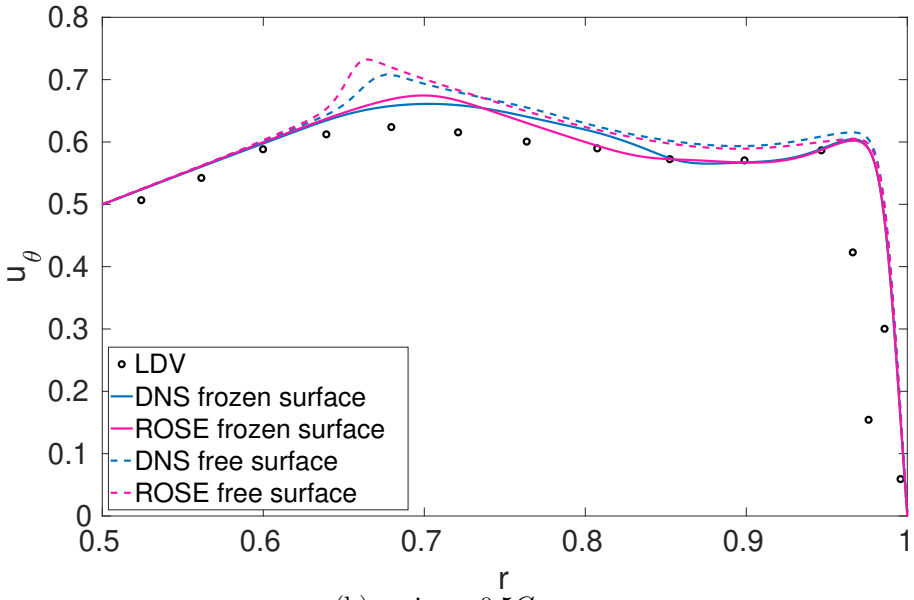

(b) u_z in z=0.5G

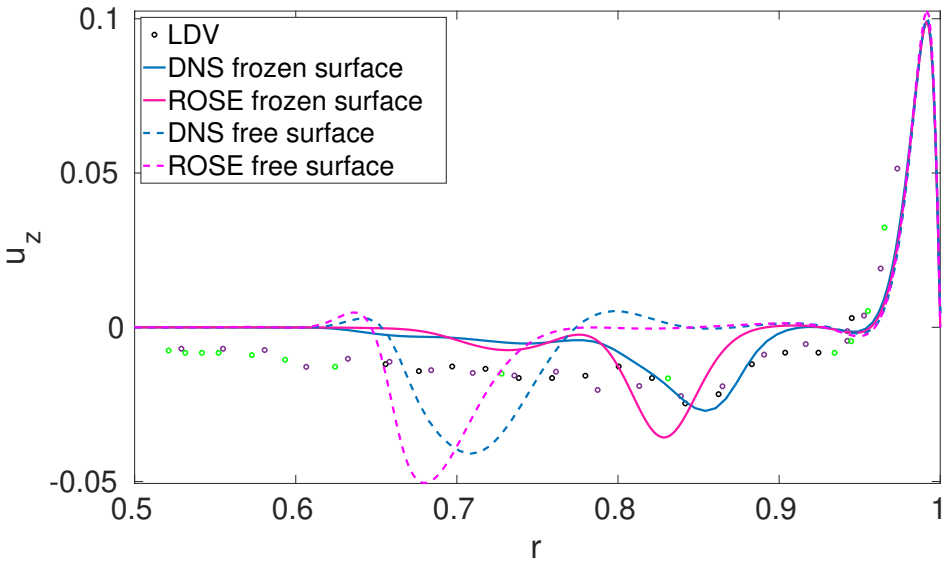

Figure VIII.1 – Comparison of velocity profiles : ROSE base flow, DNS mean flow(for both free and frozen condition) and LDV measurements, for G=1/14 and Re=18620.

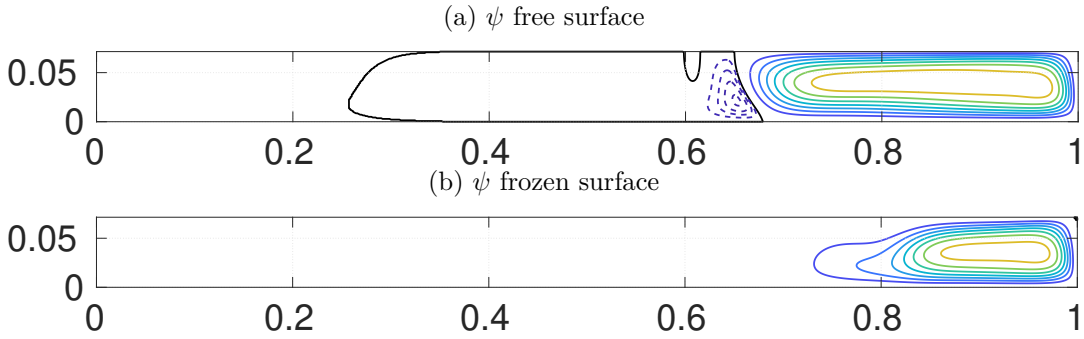

Figure VIII.2 – Comparison of the stream function $\psi(r,z)$ between free and frozen surface conditions, at Re = 18620 and G=1/14. Contours are the same for both figures. Negatives and positives contours use different scales to highlight the weak recirculation bubble. Negatives contour values (dashed): 4 equispaced levels in [ψ_{min} - ψ_{min}/5]. Positives contour values : (solid lines): 9 values equispaced levels in [ψ_{max}/10 - ψ_{max}]. Zero contour level (solid black lines). ψ_{min} = -8.1.10^{-5} and ψ_{max} = 2.3.10^{-3}.

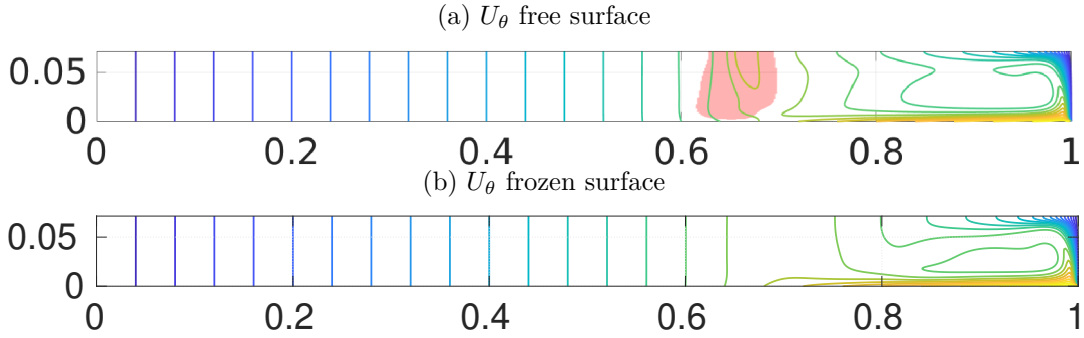

Figure VIII.3 – Comparison of the azimuthal velocity $U_\theta(r,z)$ between free and frozen surface conditions, at Re = 18620 and G=1/14. 21 equispaced levels in [0 - 1]. Translucent red patches represent overshoot areas, i.e locations where $U_\theta \geq 1.01\ r$.

of the secondary flow in the meridional plan, while figures VIII.3a and VIII.3b point out the absence of overshoot in U_θ.

Instability threshold

The effects of the frozen boundary condition are not limited to the base flow : the important drop observed for a wave number m=5 was already reminded above. The evolution of Re_c for m=4 was also investigated numerically. Indeed, instability thresholds for m=4 and m=5 were close for the free surface condition, and, as reported in chapter VI, this neighbourhood was also experimentally observed. Therefore, the same proximity in thresholds for m=4 and m=5 is expected with the frozen surface condition. Re_c and f for both modes and both boundary conditions are compared in table VIII.1.

The critical Reynolds number for m=4 follows an equivalent drop than for m=5 : it falls by 35%, from 17246 to 11152. The relative gap that separates m=4 and m=5 is

	free surface				frozen surface			
	m=4		m=5		m=4		m=5	
	hub	no hub	hub	no hub	hub	no hub	hub	no hub
Re_c	17536	17246	17019	17006	10217	11152	10486	10555
f	0.692	0.688	0.711	0.709	0.816	0.811	0.817	0.814

Table VIII.1 – Comparisons on Re_c and f for modes 4 and 5 for G=1/14, and both boundary condition. Influence of the hub is also inspected. The hub radius is 0.5. Meshes used are 351×51 and 701×101, with and without hub, respectively.

therefore wider for the frozen boundary condition with slightly less than 6% gap, when it was only 1.4% for the free surface. The drop in Re_c is followed by a small increase of the frequency f, that respectively gains 18% and 15% for m=4 and m=5. For this last wavenumber, the comparison with experimental value (f=0.764) does not evolve much : from 7.2% to 6.5%, compared to free and frozen surface conditions, respectively.

Table VIII.1 also contains results for computation done with a hub of $0.5R$. Many of our first simulations were done with a such hub, in a effort to limit the computational costs. Regarding the minor variations of Re_c and f, it could be easy to conclude that the presence of the hub has minor effects on the instability. However the under-evaluation of Re_c for the frozen surface leads to predict m=4 as the most unstable mode, instead of m=5. The hub influence is not the same, whether simulation is performed with the free or the frozen condition. In the first case, the hub tends to over-evaluate Re_c and f, but in the second case, the trend is not as clear : Re_c is lowered, but f is a bit higher. The maximum gap on Re_c is observed for m=4, in the frozen case, with 8.4% difference between simulations with and without hub. This is also the less favourable case for the frequency, with a 0.62% gap.

Following the same protocol than for the free surface condition, as explained in section V.2.4 (page 70), we cross-checked the value of Re_c with DNS computations. Note that in DNS, the change in the boundary condition is easily applied, as we simply impose $u_r = 0$, in $z = G$ for the frozen case.

Re	10200	10300
a	-0.0079264	-0.0058641

Table VIII.2 – Decay rates a of the most unstable mode (m=5) between t=$t_{impulse}$+1200 and $t_{impulse}$+2100, for Re=10200 and 10300, with the frozen boundary condition. For both cases, $t_{impulse} = 300$.

According to the slopes values reported in table VIII.2, Re_c is estimated at 10584, which represents a gap of only 0.27% compared to LSA prediction.

Instability pattern in numerics

In order to compare instability pattern with the free surface case, we performed a DNS run at Re=18620, without any restriction on θ, and therefore, no forcing nor filtering of the mode. Figure VIII.4 represents the axial vorticity at the surface at this Reynolds number.

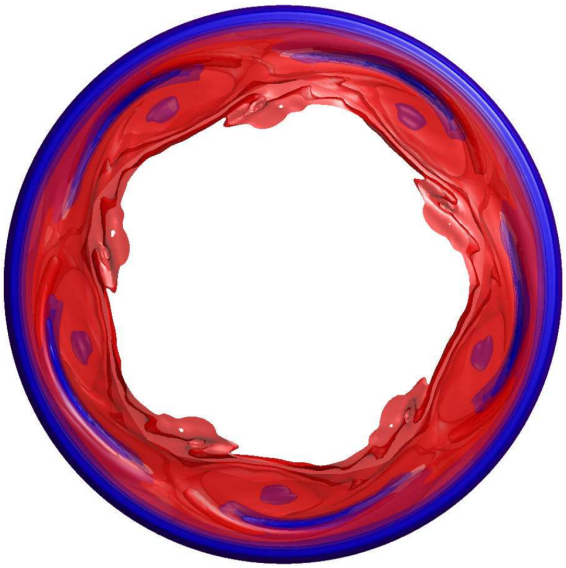

Figure VIII.4 – Axial vorticity pattern fort Re=18620 and G=1/14. Red areas correspond to $\omega_z > 0$, and blue areas to $\omega_z < 0$. Intensity of vorticity is translated by translucence of 5 isosurfaces between ω_z=-1.73 to 0 for negative values, and of 5 other isosurfaces for positives values of ω_z, between 0 to 2.44. This snapshot correspond to t=1200.

The wave number m=5 is perfectly visible in figure VIII.4, with a completely different face compared to the computed pattern for the free surface, that are shown in chapter II. With time series, the corresponding frequency was evaluated to f=0.809, i.e only 0.6% lower than predicted by ROSE prediction. Time series also present a simpler dynamics than in the free surface case : figure VIII.5 displays a purely sinusoidal signal, qualitatively closer to experimental data.

We previously observed in chapter VI that ROSE and DNS match nicely on vorticity pattern of fluctuations at the surface. For the frozen surface and close to Re_c, this agreement still occurs, as shown in figures VIII.6a and VIII.6b.

However, as soon as Re moves away too much from Re_c, ROSE does not seem to be able to reproduce the instability pattern. Figure VIII.7 illustrates differences in the vorticity pattern of fluctuations between ROSE and DNS, at Re=18620. These figures corresponds to the fluctuations part of the flow shown in figure VIII.4. Note that figures VIII.7b and VIII.7c computed with Sunfluidh at Re=18620 show a better agreement with the experiment than the simulations performed for a Reynolds number closer to

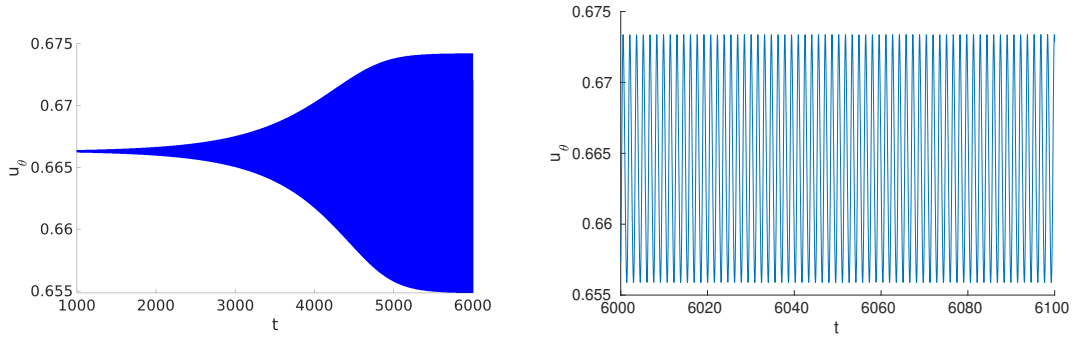

Figure VIII.5 – Temporal series of u_θ for G=1/14 and Re=10700. The right figure is a zoom of the last iteration of the code, between t=6000 to 6100. The probe is located at (0.68,0,0.5G).

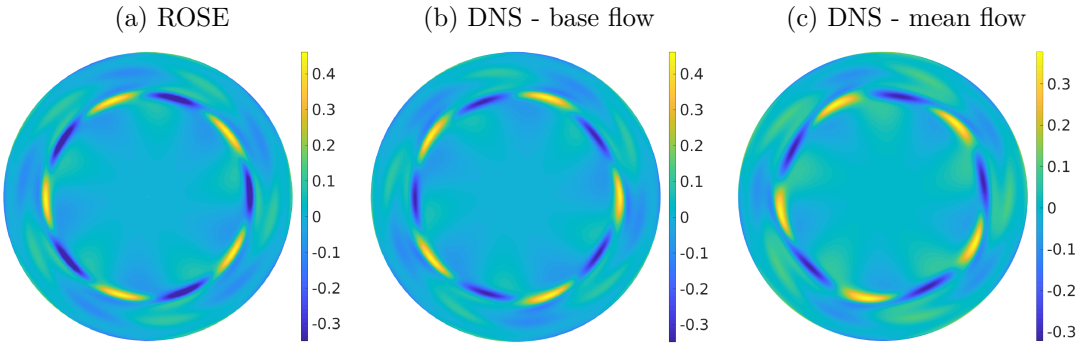

Figure VIII.6 – Vorticity pattern of fluctuations obtained with ROSE (left) and Sunfluidh (middle and right) in z=G, for G=1/14 and Re=10700. Figure VIII.6b correspond to fluctuations obtained by the subtraction of the 2D axisymmetric base flow, while figure VIII.6c was obtained by subtraction of the spatial averaged mean flow. The vorticity field from ROSE was normalized with respect to the maximum absolute value of vorticity of figure VIII.6b. The colorbar was also restricted to the same vorticity span.

Re_c, where a pentagon shape is only barely visible when the mean flow is subtracted (fig. VIII.6c). Indeed, none of the visualizations of the figure VIII.7 convincingly reproduces the patterns observed in the experiment.

Hysteresis in frozen surface simulations ?

Like we did in section VI.1.3, we performed a series of simulation using DNS, to check for the existence of hysteresis. Starting from an initial state for Re=18620, the value of Re is lowered to [10780,10192], by steps of 196. The five simulations are displayed in figure VIII.8.

We recall that for Re=18620 and a frozen surface, the velocity time series is purely sinusoidal, without the complicated dynamics observed for the free surface. For lower

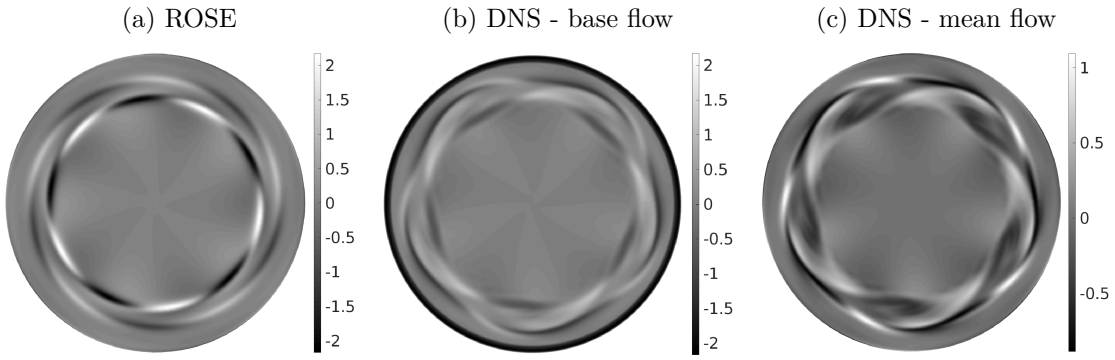

Figure VIII.7 – Vorticity pattern of fluctuations obtained with ROSE (left) and Sunfluidh (middle and right) in z=G, for G=1/14 and Re=18620. Pattern from ROSE was normalized with respect the absolute value of the minimum of vorticity obtained in the DNS with subtraction of the 2D axisymmetric base flow (middle). Right figure corresponds to the fluctuations observed from the subtraction of the spatially averaged mean flow.

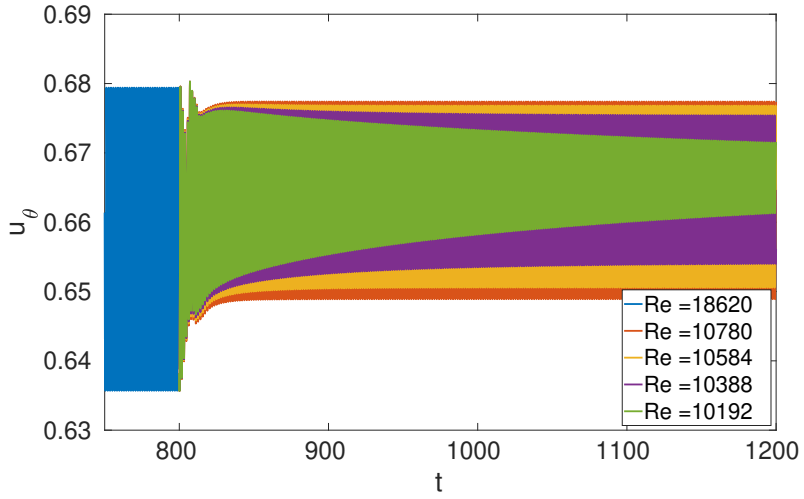

Figure VIII.8 – Numerical spin-down phases with a frozen surface, from Re=18620 to Re= [10780,10192], by steps of 196. The probe is located at (0.68,0,0.9G).

values of Re, the signals remain sinusoidal. Yet, as soon as $Re < Re_c$, the amplitude of the oscillations is decreasing in time. Re_c was estimated between 10555 and 10584, according to ROSE and Sunfluidh predictions, respectively. Indeed, the decrease of the amplitude is clearly visible on the green curve (Re=10192). It is also existent for the purple curve (Re=10388), although less visible due to the small decay rate in the vicinity of Re_c. Still, this vanishing of the instability for $Re > Re_c$ in a spin-down phase is the evidence of the non-existence of hysteresis in simulations with a frozen surface.

G=0.25

The choice for the frozen condition in the case of G=1/14 was globally positive, although quantitative gaps with experiments remained. The application of this condition to G=0.25 is also expected to have a positive influence on numerical results and therefore, to get closer to experiments. In particular, the switching of the most unstable mode observed with the hub for G=1/14 lets expect a possible changeover from m=2 to m=3 for G=0.25.

Instability threshold

In section VI.3, we saw that the most unstable mode predicted by ROSE has got an azimuthal wave number m=2, while in experiments, the mode m=3 growth first. Using the same grid as before (401×101), new ROSE computations were performed to determine Re_c with the frozen condition.

	free surface		frozen surface	
	m=2	m=3	m=2	m=3
Re_c	3481	4691	4516	5320

Table VIII.3 – Evolution of Re_c between free and frozen surface boundary conditions for azimuthal numbers m=2 and m=3, in the case G=0.25.

The results gathered in table VIII.3 show a completely unexpected behaviour of the instability threshold : while the frozen condition lowered Re_c for G=1/14, here, for G=0.25, it pushes Re_c even higher, increasing relative difference with the experimental value of Re_c (around 2000). The absolute difference between m=2 and m=3 remains almost constant : 1210 for the free surface, and 1204 for the frozen surface. No mode switching is present, and the most unstable one, according to linear stability analysis, is still m=2.

Base flow

The evolution of the base flow for G=0.25 is similar to the case G=1/14 : application of the frozen condition cancels the overshoot in u_θ, and reduces the length of the recirculation.

However these modifications, visible in figure VIII.9, seem less dramatic than for G=1/14. It also means that no connection exists between the vanishing of the overshoot

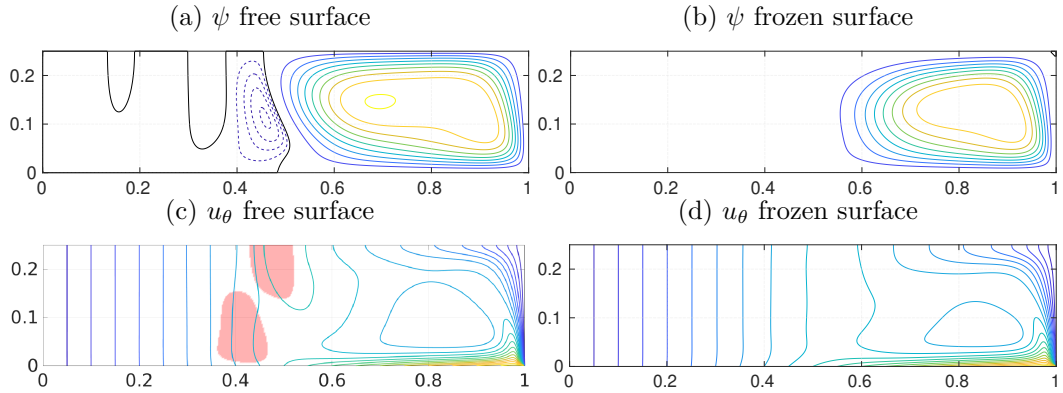

Figure VIII.9 – Comparison of ψ (top) and u_θ (bottom) between the free surface and the frozen surface. G=0.25 and Re=3000. Red patches correspond to overshoot areas, *i.e.* locations where $u_\theta > r\omega$. ψ isovalues are linearly spaced in three subspaces : 5 isovalues between ψ_{min} and $\frac{\psi_{min}}{5}$, 10 isovalues between $\frac{\psi_{max}}{10}$ and ψ_{max}, and the black isocontour for ψ=0. ψ_{min}=-2.32×10^{-4} and ψ_{max}=9.52×10^{-3}. For u_θ, 20 isovalues are linearly spaced between 0 and 1.

and the Re_c drop.

Despite the lack of agreement on Re_c and m, the base flow computed with the frozen surface condition is revealed to be closer to experimental measurements. Although this agreement is not perfect on u_θ (figure VIII.10a), for $r \in$[0.7,1], the behaviour of u_θ is caught more accurately in the frozen surface simulation. As for G=1/14, the region where the velocity is maximum (for radius around 0.5) is still over-evaluated in simulations, although the overshoot is damped. The agreement is much more convincing on u_z (figure VIII.10b), since the profile corresponding to the frozen surface condition follows the experimental data. The location of the minimum of u_z indeed matches with the experimental value around r=0.7.

As for G=1/14, the effect of the frozen surface boundary condition on the base flow are quite positive. Yet, the DNS computation performed with this boundary condition for Re=5545 gives quite similar vorticity pattern (fig. VIII.11) than the previous simulation that was performed with the free surface boundary condition (fig. VI.25b, page 96). Thus, we can not claim here much of an improvement.

Higher aspect ratios

In the three others considered aspect ratios, G=1, G=1.5 and G=2, experiments and numerical simulations with the free surface boundary condition were pretty close. Only G=1.5 was quite problematic, since no experimental frequencies matched numerical prediction. According to previous sections, very small variations of the frequency between free and frozen surface models do not let expect an amelioration of this issue. Still, comparisons for the three aspect ratios ≥ 1 were performed : if agreements are lost with the frozen surface condition, this would definitely discredit this model.

(a) u_θ in z=0.8G

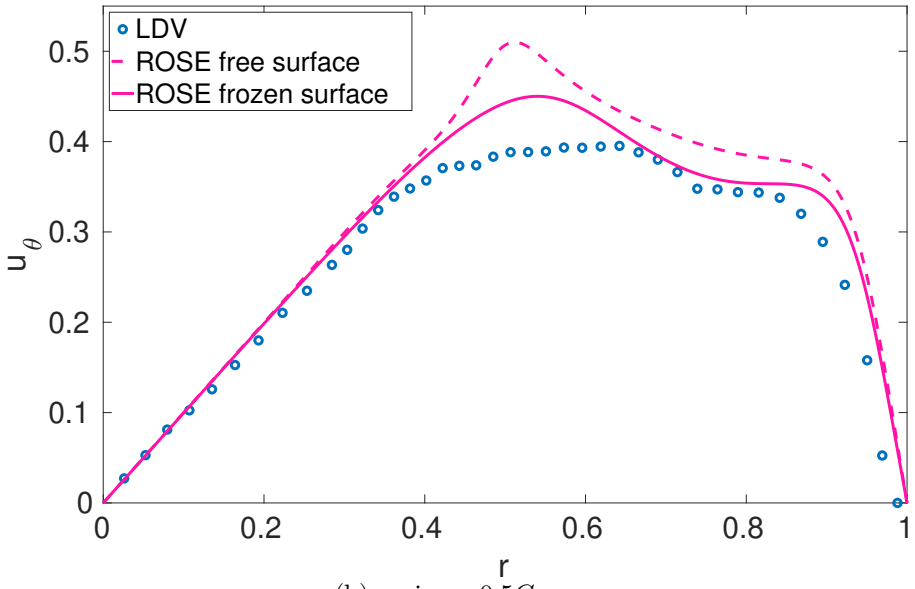

(b) u_z in z=0.5G

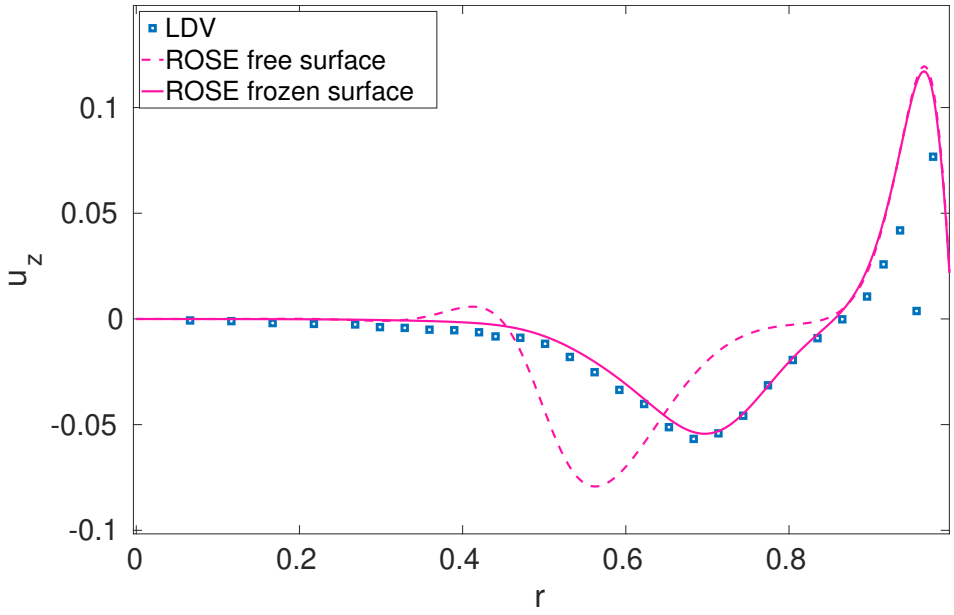

Figure VIII.10 – Comparison of velocity profiles : ROSE base flow and LDV measurements, for G=0.25 and Re=1895.

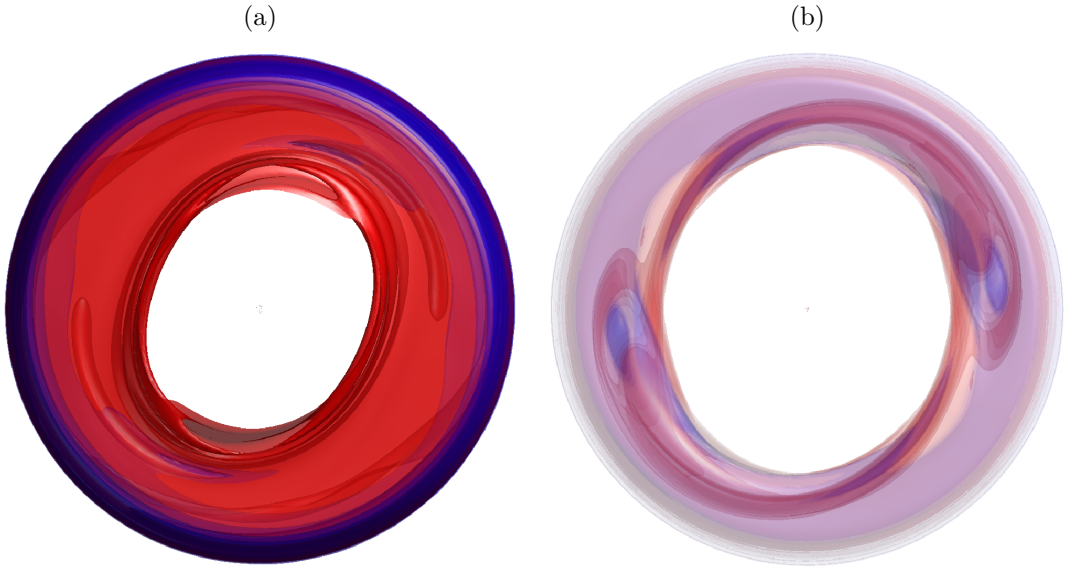

Figure VIII.11 – Axial vorticity pattern for G=0.25 and Re=5545. Figure on the left is composed of 10 isosurfaces : 5 red surfaces equally spaced in [0,2.16], and 5 blue surfaces, equally spaced in [-1.07,0]. Bounds corresponds to $\omega_{z\ max}$ and $\omega_{z\ min}$. Tuning these scales allows to see spots of negative vorticity ($\omega_z \in$ [-0.06,0]) in the figure on the right.

G=1

For G=1, only U_z profiles for $Re < Re_c$ were confronted. Since below Re_c, base flow and mean flow are identical, only computed profiles using ROSE are compared in the figure VIII.12.

A quick glance on the comparison of U_z profiles suggests that the modification of the boundary condition at the surface produces only minor changes in the base flow. This is confirmed by the comparison of ψ and u_θ in figure VIII.13. On the stream function isovalues (fig. VIII.13a), only changes are a small reduction of the size of the bubble attached to the axis, and a tiny vertical crush of the main recirculation in the meridional plan. This last evolution is not surprising, since u_r=0 at the surface, and that such phenomenon was observed for $G \leq$0.25. The modification of the isovalues of u_θ are also limited. Note that no overshoot is present, even with the free surface condition. G=1 seems almost insensitive to variations of the surface boundary condition.

G=1.5

For G=1.5, experiments and numerics were compared slightly above Re_c, at Re=2356. Unfortunately, it was not expected that this Re would be below the critical Reynolds number in computation using the frozen surface condition. Indeed, the most unstable mode is m=4 at Re_c=2375. We remind that, with the free surface condition, the most unstable mode was m=1, at Re_c=2150. The effects of the modification of the boundary condition at the surface on the five first modes are given in table VIII.4.

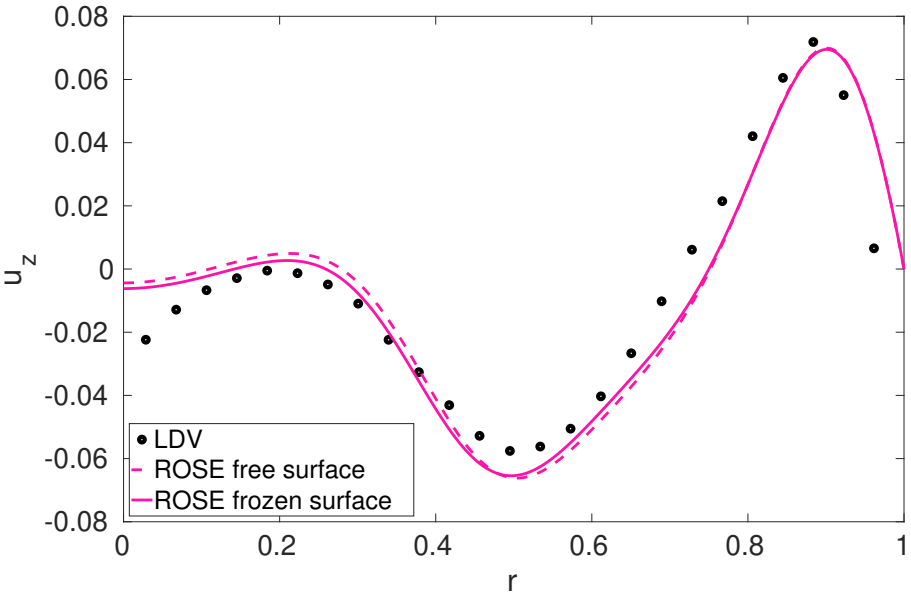

Figure VIII.12 – Comparison of experimental data and ROSE computed u_z profile, in z=0.5G, for G=1 and Re=1120.

m	0	1	2	3	4
Re_c	2909	2802	2882	2911	2375
f	0.342	-0.144	0.294	0.312	0.211

Table VIII.4 – Re_c and f of modes 0 to 5 for G=1.5, with the frozen surface condition. The values for the free surface condition are given in table VI.9, page 100.

The DNS performed at Re=2356 confirms that the flow is not yet unstable : despite the introduction of a pulse at t=400, oscillations in velocity time series are decaying (see .fig VIII.14). This decay is very slow which confirms that although Re_c is larger than 2356, it is probably very close to this value, which is in good agreement with ROSE prediction of Re_c=2375. Moreover, the vorticity of fluctuations at t=7200 shows that the most unstable mode, *i.e.* the one that decays the last, is m=4 (.fig VIII.15), with a pseudo-frequency f=0.210 on the time span Δt=[7600-7900], in perfect agreement with ROSE predictions reported in table VIII.4.

In our experiments at Re=2356, secondary peaks are visible at $f \times m$=0.838. We recall that the notation $f \times m$ is used since the wavenumbers are unknown in experiments at G=1.5, and therefore, frequencies are not normalized regarding the mode. However, if m=4, this frequency corresponds to f=0.209 which nicely matches the reported frequency for such wave number in table VIII.4. However in the Fourier transforms obtained from experimental time series, the peak corresponding to m=4 never appeared predominant.

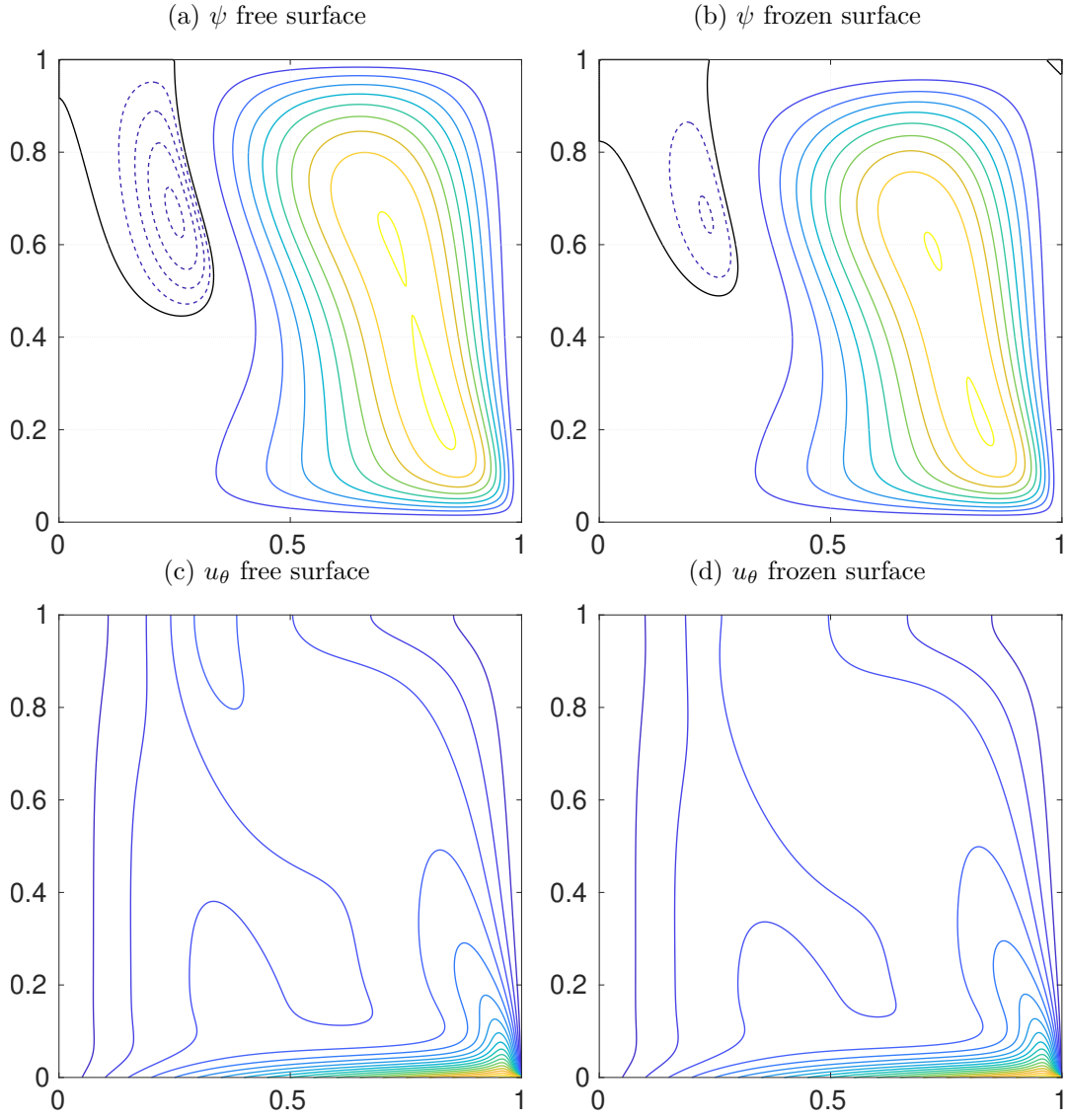

Figure VIII.13 – Comparison of ψ (top) and u_θ (bottom) between the free surface and the frozen surface. G=1 and Re=1120. ψ isovalues are linearly spaced in three groups : 5 isovalues between ψ_{min} and 0, and 9 isovalues between $\frac{\psi_{max}}{10}$ and ψ_{max}. ψ_{min}=-2.3×10^{-4} and ψ_{max}=9.5×10^{-3}. The last subspace is represented by the plain black line, for ψ=0. For u_θ, 21 isovalues are linearly spaced between 0 and 1. Simulations were performed on a 301×301 mesh grid.

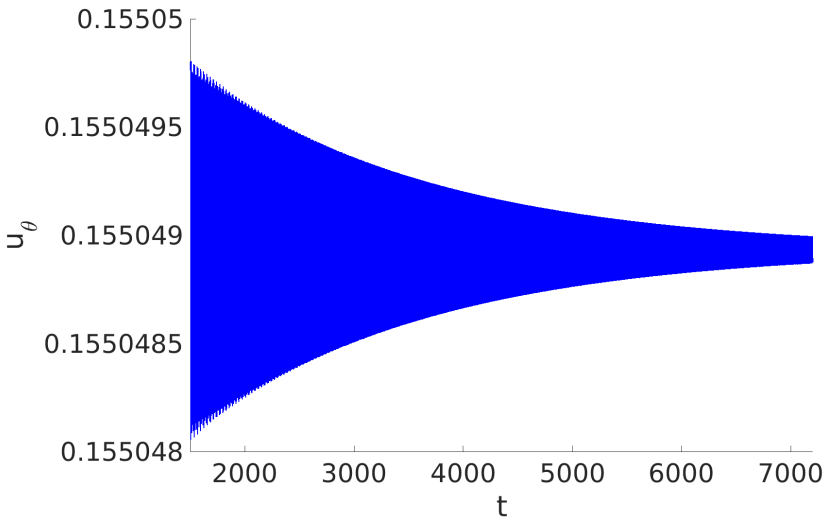

Figure VIII.14 – Decay of the oscillations in a time series of u_θ, for Re=2356 and G=1.5. The probe is located at (0.5,0,0.9G).

Figure VIII.15 shows the isosurfaces of the axial vorticity of the decaying mode m=4. This can be compared to figure VI.31 of the mode m=1 predicted as the most unstable in the free surface case. During experiments, injection of ink at the surface was not efficient to visualize pattern and therefore, no comparison with figure VIII.15 is possible. Note that the frequency of the mode m=1 with the free surface condition is very low. One can suggest that the mixing time of ink is shorter than the revolution time of m=1 and therefore, no visualisation is possible with ink although the mode could exist.

G=2

Applying the frozen surface condition to G=2 has almost no impact on figures. The most unstable mode predicted by ROSE is still m=4, like previously reported for the free surface condition. Re_c and f also present only moderate evolutions. Indeed, they respectively move from 1914 to 1987, and from 0.157 to 0.160. Changes in the axial vorticity pattern are difficult to quantify. However a square shape is drawn by low vorticity isosurface (fig. VIII.16). This square is compatible with the pattern experimentally visualized for m=4 and G=1/14 in figure VI.16. Unfortunately, we have no clear visualisation of the pattern for G=2, except blurred DPIV snapshots from [35] and [37] that do not allow for discrimination between numerical results obtained with the free and the frozen surface conditions.

As shown previously for G=1, we can only conclude that larger aspect ratios are less sensitive to the condition applied at the surface.

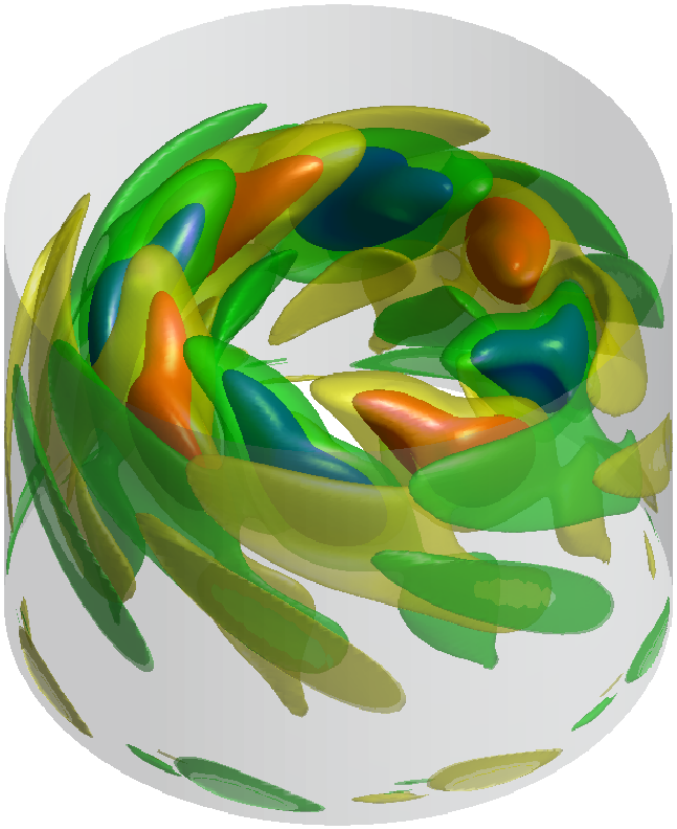

Figure VIII.15 – Isosurfaces of axial vorticity of the perturbations at t=7200 and Re=2356, for G=1.5. Red and blue patches correspond to ω=$\pm$2.2$\times10^{-6}$, while yellow and green patches correspond to ω=$\pm$8.0$\times10^{-7}$. The vorticity of the perturbations is very small, since the flow fields tend to steadiness. Still, the mode m=4 is clearly visible.

Conclusion on the frozen surface model

Changing the surface boundary condition from the classical free-slip model to another one with a frozen radial velocity brings interesting results for G=1/14 : Re_c drops by approximately 35% for both modes m=4 and 5. However, it remains way above the experimental Re_c. Despite this mismatch on figures, numerically computed axial vorticity pattern shows an excellent similarity with experimental observations. In addition, computed velocity profiles show no more trace of overshoot and are closer to profiles extracted from LDV measurements.

Unfortunately, good trends obtained on the Reynols number for G=1/14 were not reproduced for G=0.25 : the new boundary conditions actually pushed Re_c further, for both mode m=2 and 3, thus increasing the gap with experiments. The most unstable mode remains unchanged : m=2 is still the first one to grow, as for the free surface condition. Obviously, such a simplistic model as the frozen surface condition cannot fill the gap between numerics and experiments.

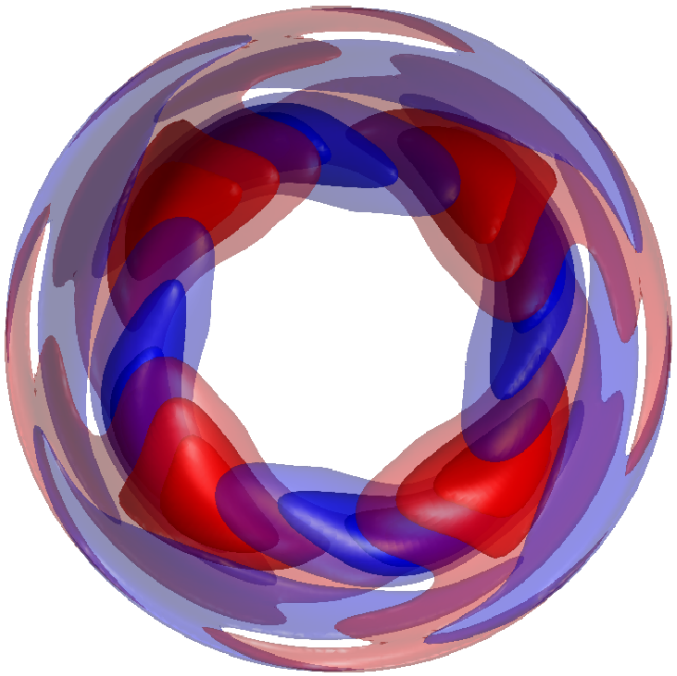

Figure VIII.16 – Isosurface of axial vorticity for perturbations at t=4000, Re=2100, and for G=2. Red and blue patches respectively correspond positive and negatives isosurfaces of vorticity. Both are divided in five isosurfaces between 0 (fully translucent) to ±0.1455 (fully opaque). The square shape of m=4 is visible through the translucent blue patches on the outer region.

On higher aspect ratios ($G > 1$), the influence of the new boundary condition remains limited : the base flow is almost unchanged, and the instability pattern do not evolve much. The only noticeable difference is the most unstable mode for G=1.5, that swaps from 1 to 4. However, agreement with experiments at this aspect ratio is limited by the experimental encountered difficulties, especially the lack of visualization of the unstable mode.

Hybrid modelling

Robin condition at the interface

Although it was evident that the frozen surface condition was not the solution to mismatches, it convinced us to explore more deeply the evolution of the flow and its instability regarding the surface condition. The first limit to the frozen condition had already made us give up the hypothesis of mechanical vibrations. However, the radial velocity forced to zero at the surface is too unrealistic to efficiently represent the flow in our experiment. Indeed, at the exception of some experiments with Kalliroscope, we never observed u_r^S=0 in experiments. However, we suggested that u_r^S could be curb by a front of pollutant that may exist where the recirculation in the meridional plan dives from the surface to the disc. Thus, we needed to create a new boundary condition that would not completely slow down u_r^S, but where we could tune this braking using one parameter only. The idea was then to build this boundary condition as an interpolation function between the free and the frozen conditions, and to study the influence of this parameter on the flow. For this part, we only used ROSE and thus, all equations and results are related to this code. We remind that the boundary conditions for the free surface were $\frac{\partial u_r}{\partial z} = \omega_\theta = 0$ (eq.(V.5)), while for the frozen surface, we simply had $u_r = 0$ which leads to eq.(VIII.1) in ROSE. From these two conditions, we can write :

$$(1-\kappa)\omega_\theta + \kappa u_r = 0.$$

Where κ is an ad hoc tuning parameter, assumed uniform on the whole surface. Since $\omega_\theta = \frac{\partial u_r}{\partial z} - \frac{\partial u_z}{\partial r}$ and u_z=0 at the surface, this leads to :

$$(1-\kappa)\frac{\partial u_r}{\partial z} + \kappa u_r = 0, \tag{VIII.2}$$

which is a Robin condition on u_r at the surface. In ROSE, this last condition is easy to apply to the perturbations. However, the base flow is computed in (ω,ψ,Γ) variables. In order to keep the second order accuracy on the spatial discretization, u_r is expressed using the relation between u_r and $\partial\psi/\partial z$:

$$u_r = \frac{1}{r}\frac{\partial \psi}{\partial z},$$

the link between ω_θ and the second derivative of ψ at the surface :

$$\omega_\theta = \frac{\partial u_r}{\partial z} = \frac{1}{r}\frac{\partial^2 \psi}{\partial z^2},$$

and the Taylor expansion at the second order of ψ :

$$\psi(z-\delta_z) = \psi(z) - \delta_z\frac{\partial \psi}{\partial z} + \frac{\delta_z^2}{2}\frac{\partial^2 \psi}{\partial z^2} + o(\delta z^3),$$

where δ_z is the vertical step of the mesh. Now, $\partial\psi/\partial z$ can be expressed as a function of ψ and ω_θ :

$$\frac{\partial \psi}{\partial z} = \frac{1}{\delta_z}\left(\psi(z) - \psi(z-\delta_z)\right) + \frac{\delta_z}{2} r\omega_\theta$$

Finally, considering that in z=G, ψ=0, the discretized condition for the base flow is :

$$(1-\kappa)\omega_\theta + \kappa\left(\frac{\delta_z}{2}\omega_\theta - \frac{1}{r\delta_z}\psi(G-\delta_z)\right) = 0$$

With equation (VIII.2), we see that for κ=0, the boundary condition is the same as the free surface, while if κ=1, the boundary condition corresponds to the frozen surface. We checked the values of critical Reynolds number in both cases, for m=5, in order to validate our code. The results are reported in table VIII.5.

	ROSE	ROSE hybrid	ROSE hybrid (hub)
free surface (κ=0)	17006	17006	17082
frozen surface (κ=1)	10555	10555	10465

Table VIII.5 – Comparison of Re_c values of m=5, for G=1/14, and the three variants of ROSE. The hub radius is 0.5, and the mesh size for this case 351×101. Other cases use the standard 701×101 mesh. The presence of the hub is discussed at the end of the section.

The results are very consistent with former ROSE computations with free and frozen surface conditions.

Parametric study on G=1/14

Now that we are able to obtain the same thresholds for the two limit cases of κ, we varied κ to see how Re_c evolves between these extrema. The simulations were done for three modes, from m=3 to m=5.

The first noticeable point is that the evolution of Re_c regarding κ is not the gentle linear slope that could have been expected. On the left side of figure VIII.17, the increase of κ is followed by an increase of Re_c (blue points). But after a certain value of κ, the curves show a dramatic variation of the slope, resulting of an impressive drop of Re_c. If we focus on m=5, this brutal alteration occurs for $\kappa \approx$0.79, and can be interpreted owing to figure VIII.18. Here, we can observe a discontinuity in the frequency of the mode, regarding κ. This means, although azimuthal wave number is still m=5, that the most unstable mode is a second unstable branch (pink points), and that a point close to $\kappa \approx$0.79, Re_c=26070 is actually a point of codimension 2. This point exists when, for given parameters, two eigenvalues become unstable in the same time.

For m=4, the point of codimension two is not as marked as for m=5 : the jump in frequencies in figure VIII.18 corresponds to κ=0.84, for which the slope of Re_c seems almost continuous in figure VIII.17. The drop of Re_c only happens for κ=0.88. The case m=3 also displays the same drop, but it occurs for κ between 0.95 and 1. No further investigation was performed in order to locate the point of codimension 2 of the mode m=3 more precisely.

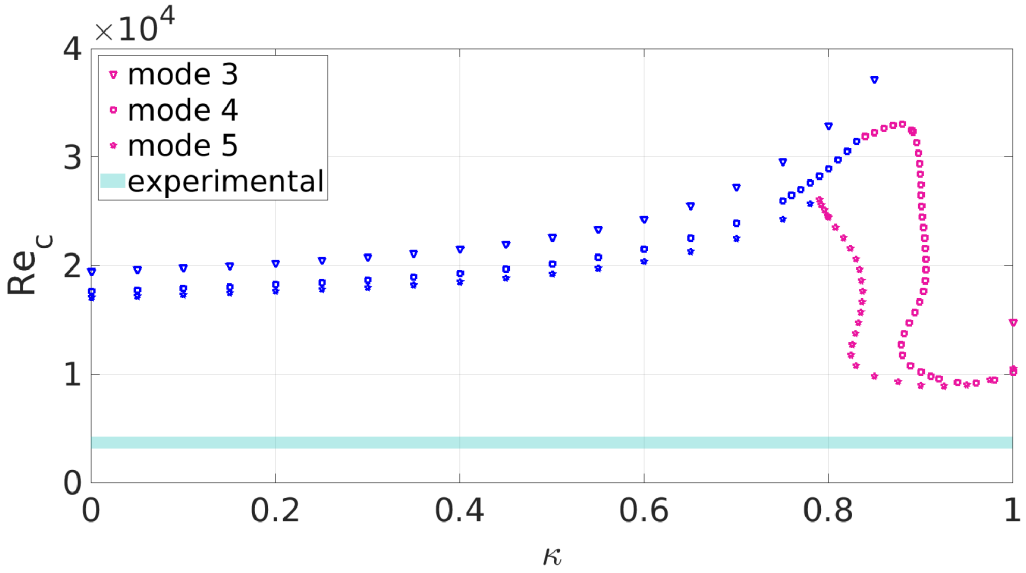

Figure VIII.17 – Neutral curves for m=3 to 5. The variation of color indicates a jump between two unstable branches with a common value of m. The blue stripe corresponds to the experimental values of Re_c.

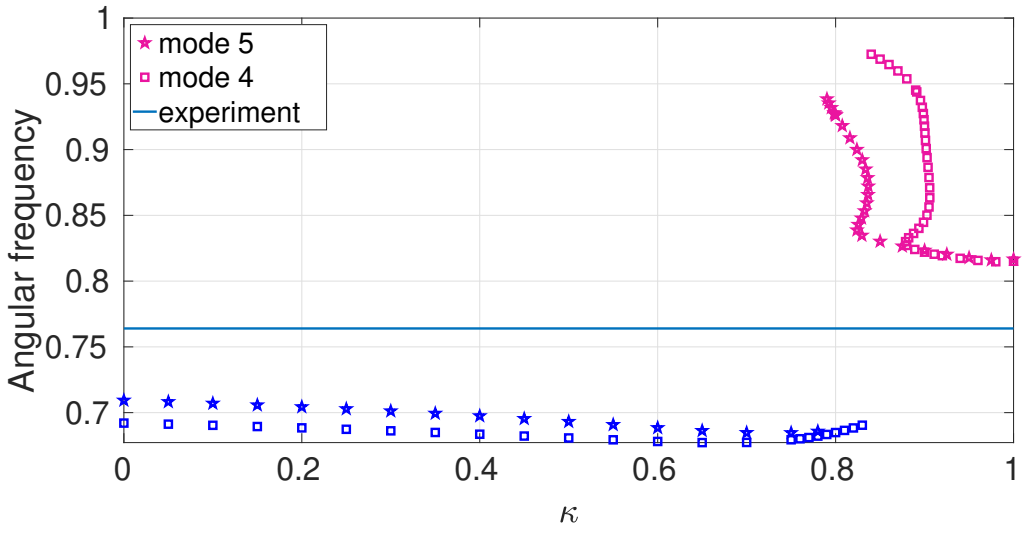

Figure VIII.18 – Frequencies for m=4 to 5. The variation of color indicates a jump between two unstable branches with a common value of m. The blue line corresponds to the experimental value obtained using LDV.

The second important point concerns the supposed most "favourable" pair of parameters for which the gap with experimental value of Re_c is smallest, Re_c=8868 and κ=0.925 : although it matches the most unstable mode detected in experiments, this Re_c value is still 108.6% larger than the experimental one. The frequency does not help much to determine which branch corresponds to experiments, as the experimentally measured frequency has almost the same gap with frequencies for κ=0 and κ=1 (respectively 7.2% and 6.9%). The gap on f for κ=0.925 is 7.4%. Any experimental imperfection, or measurement inaccuracy can easily justify a mistake of 0.5%. However, from section Instability pattern at Re_c and Instability pattern in numerics, the visual aspects of vorticity pattern at the surface are known for both branches. It was already demonstrated that the frozen surface (κ=1) shares better qualitative visual with experiments than the free surface (κ=0). Therefore, one expects the pink branch to be more representative of the instability observed in experiments than the blue branch.

Evolution of the base flow regarding κ

Although no couple of parameters seems to provide a close solution to experiments, we still focus on the evolution of the base flow regarding κ. Especially, we were interested in the length of the recirculation for κ=0.925. We see in figure VIII.19 that the minimum value of u_z for κ=0.925 is located in r=0.806. We remind that in experiments, minimum value of u_z is estimated close to r=0.85. The case κ=1 - equivalent to the frozen surface - remains the closer to experiments.

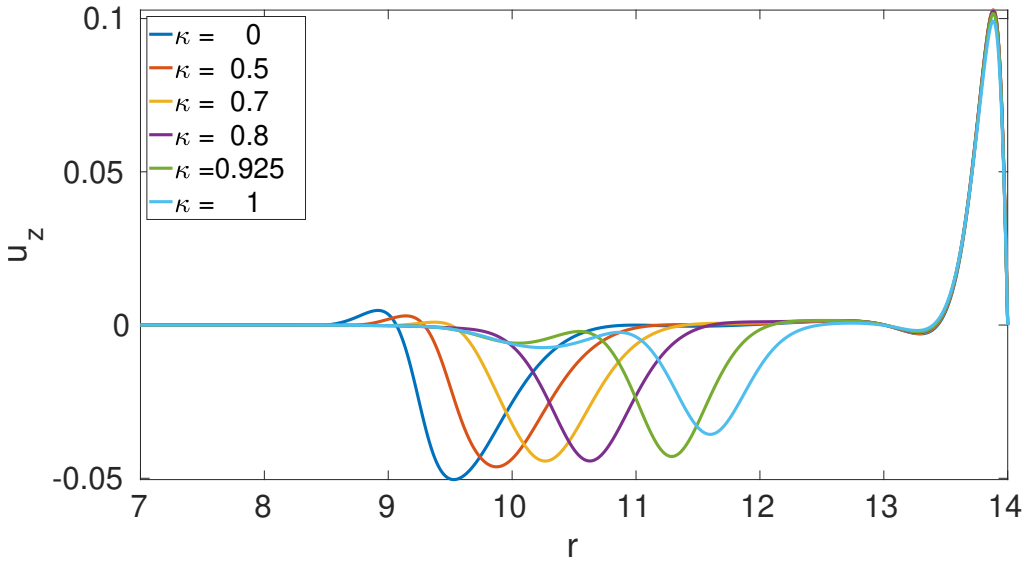

Figure VIII.19 – u_z profiles for various values of κ, in z=0.5G, at Re=18620 and G=1/14.

κ also has an effect on the overshoot of u_θ. In figure VIII.19, we clearly see a monotonic damping of the overshoot with the increase of κ. Finally, this overshoot completely vanishes for κ between 0.7 and 0.8, which corresponds to the jump of the unstable branch. Note that u_θ profiles for κ=0.925 and κ=1 are almost perfectly merged.

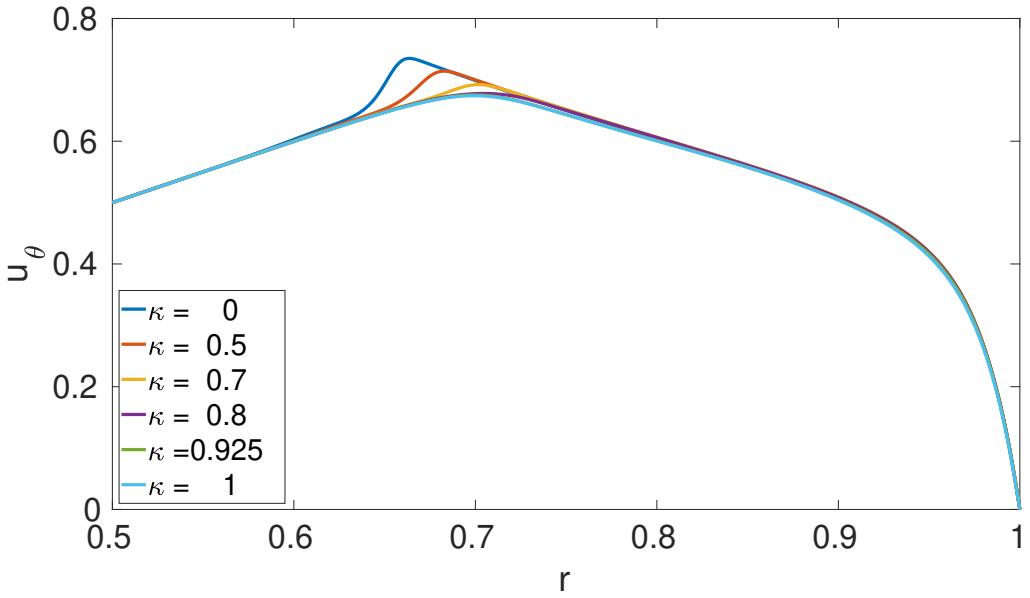

Figure VIII.20 – u_θ profiles for various values of κ, in z=0.5G, at Re=18620 and G=1/14.

G=0.25

As the actual behaviour of Re_c with respect to κ was unexpected, a similar parametric study was performed for G=0.25, on a 401×101 grid. An equivalent drop of Re_c, followed by an ascending slope could explain results for the frozen surface condition, while allowing the existence of a most favourable case for an intermediate value of κ. However, this time, only a soft and almost monotonic increase of Re_c regarding κ is observed, as shown in figure VIII.21.

The tiny decrease of Re_c for m=3, for κ between 0.95 and 1 seems to share the behaviour of the same mode for G=1/14. Thus, one can think that the jump of unstable branch occurs only for m >2. But frequencies of the modes shows no discontinuities (see figure VIII.22), and a closer look at eigenvalues for m=3 and κ=[0.9,1] confirms there is no second unstable branch (see fig. VIII.23).

While G=1/14 brings new elements for each new model of surface condition, G=0.25 keeps being enigmatic.

G=2

We previously saw that, for this aspect ratio, experiments and numerics match pretty well, whether free or frozen conditions were used. The application of the Robin condition to G=2 is therefore not performed for the sake of getting a better agreement, but to check if a jump of unstable branch is also present for such aspect ratio. The grid used is 201×401.

Figures VIII.24a and VIII.24b show evolutions of Re_c and f respectively. Both show

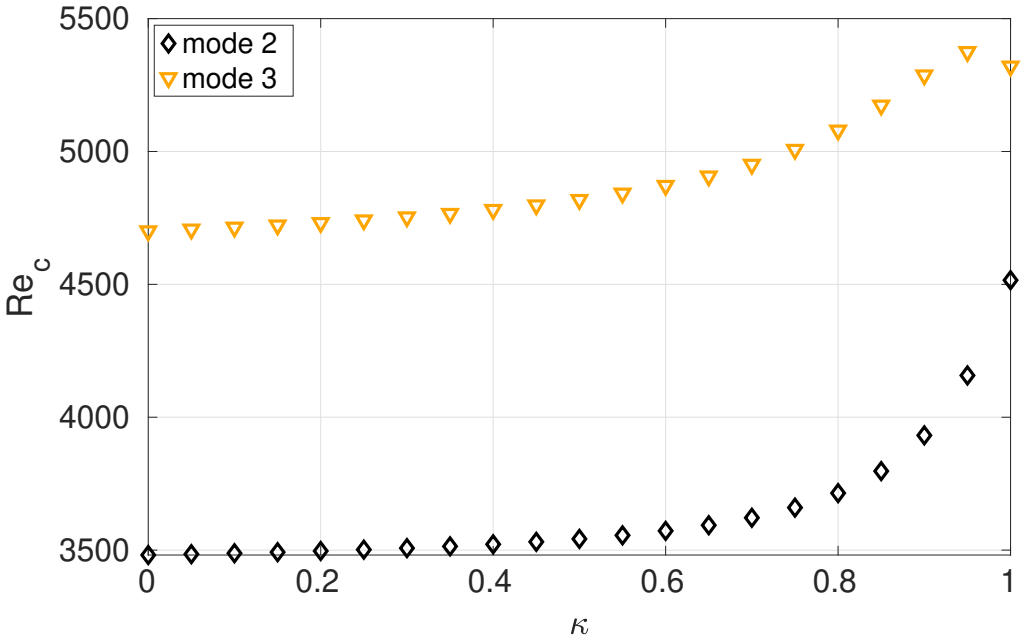

Figure VIII.21 – Neutral curves for m=2 and 3, G=0.25.

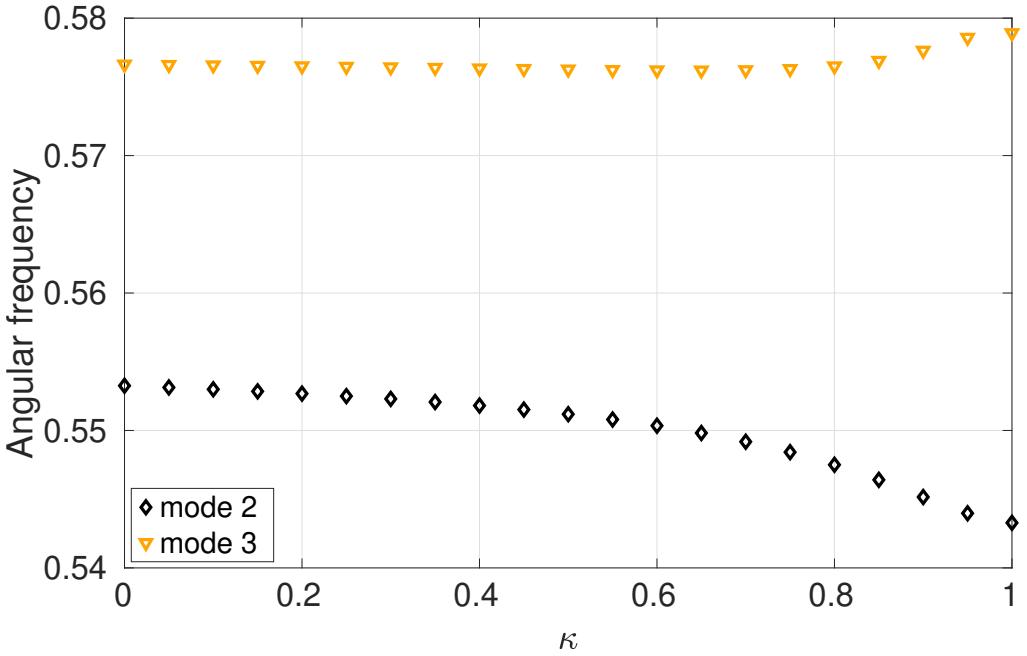

Figure VIII.22 – Frequencies of m=2 and 3 with respect to κ for G=0.25.

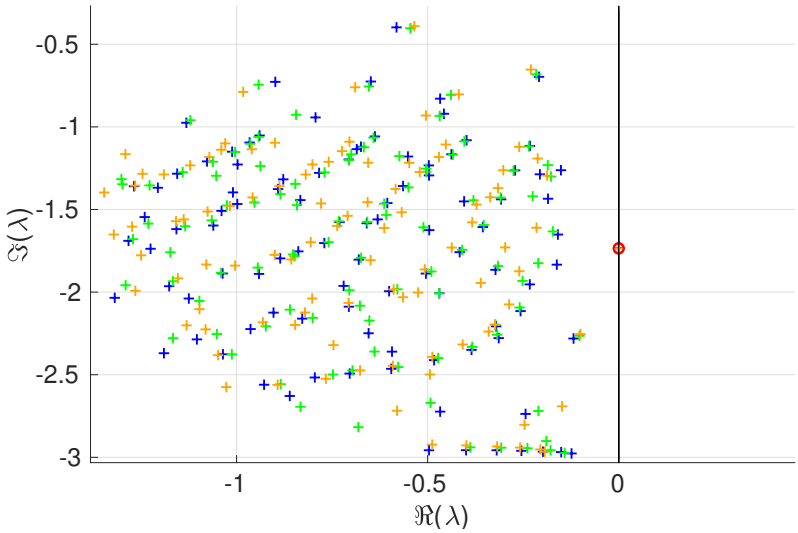

Figure VIII.23 – Evolution of eigenvalues of the mode m=3, for G=0.25 and Re=Re_c. Three values of κ are superposed : 0.9 in blue, 0.95 in green, and 1 in orange. The red spot circles the most unstable value for the three cases.

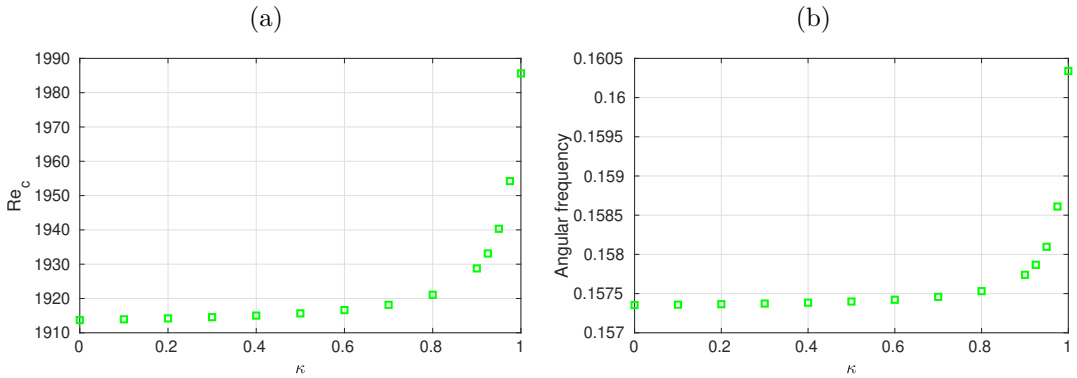

Figure VIII.24 – Neutral curve (VIII.24a) and evolution of frequency (VIII.24b) regarding κ for m=4 and G=2.

an exponential-like increase of their respective slopes. However, their variations are very restricted : Re_c evolves less than 4%, while variation of f is only 2%. Previous observations of small differences in vorticity pattern between the free surface (κ=0) and the frozen surface (κ=1) conditions, led us believe in the existence of a second unstable branch. However this parametric study denies this possibility.

Conclusion on the Robin condition

The hybrid model, initially built for a better understanding of the evolution of the flow between free and frozen conditions, revealed a much more complex transition than expected. It highlighted the existence of a second unstable branch for large value of κ, which explains the difference in axial vorticity patterns at the surface. However, no value of κ allowed for significant progress in the reduction of the discrepancy with experimental

Re_c and f, and the frozen surface still appears to be most "favourable" case.

Note that the computations for G=1/14 where done with a hub : it is only after that all the simulations required for the neutral curve VIII.17 were performed that the influence of the hub was tested on an other mode than m=5, and that we realized that it was responsible for the swap of the most unstable mode. However, as the Robin condition was not convincing, and that simulations without hub would obviously not lower Re_c, it was deemed necessary to correct this part. According to results in table VIII.1, we can estimate that the only probable effect would be a small shift of Re_c and f values, which would have lead to a slight vertical distortion of curves in figures VIII.17 and VIII.18.

Although it was learnt from smallest aspect ratios that the Robin condition was not representative of the real surface, the parametric study was still performed for G=2. It confirms the almost stable behaviour of Re_c and f for a given mode, whatever the condition at the surface, and the absence of another unstable branch. This explains that the agreement between numerics and experiments is easier of obtain for higher aspect ratios.

Chapter IX

Surface tension gradient as a boundary condition

The mismatches reported in chapter VI do not seem to have a connection with displacements of the rotating disc, but appear to be partially cancelled by the application of the raw frozen surface condition in chapter VIII. The results are convincing enough to consider that simulations with a free slip condition are not representative of the flow in our laboratory experiments. However, the simulations that show the best agreement with experiments were performed with the frozen surface condition, which can hardly be experimentally justified... The relative failure of the Robin condition to find an intermediate value of κ that would solve this paradox contrasts with the discovery of the second unstable branch, that exists even for non completely frozen surface. This nuance is a tenuous hope for a surface boundary condition that could be compatible with experimental observations of the surface, and that would give rise to the right unstable branch. Therefore the exploration of the influence on the flow of the condition at the surface was pursued with a more complex model. Considering that the surface tension varies with the random deposition of ambient air pollution, a convection diffusion equation is used in order modelize the concentration of these pollutants at the interface. However, the difficulty was to close the model with a link between unknown concentrations of pollutants and the velocity field. The sparkle came from the article [41], where the authors numerically reproduced the experience in [38]. There, an insoluble surfactant was voluntarily added onto the surface. This surfactant was clearly identified, and its concentration carefully controlled. More details on theses articles are given below.

In our case, we have no clue of the pollution type, nor its concentration. Indeed, it is not in our ambition to know the precise chemical composition of the pollutants involved. Our objective was to build a model based on [41], but that would be independent of any chemical species. Such a model has to verify at least two empirical hypotheses :

- Only a small amount of pollutants is sufficient to reduce the Re_c drop.
- The value of Re_c is almost constant on an undetermined span of pollutants quantity.

The first point is easily understandable : even if we suspect pollutants to play the same role as a surfactant, our experiment is not covered by dust, and the surface appears clean although no vacuum is made around it. The second point comes from the reproducibility of experiments. Indeed, the atmosphere is not controlled in experiments, and thus, the quantity of pollutants can not be considered as a constant for every experiments realized. Yet, for a given G, the value of Re_c determined with LDV was almost invariant from one experiment to another.

Surface tension and surfactant

Surface tension is a phenomenon linked to microscopic interactions between molecules at the surface of a liquid. Fluids adapt the shape of their surface in order to minimize the surface area, and their energy. At the air-water interface, the cohesion forces (attraction of liquid particles between each other) are stronger than adhesion forces (attraction of liquid particles by air particles). This leads to an elastic behaviour of the interface. The same competition happens on solid-liquid boundaries, and are responsible for the contact

angles, and thus for the shape of the interface.

Figure IX.1 – Water drops on a leaf keep a spherical shape thanks to surface tension, instead of spreading on the leaf.

Surface tension can be lowered by the addition of a surface-active compound, called surfactants. Figure IX.2 illustrates behaviour of surfactant regarding its concentration. The hypothesis we made was that pollutants act macroscopically like a small concentration of surfactants, and thus, stay at the surface (only a negligible amount of pollutant is advected in the bulk). This hypothesis is reasonable as experiments are clean enough to not see any pollutant cluster. Micelles are clusters of surfactant particles that create a macroscopic structure. They occur only under strong enough surfactant concentrations and are found in the bulk of the fluid, not at the interface.

Measurement of surface tension can be done in many ways. Traditional methods consist in evaluating the force required to detach an object delicately pulled out of the immobile surface of a liquid layer. This item can be a ring (De Noüy method), a needle (De Noüy-Padday method) or a plate (Wilhelmy method). Other solutions use drops, by evaluating the maximum length of the boundary between a drop and a vertical tube from where it falls (pendant drop method). Despite all of these existent methods, no solution exists to evaluate dynamically the evolution of the surface tension.

Water is known to be very sensitive and its surface tension is easily modified from the classical value of 72.8 $10^{-3} N.m^{-1}$ (at $20°C$). The surface tension influence was evaluated experimentally. As we were not able to guarantee the ideal value of surface tension, we choose to heavily lower it with the addition of a small amount of surfactant (drop of dishwashing liquid). No difference in Re_c was found, and therefore, the role of surface tension was initially neglected. Note that the experiment with dishwashing liquid was done with Kalliroscope.

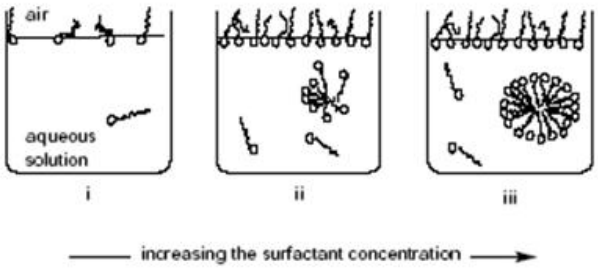

Figure IX.2 – For low concentration, surfactant are concentrated at the interface (left). With the increase of the concentration, surface is saturated, and surfactant are absorbed (middle). Once the fluid is saturated, surfactant particles gather themselves in micellar structure (right). This means that the concentration of surfactant is above the critical micellar concentration (CMC).

Bibliography

The aim of this complementary bibliography is not to provide an overview of studies on surfactants and colloids, but to introduce some papers that feed upcoming thoughts. In every articles, authors employ the Boussinesq-Scriven surface fluid model for a Newtonian gas/liquid interface so that the surface stress tensor $\mathbf{S}^s$ is

$$\mathbf{S}^s = (\sigma + (\kappa^s - \mu^s)\nabla^s \cdot \mathbf{u}^s)\mathbb{1}^s + 2\mu^s \mathbf{D}^s$$

where κ^s is the surface dilatational viscosity, μ^s is the surface shear viscosity, σ is the equilibrium surface tension, $\mathbf{u}^s$ is the surface velocity vector, ∇^s is the surface gradient operator, $\mathbb{1}$ is the tensor that projects any vector onto the surface, and

$$2\mathbf{D}^s = \nabla^s \mathbf{u}^s \cdot \mathbb{1}^s + \mathbb{1}^s \cdot (\nabla^s \mathbf{u}^s)^T.$$

The first article considered here was published by Lopez and Chen in 1998 ([72]). The authors used an ad hoc closure model between surfactant concentration and surface tension based on the tangent function :

$$\sigma - \sigma_i = -\frac{\delta}{\pi}\tan^{-1}\left(\beta\frac{c - c_i}{c_i}\right)$$

where σ and c are the dimensional surface tension and concentration, respectively, while σ_i and c_i are the reference surface tension and concentration, respectively. δ is the saturation surface pressure, and β is a non-dimensional parameter, defined as $\beta{=}-\pi c_i \partial\sigma/(\delta\partial c)$. This modelling allows for a study of the influence of the pollutant concentration at the surface of a flow driven by a rotating disc, in a cylindrical cavity, *i.e.* the exact same configuration as ours, but with an aspect ratio $G{=}2.5$. The conclusion is that even a small amount of contaminant can influence both interfacial and bulk flow.

In 2000, Lopez and Hirsa, considered an annular channel to study the coupling between the bulk flow and an interface in the presence of an insoluble surfactant ([70]). This time, the autors used a closure equation based on the hyperbolic tangent :

$$\bar{\sigma} = 1 + \frac{a_1}{\sigma_c}\tanh(a_2(1-\bar{c}))$$

where $\bar{\sigma}$ is the dimensionless surface tension, σ_c=66 $mN.m^{-1}$ is a characteristic surface tension, and $\bar{c}$ is the dimensionless surfactant concentration. a_1=6.3 and a_2=6.2 are two parameters used to fit the model to experimental measurements with Hemicyanine. Among the profiles published in this article, those on the radial velocity at the surface reveals that u_r tends to zero everywhere along the surface while the surfactant concentration is increasing : authors wrote that "Marangoni stress makes the interface act like a no-slip condition".

Using the same configuration as in [70], Hirsa *et al.* published in 2001 experimental results of velocity fields for various concentrations of K1 vitamin at the surface ([39]). This insoluble surfactant was used for its zero value surface shear viscosity μ^S on the considered range of concentration. In this article, the experimental approach is followed by a numerical comparison where another closure equation was used to link the pollutant concentration and the surface tension. This closure equation was this time based on the exponential function :

$$\sigma(c) = \frac{a_2 + a_3 c + a_4 c^2}{1 + \exp(a_0 a_1 - a_1 c)} + \frac{a_5 + a_6 c^2}{1 + \exp(a_1 c - a_0 a_1)}$$

where σ and c are respectively the dimensional surface tension and the dimensioned concentration of surfactant at the interface. Parameters a_0 to a_1 are dimensional parameters to fit the experimental data (see below, fig. IX.3). Results show a very good agreements between numerics and experiments. This paper was followed by a second one, from the same authors, on the use of the annular channel flow to determine the surface shear viscosity μ^S ([71]).

Still using K1 vitamin monolayer, Vogel & al ([38]) studied macroscopic and microscopic patterns at the surface of a flow driven by a rotating disc located at the bottom of a fixed cylindrical cavity, for G=0.25. Re_c in presence of K1 vitamin is estimated between 1900 and 2000, with an azimuthal wavenumber m=3, *i.e.* the same threshold than Lopez *et al.* in [37].

The previous article is at the origin of the publication [41], by Kwan and Shen. The core of the paper is a study of the mathematical background behind the experiment of Vogel *et al.*, using the same closure equation as Hirsa *et al.* ([39]). The authors give the Taylor expansion of this model :

$$\sigma(c) \sim 72.4 - 4.2 \times 10^{-13} c - 0.15 c^2 - 6.5 \times 10^{-11} c^3 - 4.95 \times 10^{-10} c^4 - 3 \times 10^{-9} c^5 + ...$$

Besides this equation, the main interest for us is in the two last pages, with the results of a simulation with the same closure model than [71]. For G=0.25 and c_0=0.4 $mg.m^{-2}$, Re_c was estimated at 1050. With the free surface condition, this Re_c was 3481, according to ROSE computation. Although not commented by the authors, and more than the Re_c drop, the most interesting result is the unstable mode predicted in their simulation : for c_0=0.4 $mg.m^{-2}$ the first one to growth is m=3, in agreement with[35] and our own experiments, while all our previous computations predicted m=2.

In a different configuration - a micro channel with super hydrophobic surface - Peaudecerf *et al.*, explain how pollutants can gradually change the boundary condition from free slip to no slip ([73]) . The main interest of a micro channel is to create an air cushion between the wall and the liquid. As a consequence, the friction on the wall is so reduced that it is almost a free slip. But in presence of pollutant, this slipping effect is cancelled and the drag can be even more important than in the case of the simple wall.

The last element of the bibliography was published in 2017, by Bandi *et al.*. In this paper ([74]), authors demonstrated that for concentrations less than 15% of the critical micellar concentration (CMC), the flow is dominated by adsorbed surfactant. This means, that there is no diffusion of the surfactant inside the bulk for small concentration. The CMC corresponds to the concentration of pollutant beyond which pollutant clusters (see figure IX.2).

These articles reveal that for a small amount of surfactant, which could be atmospheric pollution, only the surface boundary condition has to be modified, compared to the ideal pollutant-free surface. But this sole modification is sufficient to generate a heavy evolution of the bulk flow. However, none of the previous authors explored the influence of the surfactant, and, by extension, pollutant, on potential instability thresholds.

New boundary conditions in z = G

Since surface tension σ is no longer assumed constant, equations (IV.8) and (IV.10) are no longer valid. At the surface, the balance of surface force is :

$$\int_S \mathbf{n}\cdot\mathbf{S}dA = \int_C \mathbf{n}\cdot\mathbf{S}^s dl \tag{IX.1}$$

where $\mathbf{S}$ is the same stress tensor than in section Dynamic boundary conditions, $\mathbf{S}^s$ is the surface stress tensor and $\mathbf{n}$ is a normal vector to the surface. For $\mathbf{S}^s$, we use a Boussinesq-Scriven model, where the surface dilatational viscosity κ^s and the surface shear viscosity μ^s are neglected. As a consequence, $\mathbf{S}^s$ is reduced to $\mathbf{S}^s = \sigma\mathbb{1}$. Using the Stokes theorem (see appendix A), one can write :

$$\int_C \mathbf{n}\cdot\mathbf{S}^s dl = \int_S [\nabla^s\sigma - \sigma\mathbf{n}(\nabla^s\cdot\mathbf{n})]dA. \tag{IX.2}$$

Here, ∇^s is the surface gradient operator, defined as $\nabla^s = (\mathbb{1} - \mathbf{n}\otimes\mathbf{n})\cdot\nabla$, since σ is only defined at the interface. Under the flat surface hypothesis, we have $\mathbf{n} = \mathbf{e_z}$, and thus $\sigma\mathbf{n}(\nabla^S\cdot\mathbf{n}) = 0$. Besides, considering that S is an arbitrary surface, the surface stress balance can be reduced to :

$$\mathbf{e_z} \cdot \mathbf{S} = \nabla^s \sigma$$

Therefore, the new boundary conditions at the surface are :

$$\begin{cases} \dfrac{\partial u_r}{\partial z} = \dfrac{1}{\mu}\dfrac{\partial \sigma}{\partial r} \\ \dfrac{\partial u_\theta}{\partial z} = \dfrac{1}{\mu r}\dfrac{\partial \sigma}{\partial \theta}, \end{cases}$$

which can be respectively non-dimensionalized as :

$$\begin{cases} \dfrac{\partial u_r}{\partial z} = \dfrac{1}{Ca}\dfrac{\partial \sigma}{\partial r} \\ \dfrac{\partial u_\theta}{\partial z} = \dfrac{1}{Ca}\dfrac{1}{r}\dfrac{\partial \sigma}{\partial \theta}. \end{cases}$$

$Ca = \frac{\mu \Omega R}{\sigma_0}$ is the capillary number, and σ_0 is the reference surface tension. Note that it is not required to apply the condition on $\partial u_\theta / \partial z$ to the base flow, as it is axisymmetric. The impermeability of the surface is conserved, and thus we keep the same condition on u_z :

$$u_z = 0$$

Closure equation

The main idea behind this model is the connection between the pollutants concentration c at the surface, and the surface tension σ. Thus, an equation that links these two quantities has to be postulated in order to close the system. The equation used here is directly derived from [39] and [41].

There, the authors used the sophisticated model IX.1.1. We choose to start from the Taylor expansion IX.1.1 of this model, since its derivation is simpler and allows for an easier implementation into ROSE. Actually, a closer look at the equation IX.1.1 reveals that the c^2 term is predominant. Therefore we only use this leading term of the Taylor expansion, which comes down to :

$$\sigma = \sigma_0 (1 - \frac{\alpha}{2\sigma_0} c^2) \tag{IX.5}$$

where α=0.3 is a dimensional parameter specific to the surfactant. Such models are by nature dedicated to one specific specie. In our experiment, no surfactant was added on the surface and the pollution is not the result of only one pollutant. Therefore, the previous expression needed to be modified in order not to have any α dependency. Considering the dimensionless form of equation (IX.5)

$$\bar{\sigma} = 1 - \frac{\alpha}{2\sigma_0} C_0^2 \bar{c}^2, \tag{IX.6}$$

where $\bar{\sigma} = \sigma / \sigma_0$, and $\bar{c} = c / C_0$, and

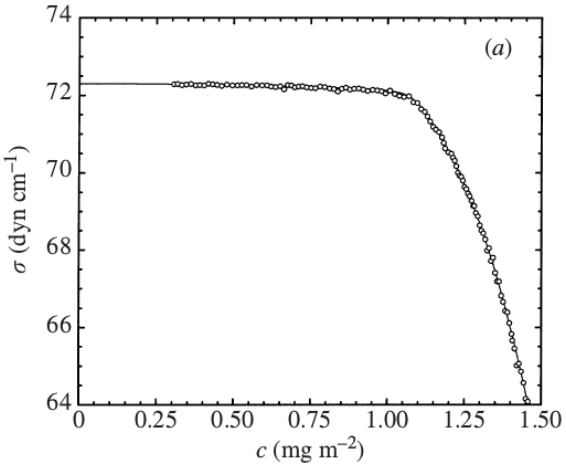

Figure IX.3 – Comparison between modelization of $\sigma(c)$ and experimental data for K1 vitamin. Figure extracted from [71].

$$\beta = \frac{1}{Ca}\frac{\alpha C_0^2}{\sigma_0}. \tag{IX.7}$$

Equation (IX.6) can be rewritten as

$$\bar{\sigma} = 1 - \frac{1}{2}Ca\beta\bar{c}^2. \tag{IX.8}$$

Combining (IX.8) and (IX.4) gives the boundary condition depending on c instead of σ :

$$\begin{cases} \dfrac{\partial u_r}{\partial z} = -\beta c \dfrac{\partial c}{\partial r} \\ \dfrac{\partial u_\theta}{\partial z} = -\dfrac{\beta c}{r}\dfrac{\partial c}{\partial \theta}. \end{cases}$$

Convection-Diffusion equation at the surface

To compute the pollutant concentration, a convection-diffusion equation is added at the surface. Since the amount of pollutant is supposed small enough ($C_0 \ll$ CMC), pollutant is only advected along the surface and not into the bulk ([74]). The convection-diffusion equation is :

$$\frac{\partial c}{\partial t} = \nabla \cdot (D\nabla c) - \nabla \cdot (\mathbf{v}c) + F$$

Here, D is the diffusivity of the surfactant, $\mathbf{v}$ is the velocity field, and F represents the volume sources. Since no chemical reaction is considered, $F = 0$, and D is assumed constant. According to [75], since c is only defined at the surface, previous equation can be rewritten as :

$$\frac{\partial c}{\partial t} + \nabla^s \cdot (\mathbf{v}c) = D\Delta^s c,$$

where ∇^s is the surface operator defined previously, and $\Delta^s = \nabla^{s2}$. Considering only the divergence part, and decomposing $\mathbf{v}$ into components along the surface, $\mathbf{u}^s$ and normal to the surface $(\mathbf{v}\cdot\mathbf{n})\mathbf{n}$, one can write :

$$\nabla^s \cdot (\mathbf{v}c) = \nabla^s \cdot (c\mathbf{u}^s) + \nabla^s \cdot ((c\mathbf{v}\cdot\mathbf{n})\mathbf{n})$$

We remind that we made the hypothesis of a flat free surface, thus $\mathbf{n} = \mathbf{e_z}$, and $\mathbf{v}\cdot\mathbf{n} = u_z = 0$ at the surface. As a consequence, the latest expression reduces to

$$\nabla^s \cdot (\mathbf{v}c) = \nabla^s \cdot (c\mathbf{u}^s).$$

Finally the convection-diffusion equation can be simplified to :

$$\frac{\partial c}{\partial t} + \nabla^s \cdot (c\mathbf{u}^s) = D\Delta^s c,$$

and non-dimensionalized as :

$$\frac{\partial \bar{c}}{\partial \bar{t}} + \nabla^s \cdot (\bar{c}\bar{\mathbf{u}}^s) = \frac{1}{Pe}\Delta^s \bar{c}, \tag{IX.9}$$

Pe is a Péclet number, defined here as $Pe = \frac{\omega R^2}{D^s}$. In the upcoming chapter, all variables are non-dimensionalized. Therefore, for a better reading, the notation $\bar{.}$ is dropped.

As written in chapter II, β can be seen as a ratio between a Marangoni number and the Péclet number. Indeed, the Marangoni number is not based on temperature, but on concentration, and therefore, the thermal diffusivity is replaced by the replaced by the diffusion coefficient. According to equation (IX.6), $(\alpha C_0) \propto \frac{\partial \sigma}{\partial C}$, and thus, $Ma = (\alpha C_0)\frac{RC_0}{\mu D^s}$. Using the definition of Péclet given above, the result of Ma/Pe is exactly (IX.7).

Base flow

We saw in chapter V that fields were decomposed according to a complex ansatz. The concentration c is treated the same way : $c(r,\theta,t) = C(r) + \epsilon\Re(c^*(r)e^{\lambda t + im\theta})$. For the base flow, that is steady and axisymmetric, $\frac{\partial .}{\partial t} = 0$ and $\frac{\partial .}{\partial \theta} = 0$. Thus, the convection-diffusion equation for the base flow becomes:

$$\frac{1}{r}\frac{\partial (rCu_r)}{\partial r} - \frac{1}{Pe}\frac{1}{r}\frac{\partial}{\partial r}(r\frac{\partial C}{\partial r}) = 0. \tag{IX.10}$$

A new boundary condition also has to be implemented. We previously wrote that no chemical reaction was considered and that the global concentration is supposed to remain constant, which translates to :

$$\frac{1}{\pi}\int_0^{2\pi}\int_0^1 c(r,\theta,t) r dr d\theta = 1.$$

For the base flow, this constraint resumes to :

$$2\int_0^1 C(r)rdr = 1.$$

Numerically, this condition is implemented on the node at r=1 in the coupled system of equations otherwise undetermined. In $r = 0$:

$$\frac{\partial C}{\partial r} = 0 \tag{IX.11}$$

according to the symmetry at the axis. Note that all integrals are approximated in ROSE using a trapezoidal rule, coherent with the second order approximation.

Perturbation

The equation for the perturbations of c can be deduced by subtracting (IX.10) from (IX.9). This leads to

$$-\lambda c^* = \frac{1}{r}\left(\frac{\partial r C u_r^*}{\partial r} + \frac{\partial r U_r c^*}{\partial r}\right) + \frac{imU_\theta c^*}{r} - \frac{mCu_\theta^*}{r} - \frac{1}{Pe^s}\left(\frac{\partial^2 c^*}{\partial r^2} + \frac{1}{r}\frac{\partial c^*}{\partial r} - \frac{m^2 c^*}{r^2}\right).$$

The boundary conditions for the perturbations are different from those applied to the base flow. Here, two cases must be distinguished. The first one is m=0, and the second is m >0.

- m=0

  The mode m=0 is an axisymmetric mode. Thus, an equivalent condition to (IX.11) must be imposed to perturbations :

  $$\frac{\partial c^*}{\partial r} = 0 \text{ at } r = 0.$$

  Then, the conservation of the concentration still have to be respected. For the perturbations, the constraint on the concentration is no more equal to 1, but to 0.

  $$\int_0^1 c^*(r)rdr = 0 \text{ at } r = \mathrm{R}.$$

- m>0

  For m >0, perturbations are no longer axisymmetric. The only solution to avoid a singularity at r=0 is to impose $c^*(r{=}0){=}0$, while at $r = 1$, no mass flux crosses the wall. Thus, it yields $\frac{\partial c^*}{\partial r} = 0$.

Boundary conditions for velocities on wall and disc

Now that we have determined the boundary condition for c, we must set the boundary conditions on velocity components. On the wall and on the disc, they are unchanged from chapter IV : impermeability and no-slip condition lead to the same equations than IV.5 and IV.6 :

$$u_r = u_\theta = u_z = 0$$

and

$$\begin{cases} u_r = u_z = 0 \\ u_\theta = r. \end{cases}$$

Validity and Validation

Before we realize an in-depth study on the considered aspect ratios, we verified the implementation in ROSE and the validity of the first order closure equation, with a comparison to [39] and [41].

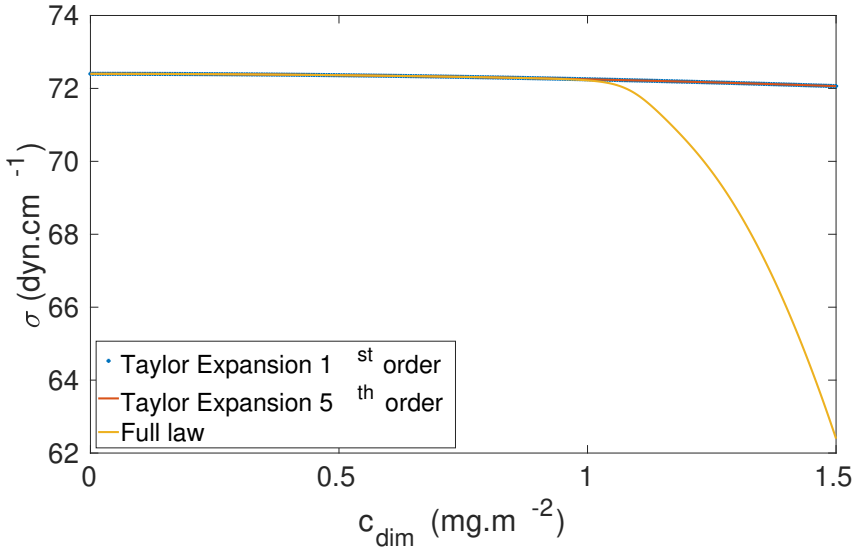

Figure IX.4 – Comparison of the first order Taylor expansion model, to fifth order Taylor expansion and complete model from [39], corresponding to figure IX.3.

One can see from figure IX.4 that 1^{st} and 5^{th} order Taylor expansions match perfectly. Therefore, there is no need to code such a high order in ROSE. However, the gap with the complete closure equation quickly increases after c=1 $mg.m^{-2}$. This correspond to the beginning of the transition to a second plateau, where σ saturates to a lower value. The fact that our model does not capture this behaviour means that the value of σ in our computations remains close to σ_0 even for very large values of c, (and thus of β). As it will be seen in this chapter, the small variations of σ allowed by our model are already sufficient to highlight the influence of the condition at the interface.

We now validate this new version of ROSE. We compare first $U_r(r)$ and $C(r)$ profiles in $z = G$, computed on a 401×101 grid, to data from [41] (G=0.25, Re=1000). The Péclet number is set to 1000, and β=0.663.

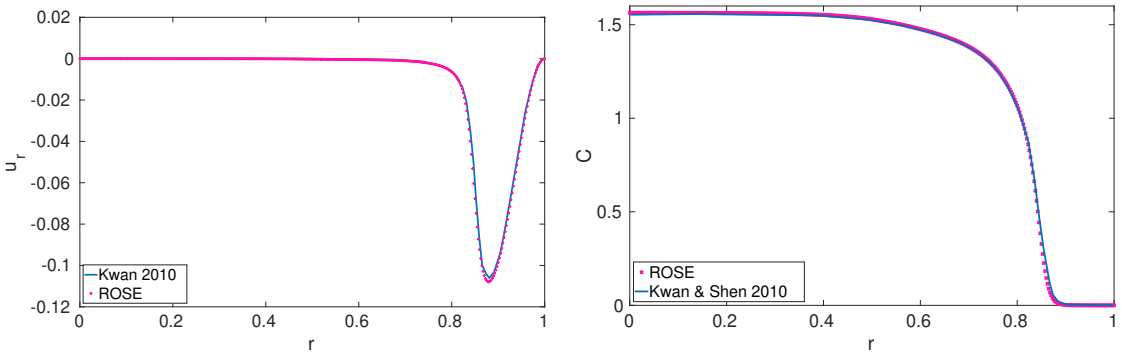

Figure IX.5 – Comparaison of baseflow radial velocity U_r (left) and concentration C (rigth) at the surface ($z = G$), for G=0.25,β=0.663 and Re=1000.

According to figure IX.5 the agreement is excellent on the base flow between ROSE and the DNS from [41]. Minor gaps appear, which can be attributed to inaccuracy of the data from [41], as it was extracted directly on the graph.

For the same parameters, the authors report that the flow loses its stability around Re_c=1050, via a supercritical Hopf bifurcation. The primary instability at this value of Re displays an azimuthal wavelength m=3. A computation with ROSE gave Re_c=908. This represents a gap of 13.5% with [41]. Note that in this article, the authors used a DNS code based on a spectral method. They did not provide any explanation on how they determined the value of Re_c. They only indicated that "the base flow remains stable up to about Re=1050".

Effect of pollutant concentration

In the same way we explored the influence of κ on Re_c for the Robin condition in the previous chapter, we now perform a parametric study of $Re_c(\beta)$. For G=1/14, the results were highly positive. A soon as β was larger than 0.14, Re_c drops below 3000; and stays close to this value for β up to 5. Similarly to the Robin condition, two unstable branches cross at a codimension 2 point. The frequencies for $\beta \geq$2.5, are close to the experimental value of f. More details were given in chapter II, and except for the comparison of base flows and the verification of the selected value of the Péclet number made for G=1/14, the rest of this chapter is dedicated to the application of the pollutant model to $G >$1/14.

Discussion on the Péclet number

The Péclet number that appears in equation IX.9 is arbitrary set to 1000, following the value given in [71] and [41]. This number compares convection effects ($r^2\omega$) to diffusion (D). In water, $D \approx 10^{-5}\ cm^2.s^{-1}$ at 298 K. For a rotation rate of 1 rpm in our smallest cavity, which represent the smallest value for convection, $r^2\omega \approx 0.2\ cm^2.s^{-1}$, and then $Pe \approx 2*10^4$. As the minimum experimental value of Pe is twenty times larger than the numerical one, one may question the validity of this approximation. Therefore, we computed the base flow for seven Péclet numbers, at Re=10000, for β=0.3 and for

G=1/14. The results are exhibited in figures IX.6a and IX.6b.

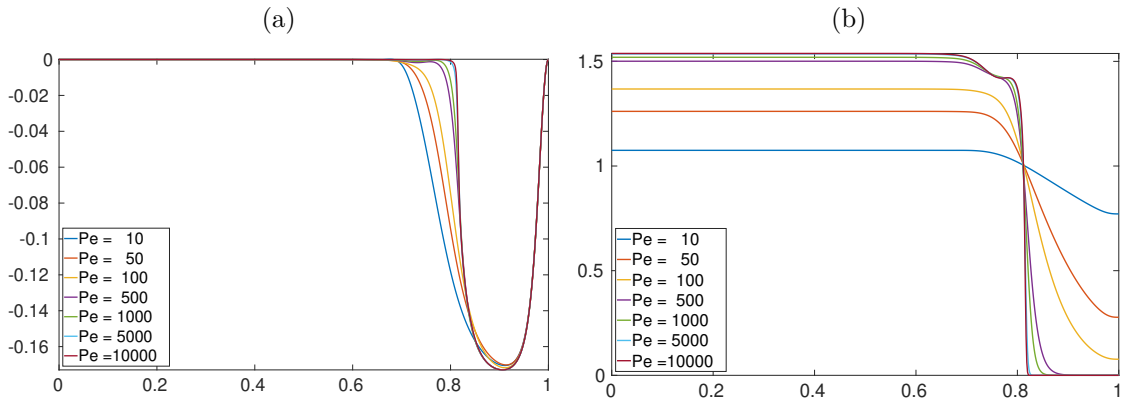

Figure IX.6 – Influence of the Péclet number on $U_r(r)$ (left) and $C(r)$ (right) in z= G, for G=1/14, β=0.3 and Re=10000.

For Pe <1000, the variation in velocity profile (IX.6a) and in concentration profile (IX.6b) at the surface are obvious : the increase of Pe straightens the pollutant front at r ≈0.82, and increases the radial velocity gradient $\partial u_r/\partial r$ at the same radius. For Pe >1000, this evolution is not that marked, and profiles for Pe ≥5000 even merge. Differences between Pe=1000 and larger values are not signifiant, and therefore, this approximation on Pe appears coherent. Moreover, the high values of the Péclet number impose to increase the grid resolution to compensate the stronger gradients.

G=1/14

In chapter II, no direct comparison of the effect of β on the base flow with LDV profiles was made. Therefore, the influence of β on both u_r and u_θ is detailed in this section.

Figure IX.7a focuses on u_θ. The effect of β is evident as soon as $\beta \geq 0.5$. Indeed, the overshoot in r=[0.68,0.69] completely vanishes for such values. Actually, the overshoot is no longer present as soon as $\beta \approx 0.2$. Despite the fact that this evolution came for low values of β, ROSE base flow gets closer to LDV profile only for $\beta \geq 4$.

This last observation is corroborated by figure IX.7b. In this figure, as in figure IX.7a, the curves for β=4 are very close to the frozen surface velocity profile and to the experimental profile. The large gap between experimental points and simulations for r=[0.5,0.8] is probably caused by the imperfect verticality of the laser. If the two lasers beams are not in the same vertical plan, the LDV device capture a projection of u_θ. Since the amplitude of u_θ is much larger than that of u_z, even a small projection of u_θ can influence u_z measurement. This is coherent with the slope observed in experimental data in figures IX.7b.

(a) u_θ in z=0.8G

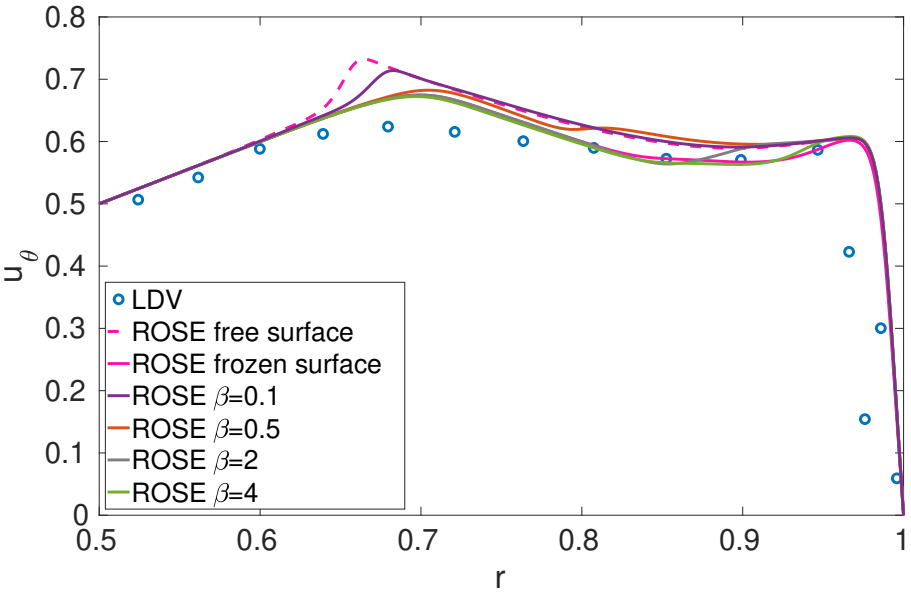

(b) u_z in z=0.5G

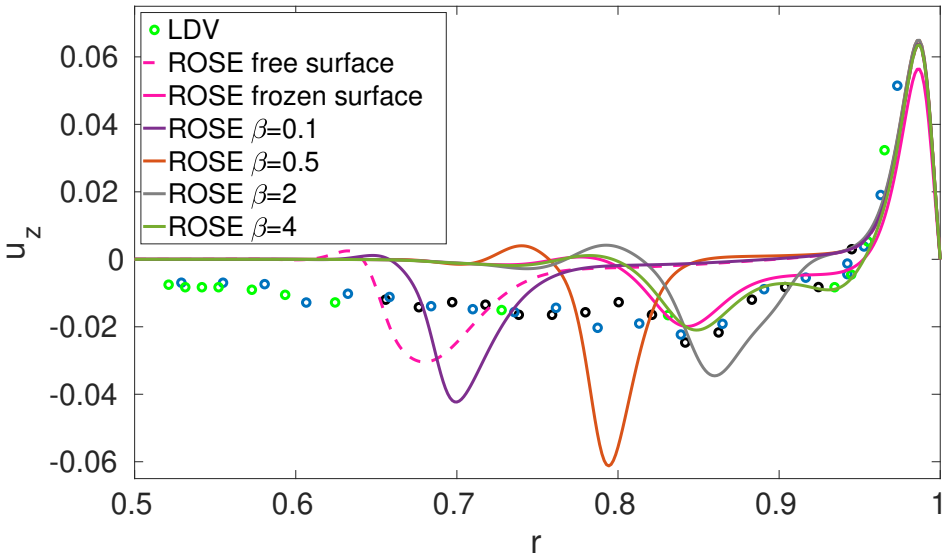

Figure IX.7 – Comparison of ROSE base flow for four different values of β, with the LDV measurements introduced in previous chapters, for G=1/14 and Re=18620. Note that the three different colors for u_z LDV data belongs to three different experiments.

G=0.25

For G=0.25, the focus is on m=2 and 3, since they are azimuthal wavenumbers for which mismatches between numerics and experiments were observed : ROSE predicts a most unstable mode m=2 at Re_c=3481 while our experiments, in agreement with [37], exhibits a m=3 azimuthal wavenumber at $Re_c \approx$2000. The application of the frozen surface condition did not solve this contradiction. However, we saw in figure IX.5 that for the base flow, ROSE displayed a good agreement with [41], where authors numerically reproduce experiments at G=0.25. Therefore we can expect our pollutant model to have a value of Re_c closer to experiments.

First, the base flows for various β are compared with LDV profile in figure IX.8. For β as low as 0.1, the overshoot on u_θ, which existed for the free surface condition, disappears. However, the best agreement between the base flow and the LDV profile is only obtained for $\beta \geq 1.85$. After this value, the base flow does not evolve much, and is almost indistinguishable with the profile obtained for the frozen surface condition (figure IX.8a). Concerning the azimuthal velocity component, the fitting is obtained as soon as $\beta \geq 1.25$. Above this value, the computed profiles are completely merged with the profil obtained with the frozen surface condition (figure IX.8b).

The results for $Re_c(\beta)$ are introduced in figure IX.9. One can see a behaviour close to what was previously observed for m=5 in the case G=1/14 : Re_c curves for both m=2 and 3 present a cusp, followed by a drop of Re_c. As commented previously, this corresponds to a jump to a second unstable branch, highlighted in figure IX.10 by a discontinuity in the frequency of the most unstable mode. For m=2 this occurs at β=1.25, and at β=0.25 for m=3. It is also for β=0.25 and Re_c=4000 that m=3 become the most unstable mode and remains it up to β=0.75 and Re_c=1000. Re_c of both modes are then very close, up to β=1.6, where the gap is increasing. It is interesting to remind that in [37], the authors noted that a mode m=2 grew first when lower quality water was used : in figure IX.9 one may suggest that this observation correspond to the interval $\beta \in [1;2]$ where m=2 is the most unstable mode. But this seems to be unlikely, since the results for G=1/14 tend to show that velocity profiles from experiments performed with distilled water match with numerics only for β >4 (see figure IX.7).

The most important feature of the figure IX.9 are represented by the gray triangles. This "buckle" delimits a range of parameters (β,Re), inside which the flow is unstable. For a given β - lets keep β=4 - one can see that for $Re \in [0;1334]$, the flow is stable. Then for $Re \in [1334;2793]$ the mode m=3 is unstable. However increasing Re stabilize the flow up to Re=4614, where the mode m=2 becomes unstable. This evolution can be put in parallel to the experimental sequence displayed in figures VI.20a and VI.21 : in this experiment, the mode m=3 was visible around Re=2150, before the flow restabilizes for $Re \approx$3700 and becomes axisymmetric. It evolves to an ellipse for $Re \approx$4930, and then to a undefined pattern for $Re \approx$5240. The mode m=2 then grows for $Re \approx$5545. Theses experimental thresholds are not very accurate, but still, the similarities with the simulation are sticking. Moreover, the undefined pattern, kind of a mix between m=2 and m=3, could find the beginning of an explanation in the vicinity of the modes 2 and 3 for β=4

(a) u_θ in z=0.8G

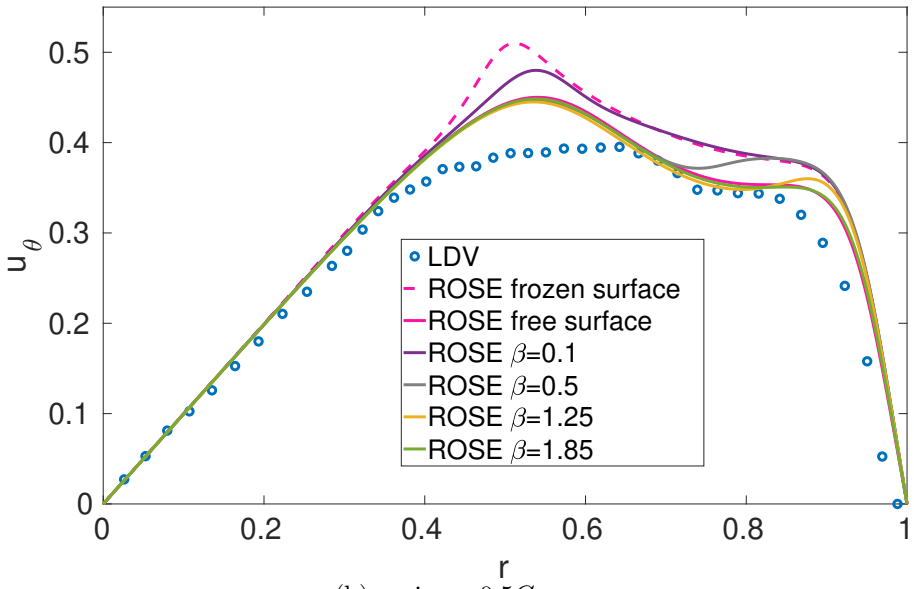

(b) u_z in z=0.5G

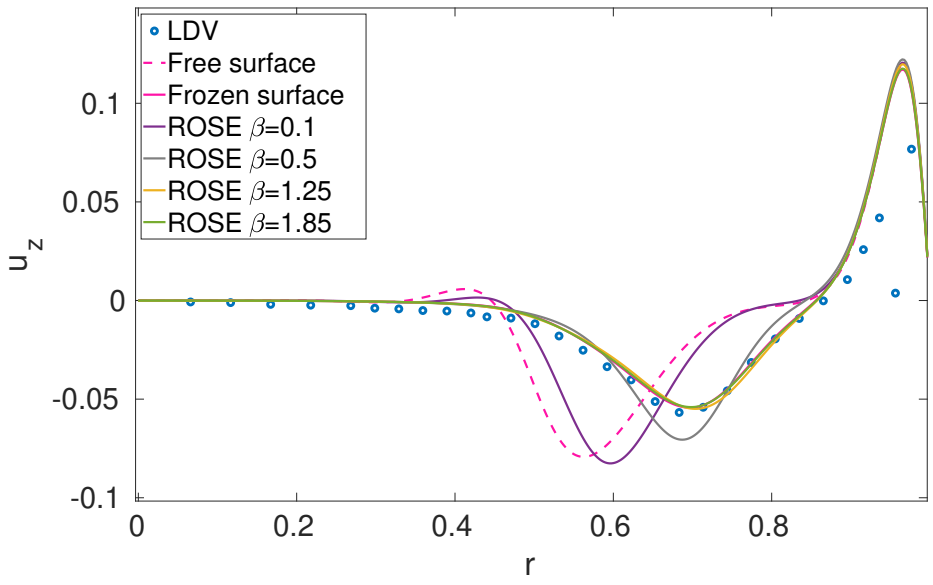

Figure IX.8 – Comparison of ROSE base flow for four different value of β, with the LDV measurements introduced in previous chapters, for G=0.25 and Re=1895.

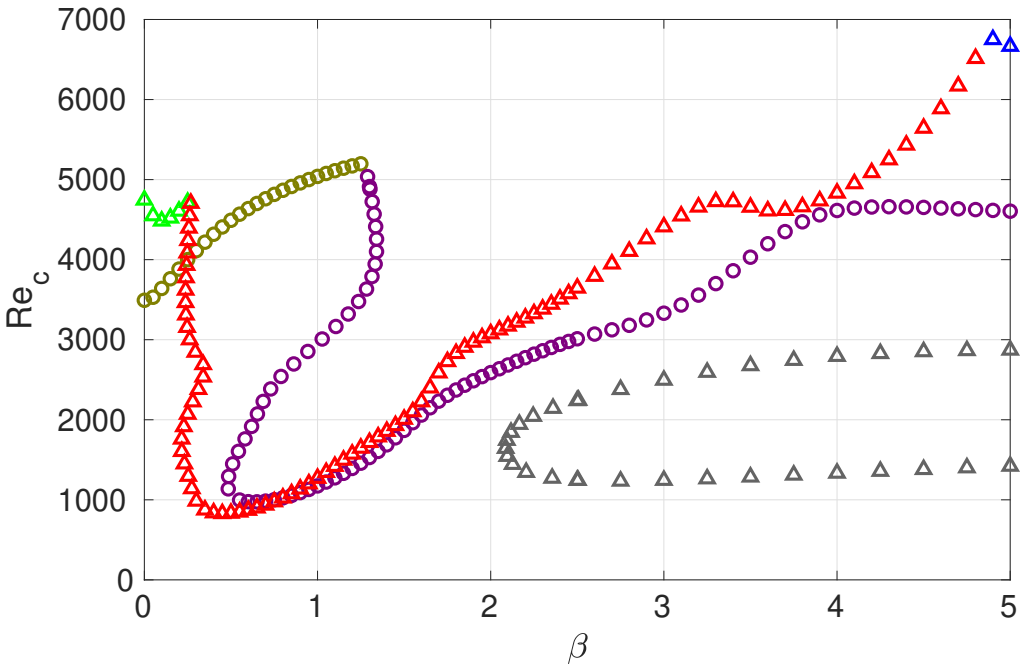

Figure IX.9 – Neutral curves $Re_c(\beta)$ for modes m=2 (circles) and m=3 (triangles), in the case G=0.25. The changing in the colors for a given mode represents the different branches of each mode.

and Re ≈4900. Like for G=1/14, the critical Reynolds number of the most unstable mode does not evolve much for β >5 : for β =5, Re_c=1421, while for β=100, Re_c=1832. This represents a variation of 29% of Re_c for an increase of 1900% of β. Interestingly, and once gain, like for G=1/14, the Re_c value for β ≥100 agrees even better with the experimental Re_c : the error with values reported in table VI.6 and in page 93 are between 2% and 13%.

For β ≥4.9 and Re >6500, another branch appears for m=3 (blue triangles). It is reported as a different branch, but note that it can be the continuation of the first one (in green), according to its frequency (see figure IX.10).

Discontinuities in frequencies are less marked than for G=1/14. For both modes the gap between the frequency for β=0 (free surface) and β=0.75 is less than 2%. Therefore, no experimental measurement can confirm which branch is actually growing in experiments, since the gap between their respective frequencies is of the same order of magnitude than the experimental uncertainty.

G=1.5

We previously observed a variation in the most unstable mode between free and frozen surface conditions, from m=1 to 4 respectively. We expect to observe the same behaviour with the increase of β. However, experiments shown many frequencies, and therefore, we

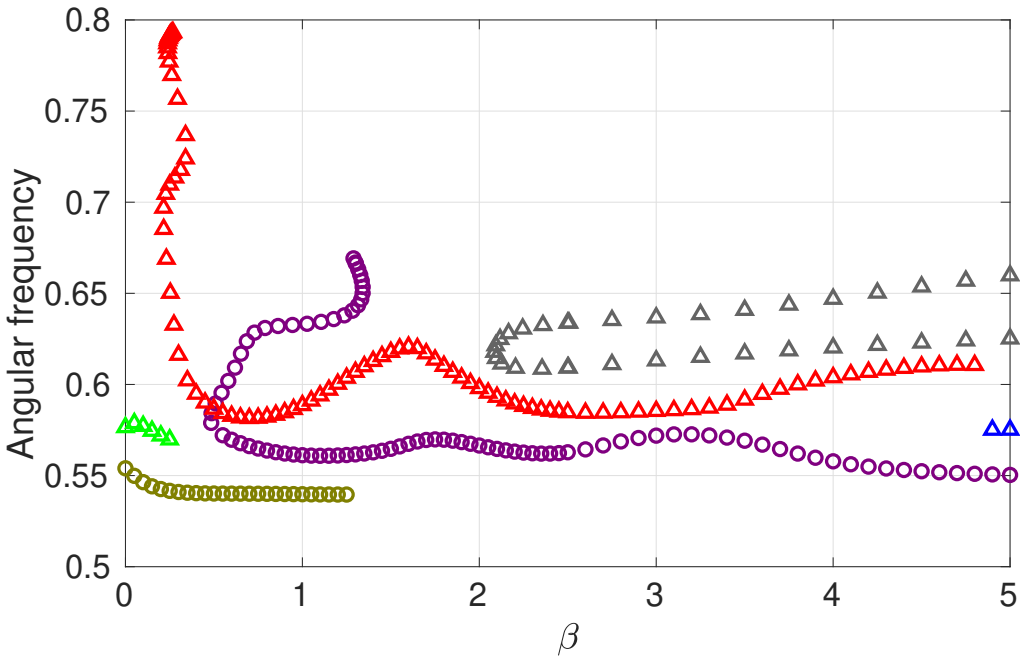

Figure IX.10 – Frequencies $f(\beta)$ of modes m=2 and m=3, associated to curves in figure IX.9.

did not restrict our study to the lone m=1 and m=4, but we included all modes from 0 to 5, in order to find a match with experimental data. Grid used here was 201×301.

As we anticipated, figure IX.12 reveals that the mode m=4 become more unstable than m=1. However we did not forecast that this would happen for such a low β value : transition occurs between β=0 and β=0.05, and this does not evolve any more up to β=1. Therefore, we can expect the mode m=4 to be the first mode to growth in experiments. On the contrary to lower aspect ratio detailed previously, only two others modes present a jump of unstable branch on the selected β span. Indeed modes m=2 and m=3 evolve quietly, without discontinuity. The axisymmetric mode m=0 jumps on a second unstable branch between β=0.05 and β=0.1, while the transition for m=1 only takes place between β=0.8 and β=0.85. Above these values, Re_c for m=1 is close to be perfectly constant, around 2600.

These jumps are emphasized in figure IX.12 by the discontinuity of the respective frequencies of these modes. Apart from that, figure IX.12 does not show the same tortuous frequency curves than for lower G : for every modes from 0 to 5, frequencies are almost constant, except when a jump of branch occurs. Figure IX.13 illustrates the switching of eigenvalues for m=0.

The constant value of frequencies does not help much to find an agreement with experimentally determined frequencies. We remind that Re_c is only known to be above 1820. Frequencies of oscillations occurring at Re=2180 and 2540 are $m \times f \approx$0.48, which

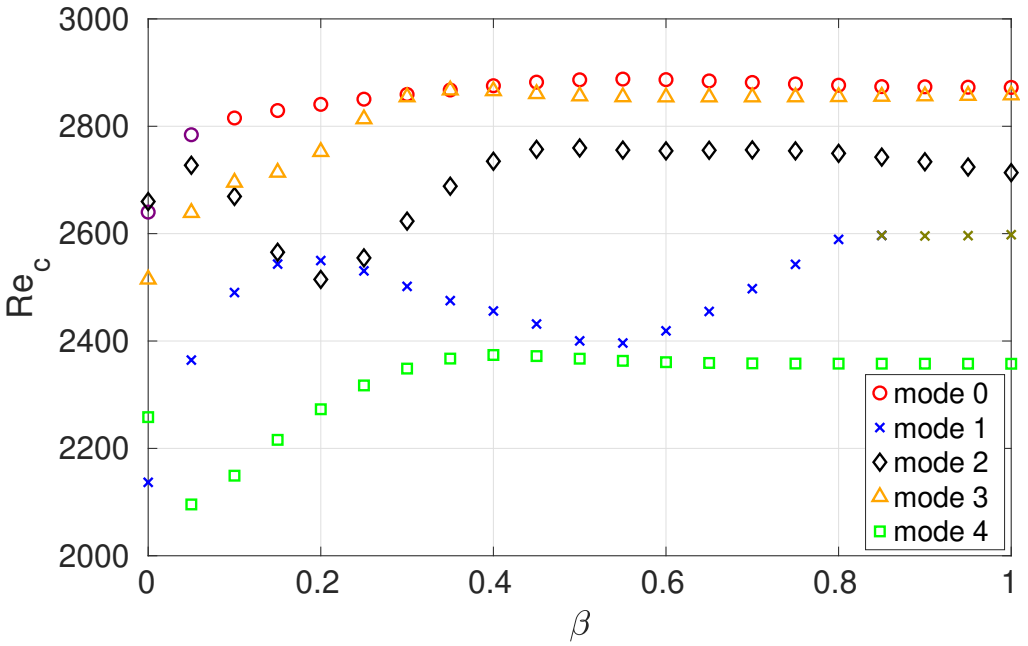

Figure IX.11 – Neutral curves $Re_c(\beta)$ for modes m=0 to m=1, in the case G=1.5.

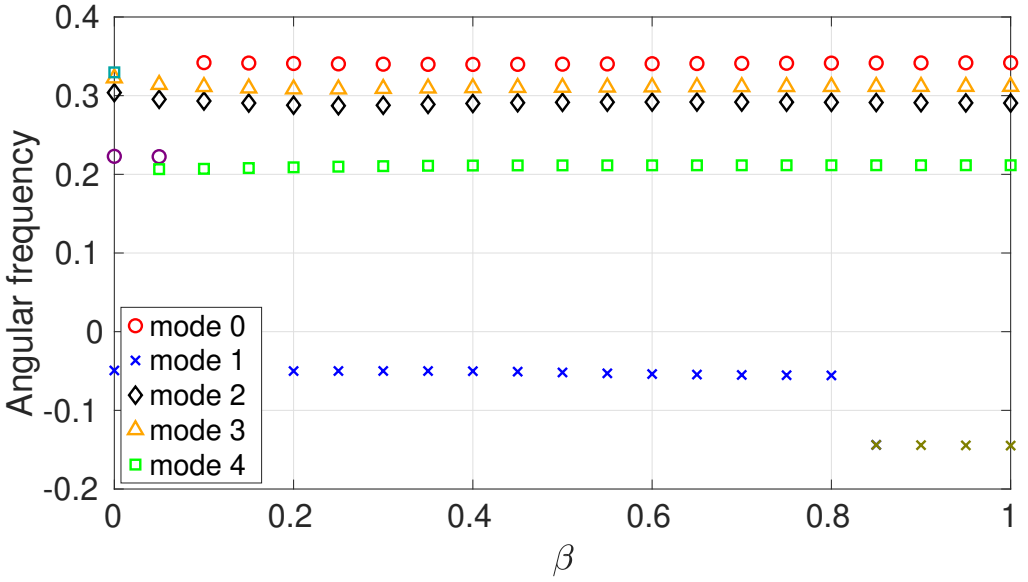

Figure IX.12 – Frequencies of modes 0 to 4, for G=1.5, at their respective Re_c.

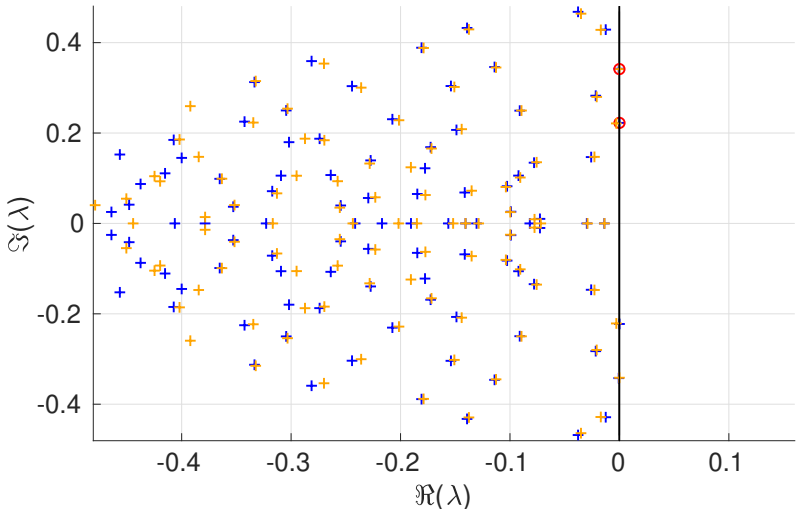

Figure IX.13 – Eigenvalues of m=0 at Re=Re_c, for β=0.05 (in blue), and for β=0.15 (orange), in the case G=1.5. For β=0.05, the most unstable eigenvalue has an imaginary part $\Im(\lambda)$=±0.22, while for β=0.15, this eigenvalue becomes stable ($\Re(\lambda)$ <0). A second eigenvalue, with an imaginary part $\Im(\lambda)$=±0.34 becomes the most unstable. Red circles highlight unstables eigenvalues.

does no match any of the frequencies in figure IX.12. We can notice that it is the only aspect ratio for which no frequency matching is observed. It is also the only aspect ratio where experiments of Re_c findings were done in the small cavity. This set-up shows a strong presence of the main mode of vibration of the disc in measurements. Although the stimulation of unstable modes by the disc rotation rate did not seem relevant, the presence of non-negligible oscillation in velocity time series alters the threshold detection and the evaluation of the frequency associated to Re_c.

G=2

We already had a good agreement between experiments and numerics with the free surface condition for G=2. The application of the frozen surface did not change the unstable branch, and only increased the Re_c from 1914 to 1987. Therefore, we only check, for m=4, that Re_c and f variations are negligible. Figure IX.14a confirms the Re_c evolution notified for the frozen surface condition : we obtain the exact same values than the frozen surface condition.

According to figure IX.14b, the same conclusion can be applied to f, that only increases by 2% between β=0 and β=1. We can notice that both Re_c and f are constant for $\beta \geq 0.3$. In any case, Re_c and f are consistent with experimental measurements from ref. [35].

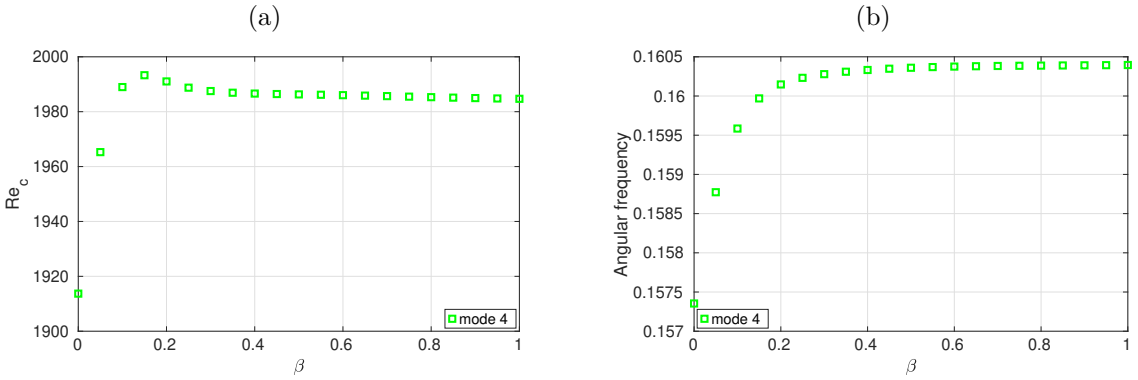

Figure IX.14 – Neutral curve and evolution of frequency regarding β for m=4 and G=2.

Conclusion on the pollutant model

Starting from a surfactant model, we built a more generic model, not based on any specific chemical specie. The main restriction of this model is the range of the control parameter : its validity is probably limited to low concentrations of pollutant. However, this corresponds to the experimental condition we look to replicate.

The application of this model to G=1/14 gives four main results :

- The Re_c of the most unstable mode, m=5 dropped below 3000 for $\beta \geq 0.15$.
- Re_c is almost constant whatever is the value of β above 0.15.
- The frequency is in better agreement with experimental measurements.
- Agreement on the base flow is better for $\beta \geq$4.

The application of this model to G=0.25, in order to check its range of application, also gives very convincing results, especially for $\beta \geq 2.08$. Indeed, above this value, a new unstable branch has been discovered which has shed new light on our previous experiments for G=0.25. Although ROSE cannot be used to explore the non linear dynamics, the evolution observed in the experiment may be explained step by step with the neutral curve IX.9. Moreover, the same asymptotic trend as for G=1/14 was observed in Re_c for $\beta >$5.

Regarding the largest aspect ratios, this model confirms the reduced influence of the surface condition. Although we still notice a mode switching for G=1.5, from m=1 to m=4, both Re_c and f have very restricted variations. Unfortunately, probable experimental issues do not allow us to conclude on any experimental match. Yet, experimental agreement is excellent for G=2.

Globally, this model performs better than the free and frozen surface model : agreements between experiments and numerics for G=1/14 and G=0.25 are far better than

they were, both with free and frozen model, while they remain excellent for G=2. Nevertheless, it is still difficult to link the state of the surface to β, and thus to perform DNS with the *adequate* value. The cost in time to perform the simulation is also increased.

Sensitivity to mixed conditions : a second glance on the frozen interface condition

While we were working on the hybrid model, we experimented to apply a different boundary condition on the base flow and on the perturbations, for the free and frozen cases. The results obtained did not match any experimental results, and we only conclude that the most favourable combination of boundary condition for G=1/14 in order to lower Re_c was to apply the frozen condition on the base flow and the free condition to perturbations. This set of boundary conditions is reported as "mixed condition". The results obtained using the most complex model including surface tension renewed the interest for these previous numerical explorations. Results for G=1/14 have already been discussed in chapter II, and thus we mostly deal with aspect ratios from 0.25 to 2 in this section. Still, it is reminded that for G=1/14, applying a frozen surface surface condition to the base flow, and a free surface condition to perturbations led to a drop of Re_c from 17006 to 2776 for m=5, which is only 5.4% lower than the prediction of ROSE with the pollutant model (by comparison to Re_c=2934, for β=5). This drop was also present for m=4, with a final value of Re_c equals to 2714, *i.e.* very close to m=5, which corresponds to observations with the pollutant model, although here m=4 is more unstable that m=5.

G=0.25

The frozen surface condition for G=0.25 was not satisfying, resulting in an increase of Re_c. The most unstable mode was unchanged from simulation with free surface condition, and was m=2, which did not match the m=3 observed experimentally. As for G=1/14, we applied the mixed condition to G=0.25 : an initial calculation of the base flow with a frozen surface condition, followed by a computation of perturbations with the free surface condition, for both m=2 and m=3 azimuthal wave numbers. The results are shown in table IX.1.

m	2	3
Re_c	3625	1588
f	0.540	0.620

Table IX.1 – Re_c for m=2 and 3, and G=0.25, with mixed boundary conditions.

m	2	3
Re_c	4293	1421
f	0.548	0.625

Table IX.2 – Re_c for m=2 and 3, and G=0.25, for β=5.

The first important observation concerns the most unstable mode : while the free, the frozen, and the hybrid condition forecast that m=2 grows first, the mixed condition is able

to correctly predicts that m=3 is actually the most unstable mode, in agreement with the experiments, and the pollutant model. Compared to this last model, and similarly to the result for G=1/14, Re_c determined with the mixed condition is slightly under evaluated by 10% (compared to the case β=5). However, the error on the frequency is below 1%.

It is interesting to notice that the Re_c predicted by this model for m=3 is very close to the one found in our smallest cavity, and reported page 93. Indeed, our experimental Re_c is only 1.7% higher than the Re value reported in table IX.1, while the corresponding frequency is only 3.5% smaller.

Higher aspect ratios

Mixed conditions were also applied to larger aspect ratio, such as G=1.5 and 2. In the first case, and like we did previously for the neutral curve, we look for the Re_c values of modes 0 to 4. Results are given in table IX.3.

m	0	1	2	3	4
Re_c	2918	2459	2643	2855	2375
ΔRe_c (%)	1.6	5.4	2.6	0.1	0.7
f	0.338	0.0469	0.291	0.311	0.212
Δf (%)	1.2	208	0.14	0.16	0.19

Table IX.3 – Re_c for m=0 to 4, and G=1.5, with mixed boundary conditions. ΔRe_c is the relative gap with Re_c predicted in the pollutant model, for β=1, while Δf is the relative gap with the frequency associated to this Re_c value.

First, the prediction of the most unstable mode (m=4) matches the results introduced earlier with the pollutant model. Actually, the stability ranking of the modes is respected : 4, 1, 2, 3, 0. Moreover, except for m=1, relative gaps with the pollutant model remain limited (below 3%) both for Re_c and f.

In the second case, for G=2, we saw chapter VIII that there is almost no variation of Re_c regarding the pollutant concentration, and that no jump of unstable branch occurs. Therefore, we do not expect different results to what was already introduced before. Indeed, for m=4, Re_c=1987 and f=0.160. Re_c is 0.09% higher to its equivalent with the frozen surface condition, while the variation on the frequency is even less relevant. Indeed, this matches perfectly the experimental thresholds in [34] and [37].

Discussion on mixed conditions

Results from the mixed condition are very appealing, but the use of different boundary conditions for the base flow and perturbations is as tedious as the frozen surface condition to justify. We can only attempt to share our feeling about the reasons of such a condition : when the surface of the fluid is contaminated by a sufficient amount of pollutants, its surface tension freezes the interface, and does not allow the radial velocity to flow along the interface. However small disturbances can still occur. The surface does not act

like a rigid lid, but more like an elastic boundary, that accept small variations around an equilibrium state.

Right now, the segregation of boundary conditions can only be done in the linear stability analysis. However, modifications of the DNS code should allow for such implementation, and therefore, to obtain visualisations of vorticity patterns, to check the coherence of such computed flows. However, eigenmodes computed with ROSE tend to get closer to the frozen unstable branch than to the free one, and one can have good expectations about upcoming 3D simulations.

Chapter X

Conclusion & outlooks

Conclusion

The realisation of an experimental bench to undertake the study of a flow generated by a rotating disc with a flat free surface initially brought more interrogations than answers. Indeed, a previous numerical study [42] had shown a very good agreement with former experiments [40], especially on Re_c and azimuthal wave number for $G \geq 1/14$. But experiments in LIMSI's cavity exhibit a primary instability for a Reynolds number much lower than expected. The gap was non negligible : for G=1/14, experimental Re_c was 75% smaller than predicted by the linear stability analysis.

As the agreement of numerical simulations with the IRPHE experiments was good (less than 5% gap), it was obvious that our bench had some flaw that forced instability growth. Various tests were run to identify this flaw : influence of the gap between the disc and cavity wall, influence of viscosity, of markers, ..., without any result but the inconstant behaviour of Kalliroscope. We suggested that mechanical vibrations, from the motor, or bearings, may trigger instability prematurely. The decision to build a new experimental set-up originates from such hypothesis. We intended to use electroactive actuators to compensate for mechanical noise. The creation of the bench, and of its control loop would required the expertise of GeePs laboratory, also involved in the project. In the long run, we expected to fully control this instability thanks to this demonstrator : avoid instability or select the first mode to grow.

Unfortunately, the analysis of vibrating modes of the disc did not indicate any matching with instability frequencies. Therefore, this hypothesis was quickly judged irrelevant. Moreover, for G=0.25, the experimental value of Re_c did match with published results [37], where the same discrepancies between numerics and experiments were noticed. Again, we faced a deadlock.

Nevertheless, we did fully start afresh. All previous failures in the identification of discrepancies causes delineate a path. Indeed, we gave a new interest to a single computation of the flow, using a boundary condition suggested in [69]. Although the Re_c between this simulation from ROSE and experiment still differ from 60%, the use of new tools highlighted unexpected conclusions. Indeed, DNS computation allows visualisations of axial vorticity pattern that reveal to be closer to experiments snapshots. Moreover, the access to LDV device definitely confirms that previous simulations did not reproduce the right flow, and that previous agreements with experiments were serendipitous. Right now, the focus of the thesis slips from vibrations of the bottom of the cavity, to inability of the free surface condition to replicate in simulations the effective condition at the interface.

However, we were only at the beginning of the road : the first alternative to free surface condition, that consisted in freezing the radial velocity at the surface, did not provide any quantitative agreement neither for G=1/14, nor G=0.25. This last case seemed even more problematic, as even the predicted mode in simulations did not match the experimental one... Therefore, we experimented successive boundary conditions on G=1/14, while other aspect ratio were mostly used for validation.

To understand how the transition in the flow between the free and frozen surface condition happens, we introduced a simple model, built as a linear interpolation between the two previous boundary conditions. This translates as a Robin condition on the radial velocity at the interface, monitored by a new parameter
kappa. Although the progress on the reduction of Re_c was limited, this modelling allows to discover a new unstable branch for a given mode. This new branch appeared in a better agreement with experiments. Moreover, this branch already existed for κ <1, *i.e.* for a non-completely frozen surface, which was more coherent with experimental observations. We now had to find a way to catch this branch to a lower Reynolds.

After few unsuccessful tries to modify the Robin condition in order to lower the critical Reynolds number, the reading of articles on the influence of a Langmuir monolayer on a flow motivated to implement a much more complex model into our linear stability analysis code. Under the hypothesis of low pollutant concentration at the surface, no pollutant penetrates the bulk. Therefore, using a 2D convection-diffusion equation, we modelled the variations of pollutant concentration at the interface. Then, a closure equation linked the surface tension to pollutants concentrations. We chose a simple approach, decoupled from any specific chemical species, with a quadratic dependence of the surface tension on the concentration. The independence of the model regarding the nature of the pollutant was a key point of the creation of this model : in experiments, we had no clue about the precise chemical composition of the interface. Thus, in the model, the state of the surface is governed by a new control parameter, β. This closure equation proved sufficient for the range of values of β considered.

The results of this model went beyond our expectations. Firstly, we observed a massive drop of Re_c for a low β value. This Re_c then showed an asymptotic behaviour up to the limit of validity of β and even beyond. This plateau explains well the reproducibility seen in experiments, although the laboratory atmosphere was not controlled. The corresponding value of Re_c is 40% smaller than the experimental threshold, for G=1/14. The frequency of the eigenmode also better match LDV measurements.

The application of the model to G=0.25 has made possible to predict for the first time the mode m=3 as the most unstable. The neutral curve is even more tortuous than for G=1/14 : similarly to this case, the drop of Re_c appears after the crossing of two unstable branches. However, and on the contrary to the case G=1/14, this new most unstable branch does not seem to have an asymptotic behaviour for the highest β values considered. Indeed this asymptotic behaviours was observed by a third branch, that defines a "bubble" of instability, and that may explain the evolution of the flow in the experiments, while Re in increased.

The pollutant model did not only show motivating results. It also gave a new interest to a series of four simulations done one year before. Initially, they were performed to identify the role of the frozen surface on Re_c, whether this condition was applied to the base flow or to perturbations. We found that the lowest Re_c was obtained for a "frozen" base flow, whereas perturbations were computed with a free surface condition. However, at this time, this Re_c was not judged relevant. Surprisingly it matches with the results

of the pollutant model for sufficiently large β. Therefore, the mixed boundary condition was reconsidered : could it be a simple and time-saving solution to compute this flow ? Indeed, the agreements for G=1/14 are confirmed by the excellent results for G=0.25 : not only does the mixed condition model give a good agreement on Re_c, but it is also able to predict m=3 as the most unstable mode.

Larger aspect ratios were also experimented, although our cavity is limited to G=1.5. Quickly we suggested that the surface condition has a very low impact on such G. Computations tends to confirm this. Despite the low variation of Re_c and f, we still observed for G=1.5 a switching of the most unstable mode with the pollutant model. This switch is also present in the mixed condition model, that gave astonishing agreement with results from the more complex model based on the concentration of a pollutant at the interface.

To conclude on our work in this thesis, we may simply say that we demonstrate that the standard free surface condition is not able to effectively represent the air-water interface. One suggested to change the fluid, since water is well-known for its sensitive condition at the interface. Yet experiment proved that results were not that erratic. After sweeping through various models, we finally were able to propose a solution that answer the discrepancies observed between experiments and numerics that existed for a rotating flow with an air-water interface. Although this solution remains perfectible, it confirms that very small surface tension variations are at the origin of discrepancies between numerics and experiments.

Outlooks

As for many research work, any single answer brings dozen of new interrogations. Indeed, although we attempted to gather in this thesis the largest spectrum of investigations on the role of surface tension on the studied instability, there is much left to do.

In the direct continuation of this work, it would be interesting to implement the pollutant model and the mixed condition model into the DNS code. This would allow for visualizing instability patterns, and to compare each others to experimental pictures. Both models also have to tested on other aspect ratios. Since publications are not legion, this means modifying the experimental set-up to study higher G values, to avoid optical issue with LDV, and even to plan the realisation of PIV measurements.

About the large aspect ratios, experimental difficulties limited our field of analysis, although many possibilities are offered. Thanks to the effectiveness of the linear stability analysis code, it would be interesting to draw the curve of Re_c versus G, *i.e.* to extend the figure 3. of [43] to larger values of G, and to determine for which aspect ratio the influence of the surface state vanishes.

Very small aspect ratios are also very complex to study experimentally, mostly because of the uncertainty on the height the fluid. But such G values always display heavy discrepancies between numerics and experiments. Therefore, a new glance at these aspect ratios could be very interesting, especially for the validation of our models.

Another plain outlook is to find a connection between the abstract β parameter and the effective concentration of pollutants. To do so, experiments with controlled concentration of surfactant are to be considered. With a strict experimental protocol, in order to get initially a surface as clean as possible, and an accurate determination of Re_c, one may observe the variation of Re_c regarding the surfactant concentration, and thus check the fitting with the neutral curve obtained with the pollutant model.

On the contrary, one may consider changing the fluid in experiments, for another one, less sensitive to surface tension gradient, such as silicon oil. Doing so should make it possible to obtain experimental Re_c values closer to those predict with the free surface condition.

Finally, we wonder whether the surface state still plays a role on the value of Re_c of the instability that occurs at high Froude number, with a heavy surface deformation. Implementing a model such as the pollutant based one represent a consequent work : the convection-equation, although still applied to the surface only, is no longer 2D. Indeed, since the surface is no longer flat, normal vector is no longer merged with $\mathbf{e_z}$, but will depend on both $\mathbf{e_z}$ and $\mathbf{e_r}$. In addition, the code has to track the surface deformation. This last modification was already done in [51].

Appendix A

Stokes theorem

In this appendix we detailed the mathematical process to go from equation (IX.1) to equation (IX.2), using the Stokes theorem. We remind that this theorem writes :

$$\int_C \mathbf{F} \cdot d\boldsymbol{\ell} = \int_S \mathbf{n} \cdot (\nabla \wedge \mathbf{F}) dS$$

where $\mathbf{n}$ is the normal vector so the surface S.

Along the contour C, $d\boldsymbol{\ell} = \mathbf{m}d\ell$, where $\mathbf{m}$ is a normal vector to the contour C. Therefore, the equation above can be rewritten :

$$\int_C \mathbf{F} \cdot \mathbf{m} d\ell = \int_S \mathbf{n} \cdot (\nabla \wedge \mathbf{F}) dS.$$

If we note $\mathbf{F} = \mathbf{f} \wedge \mathbf{b}$, where $\mathbf{b}$ in an arbitrary constant vector, we obtain :

$$\int_C (\mathbf{f} \wedge \mathbf{b}) \cdot \mathbf{m} d\ell = \int_S \mathbf{n} \cdot (\nabla \wedge (\mathbf{f} \wedge \mathbf{b})) dS.$$

Using identities $(\mathbf{f} \wedge \mathbf{b}) \cdot \mathbf{m} = -\mathbf{b} \cdot (\mathbf{f} \wedge \mathbf{m})$ and $\nabla \wedge (\mathbf{f} \wedge \mathbf{b}) = \mathbf{f}(\nabla \cdot \mathbf{b}) - \mathbf{b}(\nabla \cdot \mathbf{f}) + \mathbf{b} \cdot \nabla \mathbf{f} - \mathbf{f} \cdot \nabla \mathbf{b} = -\mathbf{b}(\nabla \cdot \mathbf{f}) + \mathbf{b} \cdot \nabla \mathbf{f})$, the previous equation becomes :

$$\mathbf{b} \cdot \int_C (\mathbf{f} \wedge \mathbf{m}) d\ell = \mathbf{b} \cdot \int_S \left[\mathbf{n}(\nabla \cdot \mathbf{f}) - (\nabla \mathbf{f}) \cdot \mathbf{n} \right] dS.$$

Since $\mathbf{b}$ is arbitrary, this equation can be simplified to :

$$\int_C (\mathbf{f} \wedge \mathbf{m}) d\ell = \int_S \left[\mathbf{n}(\nabla \cdot \mathbf{f}) - (\nabla \mathbf{f}) \cdot \mathbf{n} \right] dS.$$

In our case, we have $\mathbf{f} = \sigma \mathbf{n}$, and since $\mathbf{n} \wedge \mathbf{m} = -\mathbf{s}$, we can write

$$\begin{cases} -\int_C \sigma \mathbf{s} d\ell = \int_S \left[\mathbf{n} \nabla \cdot (\sigma \mathbf{n}) - \nabla(\sigma \mathbf{n}) \cdot \mathbf{n} \right] dS \\ \qquad\qquad = \int_S \left[\mathbf{n} \nabla \sigma \cdot \mathbf{n} + \sigma \mathbf{n} (\nabla \cdot \mathbf{n}) - \nabla \sigma - \sigma (\nabla \mathbf{n}) \cdot \mathbf{n} \right] dS. \end{cases}$$

Since $\nabla \sigma$ is necessary tangent to the surface S, we have $\nabla \sigma \cdot \mathbf{n} = 0$. In addition, $(\nabla \sigma) \cdot \mathbf{n} = 1/2 \nabla (\mathbf{n} \cdot \mathbf{n}) = 1/2 \nabla (1) = 0$ and thus we finally access to the desired result :

$$\int_C \sigma \mathbf{s} d\ell = \int_S \left[\nabla\sigma - \sigma\mathbf{n}(\nabla\cdot\mathbf{n})\right] dS$$

Appendix B

Evaluation of the error

Experiments are always subject to a finite accuracy because of uncertainty on dimensions or measurements. Besides the errors made in the LDV measurements, that are hard to estimate because many factors are not quantified (such as gap to ideal horizontality, distance to zero, non ideal cylindricity and coaxiality of both cylinder wall, distance to ideal zero ...) we can quantify the error made on the experimental Re_c and G.

For G, only two variables are considered : the cavity radius R and the height of the fluid H. For R, tolerance are given in table B.1. H is evaluated with a graduated steel ruler, in the middle of the cavity to prevent the meniscus on the wall to alter measurement. The rule is graduated every 0.5 mm and thus the error is included between 0 and 0.5 mm. For G=1/14, in the largest cavity, this leads to an uncertainty of 5%. The method to measure H may appear archaic and inaccurate, especially for very small G, however, regarding the gap between experiments and numerics reported in chapters II and VI, it was not our priority to develop a method to obtain a better evaluation of H. Note that in [37], cavity dimensions correspond to G, and therefore are filled up to the top. For G=0.25, their cavity also have a 5% tolerance on H. If we note ΔG the variation of G, we have :

$$\Delta G = \Delta\left(\frac{H}{R}\right) = \frac{\Delta H}{R} + \frac{H\Delta R}{R^2}$$

As we are interested in the relative variation $\Delta G/G$, we can simplify the previous expression as :

$$\frac{\Delta G}{G} = \frac{\Delta H}{H} + \frac{\Delta R}{R}$$

Thus, the final estimation of the relative error made on G is the sum of relative errors on R and H, and worth 5.1% in the largest cavity, and 5.3% in the smallest cavity.

In the same way, Re depends on R, Ω and ν. The uncertainty on Ω is given by the oscillations of the tension provided by the tachometer. According to table B.1, oscillations remains limited, and the tension is known within $\pm 1mV$. As no rotation rate threshold is below 1 rpm, maximum error on Ω is only 2.2%.

Cavity	Large	Small
radius R (mm)	140.3	70
tolerance (mm)	$\pm$ 0.15	$\pm$ 0.1
variation (%)	0.1	0.3

Table B.1 – Error on the value of R for both cavities.

The rotation speed was also checked with a chronometer and a movie of the rotating disc. Agreement was as close as possible with such an elementary method.

Ω (rpm)	1	2	5	10
tension targeted (mV)	72	144	360	720
V_{min} (mV)	71.308	142.96	358.75	719.76
V_{max} (mV)	72.923	144.85	61.00	721.07
error (%)	2.2	1.3	0.63	0.18

Table B.2 – Error on the value of Ω.

The uncertainty on ν is harder to evaluate, as the kinematic viscosity is estimated with the law given in [56]. We chose to employ this law as the use of viscometer with low viscosity fluid such as water gives inconsistent results. Therefore we assessed that the error with the effective value of ν would not be worse with this law than with viscometer, but is much easier to apply. The error on ν then depends on the temperature and on the weight percentage of glycerol in the fluid. The temperature is known within an accuracy of 0.1 K.

T $(°C)$	19		20		21		25		26	
$\nu(\times 10^{-6} m^2 s^{-1})$	1.032		1.007		0.9828		0.8956		0.8757	
ΔT=0.1$(°C)$	-	+	-	+	-	+	-	+	-	+
error on ν (%)	0.247	0.246	0.244	0.243	0.240	0.239	0.226	0.225	0.233	0.222

Table B.3 – Error on the value of ν for a temperature variation of $\pm 0.1°K$ around fiver representative temperatures measured while running experiments.

Table B.2 gives an estimation of the error on ν, that remains around 0.25% on the span of temperature that is representative of temperatures that were measured in the fluid during experiments. In the case of a water glycerol mixture, the effective mass percentage is actually very delicate to estimate : although the mixture were carefully prepared with high precision scale, the composition of glycerol can evolve with time. Indeed, as glycerol absorbs water present in ambient air, its purity is no longer optimal therefore an unknown error is made on the mass percentage of the mixture. Without considering this issue, the error on ν in the case of a 40% glycerol mixture is around 0.3%.

As we did for the division earlier, we can demonstrate that $\Delta(R^2\Omega = 2\Delta R/R + \Delta\Omega/\Omega$, and thus :

$$\frac{\Delta Re}{Re} = \frac{2\Delta R}{R} + \frac{\Delta\Omega}{\Omega} + \frac{\Delta\nu}{\nu}$$

Finally, the relative error on Re values is around 2.7% in the largest cavity, and 3.1% in the smallest cavity. These errors are optimistic, but we can reasonably think that experimental Reynolds numbers are known with $\approx 5\%$ accuracy.

Appendix C

LDV corrections

This appendix is dedicated to details about the optical corrections applied to LDV measurement. [53]. Note that the notations used here do not correspond to the nomenclature. Indeed, optical standards were kept, such as λ for the wavelength, and n for optical indices. Since corrections are not the same depending on whether the measurement is made on u_θ or u_z, both configurations are considered below.

In the second case (u_z measurement), the laser beams lie in the same meridional plane, and normal vectors to interface are parallels. Thus Snell-Descartes laws give : $n_a sin(\theta_a/2) = n_c sin(\theta_c/2) = n_w sin(\theta_w/2)$ where the indices a, c & w stand for air, cavity and water, respectively. Starting from equation (III.1), and considering that $\theta_a/2 = \theta_L$ is the angle made by beams in the absence of interface crossing, we easily obtain :

$$\frac{f_r}{2u_p} = \frac{2\sin(\theta_a/2)}{\lambda_a} = \frac{2\sin(\theta_w/2)}{\lambda_w}. \tag{C.1}$$

with $\lambda_i = f/(n_i c)$, where c is the speed of light in vacuum and i index is relative to the medium crossed.

Here, crossing various media has no influence on the values of the measured velocity, and only the position of measurement is shifted. However in the first case (u_θ measurement), curvature effect affects the measurement : since normal straight lines to inner and outer walls are no longer parallel, equation (C.1) does not hold any more. Therefore a correction coefficient C_θ has to be applied.

$$C_\theta = \frac{u_{p,real}}{u_{p,measured}} \tag{C.2}$$

where $u_{p,measured}$ is estimated relatively to $\theta_a/2$, while $u_{p,real}$, should consider $\theta_w/2$. Starting from equation (III.1), we can write :

$$\begin{cases} u_{p,measured} = \dfrac{f_r \lambda_a}{2\sin(\theta_a/2)}, \\ u_{p,real} = \dfrac{f_r \lambda_w}{2\sin(\theta_w/2)}. \end{cases} \tag{C.3a}$$

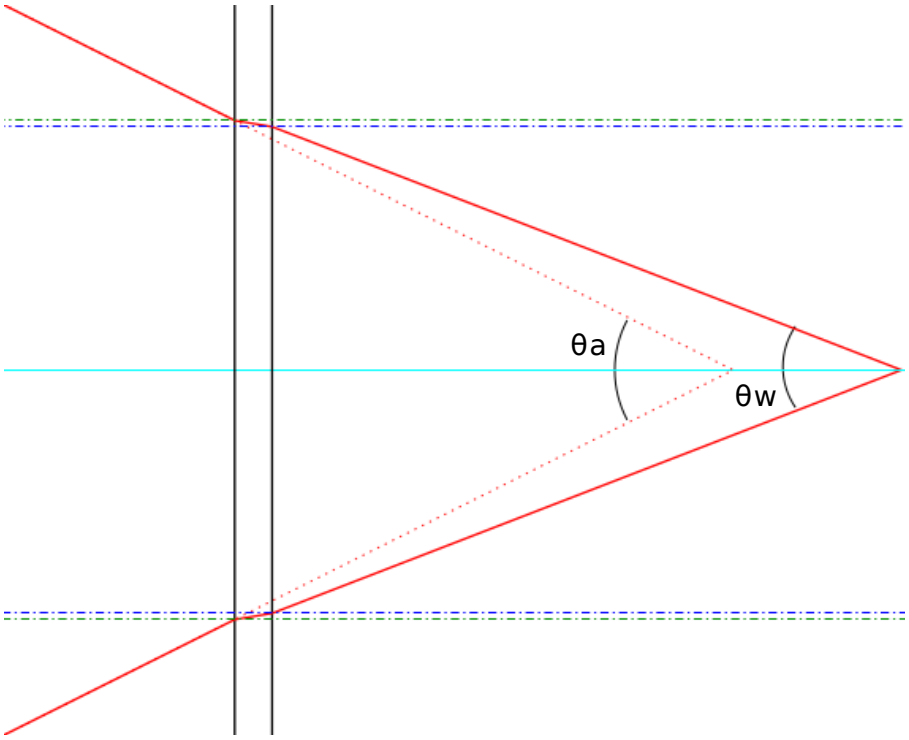

Figure C.1 – Illustration of effective path of laser beams (red plain lines) in the vertical configuration (u_z measurement). Red doted lines are the hypothetical path of beams if there was only one medium. Black plain lines are inner and outer walls of the cavity. Dark blue and green doted lines are normals to the inner wall and the outer wall, respectively. The cyan plain line is the axis of symmetry. Angles are not to scale.

Thus, from equations (C.2) and (C.3a), it quickly comes :

$$C_\theta = \frac{n_a \sin(\theta_a/2)}{n_w \sin(\theta_w/2)}$$

With these corrections, the LDV measurements give us instantaneous velocity signal in one point of the flow, through a selected time scope. The post-processing on these signals can return average and RMS velocities, or frequencies of oscillations that exist in velocity signals, owing to Fourier transform. An example of differences that exist in LDV measurements between corrected and uncorrected data is given in figure C.3.

The LDV device is able to detect particles for radius that are "outside" the cavity, as shown in figure C.3, which confirms the need for a correction. However, the theoretical correction places the zero at r <1. This under-evaluation was also observed only pure water, and with both glass (see fig. VI.32) and plexiglass walls. Error is probably caused by inaccurate refraction indices, for fluids, cavity or both of them.

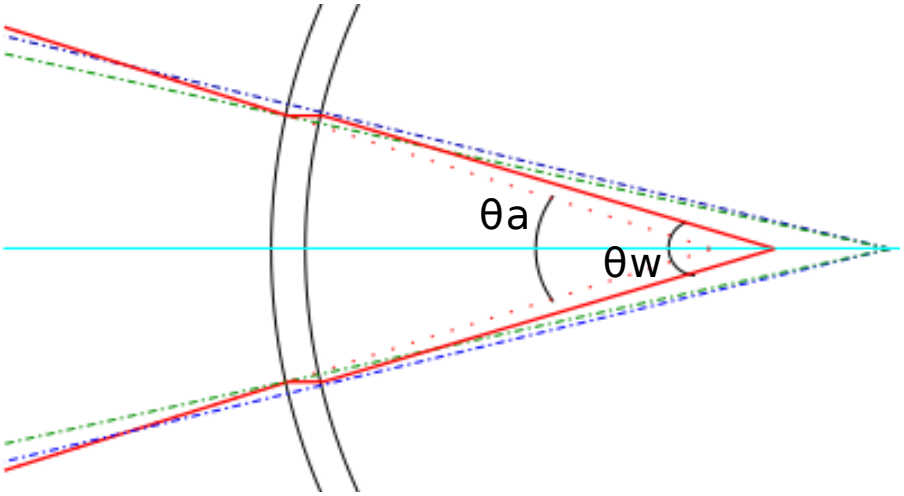

Figure C.2 – Illustration of effective path of laser beams (red plain lines) in the horizontal configuration (u_θ measurement). The color code is the same as in figure C.1. Note that normals cross at the center of the cavity.

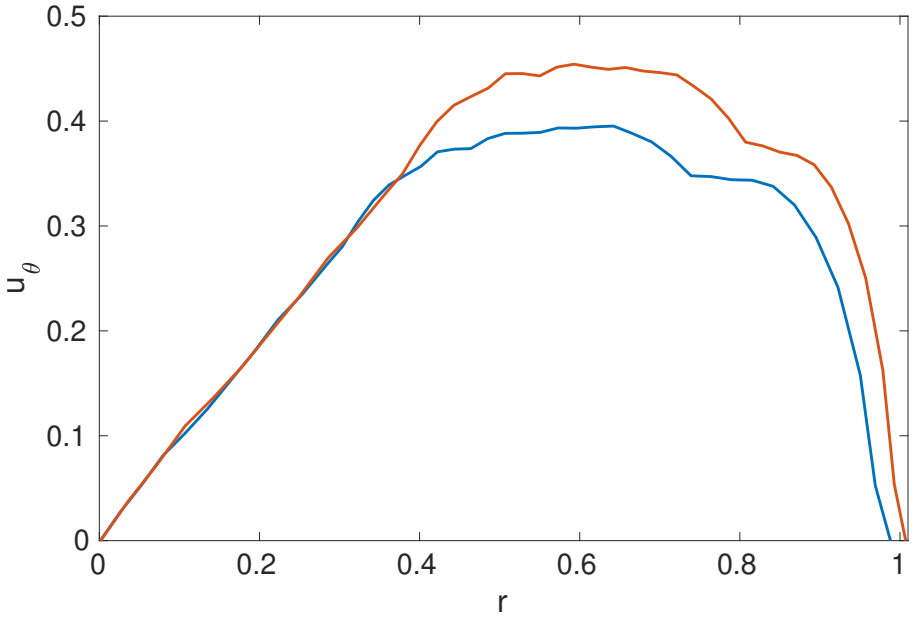

Figure C.3 – Comparaison of corrected (blue) and raw (orange) u_θ LDV profile, for G=0.25 and Re=1895. The fluid used was a 40% glycerol mixture, in the large plexiglas cavity.

Internet sources

- Figure .1 : https://svs.gsfc.nasa.gov/vis/a010000/a012500/a012550.
- Figure .2 : https://qph.fs.quoracdn.net/main-qimg-9c91ac489ef9f25bb14140897dd827a7.
- Figure .3 : https://thesis.library.caltech.edu/1143/.
- Figure .4 : http://www.earthscienceguy.com/2019/03/kelvin-helmholtz-clouds-caused-by-wind.html.
- Figure .6 : http://lgef.insa-lyon.fr/fr/content/materiaux-electro-actifs.
- Figure .7 : https://www.sciencedirect.com/science/article/pii/S0889974616304121.
- Figure I.7b : https://twitter.com/kevinmgill/status/948253930596712448.
- Figure III.4 : https://physics.stackexchange.com/questions/317051/michelson-interferometer-circular-fringes.
- Figure III.6 : https://www.compadre.org/advlabs/wiki/Taylor-Couette_Flow.
- Figure IV.1 : https://www.newscientist.com/article/dn14030-liquid-mirror-telescopes-are-a-reality-at-last/.
- Figure VII.6 : https://astropassion-jc.pagesperso-orange.fr/precession.html.
- Figure IX.1 : https://clairegogendeau.wixsite.com/tpe-bdc/la-tension-superficielle.
- Figure IX.2 : https://m.tau.ac.il/ phchlab/exp-tension-theory.html.

Bibliography

[1] V. W. Ekman, "On the influence of the Earth's rotation on the ocean-currents," *Arkiv. Mat. Astr. Fys.*, vol. 2, no. 11, pp. 1–52, 1905.

[2] T. von Kármán, "Über laminare und turbulente Reibung," *Z. Angew. Math. Mech.*, vol. 1, pp. 233–252, 1921.

[3] R. J. Lingwood, "Absolute instability of the Ekman layer and related rotating flows," *J. Fluid Mech.*, vol. 331, pp. 405–428, 1997.

[4] G. K. Batchelor, "Note on a class of solutions of the Navier-Stokes equations representing steady rotationally-symmetric flow," *Q. J. Mech. Appl. Math.*, vol. 4, pp. 29–41, 1951.

[5] K. Stewartson, "On the flow between two rotating coaxial disks," *Proc. Camb. Phil. Soc.*, vol. 49, pp. 333–341, 1953.

[6] H.-O. Kreiss and S. V. Parter, "On the swirling flow between rotating coaxial disks : Existence and nonuniqueness," *Comm. Pure Appl. Math.*, vol. 36, pp. 55 – 84, 01 1983.

[7] D. Peckham and S. Atkinson, *Preliminary results of low speed wind tunnel tests on a gothic wing of aspect ratio 1.0.* Royal Aircraft Establishment, 1957.

[8] N. Lambourne, D. Bryer, and A. R. C. (G.B.), *The Bursting of Leading-edge Vortices: Some Observations and Discussion of the Phenomenon.* Reports and memoranda / Aeronautical Research Council, H.M. Stationery Office, 1962.

[9] H. Vogel, "Experimentelle Ergebnisse über die laminare Strömung in einem Zylindrischen gehause mit darin rotierender Scheibe.," *Tech. Rep.*, pp. Max–Planck Institute, 1968.

[10] H. J. Lugt and H. J. Haussling, "Axisymmetric vortex breakdown in rotating fluid within a container," *J. Appl. Mech*, vol. 49, pp. 921–923, 11 1982.

[11] M. P. Escudier, "Observations of the flow produced in a cylindrical container by a rotating end wall," *Exp. Fluids*, vol. 2, pp. 189–196, 1984.

[12] A. Spohn, M. Mory, and E. Hopfinger, "Observations of vortex breakdown in an open cylindrical container with a rotating bottom," *Exp. Fluids*, vol. 14, pp. 70–77, 1993.

[13] E. Serre, M. Schäfer, and P. Bontoux, *Vortex breakdown in a cylinder with a free surface*, pp. 1125 – 1127. Oxford: Elsevier Science Ltd, 2003.

[14] E. Serre and P. Bontoux, "Vortex breakdown in a cylinder with a rotating bottom and a flat stress-free surface," *Int. J. Heat Fluid Flow*, vol. 28, pp. 229–248, 2007.

[15] M. Piva and E. Meiburg, "Steady axisymmetric flow in an open cylindrical container with a partially rotating bottom wall," *Phys. Fluids*, vol. 17, no. 6, p. 063603(12), 2005.

[16] R. Iwatsu, "Numerical study of flows in a cylindrical container with rotating bottom and top flat free surface," *J. Phys. Soc. Jpn.*, vol. 74, pp. 333–344, 01 2005.

[17] H. Niino and N. Misawa, "An experimental and theoretical study of barotropic instability," *J. Atmos. Sci.*, vol. 41, no. 12, pp. 1992–2011, 1984.

[18] A. C. B. Aguiar, P. L. Read, R. D. Wordsworth, T. Salter, and Y. H. Yamazaki, "A laboratory model of Saturn's north polar hexagon," *Icarus*, vol. 206, no. 2, pp. 755 – 763, 2010.

[19] A. Y. Gelfgat, "Primary oscillatory instability in a rotating disk-cylinder system with aspect (height/radius) ratio varying from 0.1 to 1," *Fluid Dyn. Res.*, vol. 47, p. 035502(14), 2015.

[20] O. Daube and P. Le Quéré, "Numerical investigation of the first bifurcation for the flow in a rotor-stator cavity of radial aspect ratio 10," *Computers & Fluids*, vol. 31, pp. 481–494, 2002.

[21] G. Gauthier, *Étude expérimentale des instabilités de l'écoulement entre deux disques*. PhD thesis, Université Paris XI, France, 1998.

[22] H. Goller and T. Ranov, "Unsteady rotating flow in a cylinder with a free surface," *J. Basic Eng.*, vol. 90, no. 4, pp. 445–452, 1968.

[23] A. Siginer and R. Knight, "Swirling free surface flow in cylindrical containers," *J. Eng. Math.*, vol. 27, no. 3, pp. 245–264, 1993.

[24] J. Mougel, D. Fabre, and L. Lacaze, "Waves in Newton's bucket," *J. Fluid Mech.*, vol. 783, pp. 211–250, 2015.

[25] G. H. Vatistas, "A note on liquid vortex sloshing and Kelvin's equilibria," *J. Fluid Mech.*, vol. 217, pp. 241–248, 1990.

[26] G. H. Vatistas, J. Wang, and S. Lin, "Experiments on waves induced in the hollow core of vortices," *Exp. Fluids*, vol. 13, pp. 377–385, 1992.

[27] T. R. N. Jansson, M. P. Haspang, K. H. Jensen, P. Hersen, and T. Bohr, "Polygons on a rotating fluid surface," *Phys. Rev. Lett.*, vol. 96, p. 174502, 2006.

[28] T. Suzuki, M. Iima, and Y. Hayase, "Surface switching of rotating fluid in a cylinder," *Phys. Fluids*, vol. 18, p. 101701(4), 2006.

[29] Y. Tasaka and M. Iima, "Flow transitions in the surface switching of rotating fluid," *J. Fluid Mech.*, vol. 636, pp. 475–484, 2009.

[30] L. Tophøj, J. Mougel, T. Bohr, and D. Fabre, "Rotating polygon instability of a swirling free surface flow," *Phys. Rev. Lett.*, vol. 110, p. 194502, May 2013.

[31] J. Mougel, D. Fabre, L. Lacaze, and T. Bohr, "On the instabilities of a potential vortex with a free surface," *J. Fluid Mech.*, vol. 824, pp. 230–264, 2017.

[32] J. M. Hyun, "Flow in an open tank with a free surface driven by the spinning bottom," *J. Fluids Eng.*, vol. 107, no. 4, pp. 495–499, 1985.

[33] R. Iwatsu, "Analysis of flows in a cylindrical container with rotating bottom and top underformable free surface," *JSME Int. Journ.*, vol. 47, no. 3, pp. 549–556, 2004.

[34] D. L. Young, H. J. Sheen, and T. Y. Hwu, "Period-doubling route to chaos for a swirling flow in an open cylindrical container with a rotating disk," *Exp. Fluids*, vol. 18, pp. 389–396, 1995.

[35] A. H. Hirsa, J. M. Lopez, and R. Miraghaie, "Symmetry breaking to a rotating wave in a lid-driven cylinder with a free surface: Experimental observation," *Phys. Fluids*, vol. 14, no. 6, pp. 29–32, 2002.

[36] R. Miraghaie, J. M. Lopez, and A. H. Hirsa, "Flow induced patterning at the air–water interface," *Phys. Fluids*, vol. 15, no. 6, pp. L45–L48, 2003.

[37] J. M. Lopez, F. Marques, A. H. Hirsa, and R. Miraghaie, "Symmetry breaking in free-surface cylinder flows," *J. Fluid Mech.*, vol. 502, pp. 99–126, 2004.

[38] M. J. Vogel, R. Miraghaie, J. M. Lopez, and A. H. Hirsa, "Flow-induced patterning of langmuir monolayers," *Langmuir*, vol. 20, pp. 5651–4, 08 2004.

[39] A. H. Hirsa, J. M. Lopez, and R. Miraghaie, "Measurement and computation of hydrodynamic coupling at an air/water interface with an insoluble monolayer," *J. Fluid Mech.*, vol. 443, pp. 271–292, 2001.

[40] S. Poncet and M. Chauve, "Shear-layer instability in a rotating system," *J. Flow Visual. Image Process.*, vol. 14, no. 1, pp. 85–105, 2007.

[41] Y. Kwan, J. Park, and J. Shen, "A mathematical and numerical study of incompressible flows with a surfactant monolayer," *Discrete Contin. Dyn. S.*, vol. 28, pp. 181–197, 2010.

[42] L. Kahouadji, *Analyse de stabilité linéaire d'écoulements tournants en présence de surface libre*. PhD thesis, Université Pierre et Marie Curie, Paris, France, October 2011.

[43] L. Kahouadji, L. M. Witkowski, and P. Le Quéré, "Seuils de stabilité pour un écoulement à surface libre engendré dans une cavité cylindrique tournante à petit rapport de forme," *Mécanique et Industries*, vol. 11, pp. 339–344, 2010.

[44] S. J. Cogan, K. Ryan, and G. J. Sheard, "Symmetry breaking and instability mechanisms in medium depth torsionally open cylinder flows," *J. Fluid Mech.*, vol. 672, pp. 521–544, 2011.

[45] N. Cousin-Rittemard, O. Daube, and P. Le Quéré, "Description des couches limites des écoulements stationnaires interdisques en configuration rotor–stator," *C. R. Acad. Sci., Ser. II b*, vol. 327, pp. 215–220, 1999.

[46] C. Nore, L. M. Witkowski, E. Foucault, J. Pécheux, O. Daube, and P. L. Quéré, "Competition between axisymmetric and three-dimensional patterns between exactly counter-rotating disks," *Phys. Fluids*, vol. 18, p. 054102, 2006.

[47] L. Martin Witkowski, I. Delbende, P. Le Quéré, and J. S. Walker, "Axisymmetric stability of the flow between two exactly counter-rotating disks with large aspect ratio," *J. Fluid Mech.*, vol. 546, pp. 193–202, 2006.

[48] E. Pélissier, "Mesures et calculs de la déformation d'une surface libre engendrée par un disque en rotation," Master's thesis, Université Pierre et Marie Curie, France, 2012.

[49] A. Faugaret, "Détermination expérimentale des seuils d'instabilité d'un écoulement engendré par un disque tournant en présence d'une surface libre," Master's thesis, Université Pierre et Marie Curie, France, 2013.

[50] A. Faugaret, "Étude des instabilités de l'écoulement engendré par un disque tournant en présence de surface libre : Confrontation expérimentale et numérique," stage M2, Université Pierre et Marie Curie, France, 2014. 15 avril – 15 septembre.

[51] W. Yang, *Études expérimentales et numériques d'écoulements tournants à surface libre déformable*. PhD thesis, Université Pierre et Marie Curie, Paris, France, Décembre 2018.

[52] F. Moisy, T. Pasutto, and M. Rabaud, "Instability patterns between counter-rotating disks," *Nonlinear Process. Geophys.*, vol. 10, 05 2003.

[53] S. G. Huisman, D. P. van Gils, and C. Sun, "Applying laser Doppler anemometry inside a Taylor–Couette geometry using a ray-tracer to correct for curvature effects," *Eur. J. Mech.* B*/Fluids*, vol. 36, pp. 115–119, 2012.

[54] K. Takamura, H. Fischer, and N. R. Morrow, "Physical properties of aqueous glycerol solutions," *J. Petrol. Sci. Eng.*, vol. 98-99, pp. 50 – 60, 2012.

[55] G. P. Association, *Physical Properties of Glycerine and Its Solutions*. Glycerine Producers' Association, 1963.

[56] N.-S. Cheng, ""formula for the viscosity of a glycerol-water mixture"," *Ind. Eng. Chem. Res.*, vol. 47, pp. 3285–3288, 05 2008.

[57] D. Borrero-Echeverry, C. J. Crowley, and T. P. Riddick, "Rheoscopic fluids in a post-kalliroscope world," *Phys. Fluids*, vol. 30, no. 8, p. 087103, 2018.

[58] M. A. Dominguez-Lerma, G. Ahlers, and D. S. Cannell, "Effects of "kalliroscope" flow visualization particles on rotating couette-taylor flow," *Phys. Fluids*, vol. 28, no. 4, pp. 1204–1206, 1985.

[59] P. Matisse and M. Gorman, "Neutrally buoyant anisotropic particles for flow visualization," *Phys. Fluids*, vol. 27, no. 4, pp. 759–760, 1984.

[60] L. Kahouadji, B. C. Houchens, and L. M. Witkowski, "Thermocapillary instabilities in a laterally heated liquid bridge with end wall rotation," *Phys. Fluids*, vol. 23, p. 104104(16), 2011.

[61] G. Ryskin and L. Leal, "Numerical solution of free-boundary problems in fluid mechanics. part 1. the finite-difference technique," *J. Fluid Mech.*, vol. 148, pp. 1–17, 1984.

[62] G. Ryskin and L. Leal, "Numerical solution of free-boundary problems in fluid mechanics. part 2. buoyancy-driven motion of a gas bubble through a quiescent liquid.," *J. Fluid Mech.*, vol. 148, pp. 19–35, 1984.

[63] G. Ryskin and L. Leal, "Numerical solution of free-boundary problems in fluid mechanics. part 3. bubble deformation in an axisymmetric straining flow," *J. Fluid Mech.*, vol. 148, pp. 37–43, 1984.

[64] L. N. Trefethen, A. E. Trefethen, S. C. Reddy, and T. A. Driscoll, "Hydrodynamic stability without eigenvalues," *Science*, vol. 261, no. 5121, pp. 578–584, 1993.

[65] W. Yang, I. Delbende, Y. Fraigneau, and L. Martin Witkowski, "Large axisymmetric surface deformation and dewetting in the flow above a rotating disk in a cylindrical tank: spin-up and permanent regimes," *Phys. Rev. Fluids*, 2019. submitted.

[66] R. Bouffanais and D. Lo Jacono, "Transitional cylindrical swirling flow in presence of a flat free surface," *Computers & Fluids*, vol. 38, pp. 1651–1673, 2009.

[67] M. Le Bars and P. Le Gal, "Experimental analysis of the stratorotational instability in a cylindrical couette flow," *Phys. Rev. Lett.*, vol. 99, p. 064502, Aug 2007.

[68] N. Abcha, N. Latrache, F. Dumouchel, and I. Mutabazi, "Qualitative relation between reflected light intensity by kalliroscope flakes and velocity field in the couette–taylor flow system," *Exp. Fluids*, vol. 45, pp. 85–94, Jul 2008.

[69] A. Spohn and O. Daube, "Recirculating flows in a cylindrical tank," in *V Int. Conf. Computational Methods and Experimental Measurement* (A. Sousa, C. A. Brebbia, and G. M. Carlomagno, eds.), (Montreal), pp. 155–166, Elsevier, July 1991.

[70] J. M. Lopez and A. H. Hirsa, "Surfactant-influenced gas–liquid interfaces: Nonlinear equation of state and finite surface viscosities," *J. Colloid Interface Sci.*, vol. 229, no. 2, pp. 575 – 583, 2000.

[71] A. H. Hirsa, J. M. Lopez, and R. Miraghaie, "Determination of surface shear viscosity via deep-channel flow with inertia," *J. Fluid Mech.*, vol. 470, pp. 135–149, 2002.

[72] J. M. Lopez and J. Chen, "Coupling between a viscoelastic gas/liquid interface and a swirling vortex flow," *J. Fluids Eng.*, vol. 120, pp. 655–661, 12 1998.

[73] F. J. Peaudecerf, J. R. Landel, R. E. Goldstein, and P. Luzzatto-Fegiz, "Traces of surfactants can severely limit the drag reduction of superhydrophobic surfaces," *Proc. Natl. Acad. Sci*, vol. 114, no. 28, pp. 7254–7259, 2017.

[74] M. M. Bandi, V. S. Akella, D. K. Singh, R. S. Singh, and S. Mandre, "Hydrodynamic signatures of stationary Marangoni-driven surfactant transport," *Phys. Rev. Lett.*, vol. 119, p. 264501, 2017.

[75] H. Stone, "A simple derivation of the time-dependent convective-diffusion equation for surfactant transport along a deforming surface," *Phys. Fluids*, vol. 2, pp. 111–112, 1990.

Antoine FAUGARET **25 septembre 2020**

Sujet : Influence de la condition à l'interface air-eau sur la stabilité d'un écoulement tournant : exploration numérique et experimentale.

Résumé : Notre étude porte sur la première instabilité qui apparait dans un écoulement engendré par un disque tournant au fond d'une cavité cylindrique fixe, avec une interface liquide-gaz non déformée. Grace à la double approche numérique et expérimentale, nous révélons un écart important sur le seuil d'apparition de cette instabilité. Après avoir supposé et infirmé que des vibrations d'origine mécanique puissent être responsables de ces écarts, notre étude s'est orientée sur l'influence de la condition limite à l'interface utilisée dans les simulations. Nous montrons que la condition de glissement libre ne permet pas de simuler le même écoulement que dans les expériences. Dans le but de réduire ces différences, nous explorons successivement plusieurs modélisations de cette interface. La prise en compte des variations de la tension de surface en fonction de la concentration d'un polluant à l'interface à notamment permis de réduire considérablement l'erreur commise sur le nombre de Reynolds critique, et de reproduire plus fidèlement l'écoulement dans les simulations.

Mots clés : Ecoulement tournant, tension de surface, simulation, DNS, analyse de stabilité linéaire, condition limite à l'interface air-eau, expérimental, vibrations, LDV

Subject : Influence of air-water interface condition on rotating flow stability : experimental and numerical exploration.

Abstract: Our study focuses on the first instability that appears in a flow generated by a rotating disc placed at the bottom of a fixed cylindrical cavity, with a flat liquid-gas interface. Owing to the dual numerical and experimental approach, we highlight a robust mismatch on the threshold of this instability. After having assumed and later ruled out that mechanical vibrations could be responsible for these mismatches, this investigation has focused on the boundary condition used in simulations at the interface air-water and its influence on the flow. We show that the free slip condition does not allow to simulate the same flow as in the experiments. Several models of this interface are explored in order to reduce the mismatches. In particular, taking into account variations in surface tension depending on the concentration of a pollutant at the interface results in a considerable reduction of the error on the critical Reynolds number, and to a more accurate reproduction of the flow in the simulations.

Keywords : Rotating flow, surface tension, simulation, DNS, linear stability analysis, boundary condition at the air/water interface, experimental, vibrations, LDV